SPECIAL ISSUE

ASTROPHYSICAL SPECTROSCOPY - A&M DATA - ASTRONOMY AND EARTH OBSERVATIONS

Based on lectures presented at
V Meeting on Astrophysical Spectroscopy -
A&M DATA - Astronomy & Earth Observations

Palić, Serbia, September 12-15, 2023

CONTRIBUTIONS OF THE ASTRONOMICAL OBSERVATORY SKALNATÉ PLESO

● VOLUME LIII ●

Number 3

December 2023

Editorial Board

CONTENTS

3

Session C: A&M DATA - ATMOSPHERE MODELS

4

The Contributions of the Astronomical Observatory Skalnaté Pleso
are available in a full version
in the frame of ADS Abstract Service
and can be downloaded in a usual way from the URL address:

''http://adsabs.harvard.edu/article_service.html''

as well as from the web-site of
the Astronomical Institute of the Slovak Academy of Sciences
on the URL address:

''http://www.astro.sk/caosp/''

The journal is covered/indexed by:

Web of Science (WoS)

WoS Core Collection: Science Citation Index Expanded

SCOPUS

Index Copernicus International

SPECIAL ISSUE
Astrophysical Spectroscopy - A&M DATA - Astronomy and Earth Observations

Edited by

Vladimir A. Srećković, Milan S. Dimitrijević, Nikola Cvetanović

Based on lectures presented at

V Meeting on Astrophysical Spectroscopy - A&M DATA - Astronomy & Earth Observations

September 12 – 15, 2023, Palić, Serbia

Institute of Physics Belgrade, University of Belgrade

http://asspectro2023.ipb.ac.rs/

Scientific Organizing Committee

Vladimir A. Srećković, co-chair (Serbia)
Milan S. Dimitrijević, co-chair (Serbia)
Nikolay Bezuglov (Russia)
Nebil Ben Nessib (Saudi Arabia)
Vesna Borka Jovanović (Serbia)
Nikola Cvetanović (Serbia)
Saša Dujko (Serbia)
Stevica Đurović (Serbia)
Zoran Grujić (Serbia)
Rafik Hamdi (Tunisia)
Magdalena D. Christova (Bulgaria)
Dragana Ilić (Serbia)
Milivoje Ivković (Serbia)
Darko Jevremović (Serbia)
Ognyan Kounchev (Bulgaria)
Bratislav P. Marinković (Serbia)
Zoran R. Mijić (Serbia)
Aleksandar Milosavljević (France)
Aleksandra Nina (Serbia)
Bratislav M. Obradović (Serbia)
Nicolina Pop (Romania)
Luka Č. Popović (Serbia)
Branko Predojević (Republic of Srpska, BiH)
Sylvie Sahal-Bréchot (France)
Igor Savić (Serbia)
Sanja Tošić (Serbia)
Nikola B. Veselinović (Serbia)

Local Organizing Committee

Aleksandra Kolarski, co-chair
Vladimir A. Sreckович, co-chair
Nikola B. Veselinovic, secretary
Zoran R. Mijić
Nenad M. Sakan
Veljko Vujčić
Nikola Cvetanović

The participants of V Meeting on Astrophysical Spectroscopy - A&M DATA – Astronomy & Earth Observations.

LIST OF PARTICIPANTS

Arnaut, Filip	Institute of Physics Belgrade, Pregrevica 118, 11080 Belgrade, Serbia
Banjanac, Radomir M.	Institute of Physics Belgrade, Pregrevica 118, 11080 Belgrade, Serbia
Barović, Jelena	University of Montenegro, Podgorica, Montenegro
Belov, Anatoly	IZMIRAN, Russian Academy of Science, Moscow, Russia
Bezuglov, Nikolai	Institute of Atomic Physics and Spectroscopy, University of Latvia, Riga, Latvia
Blanco, F.	Departamento de Física Atómica Molecular y Nuclear, Facultad de Ciencias Físicas, Universidad Complutense, Avda. Complutense s/n, E-28040 Madrid, Spain
Bofelli, J.	Laboratoire Ondes & Milieux Complexes CNRS-UMR-6294, Université du Havre, 76058 Le Havre, France
Borka, Duško	Department of Theoretical Physics and Condensed Matter Physics (020), Vinča Institute of Nuclear Sciences - National Institute of the Republic of Serbia
Borka Jovanović, Vesna	Department of Theoretical Physics and Condensed Matter Physics (020), Vinča Institute of Nuclear Sciences - National Institute of the Republic of Serbia
Bošnjaković, Danko V.	Institute of Physics Belgrade, Pregrevica 118, 11080 Belgrade, Serbia
Capozziello, Salvatore	Scuola Superiore Meridionale, Largo S. Marcellino 10, I-80138, Napoli, Italy
Christova, Magdalena D.	Department of Applied Physics, Technical University of Sofia, 1000 Sofia, Bulgaria
Ćirišan, Ana	Faculty of Ecology and Environmental Protection, Union-Nikola Tesla University, Belgrade, Serbia
Cvetanović, Nikola	Faculty of Transport and Traffic Engineering, 11010 Belgrade, Serbia
Dechev, Momchil	Institute of Astronomy and NAO, Bulgarian Academy of Sciences, Sofia, Bulgaria
Dimitrijević, Milan S.	Astronomical Observatory, Volgina 7, 11060 Belgrade, Serbia
Djuissi, E.	Laboratoire Ondes & Milieux Complexes CNRS-UMR-6294, Université du Havre, 76058 Le Havre, France

Dragić, Aleksandar L.	Institute of Physics Belgrade, Pregrevica 118, 11080 Belgrade, Serbia
Dujko, Saša	Institute of Physics Belgrade, Pregrevica 118, 11080 Belgrade, Serbia
García, G.	Instituto de Matemáticas y Fíica Fundamental, Consejo Superior de Investigaciones Científicas, Serrano 121, 28006 Madrid, Spain
Hržina, Damir	Zagreb Astronomical Observatory, Opatička 22, 10000 Zagreb, Croatia
Iacob, F.	Physics Faculty, West University of Timişoara, Timişoara, Romania
Ignjatović, Ljubinko M.	Institute of Physics Belgrade, Pregrevica 118, 11080 Belgrade, Serbia
Ilić, Luka	Barcelona Supercomputing Center, Plaça Eusebi Güell, 1-3, 08034 Barcelona, Spain
Ivanović, Nikola V.	University of Belgrade, Faculty of Agriculture, Nemanjina 6, 11080 Belgrade, Serbia
Ivković, Saša S.	University of Belgrade, Faculty of Physics, 11001 Belgrade, Serbia
Jevremović, Darko	Astronomical Observatory, Volgina 7, 11060 Belgrade, Serbia
Joković, Dejan R.	Institute of Physics Belgrade, Pregrevica 118, 11080 Belgrade, Serbia
Jovanović, Predrag	Astronomical Observatory, Volgina 7, 11060 Belgrade, Serbia
Jovović, Jovica	Faculty of Physics, University of Belgrade, P.O. Box 44, Belgrade, Serbia
Knežević, David	Institute of Physics Belgrade, Pregrevica 118, 11080 Belgrade, Serbia
Kolarski, Aleksandra	Institute of Physics Belgrade, Pregrevica 118, 11080 Belgrade, Serbia
Konjević, Nikola	Serbian Academy of Sciences and Arts, Kneza Mihaila 35, 11000 Belgrade, Serbia
Kuzmanoski, Maja	Institute of Physics Belgrade, Pregrevica 118, 11080 Belgrade, Serbia
Majlinger, Zlatko	ES "V. Gortan", Prilaz Vladimira Gortana 2, 51000 Rijeka, Croatia
Majstorović, Gordana Lj.	Military Academy, University of Defence, Veljka Lukića Kurjaka 33, Belgrade, Serbia
Maletić, Dimitrije M.	Institute of Physics Belgrade, Pregrevica 118, 11080 Belgrade, Serbia
Maljković, Jelena B.	Institute of Physics Belgrade, Pregrevica 118, 11080 Belgrade, Serbia

9

Marić, Dragana	Institute of Physics Belgrade, Pregrevica 118, 11080 Belgrade, Serbia
Maričić, Darije	Zagreb Astronomical Observatory, Opatička 22, 10000 Zagreb, Croatia
Marinković, Bratislav P.	Institute of Physics Belgrade, Pregrevica 118, 11080 Belgrade, Serbia
Marjanović, Jelena	Institute of Physics Belgrade, Pregrevica 118, 11080 Belgrade, Serbia
Mezei, J. Zs	Institute for Nuclear Research, Hungarian Academy of Sciences, H-4001 Debrecen, Hungary
Mijić, Zoran R.	Institute of Physics Belgrade, Pregrevica 118, 11080 Belgrade, Serbia
Nedić, Nikodin V.	University of Belgrade, Faculty of Physics 11001 Belgrade, P.O. Box 44, Serbia
Nikitović, Željka D.	Institute of Physics Belgrade, Pregrevica 118, 11080 Belgrade, Serbia
Obradović, Bratislav M.	University of Belgrade, Faculty of Physics, 11001 Belgrade, Serbia
Petrović, Zoran Lj.	School of Engineering, Ulster University, Jordanstown, County Antrim BT37 0QB, United Kingdom
Podraščanin, Zorica	Department of Physics, Faculty of Sciences, University of Novi Sad, Novi Sad, Serbia
Pop, Nicolina	Department of Physical Foundations of Engineering, Politehnica University of Timisoara 2 Vasile Parvan Blvd, 300223 Timisoara, Romania
Pourbeyranv, Shahrokh	International Institute of Earthquake Engineering and Seismology, Iran
Raspopović, Zoran M.	Institute of Physics Belgrade, Pregrevica 118, 11080 Belgrade, Serbia
Romštajn, Ivan	Zagreb Astronomical Observatory, Opaticka 22, 10000 Zagreb, Croatia
Roša, Dragan	Zagreb Astronomical Observatory, Opatička 22, 10000 Zagreb, Croatia
Sahal-Bréchot, Sylvie	LERMA, Observatoire de Paris, Université PSL, CNRS, Sorbonne Université, 5 Place Jules Janssen, 92190 Meudon, France
Sakan, Nenad M.	Institute of Physics Belgrade, Pregrevica 118, 11080 Belgrade, Serbia
Savić, Mihailo R.	Institute of Physics Belgrade, Pregrevica 118, 11080 Belgrade, Serbia
Schneider, I. F.	Laboratoire Aimé Cotton, CNRS, ENS Cachan and Univ. Paris-Sud, 91405 Orsay, France
Simić, Zoran	Astronomical Observatory, Volgina 7, 11060 Belgrade, Serbia

Simonović, Ilija B.	Institute of Physics Belgrade, Pregrevica 118, 11080 Belgrade, Serbia
Spasojević, Djordje	University of Belgrade, Faculty of Physics 11001 Belgrade, P.O. Box 44, Serbia
Srečković, Vladimir	Institute of Physics Belgrade, Pregrevica 118, 11080 Belgrade, Serbia
Šterc, Filip	Zagreb Astronomical Observatory, Opaticka 22, 10000 Zagreb, Croatia
Tošić, Sanja	Institute of Physics Belgrade, Pregrevica 118, 11080 Belgrade, Serbia
Traparić, Ivan	Institute of Physics Belgrade, Pregrevica 118, 11080 Belgrade, Serbia
Travar, Miloš	Institute of Physics Belgrade, Pregrevica 118, 11080 Belgrade, Serbia
Udovičić, Vladimir I.	Institute of Physics Belgrade, Pregrevica 118, 11080 Belgrade, Serbia
Veselinović, Nikola B.	Institute of Physics Belgrade, Pregrevica 118, 11080 Belgrade, Serbia
Videnović, Ivan R.	University of Belgrade, Faculty of Physics 11001 Belgrade, P.O. Box 44, Serbia
Vujčić, Veljko	Astronomical Observatory, Volgina 7, 11060 Belgrade, Serbia
Vukalović, Jelena	Faculty of Science, University of Banja Luka, Mladena Stojanovi c a 2, 78000 Banja Luka, Republic of Srpska

PREFACE

This Special Issue on Astrophysical Spectroscopy: A&M DATA - Astronomy and Earth Observations contains selected papers from the V Meeting on Astrophysical Spectroscopy: A&M DATA. The venue of the conference was at the lake Palić, in northern Serbia, and it was held from September 12 to 15, 2023. This meeting is unique in bringing together astronomers and physicists from Serbia and other countries to review and present their current research. The meeting aims at improving the knowledge within the field, as well as promoting the importance of spectroscopy for future Astrophysical and Earth-science research. It is well known that atomic and molecular spectroscopy is a key method for plasma studies in various subfields: astronomy, fusion research, atmospheric research, applied physics and industry. Reliable atomic data from verified sources are crucial for proper theoretical analysis, spectra synthesis and modelling of both laboratory and astrophysical radiation sources. For instance, for the modeling of stellar atmospheres and opacity calculations a large amount of atomic data is needed, since the chemical composition of stellar atmosphere is not known a priori. Consequently, astroinformatics and development of atomic databases are important for stellar spectroscopy. On the other hand, the emission spectroscopy of laboratory plasma requires the knowledge of atomic and molecular constants, line widths etc. To combine all these practices, the A&M Data meeting aims at making the connection between researchers that provide the data, those that create and maintain databases, and the data users, both in theory and experiment. The program was divided into several sessions (special mini-projects) dedicated to spectroscopy and data in laboratory and general plasma. The V Meeting on Astrophysical Spectroscopy was attended by 76 participants from 14 countries. They presented 19 invited talks, and 15 posters. This Special Issue contains 18 articles arranged in three sections covering the entire content of the conference. All of the papers in this issue have been subjected to rigorous peer review. Each paper that was submitted was reviewed by at least two reviewers. The organizers are grateful to the Ministry of Science, Technological Development and Innovations of the Republic of Serbia for the general support. We thank the members of the scientific and local organizing committees for their help in preparing and running this conference. Editors would like to express our gratitude to the reviewers for their effort in peer-reviewing of all contributions. Finally, we acknowledge the help and support of the Contrib. Astron. Obs. Skalnate Pleso journal. We would like to note that materials (programme, talks, proceedings, photos, etc.) from this and previous meetings are available at http://asspectro2023.ipb.ac.rs/

<div align="right">

D.Sc. V. A. Srećković, D.Sc. M. S. Dimitrijevic & D.Sc. N. Cvetanović

the editors

</div>

On the Stark Broadening of Ga II Spectral Lines - 4d–nf Spectral Series

Milan S. Dimitrijević[1,2]**, Magdalena D. Christova**[3] **and
Sylvie Sahal-Bréchot**[2]

[1] *Astronomical Observatory, Volgina 7, 11060 Belgrade, Serbia,
(E-mail: mdimitrijevic@aob.rs)*

[2] *LERMA, Observatoire de Paris, Université PSL, CNRS, Sorbonne
Université, F-92190 Meudon, France*

[3] *Department of Applied Physics, Technical University of Sofia, 1000 Sofia,
Bulgaria, (E-mail: mchristo@tu-sofia.bg)*

Abstract. Using the Semiclassical perturbation method, Stark broadening parameters, widths and shifts, have been calculated for six Ga II multiplets, belonging to the 4d–nf (n=4,5,6) spectral series. The calculations have been performed for temperatures from 5 000 K to 100 000 K and an electron density of 10^{16} cm^{-3}. The obtained results have been used to investigate regularities within spectral series. The obtained data are especially useful in astrophysics, for analyzis and synthezis of stellar spectra and modelling of atmospheres, but also for laboratory and laser produced plasmas.
Key words: Stark broadening – Ga II – line profiles – atomic data – atomic processes – line formation – stellar atmospheres

1. Introduction

Broadening of spectral lines in a medium where emitting or absorbing atoms or ions are surrounded by electrons and ions, and under the influence of their microfields, or Stark broadening, is the most important pressure broadening mechanism when we have higher electron densities in high temperature plasmas. Such conditions, convenient for Stark broadening, can often be found in stellar plasma. In such a case we need Stark broadening data for various spectral lines, in order to perform an adequate investigation (Beauchamp *et al.*, 1997; Adelman, 1989; Dimitrijević, 2003; Dimitrijević, Sahal-Bréchot, 2014). Stark broadening data are needed and for investigation, modelling and diagnostics of laboratory plasma (Konjević, 1999; Capelli, Measures, 1987; Torres *et al.*, 2006) as well as for diagnostics, optimisation and modelling of inertial fusion plasma (Griem, 1992; Iglesias *et al.*, 1998). Such data are also of interest for designing and optimisation of lasers (see e.g. Griem *et al.*, 1992; Deng *et al.*, 2006; Dimitrijević, Sahal-Bréchot, 2014) and for diagnostics and research of laser produced plasma (Gornushkin *et al.*, 1999; Nicolosi *et al.*, 1978; Sorge *et al.*, 2000).

Another research field where Stark broadening data might be very useful are various plasmas which can be found in technology (Yilbas *et al.*, 2015), as e.g. in the case of welding, melting or piercing of various metals by laser radiation, or for example if one needs to design or optimise plasma light sources (see for example Dimitrijević, Sahal-Bréchot, 2014). According to our analysis (Dimitrijević, Sahal-Bréchot, 2014; Dimitrijević, 2020), the principal research field where Stark broadening data is used is astronomy. There, these data are needed for abundance determinations, stellar spectra analysis and synthesis, stellar atmosphere modelling, opacity and radiative transfer calculations, stellar spectral type determination, modelling of subphotospheric layers, monitoring of thermonuclear reactions in stellar interiors and for other topics. Stark broadening data for spectral lines are particularly significant for investigation of different types of white dwarfs. The importance of Stark broadening for various spectral lines of different atoms and ions has been demonstrated for a number of white dwarfs of various spectral types as for example DB (Thejll *et al.*, 1991) and DA white dwarfs (Vennes, 1992; Bergeron *et al.*, 1994), as well as OB subdwarfs (Michaud *et al.*, 1989). This line broadening mechanism may be of interest and for A and late B stars (Musielok, Madej, 1988; Smith *et al.*, 1994; Israelian *et al.*, 1996; Zakharova, Ryabchikova, 1996; Leone *et al.*, 1997; Bonifacio *et al.*, 1995).

Gallium spectral lines are usually observed in stellar spectra (Smith, 1995; Dworetsky *et al.*, 1998; Vauclair, Vauclair, 1982; Smith, 1996; Castelli, Hubrig, 2004; Hubrig *et al.*, 2014; Sadakane, Nishimura, 2018; Monier, 2023). It is often overabundant in chemically peculiar (CP) stars, which are mostly of A and late B spectral type where Stark broadening is of interest, since hydrogen is mainly ionized, so that it is the principal pressure broadening mechanism. In the case of CP stars observations indicate that gallium spectral lines are prominent, strong and a proper tool for abundance determination. Consequently, Stark broadening data are needed for analysis and synthesis of such stellar spectra, as well as for modelling of stellar atmospheres, opacity and radiative transfer calculations etc.

In spite of the need for various topics in stellar physics, data on broadening of Ga II spectral lines are scarce. In order to provide new reliable Stark broadenig data for Ga II lines, we calculated here Stark broadening parameters, full widths at half intensity maximum (FWHM) - W, and shifts -d, for Ga II lines within six multiplets from 4d–nf (n=4,5,6) transitions. The calculations have been performed using the semiclassical perturbation theory (Sahal–Bréchot, 1969 a, 1969 b; Sahal–Bréchot *et al.*, 2014), and obtained results are used to consider Stark broadening regularities within the 4d–nf (n=4,5,6) spectral series.

2. The impact semiclassical perturbation method

An outline of the semiclassical perturbation method (Sahal–Bréchot, 1969 a, 1969 b), for calculations of Stark broadening parameters, FWHM - W and shift

- d, is given in Sahal–Bréchot *et al.* (2014). Collisional line broadening in the impact approximation considers a neutral (ionized) atom surrounded by a bath of perturbers. The interactions between atom/ion and perturbers do not perturb bath's distribution. Within impact approximation the interactions are separated in time. The atom/ion interacts with one perturber only for a given time which means that the mean duration of the collision is much smaller than the time interval between two interactions (collisions). In addition, atom/ion–radiation process and atom/ion–perturber interactions are decoupled: the emission of a photon arises when the interaction process is completed. The atom/ion–perturber interaction is treated by the time–dependent perturbation theory in long range approximation. Neutral atom follows straight line trajectory and ionized atom – a hyperbola. The full width at half maximum (FWHM) and shift of the line profile of an isolated non-hydrogenic spectral line are expressed by the equations (Sahal–Bréchot, 1969 a, 1969 b):

$$W \; = \; N \int v f(v) dv \left(\sum_{i' \neq i} \sigma_{ii'}(v) + \sum_{f' \neq f} \sigma_{ff'}(v) + \sigma_{el} \right)$$

$$d \; = \; N \int v f(v) dv \int_{R_3}^{R_D} 2\pi \rho d\rho \sin(2\varphi_p). \tag{1}$$

where the indexes i and f concern the initial and final level of a given transition; i' and f' are the corresponding perturbing levels, respectively; N notices the electron density; v is a perturber velocity, and v represents the Maxwellian distribution of electron velocities, and ρ is the perturber's impact parameter.

The cross sections $\sigma_{kk'}(v)$, $k = i, f$, express cross sections for inelastic interactions of emitters in initial atomic energy level with charged particles. It could be written by an integration of the transition probability $P_{kk'}(\rho, v)$, over the impact parameter ρ :

$$\sum_{k' \neq k} \sigma_{kk'}(v) = \frac{1}{2}\pi R_1^2 + \int_{R_1}^{R_D} 2\pi \rho d\rho \sum_{k' \neq k} P_{kk'}(\rho, v). \tag{2}$$

The following two equations estimate the cross section of elastic collisions between emitters and charged particles:

$$\sigma_{el} = 2\pi R_2^2 + \int_{R_2}^{R_D} 2\pi \rho d\rho \sin^2 \delta + \sigma_r,$$

$$\delta = (\varphi_p^2 + \varphi_q^2)^{\frac{1}{2}}. \tag{3}$$

where δ denotes the phase shift due to polarization (φ_p (r^{-4})) and quadrupole (φ_q (r^{-3})) potentials for atom-perturber elastic interactions. The details for cut-off parameters R_1, R_2, R_3, the Debye cut-off R_D and the symmetrization are explained in Sahal–Bréchot (1969 b) (Section 1 of Chapter 3). The term σ_r gives the contribution of Feshbach resonances (Sahal–Bréchot, 2021).

3. Stark broadening parameter calculations

With the semiclassical perturbation theoretical method (Sahal–Bréchot, 1969 a, 1969 b; Sahal–Bréchot *et al.*, 2014), here are calculated electron-impact broadening parameters, full width at half maximum of intensity (FWHM - W) and shift (d) for Ga II 4d–nf (n=4,5,6) transitions. The calculations are performed for temperatures of 5 000 K, 10 000 K, 30 000 K, 50 000 K and 100 000 K for a perturber density of 10^{16} cm^{-3}.

The needed atomic energy levels for Ga II, have been taken from Shirai *et al.* (2007). The needed oscillator strengths have been calculated in the Coulomb approximation. For details see for example Dimitrijević *et al.* (2022). The obtained results for six Ga II multiplets, are given in Table 1, for a perturber density of 10^{16} cm^{-3} and temperatures within the interval from 5 000 K up to 100 000 K.

It should be noted that the wavelengths in the Table 1 are calculated using atomic energy levels of terms making a multiplet.

From the beginning of spectroscopy, regularities and similarities are observed in wavelengths, energy levels, oscillator strengths, collision cross sections also, etc. Two factors determine principally the broadening of a spectral line in plasma, the environment around the emitting/absorbing particle as well as the atomic structure of the radiating particle. Atomic structures involve many regularities and similarities which consequence are regularities and similarities that could be found among the width and shift parameters of plasma broadened spectral lines. Generally, these regularities come from the atomic structure. In the case of pressure broadening of spectral lines in a plasma, regularities are expected in the cross sections for elastic and inelastic interactions between radiating (absorbing) particles and perturbers, which enter in the calculation of Stark broadening parameters. Consequently, sveral kinds of regularities and similarities can be found among the Stark broadening parameters (see e.g. Wiese, Konjević, 1982). (*i*) Regularities within a given spectrum for spectral lines within a multiplet, supermultiplet and transition array. For example, it is usually assumed in theoretical calculations that all lines exhibit the same width within a multiplet. (*ii*) Regularities exist and within a spectral series. (*iii*) Similarities can be found also in the case of analogous transitions which are in homologous atoms; (iv) Systematic behavior for given transitions along an isoelectronic sequence.

Table 1. This table gives Stark broadening parameters, W - full widths at half intensity maximum (FWHM) and shifts, for Ga II lines broadened by collisions with electrons in angstroms and in 10^{12} s^{-1} . Calculated wavelength of the transitions (in Å) are also given. Results are for a perturber density of 10^{16} cm^{-3} and temperatures are from 5 000 to 100 000 K. A positive shift is towards the red part of the spectrum.

Transition	T [K]	W [Å]	d [Å]	W [10^{12} s^{-1}]	d [10^{12} s^{-1}]
4d^{1}D-4f^{1}F^o	5000.	0.630	0.127	0.148	0.0297
$\lambda = 8964.6$ Å	10000.	0.523	0.103	0.123	0.0241
	30000.	0.457	0.0769	0.107	0.0180
	50000.	0.454	0.0653	0.106	0.0153
	100000.	0.451	0.0550	0.106	0.0129
4d^{1}D-5f^{1}F^o	5000.	0.640	0.280	0.548	0.239
$\lambda = 4693.6$ Å	10000.	0.577	0.229	0.494	0.196
	30000.	0.520	0.168	0.445	0.144
	50000.	0.500	0.139	0.427	0.119
	100000.	0.464	0.107	0.397	0.0912
4d^{1}D-6f^{1}F^o	5000.	0.957	0.494	1.30	0.670
$\lambda = 3728.3$ Å	10000.	0.900	0.412	1.22	0.559
	30000.	0.852	0.303	1.16	0.411
	50000.	0.818	0.247	1.11	0.335
	100000.	0.754	0.189	1.02	0.257
4d^{3}D-4f^{3}F^o	5000.	0.293	-0.00771	0.305	-0.00801
$\lambda = 4259.0$ Å	10000.	0.232	-0.0138	0.241	-0.0143
	30000.	0.169	-0.0127	0.176	-0.0132
	50000.	0.150	-0.0106	0.156	-0.0110
	100000.	0.129	-0.00864	0.134	-0.00898
4d^{3}D-5f^{3}F^o	5000.	0.492	0.0939	1.05	0.200
$\lambda = 2973.4$ Å	10000.	0.433	0.0864	0.924	0.184
	30000.	0.350	0.0812	0.745	0.173
	50000.	0.314	0.0651	0.668	0.139
	100000.	0.267	0.0482	0.570	0.103
4d^{3}D-6f^{3}F^o	5000.	0.687	0.217	1.99	0.626
$\lambda = 2554.5$ Å	10000.	0.645	0.192	1.86	0.555
	30000.	0.567	0.158	1.64	0.455
	50000.	0.522	0.129	1.51	0.374
	100000.	0.455	0.0960	1.31	0.277

With the obtained results, we will discuss here the regularities within spectral series, in order to see if the behavior in the examined spectal series of Al IV is regular in such a manner that interpolations and extrapolations within these spectral series can provide good estimates of new data and checks of con-
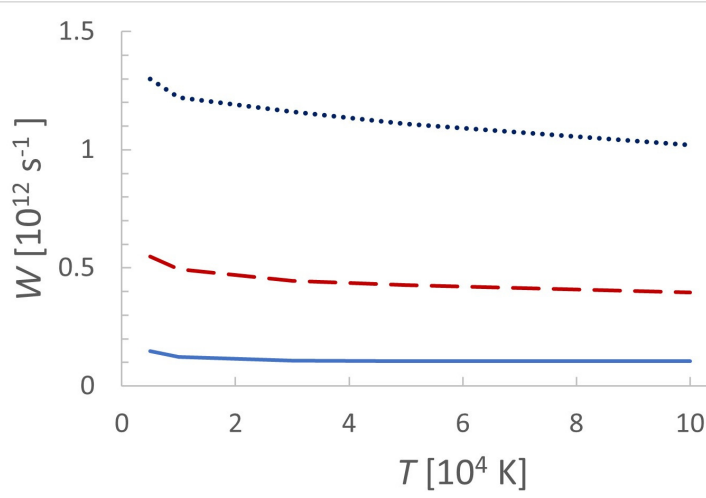
Figure 1. Behavior of Stark widths – W, in angular frequency units, with temperature, for the three members of 4d–nf spectral series (singlets). Full blue line – $4d^1D$ – $4f^1F^o$, $\lambda = 8964.6$ Å. Dashed red line – $4d^1D$ – $5f^1F^o$, $\lambda = 4693.6$ Å. Dotted dark blue line – $4d^1D$ – $6f^1F^o$, $\lambda = 3728.3$ Å. Electron density is 10^{16} cm^{-3}.
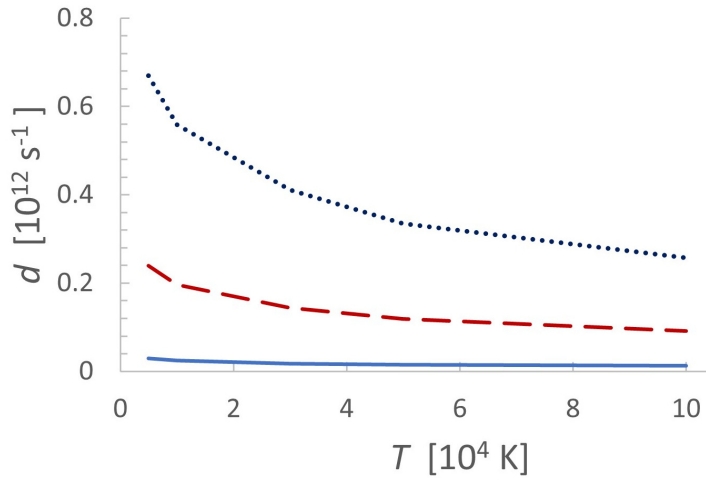
Figure 2. The same as in Fig. 1 but for the shift – d.

sistency for data existing in the literature. In order to do this, in the Table 1 are included Stark broadening parameters not only in angstroms but also in

angular frequency units, obtained by the expression:

$$W(\mathring{A}) = \frac{\lambda^2}{2\pi c} W(s^{-1}) \tag{4}$$

where c is the speed of light.

4. Discussion

We used the obtained results to study behavior of Stark broadening parameters (widths (FWHM) W, and shift d) with temperature, and with principal quantum number of the upper state, within spectral series. Fig. 1 and Fig. 2 present Stark width and shift of Ga II singlet multiplets $3d^{10}4d$ – $3d^{10}nf$ ($n = 4$–6) with the corresponding wavelengths 8964.6 Å, 4693.6 Å, and 3728.3 Å, belonging to the same spectral series. These results are obtained for perturber density of $10^{16}$ cm^{-3}. Both parameters decrease in the whole temperature interval for three spectral lines. The decrease is almost constant for higher temperatures. For $\lambda = 8964.6$ Å the Stark width varies 28 % within the 5 000 K – 100 000 K interval and Stark shift 57 %; for $\lambda = 4693.6$ Å: 28 % and 62 %, respectively, and for $\lambda = 3728.3$ Å: 21 % and 62 % for the shift. Based on these results, we can conclude that the width variations decrease with increasing of principal quantum number of the upper state. Additionally, the widths vary weakly for $T > 20 000$ K. The shift changes increase with the principal quantum number, and these changes are particularly distinguishable in the first part of the temperature interval for given line. In the first part of the curve, where variation with temperature is more pronounced, elastic collisions as well as strong collisions are more important while for higher temperatures, where variation with temperature is much smaller, the inelastic collisions become dominant. We can see that for higher temperatures, due to week variation of Stark width with temperature, the exact value of temperature is not so critical and we can use value obtained experimentally or theoretically for a specific temperature in a wider temperature range if higher accuracy is not needed.

Both parameters notably increase with n: from 8.9 times for $T = 5 000$ K to 9.6 times for $T = 100 000$ K, at the end of T-interval, for the width, and, 22.6 and 19.9 times, respectively, for the shift. If we look at these parameters in angstroms, we can see from Table 1 that these values for the widths are 1.5 and 1.7, while for the shifts they are 3.9 and 3.4 respectively. This is because in the case of Stark broadening in angstrems we have the influence of wavelength, which decreases with the increase of the principal quantum number n, while, on the other hand, due to the fact that perturbing atomic energy levels became closer to the upper level of the considered transition, values of Stark broadening parameters increase with the increase of n. Since there is no the influence of wavelength for Stark widths and shifts in angular frequency units, the increase with n is much larger.

Figure 3. Behavior of Stark widths - W with principal quantum number - n of the upper atomic energy levels for $4d^1D$ - nf^1F^o (n = 4,5,6 - singlets) spectral series, in angstroms (blue dots) and in angular frequency units: 10^{12} s^{-1} (red dots). On ordinate are arbitrary units which are angstroms for blue dots and angular frequency units for red dots. Temperature is 10 000 K and electron density 10^{16} cm^{-3}.

Figure 4. Same as in Fig. 3 but for the shift - d.

In the next two figures (Fig. 3 and Fig. 4) the dependence of Stark width and shift versus principal quantum number of the upper state for the same spectral series is given. The regularity of behavior of Stark broadening parameters within a spectral series provides possibility to interpolate or extrapolate new data and to check the consistency of experimental results or calculations. To illustrate this behavior, the values of electron density and temperature are fixed to 10^{16} cm^{-3} and 10 000 K. To see the difference of behavior with principal quantum number, we include both parameters in 10^{12} s^{-1} and in Å units. There is a significant increase of width and shift values versus n in the case of 10^{12} s^{-1} units, since in this case there is no the influence of wavelengths, as explained above. The difference between maximal and minimal width values in Å units is 72 %. The maximal shift in Å is three times larger than the minimal one. The same differences in 10^{12} s^{-1} units are 10 times for the width and 23 times for the shift. This means that broadening parameters in angular frequency units, liberated from the influence of wavelength, are more sensitive to the variation of principal quantum number. Both figures demonstrate a trend of broadening parameters within the series that could be useful for an estimation of line broadening for other members of the series and for checking the reliability of future experimental data.
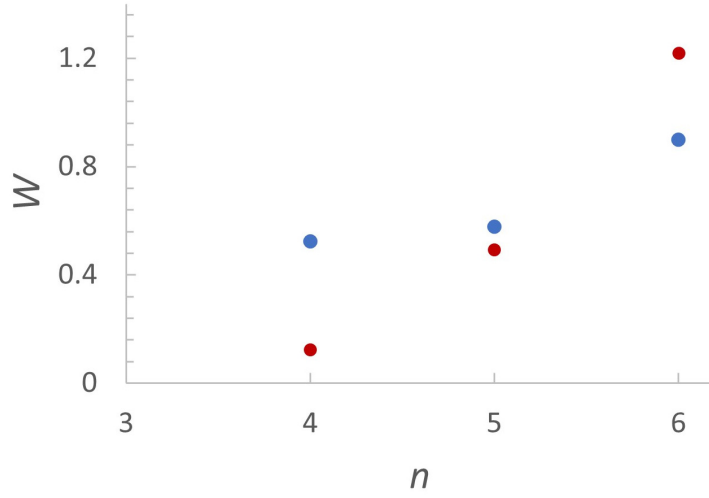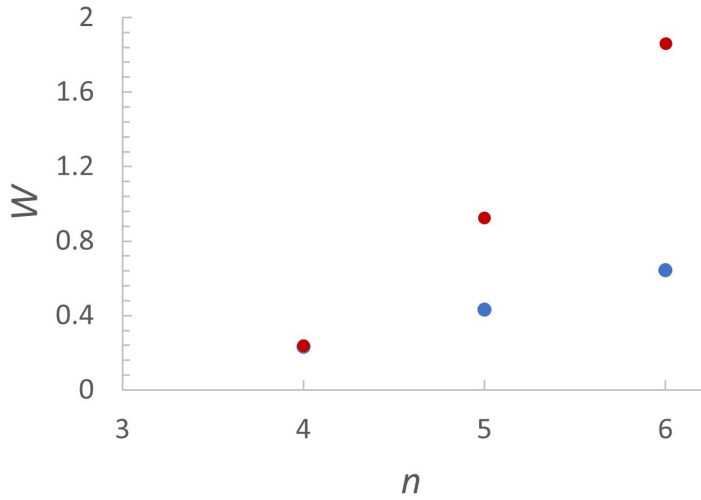

Figure 5. Behavior of Stark widths - W with principal quantum number - n of the upper atomic energy levels for 4d^{3}D – nf^3F^o (n = 4,5,6 - triplets) spectral series, in angstroms (blue dots) and in angular frequency units: 10^{12} s^{-1} (red dots). On ordinate are arbitrary units which are angstroms for blue dots and angular frequency units for red dots. Temperature is 10 000 K and electron density 10^{16} cm^{-3}.
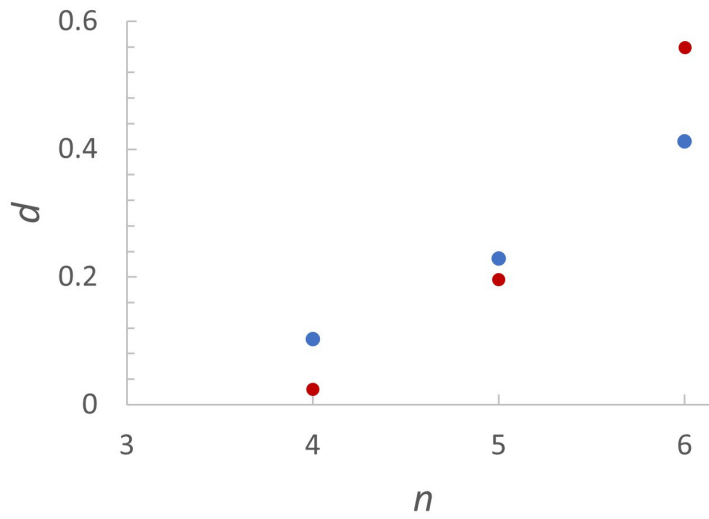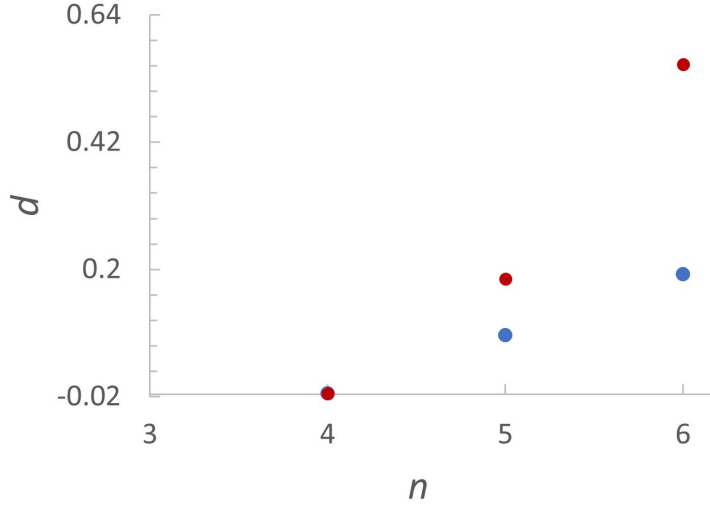
Figure 6. Same as in Fig. 5 but for the shift - *d*.

Figs. 5 and 6 show the same behavior for spectral lines of triplet transitions in
Ga II $3d^{10}4d$ – $3d^{10}nf$ ($n = 4 - 6$) spectral series. To compare Stark broadening
parameters from both series, the examined plasma conditions are the same:
perturber density 10^{16} cm^{-3} and temperature 10 000 K. The symbols for width
values in Å and in 10^{12} s^{-1} units coincide for principal quantum number of
the upper state, four. The shift values (Å and 10^{12} s^{-1}) are negative and their
symbols also coincide for $n = 4$. For $n = 5$ and $n = 6$ the shifts are positive. The
width in Å varies 3 times and the shift – 15 times. The corresponding variations
in 10^{12} s^{-1} units are 8 times and 40 times, respectively. The presentation of
Stark broadening values in angular frequency units is more suitable, since then,
the values are liberated from the influence of wavelength.

Stark widths and shifts for Ga II spectral lines calculated here will be im-
plemented as well in the STARK-B database (Sahal–Bréchot *et al.*, 2015, 2023).
This database is also a part of Virtual Atomic and Molecular Data Center
(VAMDC - Albert *et al.*, 2020). It is worth to note as well, that a link to
STARK-B exist also on the web site of the Serbian Virtual Observatory (SerVO,
http:servo.aob.rs).

The obtained data could be useful for a number of problems in astrophysics,
physics and technological plasmas, as for example for analysis and synthesis of
stellar spectra, modelling of stellar atmospheres, opacity and radiative transfer
calculations, determination of abundances of gallium, labortory plasma diag-
nostics etc.

References

Adelman, S.J.: 1989, *Mon. Not. Roy. Astron. Soc.*, **239**, 487

Albert, D., Antony, B. K., Ba, Y. A., Babikov, Y. L., Bollard, P., Boudon, V., Delahaye, F., Del Zanna, G., Dimitrijević, M. S., Drouin, B. J., Dubernet, M.-L., Duensing, F., Emoto, M., Endres, C. P., Fazliev, A. Z., Glorian, J.-M., Gordon, I. E., Gratier, P., Hill, Ch., Jevremović, D., Joblin, C., Kwon, D.-H., Kochanov, R. V., Krishnakumar, E., Leto, G., Loboda, P. A., Lukashevskaya, A. A., Lyulin, O. M., Marinković, B. P., Markwick, A., Marquart, Th., Mason, N. J., Mendoza, C., Millar, T. J., Moreau, N., Morozov, S. V., Möller, Th., Müller, H. S. P., Mulas, G., Murakami, I., Pakhomov, Yu., Palmeri, P., Penguen, J., Perevalov, V. I., Piskunov, N., Postler, J., Privezentsev, A. I., Quinet, P., Ralchenko, Yu., Rhee, Yong-Joo, Richard, C., Rixon, G., Rothman, L. S., Roueff, E., Ryabchikova, T., Sahal-Bréchot, S., Scheier, P., Schilke, P., Schlemmer, S., Smith, K. W., Schmitt, B., Skobelev, I. Yu., Srećković, V. A., Stempels, E., Tashkun, S. A., Tennyson, J., Tyuterev, V. G., Vastel, Ch., Vujčić, V., Wakelam, V., Walton, N. A., Zeippen, C., Zwölf, C. M.: 2020, *Atoms*, **8**, 76

Beauchamp, A., Wesemael, F., Bergeron, P.: 1997, *Astrophys. J. Suppl. Ser.*, **108**, 559

Bergeron, P., Wesemael, F., Beauchamp, A., Wood, M.A., Lamontagne, R., Fontaine, G., Liebert, J.: 1994, *Astrophys. J.*, **432**, 305

Bonifacio, P., Castelli, F., Hack, M.: 1995, *Astron. Astrophys. Suppl. Series*, **110**, 441

Cappelli, M.A., Measures, R.M.: 1987, *Appl. Optics*, **26**, 1058

Castelli, F., Hubrig, S.: 2004, *Astron. Astrophys.*, **425**, 263

Deng, Y.Z., Zheng, H.Y., Murukeshan, V.M., Zhou, W.: 2006, *J.Laser Micro Nanoeng.*, **1**, 136

Dimitrijević, M. S.: 2003, *Astron. Astrophys. Trans.*, **22**, 389

Dimitrijević, M. S.: 2020, *Data*, **5**, 73

Dimitrijević M. S., Christova, M. D., Sahal-Bréchot S.: 2022, *Mon. Not. Roy. Astron. Soc*, **507**, 2087

Dimitrijević, M. S., Sahal-Bréchot, S.: 2014, *Atoms*, **2**, 357

Dworetsky, M.M., Jomaron, C.M., Smith, C.A.: 1998, *Astron. Astrophys.* **333**, 665

Gornushkin, I.B., King, L.A., Smith, B.W., Omenetto, N., Winefordner, J.D.: 1999, *Spectrochim. Acta*, **54**, 1207

Griem, H.R.: 1992, *Phys. Fluids*, **4**, 2346

Hubrig, S., Castelli, F., González, J.F., Carroll, T.A., Ilyin, I., Schöller, M., Drake, N.A., Korhonen, H., Briquet, M.: 2014, *Mon. Not. Roy. Astron. Soc*, **442**, 3604

Iglesias, E., Griem, H.R., Welch, B., Weaver, J.: 1997, *Astrophys. Space Sci.*, **256**, 327

Israelian, G., Friedjung, M., Graham, J., Muratorio, G., Rossi, C., de Winter, D.: 1996, *Astron. Astrophys.* **311**, 643

Konjević, N.: 1999, *Phys. Rep.*, **316**, 339

Leone, F., Lanzafame, A.C.: 1997, *Astron. Astrophys.* **320**, 893

Michaud, G., Bergeron, P., Heber, U., Wesemael, F.: 1989, *Astrophys. J.*, **338**, 417

Monier, R.: 2023, *Astron. Astrophys. Suppl.*, **7**, 4

Musielok, B., Madej, J.: 1988, *Astron. Astrophys.*, **202**, 143

Nicolosi, P., Garifo, L., Jannitti, E., Malvezzi, A.M., Tondello, G.: 1978, *Nuovo Cim. B*, **48**, 133

Sadakane, K., Nishimura, M.: 2018, *Publ. of the Astron. Soc. of Japan*, **70(3)**, 40

Sahal–Bréchot, S.: 1969 a, *Astron. Astrophys.*, **1**, 91

Sahal–Bréchot, S.: 1969 b, *Astron. Astrophys.*, **2**, 322

Sahal–Bréchot, S.: 2021, *Atoms*, **9**, 29

Sahal–Bréchot, S., Dimitrijević, M.S., Ben Nessib, N.: 2014, *Atoms*, **2**, 225

Sahal- Bréchot, S., Dimitrijević, M.S., Moreau, N.: 2023, STARK-B Database, available online: http://stark-B.obspm.fr (accessed on 26 September 2023)

Sahal-Bréchot, S., Dimitrijević, M.S., Moreau, N., Ben Nessib, N.: 2015, *Phys. Scr.* **90**, 054008

Smith, K. C.: 1995, *Astron. Astrophys.*, **297**, 237

Smith, K.C.: 1996, *Astrophys. J. Suppl.*, **237**, 77

Smith, M.A., Hubeny, I., Lanz, T., Meylan, T.: 1994, *Astrophys. J.*, **432**, 392

Sorge, S., Wierling, A., Röpke, G., Theobald, W., Suerbrey, R., Wilhein, T.: 2000, *J. Phys. B*, **33**, 2983

Thejll, P., Vennes, S., Shipman, H.L.: 1991, *Astrophys. J.*, **370**, 355

Torres, J., van de Sande, M. J., van der Mullen, J. J. A. M., Gamero, A., Sola. A.: 2006, *Spectrochim. Acta B*, **61**, 58

Vauclair, S., Vauclair, G.: 1982, *Ann. Rev. Astron. Astrophys.*, **20**, 37

Vennes, S.: 1992, *Astrophys. J.*, **390**, 590

Wang, J.S., Griem, H.R., Huang, Y.W., Böttcher, F.: 1992, *Phys. Rev. A*, **45**, 4010

Wiese, W.L., Konjević, N.: 1982, *J. Quant. Sprectrosc. Radiat. Transf.*, **28(3)**, 185

Yilbas, B.S., Patel, F., Karatas, C.: 2015, *Opt. Laser Technol.*, **74**, 36

Zakharova, L. A., Ryabchikova, T. A.: 1996, *Astron. Lett.*, **22**, 152

Triply ionized Molybdenum lines in the spectra of the DA-type and the DO-type white dwarfs

Z. Simić[1] , **M. S. Dimitrijević[1,2] and N. Sakan[3]**

[1] *Astronomical Observatory, Volgina 7, 11060 Belgrade, Serbia,*
(E-mail: zsimic@aob.rs),

[2] *LERMA, Observatoire de Paris, F-92195 Meudon Cedex, France*

[3] *University of Belgrade, Institute of Physics, PO Box 57,*
11001 Belgrade, Serbia

Abstract. Molybdenum is trans-iron element and the most serious problem for the determination of these element abundances is the lack of atomic data. Investigations of the spectrum of the white dwarf RE 0503-289 indicate the presence of lines of multiply ionized elements such as Ga, Kr, Mo and Xe. Extreme overabundances of trans-iron elements are seen in DO white dwarfs, in a temperature range from 49500 K up to 70000 K. In this context, we have considered the lines of triply ionized molybdenum in the spectra of white dwarfs, especially of DA and DO type. Differences in the contributions of spectral line broadening for two different types of white dwarfs are due to different physical conditions, since effective temperatures and surface gravities are different. More than ten 5s - 5p transitions of Mo IV of interest for the calculation of Stark broadening parameters, width and shift, were selected. A simple modified semi-empirical approach by Dimitrijević and Konjević, 1987 was applied. The obtained results may be particularly useful for determination of molybdenum abundances in white dwarfs and for laboratory plasma diagnostics.

Key words: Stark broadening – line profiles – atomic data

1. Introduction

Our knowledge of the abundance of heavy elements in the atmospheres of white dwarfs is not complete. List of elements found in their atmospheres is limited both to those that are naturally rich and to elements with dominant ionization states, which have otherwise strong resonance lines. Analysis of heavy elements in atmospheres of many hot white dwarfs is a demanding and extensive task that necessarily uses all valid parameters obtained in the laboratory as well as theoretical calculations using valid and recognized methods. Therefore, the parameters of the Stark broadening are of great importance for stellar spectroscopy.

In Werner et al. (2012) has been reported the first detection of the noble gases krypton and xenon in a white dwarf. These observations, carried out with

the Far Ultraviolet Spectroscopic Explorer, have detected the lines of krypton VI - VII and xenon VI - VII in the ultraviolet spectrum of a hot white dwarf of the type DO with the name RE 0503-289. This star is a hot DO type WD with effective temperature of 70,000 K Dreizler & Werner (1996). Its spectrum is extraordinarily rich in unidentified absorption lines that are not observed in any other WD. Also, they discovered photospheric lines from other multiply ionized elements of the trans-iron group, namely Ga, Ge, As, Se, Mo, Sn, Te and I, of which gallium and molybdenum are new discoveries in white dwarfs as well. In the NIST database can be found 10 Mo VI lines from the FUSE spectral range as it is presented from observations in Werner et al. (2012). During this research were detected the four lines with the highest relative intensity: with wavelengths 995.811, 1038.642, 1047.184, 1182.143 Å and three of them have the largest gf values. It should be noted as well that this element was not detected before in a white dwarfs.

Many heavy elements, such as Ga, Ge, Sn and Pb, have been identified in sdB and sdOB stars by O'Toole (2004) and O'Toole & Heber (2007). In Vennes et al. (2005) was reported the observation of Ge in three H atmospheres of white dwarfs, spectral type DA, where the average abundance is nearly solar. Chayer et al. (2005) reported many heavy elements and molybdenium in the atmospheres of white dwarf, spectral type DO.

New determination of photospheric Mo abundances are obtained by Rauch et al. (2016) from spetral analysis of two type white dwarf, DA and DO. It was identified 12 Mo V and 9 Mo VI lines in the UV spectrum of RE 0503-289 and measured a photospheric Mo abundance of 1.2-3.0 x 10^{-4} (mass fraction, 22 500-56 400 times the solar abundance).

2. Method

We used a simplified modified semiempirical method by Dimitrijević & Konjević (1987), designed for Stark broadening of isolated spectral lines of singly and multiply charged ions in plasma. A more accurate semiclassical perturbation method by Sahal-Bréchot (1969a,b), Sahal-Bréchot et al. (2014) is not applicable in an adequate way due to the lack of a sufficient set of atomic data. It means that there is no data on the entire energy level scheme needed for calculations. The good knowledge on closest perturber levels for both initial and final states for the transition is crucial. The insufficient set of atomic energy levels is an obstacle for application of more precise methods, so the simplified formula was the preferred and only possible method to be used in the described case of the considered Mo IV lines. Full width at half intensity maximum follows the expression given by Dimitrijević & Konjević (1987):

$$w_{smse} = C_{fw}\frac{\lambda^2 N}{\sqrt{T}}(0.9 - \frac{1.1}{Z})\sum_{k=i,f}\left(\frac{3n^*_{l_k}}{2Z}\right)^2(n^{*}_{l_k}{}^2 - l_k{}^2 - l_k - 1) \qquad (1)$$

where wavelength λ is given in [m], perturber density N in [m^{-3}], temperature T in [K], constant $C_{fw} = 2.21577 \times 10^{-20}$ m^{2}K$^{1/2}$, and full width at half intensity of maximum w_{smse} is in [m]. Initial atomic energy level is denoted by i, and the final with f ($k = i, f$). Z denotes ion residual charges: $Z = 1$ for neutral, $Z = 2$ for singly ionized, $Z = 3$ for doubly ionized, etc. Effective principal quantum number is labelled $n^*_{l_k}$, where l_k ($k = i, f$) represents orbital angular momentum quantum number.

Formula used for Stark shift calculation depends on the case. If for transitions with $\Delta n = 0$ all levels with angular momenta $\ell \pm 1$ exist (where n denotes main principal number), summing all the allowed transitions gives the following formula for the shift:

$$d^{(1)}_{smse} \approx C_{sh} \frac{\lambda^2 N}{\sqrt{T}} (0.9 - \frac{1.1}{Z}) \frac{9}{4Z^2} S_1 \tag{2}$$

where $C_{sh} = 1.1076 \times 10^{-20}$ m^{2}K$^{1/2}$ and

$$S_1 = \sum_{k=i,f} \frac{n^{*}_{l_k}{}^2 \epsilon_k}{2l_k + 1} (n^{*}_{l_k}{}^2 - 3l_k{}^2 - 3l_k - 1) \tag{3}$$

In the general case, we can determine the shift with:

$$d^{(2)}_{smse} \approx C_{sh} \frac{\lambda^2 N}{\sqrt{T}} (0.9 - \frac{1.1}{Z}) \frac{9}{4Z^2} S_2 \tag{4}$$

where

$$S_2 = \sum_{k=i,f} \frac{n^{*}_{l_k}{}^2 \epsilon_k}{2l_k + 1} [(l_k + 1)[n^{*}_{l_k}{}^2 - (l_k + 1)^2] - l_k(n^{*}_{l_k}{}^2 - l_k^2)] \tag{5}$$

where $\epsilon_k = +1$ for $k = i$ and $\epsilon_k = -1$ for $k = f$.

In order to calculate averaged energies, we can use the expression:

$$E = \frac{\sum_J (2J + 1) E_J}{\sum_J (2J + 1)} \tag{6}$$

where E represents averaged energy, E_J energy level and J total angular momentum of a particular energy level.

3. Results and Discussion

Within the framework of this study, we added molybdenum to the elements of heavy metals as a continuation of the previously discussed elements: iridium Simić et al. (2021), rhodium Simić & Sakan (2021), rhenium Simić et al. (2023). The parameters of Stark broadening, widths and shifts, have been obtained for

27 spectral lines of Mo IV. In this case, all the conditions for the application of the simplified modified semi-empirical method are met.
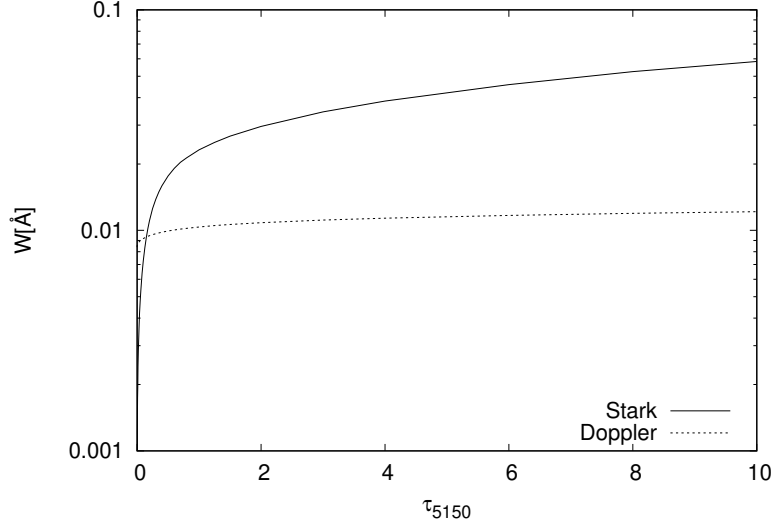
Figure 1. Dependence of electron-impact FWHM and thermal Doppler width on optical depth (τ_{5150}) in the DA White Dwarf atmosphere for Mo IV 5s $^4\mathrm{F}_{5/2}$ - 5p $^4\mathrm{F}^o_{7/2}$ ($\lambda = 1886$ Å) spectral line. Model of DA white dwarf atmosphere Wickramasinghe (1972) is with T_{eff} =15000 K and log $g = 8$.

Our calculations are performed for an electron density of 10^{17} cm^{-3} and temperatures from 5000 K to 80000 K. The energy levels are taken from Moore (1971). These results for Mo IV spectral lines are presented in Table 1. The first column presents transitions with calculated Ritz wavelengths, which are different from the experimental ones. The corresponding data for the Stark width and shift of a respective Mo IV line are given in Å, and Stark width and shift in angular frequency units in the next two columns, obtained using the formula:

$$W = \frac{\lambda^2}{2\pi c} W \,[\mathrm{s}^{-1}] \quad (d = \frac{\lambda^2}{2\pi c} d \,[\mathrm{s}^{-1}]) \tag{7}$$

where c is the light speed. The last column gives 3kT/2ΔE, where ΔE is the energy difference between the nearest perturbing level and the closest of the initial and final levels. The expression 3kT/2ΔE must be less than or equal to two for the method to be valid.

For all considered spectral lines of Mo IV the LS coupling is valid. All notations for atomic energy levels are taken from Moore (1971); Reader et al. (1980); Ralchenko et al. (2005) and NIST database.
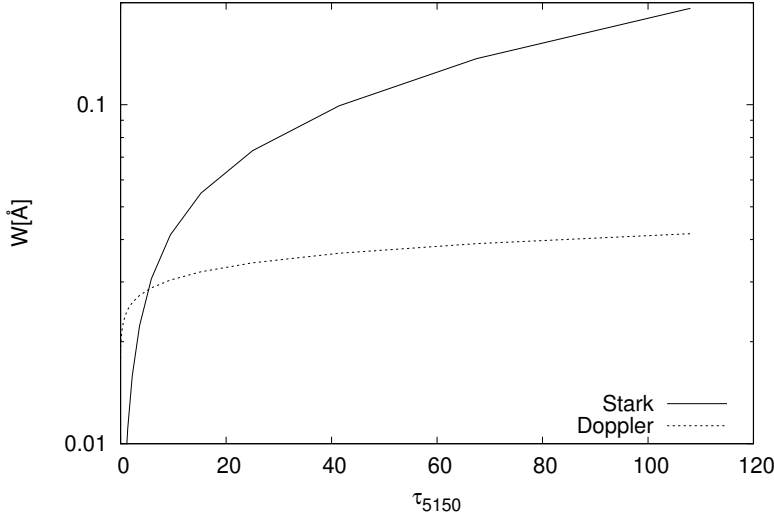
Figure 2. Stark and Doppler widths for Mo IV 5s $^4F_{5/2}$ - 5p $^4F^o_{7/2}$ ($\lambda = 1886$ Å) spectral line as a function of Rosseland optical depth (τ). This atmospheric model for DO type of WD (Wesemael, 1981) include parameters with surface gravity log $g = 6$ and $T_{eff} = 80\ 000$ K.

For correction of widths and shifts for differences due to the difference of experimental (λ_e) and theoretical wavelength or to these differences within a multiplet, one can use the expression:

$$W_e = (\lambda_e/\lambda)^2 W \quad\quad (d_e = (\lambda_e/\lambda)^2 d) \quad\quad (8)$$

where W_e and d_e are the width and shift for an experimental λ_e, and λ is a theoretical wavelength, with corresponding W and d (the width and shift) in Table 1.

We choose one of Mo IV spectral lines, 5s $^4F_{5/2}$ - 5p $^4F^o_{7/2}$ ($\lambda = 1886$ Å) and we tested how Stark and Doppler width change in a stellar atmosphere with the optical depth. We used the stellar model atmospheres for DA type of white dwarfs with parameters log $g = 8$ and $T_{eff} = 15000$ K Wickramasinghe (1972) and results are presented in Fig.1.

In the introduction of this work, we marked that spectral lines of highly charged molybdenum ions (Mo IV - Mo VII) have been observed in DO white

Table 1. Stark broadening parameters Full Widths at Half Intensity Maximum (W) and shifts (d) for Mo IV spectral lines, for a perturber density of 10^{17} cm^{-3} and temperatures from 5000 K to 80 000 K.

Transition	T(K)	W_e(Å)	d_e(Å)	W[s^{-1}]	d[s^{-1}]	3kT/2ΔE
5s - 5p $^4F_{3/2}$ - $^4F_{3/2}^o$ 1966.04 Å	5000	0.8559D-01	-0.1815D-01	0.4171D+12	-0.8847D+11	0.103
	10000	0.6052D-01	-0.1284D-01	0.2949D+12	-0.6256D+11	0.205
	20000	0.4279D-01	-0.9077D-02	0.2085D+12	-0.4423D+11	0.410
	40000	0.3026D-01	-0.6419D-02	0.1475D+12	-0.3128D+11	0.820
	80000	0.2140D-01	-0.4539D-02	0.1043D+12	-0.2212D+11	1.640
5s - 5p $^4F_{3/2}$ - 5p $^4F_{5/2}^o$ 1922.01 Å	5000	0.8242D-01	-0.1728D-01	0.4202D+12	-0.8810D+11	0.100
	10000	0.5828D-01	-0.1222D-01	0.2972D+12	-0.6230D+11	0.200
	20000	0.4121D-01	-0.8639D-02	0.2101D+12	-0.4405D+11	0.401
	40000	0.2914D-01	-0.6109D-02	0.1486D+12	-0.3115D+11	0.802
	80000	0.2060D-01	-0.4319D-02	0.1051D+12	-0.2202D+11	1.603
5s - 5p $^4F_{5/2}$ - $^4F_{3/2}^o$ 1994.67 Å	5000	0.8835D-01	-0.1881D-01	0.4183D+12	-0.8906D+11	0.104
	10000	0.6247D-01	-0.1330D-01	0.2958D+12	-0.6297D+11	0.208
	20000	0.4417D-01	-0.9405D-02	0.2091D+12	-0.4453D+11	0.416
	40000	0.3123D-01	-0.6651D-02	0.1479D+12	-0.3149D+11	0.832
	80000	0.2209D-01	-0.4703D-02	0.1046D+12	-0.2226D+11	1.664
5s - 5p $^4F_{5/2}$ - $^4F_{5/2}^o$ 1949.35 Å	5000	0.8501D-01	-0.1789D-01	0.4214D+12	-0.8869D+11	0.102
	10000	0.6011D-01	-0.1265D-01	0.2980D+12	-0.6271D+11	0.203
	20000	0.4251D-01	-0.8946D-02	0.2107D+12	-0.4434D+11	0.407
	40000	0.3006D-01	-0.6325D-02	0.1490D+12	-0.3136D+11	0.813
	80000	0.2125D-01	-0.4473D-02	0.1054D+12	-0.2217D+11	1.626
5s - 5p $^4F_{5/2}$ - $^4F_{7/2}^o$ 1886.85 Å	5000	0.8054D-01	-0.1666D-01	0.4261D+12	-0.8813D+11	0.098
	10000	0.5695D-01	-0.1178D-01	0.3013D+12	-0.6232D+11	0.197
	20000	0.4027D-01	-0.8329D-02	0.2131D+12	-0.4407D+11	0.394
	40000	0.2847D-01	-0.5889D-02	0.1507D+12	-0.3116D+11	0.787
	80000	0.2013D-01	-0.4164D-02	0.1065D+12	-0.2203D+11	1.574
5s - 5p $^4F_{7/2}$ - $^4F_{5/2}^o$ 1991.37 Å	5000	0.8909D-01	-0.1886D-01	0.4232D+12	-0.8957D+11	0.104
	10000	0.6299D-01	-0.1333D-01	0.2992D+12	-0.6333D+11	0.208
	20000	0.4454D-01	-0.9428D-02	0.2116D+12	-0.4478D+11	0.415
	40000	0.3150D-01	-0.6666D-02	0.1496D+12	-0.3167D+11	0.831
	80000	0.2227D-01	-0.4714D-02	0.1058D+12	-0.2239D+11	1.661
5s - 5p $^4F_{7/2}$ - $^4F_{7/2}^o$ 1926.19 Å	5000	0.8428D-01	-0.1753D-01	0.4279D+12	-0.8901D+11	0.100
	10000	0.5959D-01	-0.1240D-01	0.3026D+12	-0.6294D+11	0.201
	20000	0.4214D-01	-0.8766D-02	0.2139D+12	-0.4451D+11	0.402
	40000	0.2980D-01	-0.6199D-02	0.1513D+12	-0.3147D+11	0.803
	80000	0.2107D-01	-0.4383D-02	0.1070D+12	-0.2225D+11	1.607
5s - 5p $^4F_{7/2}$ - $^4F_{9/2}^o$ 1877.81 Å	5000	0.8081D-01	-0.1658D-01	0.4317D+12	-0.8856D+11	0.098
	10000	0.5714D-01	-0.1172D-01	0.3052D+12	-0.6262D+11	0.196
	20000	0.4040D-01	-0.8290D-02	0.2158D+12	-0.4428D+11	0.392
	40000	0.2857D-01	-0.5862D-02	0.1526D+12	-0.3131D+11	0.783
	80000	0.2020D-01	-0.4145D-02	0.1079D+12	-0.2214D+11	1.567
5s - 5p $^4F_{9/2}$ - $^4F_{7/2}^o$ 1997.14 Å	5000	0.8925D-01	-0.1870D-01	0.4301D+12	-0.9011D+11	0.103
	10000	0.6311D-01	-0.1322D-01	0.3041D+12	-0.6372D+11	0.206
	20000	0.4463D-01	-0.9350D-02	0.2150D+12	-0.4506D+11	0.412
	40000	0.3156D-01	-0.6612D-02	0.1521D+12	-0.3186D+11	0.825
	80000	0.2231D-01	-0.4675D-02	0.1075D+12	-0.2253D+11	1.649
5s - 5p $^4F_{9/2}$ - $^4F_{9/2}^o$ 1926.21 Å	5000	0.8546D-01	-0.1766D-01	0.4339D+12	-0.8967D+11	0.100
	10000	0.6043D-01	-0.1249D-01	0.3068D+12	-0.6340D+11	0.201
	20000	0.4273D-01	-0.8831D-02	0.2169D+12	-0.4483D+11	0.402
	40000	0.3022D-01	-0.6244D-02	0.1534D+12	-0.3170D+11	0.803
	80000	0.2137D-01	-0.4415D-02	0.1085D+12	-0.2242D+11	1.607

Table 1. Continued

Transition	T(K)	$W_e(\text{Å})$	$d_e(\text{Å})$	$W[s^{-1}]$	$d[s^{-1}]$	$3kT/2\Delta E$
5s - 5p $^2F_{5/2}$ - $^2F^o_{5/2}$ 2231.80 Å	5000	0.1156D+00	-0.2505D-01	0.4371D+12	-0.9472D+11	0.116
	10000	0.8173D-01	-0.1771D-01	0.3091D+12	-0.6697D+11	0.233
	20000	0.5779D-01	-0.1252D-01	0.2185D+12	-0.4736D+11	0.465
	40000	0.4086D-01	-0.8855D-02	0.1545D+12	-0.3349D+11	0.931
	80000	0.2889D-01	-0.6261D-02	0.1093D+12	-0.2368D+11	1.862
5s - 5p $^2F_{5/2}$ - $^2F^o_{7/2}$ 2146.66 Å	5000	0.1082D+00	-0.2303D-01	0.4421D+12	-0.9413D+11	0.112
	10000	0.7647D-01	-0.1628D-01	0.3126D+12	-0.6656D+11	0.224
	20000	0.5408D-01	-0.1151D-01	0.2210D+12	-0.4706D+11	0.448
	40000	0.3824D-01	-0.8141D-02	0.1563D+12	-0.3328D+11	0.895
	80000	0.2704D-01	-0.5757D-02	0.1105D+12	-0.2353D+11	1.791
5s - 5p $^2F_{7/2}$ - $^2F^o_{5/2}$ 2345.95 Å	5000	0.1288D+00	-0.2824D-01	0.4410D+12	-0.9667D+11	0.122
	10000	0.9110D-01	-0.1997D-01	0.3118D+12	-0.6835D+11	0.245
	20000	0.6442D-01	-0.1412D-01	0.2205D+12	-0.4833D+11	0.489
	40000	0.4555D-01	-0.9985D-02	0.1559D+12	-0.3418D+11	0.979
	80000	0.3221D-01	-0.7061D-02	0.1102D+12	-0.2417D+11	1.957
5s - 5p $^2F_{7/2}$ - $^2F^o_{7/2}$ 2252.05 Å	5000	0.1201D+00	-0.2587D-01	0.4460D+12	-0.9608D+11	0.117
	10000	0.8491D-01	-0.1829D-01	0.3154D+12	-0.6794D+11	0.235
	20000	0.6004D-01	-0.1293D-01	0.2230D+12	-0.4804D+11	0.470
	40000	0.4246D-01	-0.9146D-02	0.1577D+12	-0.3397D+11	0.939
	80000	0.3002D-01	-0.6467D-02	0.1115D+12	-0.2402D+11	1.879
5s - 5p $^4F_{3/2}$ - $^4D^o_{1/2}$ 1821.72 Å	5000	0.7545D-01	-0.1536D-01	0.4282D+12	-0.8716D+11	0.095
	10000	0.5335D-01	-0.1086D-01	0.3028D+12	-0.6163D+11	0.190
	20000	0.3772D-01	-0.7678D-02	0.2141D+12	-0.4358D+11	0.380
	40000	0.2668D-01	-0.5429D-02	0.1514D+12	-0.3081D+11	0.760
	80000	0.1886D-01	-0.3839D-02	0.1071D+12	-0.2179D+11	1.520
5s $^4F_{3/2}$ - 5p $^4D^o_{3/2}$ 1795.73 Å	5000	0.7370D-01	-0.1487D-01	0.4305D+12	-0.8689D+11	0.094
	10000	0.5212D-01	-0.1052D-01	0.3044D+12	-0.6144D+11	0.187
	20000	0.3685D-01	-0.7437D-02	0.2153D+12	-0.4344D+11	0.375
	40000	0.2606D-01	-0.5259D-02	0.1522D+12	-0.3072D+11	0.749
	80000	0.1843D-01	-0.3719D-02	0.1076D+12	-0.2172D+11	1.498
5s $^4F_{5/2}$ - $^4D^o_{3/2}$ 1819.58 Å	5000	0.7588D-01	-0.1538D-01	0.4317D+12	-0.8747D+11	0.095
	10000	0.5365D-01	-0.1087D-01	0.3053D+12	-0.6185D+11	0.190
	20000	0.3794D-01	-0.7688D-02	0.2158D+12	-0.4374D+11	0.379
	40000	0.2683D-01	-0.5436D-02	0.1526D+12	-0.3093D+11	0.759
	80000	0.1897D-01	-0.3844D-02	0.1079D+12	-0.2187D+11	1.518
5s - 5p $^4F_{5/2}$ - $^4D^o_{5/2}$ 1819.51 Å	5000	0.7587D-01	-0.1537D-01	0.4317D+12	-0.8747D+11	0.095
	10000	0.5365D-01	-0.1087D-01	0.3053D+12	-0.6185D+11	0.190
	20000	0.3794D-01	-0.7687D-02	0.2159D+12	-0.4374D+11	0.379
	40000	0.2683D-01	-0.5435D-02	0.1526D+12	-0.3093D+11	0.759
	80000	0.1897D-01	-0.3843D-02	0.1079D+12	-0.2187D+11	1.518
5s - 5p $^4F_{5/2}$ - $^4D^o_{7/2}$ 1771.35 Å	5000	0.7264D-01	-0.1448D-01	0.4361D+12	-0.8695D+11	0.092
	10000	0.5136D-01	-0.1024D-01	0.3084D+12	-0.6149D+11	0.185
	20000	0.3632D-01	-0.7242D-02	0.2180D+12	-0.4348D+11	0.369
	40000	0.2568D-01	-0.5121D-02	0.1542D+12	-0.3074D+11	0.739
	80000	0.1816D-01	-0.3621D-02	0.1090D+12	-0.2174D+11	1.478
5s - 5p $^4F_{7/2}$ - $^4D^o_{5/2}$ 1856.06 Å	5000	0.7927D-01	-0.1616D-01	0.4335D+12	-0.8835D+11	0.097
	10000	0.5606D-01	-0.1143D-01	0.3065D+12	-0.6247D+11	0.194
	20000	0.3964D-01	-0.8079D-02	0.2167D+12	-0.4418D+11	0.387
	40000	0.2803D-01	-0.5713D-02	0.1533D+12	-0.3124D+11	0.774
	80000	0.1982D-01	-0.4040D-02	0.1084D+12	-0.2209D+11	1.548

Table 1. Continued

Transition	T(K)	$W_e(\text{Å})$	$d_e(\text{Å})$	$W[s^{-1}]$	$d[s^{-1}]$	$3kT/2\Delta E$
5s -5p $^4F_{7/2}$ - $^4D^o_{7/2}$ 1805.98 Å	5000	0.7581D-01	-0.1521D-01	0.4378D+12	-0.8783D+11	0.094
	10000	0.5361D-01	-0.1075D-01	0.3096D+12	-0.6211D+11	0.188
	20000	0.3791D-01	-0.7604D-02	0.2189D+12	-0.4392D+11	0.377
	40000	0.2680D-01	-0.5377D-02	0.1548D+12	-0.3105D+11	0.753
	80000	0.1895D-01	-0.3802D-02	0.1095D+12	-0.2196D+11	1.507
5s -5p $^4F_{9/2}$ - $^4D^o_{7/2}$ 1850.70 Å	5000	0.8001D-01	-0.1617D-01	0.4400D+12	-0.8893D+11	0.096
	10000	0.5658D-01	-0.1143D-01	0.3112D+12	-0.6289D+11	0.193
	20000	0.4001D-01	-0.8086D-02	0.2200D+12	-0.4447D+11	0.386
	40000	0.2829D-01	-0.5717D-02	0.1556D+12	-0.3144D+11	0.772
	80000	0.2000D-01	-0.4043D-02	0.1100D+12	-0.2223D+11	1.544
5s -5p $^2F_{5/2}$ - $^2D^o_{5/2}$ 2231.79 Å	5000	0.1156D+00	-0.2505D-01	0.4371D+12	-0.9472D+11	0.116
	10000	0.8172D-01	-0.1771D-01	0.3091D+12	-0.6697D+11	0.233
	20000	0.5779D-01	-0.1252D-01	0.2185D+12	-0.4736D+11	0.465
	40000	0.4086D-01	-0.8855D-02	0.1545D+12	-0.3349D+11	0.931
	80000	0.2889D-01	-0.6261D-02	0.1093D+12	-0.2368D+11	1.862
5s -5p $^2F_{5/2}$ - $^2D^o_{7/2}$ 2146.66 Å	5000	0.1082D+00	-0.2303D-01	0.4421D+12	-0.9413D+11	0.112
	10000	0.7647D-01	-0.1628D-01	0.3126D+12	-0.6656D+11	0.224
	20000	0.5408D-01	-0.1151D-01	0.2210D+12	-0.4706D+11	0.448
	40000	0.3824D-01	-0.8141D-02	0.1563D+12	-0.3328D+11	0.895
	80000	0.2704D-01	-0.5757D-02	0.1105D+12	-0.2353D+11	1.791
5s -5p $^2F_{7/2}$ - $^2D^o_{7/2}$ 2252.06 Å	5000	0.1201D+00	-0.2587D-01	0.4460D+12	-0.9608D+11	0.117
	10000	0.8491D-01	-0.1829D-01	0.3154D+12	-0.6794D+11	0.235
	20000	0.6004D-01	-0.1293D-01	0.2230D+12	-0.4804D+11	0.470
	40000	0.4246D-01	-0.9146D-02	0.1577D+12	-0.3397D+11	0.939
	80000	0.3002D-01	-0.6467D-02	0.1115D+12	-0.2402D+11	1.879
5s -5p $^2F_{5/2}$ - $^2G^o_{7/2}$ 2007.05 Å	5000	0.9657D-01	-0.1989D-01	0.4516D+12	-0.9300D+11	0.105
	10000	0.6829D-01	-0.1406D-01	0.3193D+12	-0.6576D+11	0.209
	20000	0.4828D-01	-0.9944D-02	0.2258D+12	-0.4650D+11	0.419
	40000	0.3414D-01	-0.7032D-02	0.1597D+12	-0.3288D+11	0.837
	80000	0.2414D-01	-0.4972D-02	0.1129D+12	-0.2325D+11	1.674
5s - 5p $^2F_{7/2}$ - $^2G^o_{9/2}$ 2028.94 Å	5000	0.1006D+00	-0.2062D-01	0.4605D+12	-0.9435D+11	0.106
	10000	0.7116D-01	-0.1458D-01	0.3256D+12	-0.6672D+11	0.212
	20000	0.5032D-01	-0.1031D-01	0.2302D+12	-0.4718D+11	0.423
	40000	0.3558D-01	-0.7290D-02	0.1628D+12	-0.3336D+11	0.846
	80000	0.2516D-01	-0.5155D-02	0.1151D+12	-0.2359D+11	1.693

dwarfs (Werner et al., 2012) where Stark broadening is usually dominant line broadening mechanism. Here, we used the obtained results to investigate the importance of Stark broadening in DO white dwarf atmospheres. The atmospheric model for DO type of WD (Wesemael, 1981) is for a surface gravity log $g = 6$ and $T_{eff} = 80\,000$ K. The importance of Stark broadening in DO white dwarf atmospheres is illustrated by comparison of Stark and Doppler line widths in Fig.2.

Our knowledge of the Stark broadening parameters is of great importance for the spectra of White Dwarfs, as we have shown in some of the previous studies Majlinger et al. (2015, 2017); Simić & Sakan (2020); Simić & Sakan (2021), because of all this, the Stark broadening must be taken into consideration

when investigating white dwarf atmospheres since our calculations of Mo IV spectral lines show that they are of great importance in DA and DO white dwarf-type atmospheres. Such data are also of interest for investigation, analysis and modelling of stellar, technological and laboratory plasma.

References

Chayer, P., Vennes, S., Dupuis, J., & Kruk, J. W., Abundance of Elements beyond the Iron Group in Cool DO White Dwarfs. 2005, *The Astrophysical Journal*, **630**, L169, DOI: 10.1086/491699

Dimitrijević, M. S. & Konjević, N., Simple estimates for Stark broadening of ion lines in stellar plasmas. 1987, *Astronomy and Astrophysics*, **172**, 345

Dreizler, S. & Werner, K., Spectral analysis of hot helium-rich white dwarfs. 1996, *Astronomy and Astrophysics*, **314**, 217

Majlinger, Z., Simić, Z., & Dimitrijević, M. S., On the Stark Broadening of Lu III Spectral Lines. 2015, *Journal of Astrophysics and Astronomy*, **36**, 671, DOI: 10.1007/s12036-015-9362-9

Majlinger, Z., Simić, Z., & Dimitrijević, M. S., Stark broadening of Zr IV spectral lines in the atmospheres of chemically peculiar stars. 2017, *Monthly Notices of the Royal Astronomical Society*, **470**, 1911, DOI: 10.1093/mnras/stx1321

Moore, C. E., Atomic Energy Levels as Derived from the Analysis of Optical Spectra – Molybdenum through Lanthanum and Hafnium through Actinium. 1971, in *Nat. Stand. Ref. Data Ser. 35, Vol. III (Reprint of NBS Circ. 467, Vol. III, 1958)* (U.S.: Nat. Bur. Stand.)

O'Toole, S. J., Beyond the iron group: Heavy metals in hot subdwarfs. 2004, *Astronomy and Astrophysics*, **423**, L25, DOI: 10.1051/0004-6361:200400027

O'Toole, S. J. & Heber, U., Abundances of Heavy Metals and Lead Isotopic Ratios in Subluminous B Stars. 2007, in Astronomical Society of the Pacific Conference Series, Vol. **372**, *15th European Workshop on White Dwarfs*, ed. R. Napiwotzki & M. R. Burleigh, 209

Ralchenko, Y., Fuhr, J. R., Jou, F. C., et al., New Generation of the NIST Atomic Spectroscopic Databases. 2005, in American Institute of Physics Conference Series, Vol. **771**, *Atomic and Molecular Data and their Applications*, ed. T. Kato, D. Kato, & H. Funaba, 276–285

Rauch, T., Quinet, P., Hoyer, D., et al., Stellar laboratories. VI. New Mo iv-vii oscillator strengths and the molybdenum abundance in the hot white dwarfs G191-B2B and RE 0503-289. 2016, *Astronomy and Astrophysics*, **587**, A39, DOI: 10.1051/0004-6361/201527324

Reader, J., Corliss, C. H., Wiese, W. L., & Martin, G. A. 1980, *Wavelengths and transition probabilities for atoms and atomic ions: Part 1. Wavelengths, part 2. Transition probabilities*

Sahal-Bréchot, S., Impact Theory of the Broadening and Shift of Spectral Lines due to Electrons and Ions in a Plasma. 1969a, *Astronomy and Astrophysics*, **1**, 91

Sahal-Bréchot, S., Impact Theory of the Broadening and Shift of Spectral Lines due to Electrons and Ions in a Plasma (Continued). 1969b, *Astronomy and Astrophysics*, **2**, 322

Sahal-Bréchot, S., Dimitrijević, M. S., & Nessib, N., Widths and Shifts of Isolated Lines of Neutral and Ionized Atoms Perturbed by Collisions With Electrons and Ions: An Outline of the Semiclassical Perturbation (SCP) Method and of the Approximations Used for the Calculations. 2014, *Atoms*, **2**, 225, DOI: 10.3390/atoms2020225

Simić, Z., Milovanović, N., Sakan, N., & Malović, M., On the Stark broadening of the Re II spectral lines. 2023, *Advances in Space Research*, **71**, 1287, DOI: 10.1016/j.asr.2022.07.079

Simić, Z. & Sakan, N. M., The electron-impact broadening of the Nb III for 5p-5d transitions. 2020, *Monthly Notices of the Royal Astronomical Society*, **491**, 4382, DOI: 10.1093/mnras/stz3362

Simić, Z. & Sakan, N. M., Stark Widths and Shifts of Rh II in Chemically Peculiar Stars. 2021, *International Astronomy and Astrophysics Research Journal*, **3**, 37

Simić, Z., Sakan, N. M., Milovanović, N., & Martinović, M., Singly Ionized Iridium Spectral Lines in the Atmosphere of Hot Stars. 2021, *International Astronomy and Astrophysics Research Journal*, **3**, 33, DOI: 10.1051/0004-6361/201118205

Vennes, S., Chayer, P., & Dupuis, J., Discovery of Photospheric Germanium in Hot DA White Dwarfs. 2005, *The Astrophysical Journal*, **622**, L121, DOI: 10.1086/429667

Werner, K., Rauch, T., Ringat, E., & Kruk, J. W., First Detection of Krypton and Xenon in a White Dwarf. 2012, *The Astrophysical Journal Letters*, **753**, L7, DOI: 10.1088/2041-8205/753/1/L7

Wesemael, F., Atmospheres for hot, high-gravity stars. II. Pure helium models. 1981, *Astrophysical Journal, Suppl. Ser.*, **45**, 177, DOI: 10.1086/190712

Wickramasinghe, D. T., Model atmospheres for DA and DB white dwarfs. 1972, *Memoirs of the Royal Astronomical Society*, **76**, 129

On the Stark broadening of Al IV spectral lines in stellar atmospheres

Magdalena D. Christova[1] and **Milan S. Dimitrijević**[2,3]

[1] *Department of Applied Physics, Technical University of Sofia, 1000 Sofia, Bulgaria, (E-mail: mchristo@tu-sofia.bg)*

[2] *Astronomical Observatory, Volgina 7, 11060 Belgrade, Serbia, (E-mail: mdimitrijevic@aob.rs)*

[3] *LERMA, Observatoire de Paris, Université PSL, CNRS, Sorbonne Université, F-92190 Meudon, France*

Abstract. The influence of Stark broadening on Al IV spectral lines in the visible part of the spectrum of A-type star and DO white dwarf atmospheres is analyzed. It has been demonstrated that it is negligible for considered spectral lines in the case of A-type stars and dominant in the case of DO white dwarfs. Also, regularitis of Stark widths and their temperature dependence have been discussed.

Key words: Stark broadening – spectral line shapes – atomic data – Al IV

1. Introduction

One of the first studies dealing with Stark broadening of aluminum spectral lines is presented in Mazing *et al.* (1964) and since than a great number of studies of Stark broadening of spectral lines of aluminum in different ionization degrees, witnessing on its importance, have been published. The needs for Stark broadening data for spectral lines of aluminum ions in astrophysics stimulated particularly the efforts on that subject (Dimitrijević; Sahal-Bréchot, 1994; Elabidi, 2021). For example results for 7 Al XI spectral lines for perturber densities 10^{18} cm^{-3} – 10^{23} cm^{-3} and temperatures: 500 000 K – 4 000 000 K are provided in Dimitrijević and Sahal-Bréchot (1994). Elabidi (2021) calculated Stark broadening parameters for 20 Al IV lines in UV, belonging to 2p^6–3s, 3s–3p and 3p–3d transitions. For calculations he used quantum mechanical theory (Elabidi, 2004; Elabidi *et al.*, 2008), while in Dimitrijević and Sahal-Bréchot (1994), the semiclassical perturbation formalism (Sahal-Bréchot, 1969 a b) is applied.

Aluminum is the twelfth most common chemical element in the cosmos and its spectral lines are largely presented in the observed stellar spectra. That implies the astrophysical importance of aluminum. Aluminum abundances in giants and dwarfs are for example determined in Smiljanic *et al.* (2016) within

the Gaia-ESO Survey. Carretas *et al.* (2018) determine aluminum abundances for red giant branch (RGB). For a total of 108 RGB stars in NGC 2808 [Al/Fe] ratios are gathered. The atmospheric abundance of aluminum is derived for a sample of normal, superficially normal and HgMn–type main–sequence late–B stars (Smith, 1993). According to Fernández–Trincado *et al.*, stars with higher levels of aluminium and nitrogen enrichment are often key pieces in the chemical makeup of multiple populations in almost all globular clusters (GCs). With the help of APOGEE spectra, they reported the discovery of 29 mildly metal–poor stars wich atmospheres have overabundance of aluminum (Al–rich stars).

Plasma diagnostics using spectral line profiles and line broadening is a powerful tool to understand the interactions in the plasma environment. Such data are significant to obtain reliable modelling of plasma processes. Interactions between emitters (atoms or ions) and surrounding particles results in broadening and shifting of spectral line profiles known as pressure broadening. Stark broadening is a type of pressure broadening where the interactions between emitters and charged particles are of interest. Stark broadening data are applicable in fundamental research as astrophysics (Beauchamp *et al.*, 1997), investigations of laboratory plasma (Konjević, 1999; Belostotskiy *et al.*, 2010; Zhou *et al.*, 2022), laser produced plasma (Gornushkin, 1999; Nicolosi *et al.*; Sorge *et al.*, 2000), inertial fusion experiments (Griem, 1992; Iglesias *et al.*, 1887) and others. They find application also in technological and industrial plasma (Yilbas *et al.*, 2015; Hoffman *et al.*, 2006), as well as for laser design and development (Wang *et al.*, 1992).

Recently, we calculated Stark widths at half maximum (FWHM) for 23 Al IV multiplets using modified semiempirical method (Dimitrijević; Christova, 2023). The studied lines belong to the visible part of the spectrum. Values for the temperature are 10 000 K, 20 000 K, 40 000 K, 80 000 K and 160 000 K, and the perturber density is 10^{17} cm^{-3} .

In this work, we perform an analysis of the Stark broadening influence on the Al IV spectral lines in the visible part of A-type star and DO white dwarf spectra, by comparison of Stark and Doppler widths versus Rosseland optical depth, with the help of Kurucz (1979) and Wesemael (1981) models of stellar atmospheres. Additionally, temperature dependence of Stark broadening for spectral lines within one multiplet, one spectral series and one supermultiplet will be discussed and the similarities of Stark widths (Wiese; Konjević, 1982) for spectral lines within a multiplet will be considered.

The data on Al IV Stark broadening parmeters will be of interest for a number of research topics in astronomy, in particular for white dwarf spectra analysis and synthesis and modelling of their atmospheres, for abundance determination and radiative transfer and opacity calculations. They will be also useful for laboratory, fusion and laser-produced plasmas investigation and modelling.

2. Theory

The modified semiempirical method (MSE - Dimitrijević, Konjević, 1980, for the applications see Dimitrijević, 2020) has been described many times so that only basic details will be presented here. In this method, the full width at half intensity maximum (FHWM) is given as:

$$W_{MSE} = N \frac{8\pi}{3} \frac{\hbar^2}{m^2} \Big(\frac{2m}{\pi kT}\Big)^{1/2} \frac{\pi}{\sqrt{3}} \frac{\lambda^2}{2\pi c} \times$$

$$\times \{\sum_{\ell_i \pm 1} \sum_{L_{i'} J_{i'}} \vec{R}^2[n_i \ell_i L_i J_i, n_i(\ell_i \pm 1)L_{i'} J_{i'}]\widetilde{g}(x_{\ell_i, \ell_i \pm 1})+$$

$$+ \sum_{\ell_f \pm 1} \sum_{L_{f'} J_{f'}} \vec{R}^2[n_f \ell_f L_f J_f, n_f(\ell_f \pm 1)L_{f'} J_{f'}]\widetilde{g}(x_{\ell_f, \ell_f \pm 1})+$$

$$+ \Big(\sum_{i'} \vec{R}^2_{ii'}\Big)_{\Delta n \neq 0} g(x_{n_i, n_i+1}) + \Big(\sum_{f'} \vec{R}^2_{ff'}\Big)_{\Delta n \neq 0} g(x_{n_f, n_f+1})\}. \tag{1}$$

Here, the index i is for the initial and index f for the final atomic energy level. The square of the matrix element $\{\vec{R}^2[n_k \ell_k L_k J_k, (\ell_k \pm 1)L_{k'} J_{k'}], \quad k = i, f\}$ may be expressed as:

$$\vec{R}^2[n_k \ell_k L_k J_k, n_k(\ell_k \pm 1)L'_k J'_k] =$$

$$\frac{\ell_>}{2J_k + 1} Q[\ell_k L_k, (\ell_k \pm 1)L'_k] Q(J_k, J'_k)[R^{n_k^*(\ell_k \pm 1)}_{n_k^* \ell_k}]^2. \tag{2}$$

Here, $\ell_> = \max(\ell_k, \ell_k \pm 1)$ and

$$\Big(\sum_{k'} \vec{R}^2_{kk'}\Big)_{\Delta n \neq 0} = \Big(\frac{3n_k^*}{2Z}\Big)^2 \frac{1}{9}(n_k^{*2} + 3\ell_k^2 + 3\ell_k + 11). \tag{3}$$

In Equation (1)

$$x_{\ell_k, \ell_{k'}} = \frac{E}{\Delta E_{\ell_k, \ell_{k'}}}, \quad k = i, f$$

$E = \frac{3}{2}kT$ is the electron kinetic energy and $\Delta E_{\ell_k, \ell_{k'}} = |E_{\ell_k} - E_{\ell_{k'}}|$ is the energy difference between levels ℓ_k and $\ell_k \pm 1$ ($k = i, f$),

$$x_{n_k, n_k+1} \approx \frac{E}{\Delta E_{n_k, n_k+1}},$$

where for $\Delta n \neq 0$, the energy difference between energy levels with n_k and n_k+1, $\Delta E_{n_k, n_k+1}$ is represented by the following equation:

$$\Delta E_{n_k, n_k+1} = 2Z^2 E_H / n_k^{*3}, \tag{4}$$

where $n_k^* = [E_H Z^2/(E_{ion} - E_k)]^{1/2}$ is the effective principal quantum number, N the electron density, T the temperature, Z the residual ionic charge (e.g. $Z=4$ for Al IV), E_{ion} the appropriate spectral series limit, $Q(\ell L, \ell' L')$, multiplet factor and $Q(J, J')$ line factor (Shore, Menzel, 1965). The needed Gaunt factors are $g(x)$ (Griem, 1968; Griem, 1974) and $\widetilde{g}(x)$ (Dimitrijević, Konjević, 1980). For radial integrals $[R_{n_k^* \ell_k}^{n_k^* \ell_k \pm 1}]$ the Coulomb approximation Bates, Damgaard, 1949) was applied with the help of tables in Oertel and Shomo (1968).

3. Results and Discussion

In order to investigate and demonstrate the importance of Stark broadening of Al IV lines for modelization of stellar atmospheres, we took one atmosphere model of an A-type star (Kurucz, 1979) and one of a DO white dwarf (Wesemael, 1981) and three spectral lines in the visble part of the spectrum, since such lines are particularly important for astronomy. The corresponding transitions are: $2s^2\ 2p^5\ (^2P_{3/2}^o)4p^2[1/2]_1 - 2s^2\ 2p^5\ (^2P_{3/2}^o)4d^2[1/2]^o$, $\lambda = 3279.6$ Å, $2s^2$ $2p^5\ (^2P_{3/2}^o)4p^2[1/2]_0 - 2s^2\ 2p^5\ (^2P_{3/2}^o)4d^2[1/2]^o$, $\lambda = 4210.3$ Å and $2s^2\ 2p^5$ $(^2P_{3/2}^o)4p^2[5/2] - 2s^2\ 2p^5\ (^2P_{3/2}^o)4d^2[3/2]^o$, $\lambda = 3411.8$ Å. Two first lines belong to the same multiplet and all three belong to the same supermultiplet. Using the modified semiempirical method (Dimitrijević, Konjević, 1980), we calculated Stark widths (FWHM) for Roseland optical depths, temperatures and electron densities in different points of the model. The obtained results, together with the corresponding thermal Doppler widths, are presented in Table 1, for A-type star atmosphere and in Table 2 for DO white dwarf. In order to beter investigate similarities and regularities of Stark widths within multiplet, supermultiplet and spectral series, Stark and Doppler widths are given in angstroms as well as in angular frequency units.

Comparison of Stark and thermal Doppler widths of three Al IV lines 3279.6 Å, 4210.3 Å, and 3411.8 Å, are presented in Figs. 1-4, as a function of Rosseland optical depth for conditions corresponding to atmospheres of an A–type star (Figures 1 and 2) and DO white dwarf (Figures 3 and 4). Figures 1 and 3 illustrate the case when widths are expressed in angstrom units and Figure 2 and 4, when they are in angular frequency units.

The model of stellar atmosphere for A-type star is taken from Kurucz (1979) with the effective temperature $T_{eff} = 8\,500$ K and logarithm of surface gravity log g = 4.5, and for DO white dwarf from Wesemael (1981), with parameters $T_{eff} = 60\,000$ K and log g = 8.0. In the case of A-type star, the Doppler broadening of all three lines dominates in the whole temperature interval and it changes very slowly. The Doppler widths for 3279.6 Å and 3411.8 Å spectral lines coincide if angstroms (Fig. 1) or angular frequency units (Fig. 2) are used. The same width for 4210.3 Å is larger 28% than those of both lines in angstrom units and lower 28 % than them in angular frequency units. Except for the first value of Rosseland optical depth (τ), three curves of Stark widths in angstroms

Table 1. Dependence of Stark (We) and Doppler (WDop) full width at half intensity maximum of Al IV $(^2P^o_{3/2})$ $4p^2[1/2]_1$ – $(^2P^o_{3/2})$ $4d^2[1/2]^o$ $\lambda = 3279.6$ Å, $(^2P^o_{3/2})$ $4p^2[1/2]_0$ – $(^2P^o_{3/2})$ $4d^2[1/2]^o$ $\lambda = 4210.3$ Å and $(^2P^o_{3/2})$ $4p^2[5/2]$ – $(^2P^o_{3/2})$ $4d^2[3/2]^o$ $\lambda = 3411.8$ Å spectral lines, on the Rosseland optical depth (τ_{Ross}) in the atmosphere of an A-type star. Model of stellar atmosphere (Kurucz, 1979) with parameters T_{eff} = 8 500 K and log g = 4.5. T is temperature and Ne electron density.

τ_{Ross}	T [K]	Ne [cm^{-3}]	We [Å]	WDop [Å]	We [10^{12}s^{-1}]	WDop [10^{12}s^{-1}]
			3279.592 Å			
0.106E-03	6164.	1.25E+12	0.939E-06	0.014	0.164E-05	0.024
0.481E-03	6410.	3.24E+12	0.238E-05	0.014	0.417E-05	0.025
0.204E-02	6616.	7.10E+12	0.514E-05	0.014	0.901E-05	0.025
0.846E-02	6826.	1.25E+13	0.890E-05	0.015	0.156E-04	0.026
0.366E-01	7101.	3.51E+13	0.245E-04	0.015	0.430E-04	0.026
0.166	7602.	1.05E+14	0.708E-04	0.015	0.124E-03	0.027
1.21	8930.	6.05E+14	0.377E-03	0.017	0.661E-03	0.029
4.34	11980.	3.36E+15	0.182E-02	0.019	0.319E-02	0.034
25.2	17938.	5.31E+15	0.244E-02	0.024	0.426E-02	0.042
118.	26137.	1.58E+16	0.624E-02	0.029	0.109E-01	0.050
			4210.296 Å			
0.106E-03	6164.	1.25E+12	0.156E-05	0.018	0.165E-05	0.019
0.481E-03	6410.	3.24E+12	0.395E-05	0.018	0.419E-05	0.019
0.204E-02	6616.	7.10E+12	0.853E-05	0.019	0.906E-05	0.020
0.846E-02	6826.	1.25E+13	0.148E-04	0.019	0.157E-04	0.020
0.366E-01	7101.	3.51E+13	0.407E-04	0.019	0.432E-04	0.020
0.166	7602.	1.05E+14	0.117E-03	0.020	0.125E-03	0.021
1.21	8930.	6.05E+14	0.625E-03	0.022	0.664E-03	0.023
4.34	11980.	3.36E+15	0.302E-02	0.025	0.321E-02	0.027
25.2	17938.	5.31E+15	0.403E-02	0.031	0.429E-02	0.032
118.	26137.	1.58E+16	0.103E-01	0.037	0.110E-01	0.039
			3411.782 Å			
0.106E-03	6164.	1.25E+12	0.587E-06	0.014	0.950E-06	0.023
0.481E-03	6410.	3.24E+12	0.149E-05	0.015	0.241E-05	0.024
0.204E-02	6616.	7.10E+12	0.322E-05	0.015	0.520E-05	0.024
0.846E-02	6826.	1.25E+13	0.556E-05	0.015	0.900E-05	0.025
0.366E-01	7101.	3.51E+13	0.153E-04	0.016	0.248E-04	0.025
0.166	7602.	1.05E+14	0.442E-04	0.016	0.716E-04	0.026
1.21	8930.	6.05E+14	0.237E-03	0.017	0.384E-03	0.028
4.34	11980.	3.36E+15	0.116E-02	0.020	0.187E-02	0.033
25.2	17938.	5.31E+15	0.154E-02	0.025	0.250E-02	0.040
118.	26137.	1.58E+16	0.398E-02	0.030	0.645E-02	0.048

Table 2. Dependence of Stark and Doppler full width at half intensity maximum of Al IV $(^2P^o_{3/2})$ $4p^2[1/2]_1$ – $(^2P^o_{3/2})$ $4d^2[1/2]^o$ $\lambda = 3279.6$ Å, $(^2P^o_{3/2})$ $4p^2[1/2]_0$ – $(^2P^o_{3/2})$ $4d^2[1/2]^o$ $\lambda = 4210.3$ Å- and $(^2P^o_{3/2})$ $4p^2[5/2]$ – $(^2P^o_{3/2})$ $4d^2[3/2]^o$ $\lambda = 3411.8$ Å spectral lines, on the Rosseland optical depth τ_{Ross} in the atmosphere of a DO white dwarf. Model of stellar atmosphere (Wesemael, 1981) with parameters $T_{eff} = 60\,000$ K and log g = 8.0. T is temperature and Ne electron density.

τ_{Ross}	T [K]	Ne [cm^{-3}]	We [Å]	WDop [Å]	We [10^{12}s^{-1}]	WDop [10^{12}s^{-1}]
			3279.592 Å			
0.101E-07	38426.	6.31E+11	0.222E-05	0.035	0.389E-05	0.061
0.140E-05	38632.	6.59E+13	0.232E-03	0.035	0.406E-03	0.061
0.103E-03	42308.	1.21E+15	0.412E-02	0.037	0.721E-02	0.064
0.108E-01	46360.	1.54E+16	0.513E-01	0.038	0.898E-01	0.067
0.131	50908.	5.87E+16	0.190	0.040	0.333	0.070
1.32	66476.	2.64E+17	0.792	0.046	1.39	0.080
13.6	108902.	1.76E+18	4.76	0.059	8.34	0.103
23.1	123731.	2.54E+18	6.66	0.062	11.7	0.109
62.9	159279.	4.54E+18	11.3	0.071	19.8	0.124
98.9	179107.	6.73E+18	16.5	0.075	28.8	0.132
			4210.296 Å			
0.101E-07	38426.	6.31E+11	0.368E-05	0.045	0.391E-05	0.047
0.140E-05	38632.	6.59E+13	0.384E-03	0.045	0.408E-03	0.048
0.103E-03	42308.	1.21E+15	0.682E-02	0.047	0.724E-02	0.050
0.108E-01	46360.	1.54E+16	0.849E-01	0.049	0.902E-01	0.052
0.131	50908.	5.87E+16	0.315	0.051	0.334	0.055
1.32	66476.	2.64E+17	1.31	0.059	1.39	0.062
13.6	108902.	1.76E+18	7.87	0.075	8.37	0.080
23.1	123731.	2.54E+18	11.0	0.080	11.7	0.085
62.9	159279.	4.54E+18	18.7	0.091	19.9	0.097
98.9	179107.	6.73E+18	27.2	0.096	28.9	0.102
			3411.782 Å			
0.101E-07	38426.	6.31E+11	0.139E-05	0.036	0.225E-05	0.059
0.140E-05	38632.	6.59E+13	0.145E-03	0.036	0.235E-03	0.059
0.103E-03	42308.	1.21E+15	0.257E-02	0.038	0.415E-02	0.061
0.108E-01	46360.	1.54E+16	0.318E-01	0.040	0.514E-01	0.064
0.131	50908.	5.87E+16	0.117	0.042	0.189	0.067
1.32	66476.	2.64E+17	0.486	0.048	0.786	0.077
13.6	108902.	1.76E+18	2.85	0.061	4.60	0.099
23.1	123731.	2.54E+18	3.98	0.065	6.45	0.105
62.9	159279.	4.54E+18	6.77	0.074	11.0	0.119
98.9	179107.	6.73E+18	9.88	0.078	16.0	0.126

are parallel and slowly increase with τ. The largest values are for 4210.3 Å- and the lowest for 3411.8 Å and their ratio is almost 2.6. The Stark widths of 3279.6 Å are in the middle, 1.7 times lower than the widths of 4210.3 Å and 1.6 times larger than the values of 3411.8 Å. Concerning the trend of Stark widths in angular frequency units (Figure 2), the behavior of three curves is the same. The values of two lines from the same multiplet (3279.592 and 4210.296 Å) coincide in the whole temperature interval which is in accordance with the conclusion in Wiese and Konjević (1982). The Stark widths of 3411.8 Å spectral line are 1.7 times lower. We can conclude that for the considered Al IV spectral lines, thermal Doppler broadening is the main broadening mechanism in the atmosphere of an A-type star.

For the conditions corresponding to atmosphere of DO white dwarfs, Stark widths of three spectral lines dominate for all optical depths, being approximately three orders of magnitude higher than the Doppler widths. Figures 3 and 4 confirm that the main broadening mechanism of spectral lines in atmospheres of DO white dwarfs is usually Stark broadening. Three Stark width curves are parallel to each other in angstrom units. Their gradient is lower in comparison to the case of A-type stars. The largest values are for 4210.3 Å and the lowest for 3411.8 Å in which casee, the variation is within 1.67 times. The Stark width values of 3279.6 Å are in the middle. The same dependence in angular frequency units confirms that lines from one multiplet have close Stark widths. In our case, they practically coincide in the whole examined Rosseland optical depth interval. The Stark width values of 3411.8 Å are 29% lower.

Our analyzis confirms the importance of Stark broadening for reliable analysis and investigation of physical nature of DO white dwarfs. The three considered lines are suitable for application in modelling of DO white dwarf atmospheres, particularly since they are in the visible part of the spectrum.

Additionally, we studied the temperature dependence of Stark widths (full width at half maximum of intensity (W)) of Al IV spectral lines belonging to six multiplets. In Figure 5 we present this dependence for spectral lines within the multiplet Al IV 4p $^2[1/2]$ – 4d $^2[3/2]^o$ with parent term $^2\mathrm{P}^o_{1/2}$. The corresponding transitions and wavelengths are: 4p $^2[1/2]_1$ – 4d $^2[3/2]^o_2$, $\lambda = 3485.1$ Å; 4p $^2[1/2]_1$ – 4d $^2[3/2]^o_1$, $\lambda = 3279.5$ Å; 4p $^2[1/2]_0$ – 4d $^2[3/2]^o_2$, $\lambda = 4550.5$ Å. Stark widths for lines with $\lambda = 3485.1$ Å and $\lambda = 3279.5$ Å coincide. In the examined temperature interval, the relative variation of Stark width (in Å) of lines within this multiplet is 94% in the whole temperature interval. The relative variation of the same width expressed in angular frequency units increases from 8% for lower temperatures to 13% for higher ones. This is in accordance with the conclusion of Wiese and Konjević (1982), that the variation of Stark width in angular frequency units for lines from one multiplet is of the order of several percent.

In the next two figures Stark widths within two spectral series are presented. Figure 6 shows the temperature dependence of three spectral lines belonging to
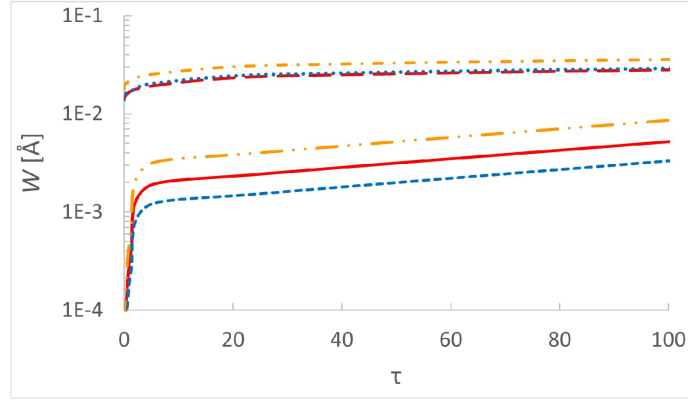
Figure 1. Dependence of Stark and Doppler full width at half intensity maximum (W - in angstroms) of Al IV 3279.6 Å (red, Stark – solid line, Doppler – long dashes), 4210.3 Å (blue, Stark – dashes, Doppler – dots), and 3411.8 Å (orange, Stark – dash dot dot, Doppler – short dash dot) spectral lines, on the Rosseland optical depth (τ) in the atmosphere of an A-type star. Model of stellar atmosphere (Kurucz, 1979) with parameters $T_{eff} = 8\ 500$ K and log g $= 4.5$.
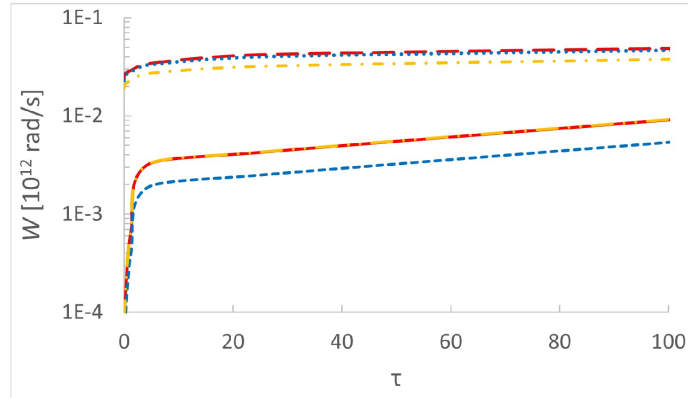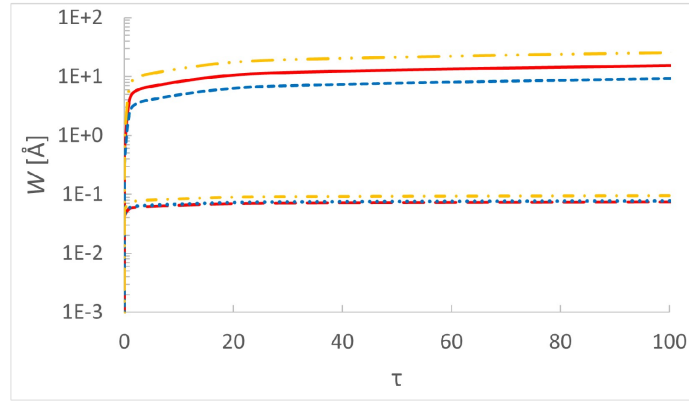

Figure 2. Dependence of Stark and Doppler full width at half intensity maximum (W - in angular frequency units) of Al IV 3279.6 Å (red, Stark – solid line, Doppler – long dashes), 4210.3 Å (blue, Stark – dashes, Doppler – dots), and 3411.8 Å (orange, Stark – dash dot dot, Doppler – short dash dot) spectral lines, on the Rosseland optical depth (τ) in the atmosphere of an A-type star. Model of stellar atmosphere (Kurucz, 1979) with parameters $T_{eff} = 8\ 500$ K and log g $= 4.5$.

Figure 3. Dependence of Stark and Doppler full width at half intensity maximum (W- in angstroms) of Al IV 3279.6 Å (red, Stark – solid line, Doppler – long dashes), 4210.3 Å (blue, Stark – dashes, Doppler – dots), and 3411.8 Å (orange, Stark – dash dot dot, Doppler – short dash dot) spectral lines, on the Rosseland optical depth (τ) in the atmosphere of a DO white dwarf. Model of stellar atmosphere (Wesemael, 1981) with parameters $T_{eff} = 60\ 000$ K and log g = 8.0.
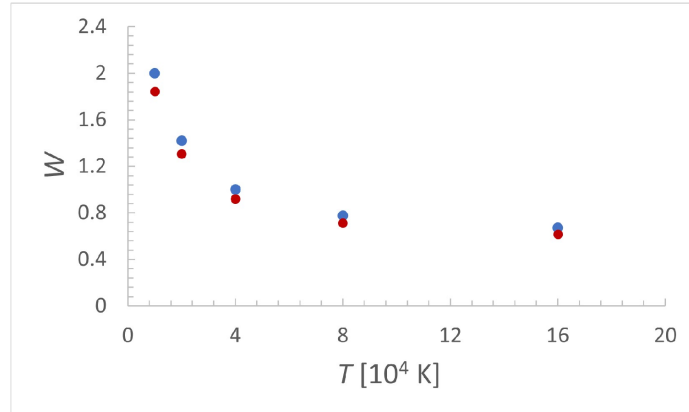
Figure 4. Dependence of Stark and Doppler full width (W - in angular frequency units) at half intensity maximum of Al IV 3279.6 Å (red, Stark – solid line, Doppler – long dashes), 4210.3 Å (blue, Stark – dashes, Doppler – dots), and 3411.8 Å (orange, Stark – dash dot dot, Doppler – short dash dot) spectral lines, on the Rosseland optical depth (τ) in the atmosphere of a DO white dwarf. Model of stellar atmosphere (Wesemael, 1981) with parameters $T_{eff} = 60\ 000$ K and log g = 8.0.

three multiplets from one spectral series with parent term $^2P^o_{1/2}$. The corresponding transitions and wavelengths are as follows: $2s^2\ 2p^5\ (^2P^o_{1/2})4s\ ^2[1/2]^o$ − $2s^2\ 2p^5\ (^2P^o_{1/2})4p\ ^2[1/2]$, $\lambda = 4515.6$ Å; $2s^2\ 2p^5\ (^2P^o_{1/2})4s\ ^2[1/2]^o$ − $2s^2\ 2p^5$ $(^2P^o_{1/2})4p\ ^2[3/2]$, λ 4520.2 Å; $2s^2\ 2p^5\ (^2P^o_{1/2})4p\ ^2[1/2]$ − $2s^2\ 2p^5\ (^2P^o_{1/2})4d$ $^2[3/2]^o$, $\lambda = 3485.1$ Å. The three curves are almost parallel in the examined T-interval. The widths of 4515.6 Å and 3485.1 Å are close and the width of 4520.2 Å is almost twice times larger. This line has the largest Stark width values of all studied lines in this work. It could be very useful for spectroscopic diagnostics and abundance determinations. The width variation in angstrom units between 4515.6 Å and 3485.1 Å is from 43% for lower temperatures to 19% for higher ones. The largest relative change of W in angular frequency units within the series, i.e between 4520.2 Å and 3485.1 Å varies from 59% to 35% with increase of the temperature. Elastic collisions determine Stark broadening of 4515.6 Å and 4520.2 Å for lower temperatures while inelastic dominate for higher ones.

Figure 7 shows the behavior of Stark widths versus temperature of spectral lines from three multiplets within one spectral series with parent term $^2P^o_{3/2}$. The corresponding transitions and wavelengths are: $2s^2\ 2p^5\ (^2P^o_{3/2})4s\ ^2[3/2]^o$ − $2s^2$ $2p^5\ (^2P^o_{3/2})4p\ ^2[1/2]$, $\lambda = 5224.1$ Å; $2s^2\ 2p^5\ (^2P^o_{3/2})4p\ ^2[1/2]$ − $2s^2\ 2p^5\ (^2P^o_{3/2})4d$ $^2[3/2]^o$, λ 3279.6 Å; $2s^2\ 2p^5\ (^2P^o_{3/2})4p\ ^2[1/2]$ − $2s^2\ 2p^5\ (^2P^o_{3/2})4d\ ^2[3/2]^o$, $\lambda = 3108.0$ Å. Three curves have the same trend with temperature. The largest Stark broadening is manifested for 3279.6 Å spectral line. The temperature sensitivity of the width indicates that this line is suitable for spectroscopic diagnostics. Their widths in Å units are larger from 3.5 to 2.7 times than Stark width of 3108.0 Å line which presents the lowest broadening in the series. The relative width (in angular frequency units) change between 3279.6 Å and 3108.0 Å-decreases from 34% to 27% when temperature increases.

Figure 8 presents temperature dependence of Stark width in both units, angstroms and angular frequency unites for spectral line $\lambda = 4520.2$ Å. This line has the largest Stark width in the group of spectral lines considered in this study, as it was written above. The trend of W is the same for both units and decreases almost 3 times in the temperature interval. From the point of view of astrophysical and laboratory plasma diagnostics, the important temperature interval is up to 40 000 K where the Stark broadening is very sensitive to temperature.

4. Conclusions

We calculated Stark widths for Al IV spectral lines originating from three transitions, as a function of Rosseland optical depth for one A-type star atmosphere model and one model of DO white dwarf atmosphere. Stark broadening is negligible in comparison with thermal Doppler broadening in A-type star atmosphere for considered Al IV lines and dominant in the case of DO white dwarfs. It is
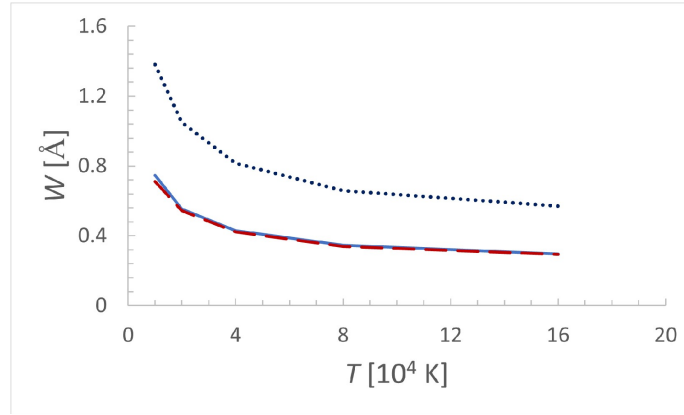
Figure 5. Temperature dependence of Stark width (in angstroms) of spectral lines from one Al IV multiplet 4p $^2[1/2]$ - 4d $^2[3/2]^o$ with parent term $^2P^o_{1/2}$: $\lambda = 3485.1$ Å (blue solid line); $\lambda = 3279.5$ Å (red dashes) and $\lambda = 4550.5$ Å (dark blue dots). Stark widths are due to collisions with electrons. The perturber density is 1.10^{17} cm^{-3}.
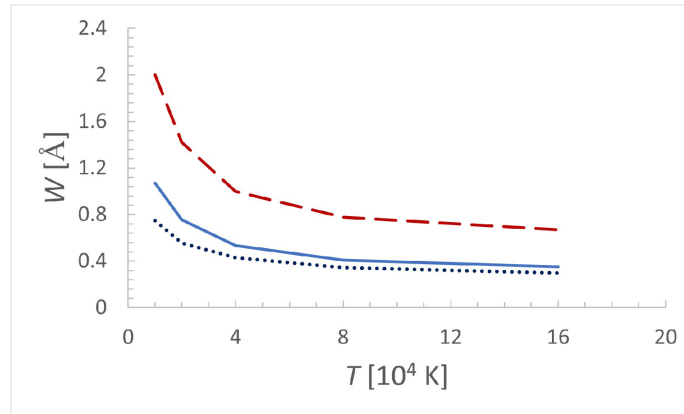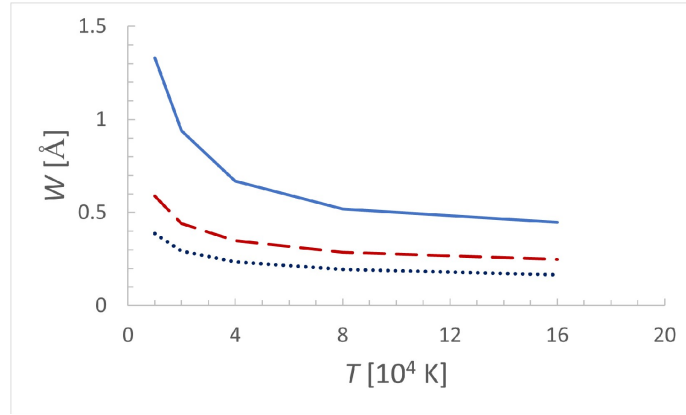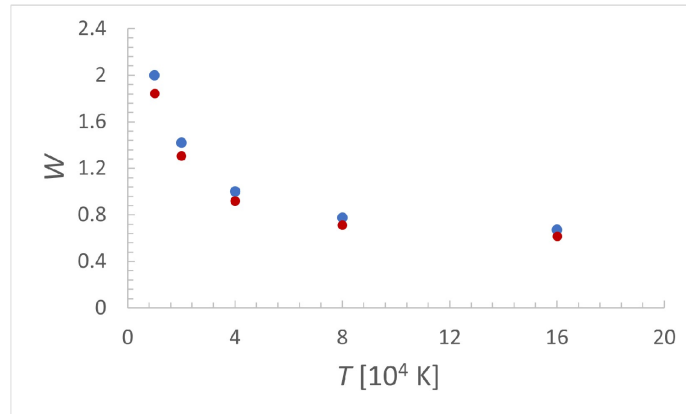

Figure 6. Temperature dependence of Stark width of spectral lines within one spectral series with parent term $^2P^o_{1/2}$ corresponding to three Al IV multiplets: 4s $^2[1/2]^o$ - 4p $^2[1/2]$ $\lambda = 4515.6$ Å (blue solid line); 4s $^2[1/2]^o$ - 4p $^2[3/2]\lambda = 4520.2$ Å (red dashes) and 4p $^2[1/2]$ - 4d $^2[3/2]^o$ $\lambda = 3485.1$ Å (dark blue dots). Stark widths are due to collisions with electrons. The perturber density is 1.10^{17} cm^{-3}.

Figure 7. Temperature dependence of Stark width of spectral lines within one spectral series with parent term $^2P_{3/2}^o$ corresponding to three Al IV multiplets: 4s $^2[3/2]^o$ - 4p $^2[1/2]$ $\lambda = 5224.1$ Å (blue solid line); 4p $^2[1/2]$ - 4d $^2[1/2]^o$ $\lambda = 3279.6$ Å (red dashes) and 4p $^2[1/2]$ - 4d $^2[1/2]^o$ $\lambda = 3279.6$ Å (dark blue dots). Stark widths are due to collisions with electrons. The perturber density is 1.10^{17} cm^{-3}.

Figure 8. Temperature dependence of Stark width of a spectral lines belonging to Al IV multiplet 4s $^2[1/2]^o$ - 4p $^2[3/2]$ with parent term $^2P_{3/2}^o$ and $\lambda = 4520.2$ Å. Stark width is illustrated in both units: Å (blue solid circle) and 10^{12} s^{-1} (red solid circle). Stark widths are due to collisions with electrons. The perturber density is 1.10^{17} cm^{-3}.

obvious that Stark broadening must enter in the calculation of models of white dwarf atmospheres in order to obtain adequate interpretation of physical processes. The agreement of line widths within a multiplet is much better if they are expressed in angular frequency units than in angstroms, because in that case, they are liberated from the influence of wavelength. Their differences are several percent, as predicted. Also, for two examined spectral series, the variations of Stark widths are much lower when they are expressed in angular frequency units than in angstrom units. Stark broadening of spectral lines 4520.2 Å, 4550.5 Å and 5224.1 Å is sensitive to the temperature changes for temperatures lower than around 40 000 K, so that they could be applied for plasma diagnostics of different plasmas in astrophysics, laboratory and technology.

References

Bates, D.R., Damgaard, A.: 1949, *Philos. Trans. R. Soc. Lond. Ser. A*, **242**, 101

Beauchamp, A., Wesemael, F., Bergeron, P.: 1997, *Astrophys. J. Suppl. Ser.*, **108**, 559

Belostotskiy, S.G., Ouk, T., Donnelly, V.M., Economou, D.J., Sadeghi, N.J.: 2010, *Appl. Phys.*, **107**, 053305

Carretta, E., Bragaglia, A., Lucatello, S., Gratton, R.G., D'Orazi, V., Sollima, A.: 2018, *Astron. Astrophys.*, **615**, A17

Dimitrijević, M.S.: 2020, *Data*, **5**, 73.

Dimitrijević, M.S., Christova, M.D.: 2023, *Universe* **9**, 126

Dimitrijević, M.S., Konjević, N.: 1980, *J. Quant. Spectrosc. Radiat. Transf.*, **24**, 451

Dimitrijević, M.S., Sahal–Bréchot, S.: 1994, *Astron. Astrophys. Suppl. Ser.*, **105**, 245

Elabidi, H.: 2021, *JQSRT*, **259**, 107407

Elabidi, H., Ben Nessib, N., Sahal-Bréchot, S.: 2004, *J. Phys. B*, **37**, 63.

Elabidi, H., Ben Nessib, N., Cornille, M., Dubau, J., Sahal-Bréechot, S.: 2008, *J. Phys. B* , **41**, 025702

Fernández–Trincado, J.G, Beers, T.C., Minniti, D., Tang, B., Villanova, S., Geisler, D., Pérez–Villegas, A., Vieira, K.: 2020, *Astron. Astrophys.*, **643**, L4

Gornushkin, I.B., King, L.A., Smith, B.W., Omenetto, N., Winefordner, J.D.: 1999, *Spectrochim. Acta*, **54**, 1207

Griem, H.R.: 1968, *Phys. Rev.*, **165**, 258

Griem, H.R.: 1974, *Spectral line Broadening by Plasmas*, McGraw-Hill: New York, NY, USA

Griem, H.R.: 1992, *Phys. Fluids*, **4**, 2346

Hoffman, J., Szymański, Z., Azharonok, V.: 2006, *AIP Conf. Proc.*, **812**, 469

Iglesias, E., Griem, H.R., Welch, B., Weaver, J.: 1997, *Astrophys. Space Sci.*, **256**, 327

Konjević, N.: 1999, *Phys. Rep.*, **316**, 339

Kurucz, R.L.: 1979, *Astrophys. J. Suppl. Ser.*, **40**, 1

Mazing, M. A., Marinković, M. D., Vrublevskaia, N. A.: 1964, *Bull. Boris Kidrič Inst. Nucl. Sci.*, **15(1)**, 15

Nicolosi, P., Garifo, L., Jannitti, E., Malvezzi, A.M., Tondello, G.: 1978, *Nuovo Cim. B*, **48**, 133

Oertel, G.K., Shomo, L.P.: 1968, *Astrophys. J. Suppl. Ser.*, **16**, 175

Sahal–Bréchot, S.: 1969 a, *Astron. Astrophys.*, **1**, 91

Sahal–Bréchot, S.: 1969 b, *Astron. Astrophys.*, **2**, 322

Shore, B.W., Menzel, D.: 1965, *Astrophys. J. Suppl. Ser.*, **12**, 187.

Smiljanic, R., Romano, D., Bragaglia, A., Donati, P., Magrini, L.A.U.R.A., Friel, E., Jacobson, H., Randich, S., Ventura, P., Lind, K., Bergemann, M., Nordlander, T., Morel, T., Pancino, E., Tautvaišiene, G., Adibekyan, V., Tosi, M., Vallenari, A., Gilmore, G., Bensby, T., François, P., Koposov, S., Lanzafame, A. C., Recio-Blanco, A., Bayo, A., Carraro, G., Casey, A. R., Costado, M. T., Franciosini, E., Heiter, U., Hill, V., Hourihane, A., Jofré, P., Lardo, C., de Laverny, P., Lewis, J., Monaco, L., Morbidelli, L., Sacco, G. G., Sbordone, L., Sousa, S. G., Worley, C. C., Zaggia, S.: 2016, *Astron. Astrophys.*, **589**, A115

Smith, K.C.: 1993, *Astron. Astrophys.*, **276**, 393

Sorge, S., Wierling, A., Röpke, G., Theobald, W., Suerbrey, R., Wilhein, T.: 2000, *J. Phys. B*, **33**, 2983

Van Regemorter, H., Dy Hoang, B., Prud'homme, M.: 1979, *J. Phys. B*, **12**, 1053

Wang, J.S., Griem, H.R., Huang, Y.W., Böttcher, F.: 1992, *Phys. Rev. A*, **45**, 4010

Wesemael, F.: 1981, *Astrophys. J. Suppl. Ser.*, **45**, 177

Wiese, W.L., Konjević, N.: 1982, *J. Quant. Sprectrosc. Radiat. Transf.*, **28(3)**, 185

Yilbas, B.S., Patel, F., Karatas, C.:2015, *Opt. Laser Technol.*, **74**, 36

Zhou, Y., Li, H., Jung, J.-E.J., Ki, N.S., Donnelly, V.M.: 2022, *J. Vac. Sci. Technol. A*, **40**, 053002

Analysis of laser ablation spectral data using dimensionality reduction techniques: PCA, t-SNE and UMAP

M.S. Rabasovic[ID]**, D.M. Pavlovic and D. Sevic**[ID]

Institute of Physics, University of Belgrade, Pregrevica 118, 11080 Zemun, Serbia, (E-mail: sevic@ipb.ac.rs)

Abstract. Laser ablation is among the various methods employed for expediting the prototyping of printed circuit boards. Laser-induced breakdown spectroscopy (LIBS) serves as a convenient technique for overseeing the targeted elimination of thin layers with lasers. Consequently, this approach facilitates the rapid prototyping of printed circuit boards. In this paper the obtained LIBS data are analyzed by using data dimension reduction techniques: principal component analysis (PCA), t-SNE and UMAP to obtain an indication that copper layer is fully removed. For machine learning approach to data analysis we use Solo+Mia software package (Version 9.1, Eigenvector Research Inc, USA).

Key words: Machine learning – Dimensionality reduction – Laser induced breakdown spectroscopy

1. Introduction

Machine learning methods, including both unsupervised techniques like PCA (Principal Component Analysis) and supervised techniques like LDA (Linear Discriminant Analysis), are increasingly being employed to analyze LIBS data. These combinations of well-known machine learning algorithms with LIBS enable the swift and accurate classification of diverse samples Bellou et al. (2020); Diaz et al. (2020); Pořízka et al. (2018); Yang et al. (2020); Zhang et al. (2022).

Laser ablation offers a swift method for the rapid prototyping of printed circuit boards. A viable approach to this technique was introduced in a prior work Rabasović et al. (2016). In our application, we have harnessed laser-induced breakdown spectroscopy (LIBS) as a convenient method to both perform ablation and monitor the precise removal of thin layers using lasers. A similar technique has been detailed in a recent publication, as evidenced by Shiby & Vasa (2022). In the study by Rabasović et al. (2016), LIBS data were scrutinized through the application of correlation coefficients. Presently, with the increasing accessibility of high-speed computers capable of machine learning, the trajectory of analysis algorithms has shifted from basic numerical calculations towards more advanced artificial intelligence methods. Our initial efforts

for machine learning analysis of LIBS printed circuit board data, using principal component analysis are presented in Sevic et al. (2020). Interesting applications of machine learning algorithms for analysis of LIBS data are presented in Boucher et al. (2015); Moros et al. (2013); Serranoa et al. (2014); Rabasovic et al. (2022). State of the art approaches to the problem are reviewed in Pořízka et al. (2018); Vrábel et al. (2020); Zhang et al. (2022).

In this paper we study the spectral data by using data dimension reduction techniques based on machine learning (ML). For ML approach to data analysis we use Solo+Mia software package (Version 9.1, Eigenvector Research Inc, USA) Wise et al. (2006).

2. Methods

Our experimental arrangement for acquiring the training spectra required for data dimensionality reduction is comprehensively elucidated in Rabasović et al. (2016). In brief, spectral images capturing the optical emissions from laser-induced plasma on a printed circuit board are obtained using a streak camera. These images are temporally integrated to generate spectra at different time points. Importantly, due to the time-resolved nature of streak images, we had the ability to carefully choose time intervals for spectrum integration, ensuring that the highly intense optical emissions from the initial plasma phase were excluded.

Data dimension reduction constitutes a fundamental technique within the realm of machine learning. This method involves using a dataset with a particular structure to "train" a machine, enabling it to discern specific features within the input data. These discernible characteristics are accentuated through the process of data dimension reduction. Subsequently, the machine becomes proficient at recognizing and identifying these characteristics in newly presented data that shares a similar structure and nature. A prevalent approach for automating this analysis is by teaching the machine a low-dimensional representation of the data. Within this low-dimensional representation, each object from the original high-dimensional dataset is portrayed as a point in a reduced-dimensional space. This representation is designed in such a way that proximate points correspond to similar objects, while distant points correspond to dissimilar ones. The low-dimensional embedding lends itself to straightforward visualization.

In this study we compare principal component analysis (PCA), t-distributed stochastic neighbor embedding (t-SNE), and uniform manifold approximation and projection (UMAP) methods for analysis of LIBS spectral data to obtain indication that copper layer is fully removed on given small area of printed circuit board.

The PCA was proposed long ago, see Hotelling (1933); Karhunen (1947); Lévy (1948). Efficient implementation of t-SNE is proposed in Van der Maaten

& Hinton (2008). UMAP is proposed in McInnes et al. (2018, 2020); Sainburg et al. (2020).

Similarly to most non-linear dimension reduction techniques, t-SNE and UMAP lack the strong interpretability of PCA. In particular the dimensions of the t-SNE and UMAP embedding space have no specific meaning, unlike PCA where the dimensions are the directions of greatest variance in the source data.

For obtaining the ML models we have used the set of 40 printed circuit boards spectra. For testing purposes we used spectra from beggining and from the end of ablation process.

3. Results and discussion

Plasma breakdown optical spectra of printed circuit board at the start, when only copper is ablated; and when the substrate is fully exposed, are shown in Fig. 1. Their differences could be seen by a naked eye.
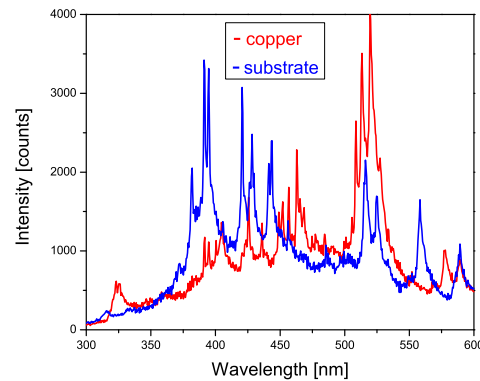
Figure 1. Plasma breakdown optical spectra of printed circuit board at the start, when only copper is ablated; and when the substrate is fully exposed.

The first two principal components of LIBS data are shown in Fig. 2. Embeddings plots for two t-SNE and UMAP components are shown in Fig. 3 and Fig. 4. Data dimension reducing techniques t-SNE and UMAP are designed for visualization of data. Using numerical results of embedding components any clustering technique will have no problem to put the test specrum into corresponding cluster.

Visual comparisons of PCA, t-SNE and UMAP plots shows the best performance of UMAP method. When reduced to two dimensions, dimension reduced spectral data are the most closely grouped by UMAP method. It should be mentioned that results presented in Fig. 4 were obtained when UMAP algorithm was initialized with parameters suggested by SOLO software. On the other hand, we had to try varying parameters for initialization of t-SNE algorithm to obtain acceptable results shown in Fig. 3.
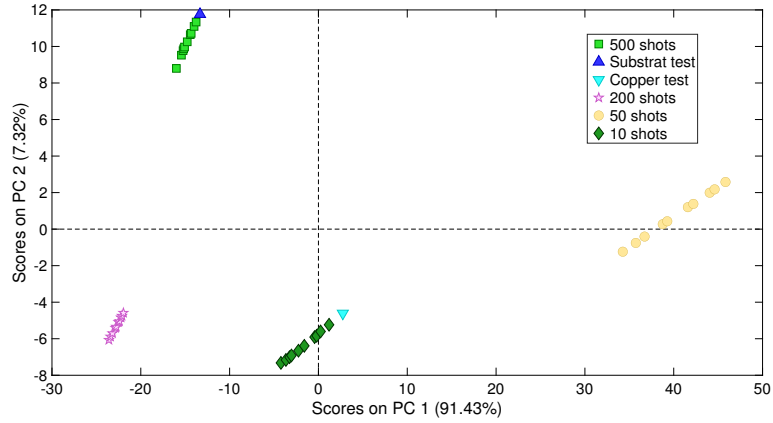
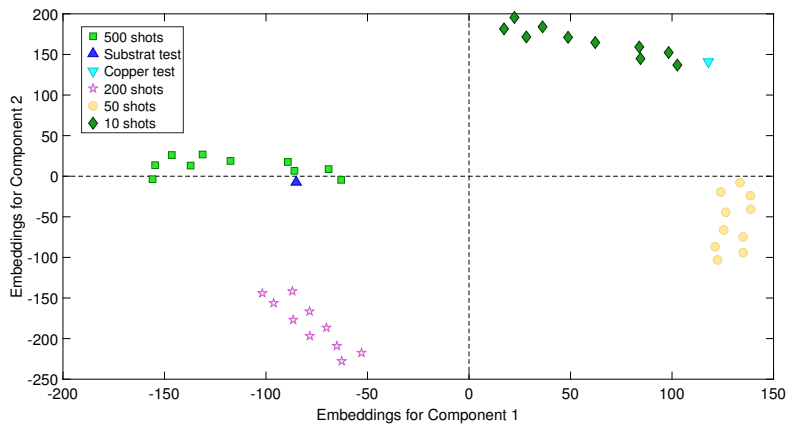**Figure 2.** Scores plot of first two principal components.

Figure 3. Embeddings plot for two t-SNE components.

4. Conclusions and Discussion

The rapid prototyping of printed circuit boards can be effectively accomplished through the application of laser ablation and LIBS. Our analysis of LIBS data related to printed circuit boards has involved the utilization of data dimension reduction techniques.

In our previous investigations, we employed correlation coefficients and PCA to determine the point at which laser ablation penetrates the composite substrate of the printed circuit board. In this particular study, we conducted a comparative analysis of PCA, t-SNE, and UMAP methods for reducing the di-
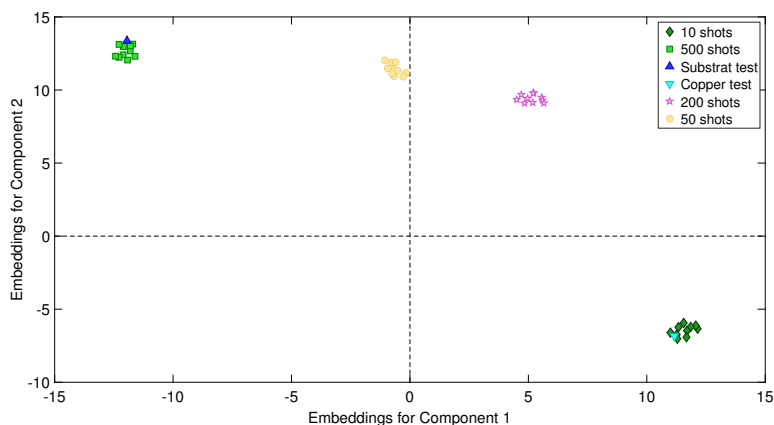
Figure 4. Embeddings plot for two UMAP components.

mensionality of spectral data. Our findings have demonstrated that the UMAP method stands out as the most promising candidate for pinpointing the precise moment when the copper layer is completely ablated.

References

Bellou, E., Gyftokostas, N., Stefas, D., Gazeli, O., & Couris, S., Laser-induced breakdown spectroscopy assisted by machine learning for olive oils classification: The effect of the experimental parameters. 2020, *Spectrochimica Acta*, **163**, 105746, DOI: 10.1016/j.sab.2019.105746

Boucher, T. F., Ozanne, M. V., Carmosino, M. L., et al., A study of machine learning regression methods for major elemental analysis of rocks using laser-induced breakdown spectroscopy. 2015, *Spectrochimica Acta*, **107**, 1, DOI: 10.1016/j.sab.2015.02.003

Diaz, D., Molina, A., & Hahn, D. W., Laser-Induced Breakdown Spectroscopy and Principal Component Analysis for the Classification of Spectra from Gold-Bearing Ores. 2020, *Applied Spectroscopy*, **74**, 42, DOI: 10.1177/0003702819881444

Hotelling, H., Analysis of a Complex of Statistical Variables into Principal Components. 1933, *Journal of Educational Psychology*, **24**, 417, DOI: http://dx.doi.org/10.1037/h0071325

Karhunen, K. 1947, *Ueber lineare Methoden in der Wahrscheinlichkeitsrechnung*

Lévy, P. 1948, *Processus stochastiques et mouvement brownien: suivi d'une note de M. Loève*

McInnes, L., Healy, J., & Melville, J., UMAP: Uniform Manifold Approximation and Projection for Dimension Reduction. 2018, *arXiv e-prints*, arXiv:1802.03426, DOI: 10.48550/arXiv.1802.03426

McInnes, L., Healy, J., & Melville, J., UMAP: Uniform Manifold Approximation and Projection for Dimension Reduction. 2020, *arXiv e-prints*, arXiv:1802.03426v3, DOI: 10.48550/arXiv.1802.03426

Moros, J., Lorenzo, J. A., Novotný, K., & Laserna, J. J., Fundamentals of stand-off Raman scattering spectroscopy for explosive fingerprinting. 2013, *Journal of Raman Spectroscopy*, **44**, 121, DOI: 10.1002/jrs.4138

Pořízka, P., Klus, J., Képeš, E., et al., On the utilization of principal component analysis in laser-induced breakdown spectroscopy data analysis, a review. 2018, *Spectrochimica Acta*, **148**, 65, DOI: 10.1016/j.sab.2018.05.030

Rabasovic, M. S., Marinkovic, B. P., & Sevic, D., Analysis of Printed Circuit Board LIBS Data Using Deep Learning. 2022, *Publications de l'Observatoire Astronomique de Beograd*, **102**, 219

Rabasović, M. S., Šević, D., Lukač, N., et al., Evaluation of laser-induced thin-layer removal by using shadowgraphy and laser-induced breakdown spectroscopy. 2016, *Applied Physics A: Materials Science & Processing*, **122**, 186, DOI: 10.1007/s00339-016-9697-3

Sainburg, T., McInnes, L., & Gentner, T. Q., Parametric UMAP embeddings for representation and semi-supervised learning. 2020, *arXiv e-prints*, arXiv:2009.12981, DOI: 10.48550/arXiv.2009.12981

Serranoa, J., Moros, J., Sánchez, C., Macías, J., & Laserna, J. J., Advanced recognition of explosives in traces on polymer surfacesusing LIBS and supervised learning classifiers. 2014, *Analytica Chimica Acta*, **806**, 107, DOI: 10.1016/j.aca.2013.11.035

Sevic, D., Rabasovic, M. S., P., G., Rabasovic, M. D., & Marinkovic, B. P., Principal Component Analysis of Printed Circuit Board LIBS Data. 2020, *Publications de l'Observatoire Astronomique de Beograd*, **99**, 117

Shiby, S. & Vasa, N. J., Nanosecond laser-assisted micro-scribing of a copper film on a dielectric material with laser-induced breakdown spectroscopy based monitoring. 2022, *Optics Laser Technology*, **147**, 107685, DOI: 10.1016/j.optlastec.2021.107685

Van der Maaten, J. P. L. & Hinton, G., Visualizing data using t-SNE. 2008, *Journal of Machine Learning Research*, **9**, 2579

Vrábel, J., Képeš, E., Duponchel, L., et al., Classification of challenging Laser-Induced Breakdown Spectroscopy soil sample data - EMSLIBS contest. 2020, *Spectrochimica Acta*, **169**, 105872, DOI: 10.1016/j.sab.2020.105872

Wise, B. M., Gallagher, N. B., Bro, R., et al. 2006, *Chemometrics tutorial for PLS Toolbox and Solo, ISBN: 0-9761184-1-6, Eigenvector Research, Inc. USA.*

Yang, Y., Hao, X., Zhang, L., & Ren, L., Application of Scikit and Keras Libraries for the Classification of Iron Ore Data Acquired by Laser-Induced Breakdown Spectroscopy (LIBS). 2020, *Sensors*, **20**, 1393, DOI: 10.3390/s20051393

Zhang, D., Zhang, H., Zhao, Y., et al., A brief review of new data analysis methods of laser-induced breakdown spectroscopy: machine learning. 2022, *Applied Spectroscopy Reviews*, **57**, 89, DOI: 10.1080/05704928.2020.1843175

New perspectives in the analysis of Stark width regularities and systematic trends

Z. Majlinger[1,2,3] **and I. Traparić**[4]

[1] *Astronomical Observatory, Volgina 7, 11060 Belgrade, Serbia*
[2] *ES "I. G. Kovačić", Kralja Tomislava 18, 51326 Vrbovsko, Croatia*
[3] *ES "V. Gortan", Prilaz Vladimira Gortana 2, 51000 Rijeka, Croatia*
[4] *Institute of Physics Belgrade, Pregrevica 118, 11080, Belgrade, Serbia*
(E-mail: traparic@ipb.ac.rs)

Abstract. Regularites and systematic trends among the sample of Stark widths obtained by using modified semiempirical method from the STARK-B database were analysed. Two different approaches are independently used – multiple regression method combined with simple cluster analysis, and random forest (RF) machine learning algorithm. Predicted values of Stark widths calculated with estimate formulae obtained from multiple regression method, and those values predicted by using RF algorithm, were compared with already known corresponding experimental Stark widths published elsewhere. Results of this analysis indicate that both of these methods can mostly predict new Stark width values within the acceptable range of accuracy.
Key words: line profile — Stark broadening -– atomic data — machine learning

1. Introduction

Stark broadening theory plays the important role in investigation of high temperature dense plasma, where the collisional processes between the charged particles contribute significantly to the spectral line broadening. From technological perspective, Stark widths and shifts of spectral lines in the spectra of neutral atoms and ions are of interest for a number of problems - for example, analysis and modelling of laboratory, laser produced, fusion or technological plasmas, accurate spectroscopic diagnostics and modelling, etc. Applications of Stark broadening theory are also various in research of astrophysical plasma as well - for example, for interpretation, synthesis and analysis of stellar spectral lines, determination of chemical abundances of elements from equivalent widths of absorption lines, opacity calculations, estimation of the radiative transfer through the stellar atmospheres and subphotospheric layers, radiative acceleration considerations, nucleosynthesis research, etc.

Calculation of Stark broadening parameters sometimes can be difficult, and it can take a time, especially if quantum theory is applied. If conditions to apply less accurate but faster quasistatic, unified, semiempirical or semiclassical methods are not satisfied, quick and simple estimates could become important, especially if we do not need a great accuracy, or there is no time for more complicated and more accurate calculations, or if we have a great number of Stark broadening parameters to calculate in very small period of time. This is very common case, for example, if astrophysical spectra are investigated. According to (Wiese, Konjevic, 1982), regularities and systematic trends (RST) can be found among the Stark widths of atomic spectral lines, which can simplify the way of obtaining these estimates. This is especially significant when some atomic data, necessary to perform more accurate Stark broadening methods of calculations, are missing. For example, the lack of atomic data, such as energy levels or transition probabilities is usually noticed in the spectral data for rare-earth elements. Analysis based on RST is mostly the only way to determine Stark widths and shifts in sometimes very complex spectra of these elements, which become more and more important in spectral investigations of hot stars of spectral type A and B, and white dwarfs (Popović, Dimitrijević, 1998).

In this investigation, we focused on searching systematic trends among great amount of Stark widths from STARK-B database (Sahal-Bréchot et al., 2014b, 2015), obtained by modified semiempirical (MSE) method (Dimitrijević, Konjević, 1981) as a continuation of our previous work on determination of unknown MSE Stark widths and studying of RST among the MSE Stark broadening parameters (see, for example, Majlinger et al., 2015, 2017a,b, 2020a). Two different methods are used to analyse the sample – classical statistical regression method, which has already been used many times in previous investigations of regularities and systematic trends, and random forest (RF) algorithm from a group of machine learning methods, which become very popular methods more often used in these days whenever some classification or non-linear regression is needed to be performed. Unlikely to previous analyses of RST, here some new atomic parameters, which have not taken into consideration before, are included. We will shortly explain both of these methods and finally discuss and compare the obtained results.

2. Methods

2.1. Simple cluster and multiple regression analysis

Estimates of Stark widths can be divided into three main groups:

- approximations derived from the theory – e.g., Cowley's formula (Cowley, 1971) or MSE formula (Dimitrijević, Konjević, 1987)

- formulae based on statistical analysis on a large number of existing Stark widths (see e.g. Purić, Šćepanović, 1999; Purić et al., 1978).

– formulae based on systematic trends noticed without statistical analysis on corresponding examples (Wiese, Konjevic, 1982).

Whether it is one type or another, the formula for estimating Stark widths for lines of multiple ionized atoms usually can be expressed as a non-linear function of atomic and plasma parameters:

$$\omega_E = f(\lambda, N_e, T, Z, E_{ion}, E_{upper}, E_{lower}) \tag{1}$$

Sometimes some of these parameters are included in the estimate implicitly, through the effective ionization potential χ_j for level j:

$$\chi_j = E_{ion} - E_j, \ j = \text{upper, lower} \tag{2}$$

according to Purić, or effective principal quantum number of the upper (n_+) or lower (n_-) level, which has already been used, for example, in MSE theory of Dimitrijević and Konjević (Dimitrijević, Konjević, 1981):

$$n_+^2 = \frac{Z^2 E_H}{\chi_{upper}} \tag{3}$$

$$n_-^2 = \frac{Z^2 E_H}{\chi_{lower}} \tag{4}$$

Here $Z - 1$ is the charge of the ion, ω_E is the estimated Stark width in Å, λ is the wavelength in Å, N_e is the perturber density in cm^{-3}, E_H is the energy of the hydrogen atom (or Rydberg constant), E_{ion} is the ionization energy, and E_j is the energy of upper or lower levels in cm^{-1} (j = upper, lower).

Immediately after the first article on Stark broadening (Holtsmark, 1919), simple approximate formulas derived from the theory began to appear. Cowley's formula (Cowley, 1971) is probably the best known among them and it is still commonly used in astrophysics. Cowley (1971) specified three different formulas, one for neutral emitters, one for electrically charged emitters (which humble Cowley contributes to Griem), and one for estimating widths for temperatures close to 10000 K. The authors use different variants of Cowley's formula in addition to the original ones from the article (Cowley, 1971), and the difference is in the neglect or addition of the lower effective principal quantum number as a number and in the values of the numerical constant in the formula (see e.g. Killian et al., 1991; Alwadie et al., 2020).

Jagoš Purić made a great effort in studying RST among the Stark width values. The first works on regularities were published by (Purić, Ćirković, 1973) and (Purić et al., 1978). Purić and his co-workers found the correlation between Stark width and difference between ionization energy and energy of the upper state (what he called the upper effective ionization potential) and a number of experimental and theoretical values of Stark widths, offering a set of different estimation formulae. In the following decades, a number of papers on this topic were published, where different correlation parameters were stated for different transitions, different charges and different homologous and isoelectronic

sequences (see e.g. Miller et al., 1980; Purić et al., 1978, 1993, 1997, 2008). This statistical research is also supported by some other authors (see e.g. Djeniže, 1999; Djeniže et al., 2001), with occasional attempts to generalize this approach for all different transitions, different elements and different charge values (Purić, Šćepanović, 1999; Scepanovic, Puric, 2013). Comparing the great amount of Stark width data from STARK-B database (Sahal-Bréchot et al., 2014b, 2015), Purić offered so-called "generalized" estimate (Purić, Šćepanović, 1999) which should be used, according to the authors, "to calculate Stark line widths of the multiply charged ion of different elements along the periodic table." These scientific articles evolve over time, so Purić and co-workers later give up searching for a universal formula for all lines and focus their statistical analysis only on individual homologous or isoelectronic series (Dojčinović et al., 2011, 2012, 2013a,b; Tapalaga et al., 2011, 2018; Jevtić et al., 2012; Trklja et al., 2019b,a). However, the possibility to apply all of these estimates to predict new unknown Stark widths should be furtherly discussed (Majlinger et al., 2017a,b, 2020b).

The final purpose of this research was to find new general estimates accurate enough to approximately predict the unknown values of Stark widths. Our assumption is that these new estimates should be related on existing estimates, e. g. Cowley's from Cowley (1971) and Purić's from Purić and Šćepanović (1999). However, after investigation of accuracy in prediction of uknown Stark widths by using of these two estimates, in the cases of MSE calculated electron-impact widths for Lu III and Zr IV spectral lines, it was obvious that they don't offer enough accurate approximation (Majlinger et al., 2017a, 2020b). At least in the case of Zr IV Stark widths, several possible reasons were suggested to explain this discrepancy (Majlinger et al., 2017b):

– numerical coefficients in estimations are not properly adjusted

– some important parameters are neglected in equation (1) but significantly contribute to the result, and

– temperature functions used in previous estimates could be incorrect

According to statistical analysis of Stark widths calculated for 143 transitions from 26 multiply charged ions of 17 elements using the modified semiempirical method, (for example, most of them are elaborated by (Dimitrijević, Konjević, 1981), and previous assumptions, new estimates of Stark widths were found. After providing simple cluster analysis (Aggarval, V., 2014) and multiple regression analysis (for example Chatterjee, Simonoff, 2014), we concluded that MSE Stark width sample has to be devided in three separate groups:

1. For a type I of transitions: nl–nl', $L = l$, $L' = l'$ (for example, $2s^1S - 2p^1P^o$, $3s^3S$–$3p^3P^o$, $3p^1P^o - 3d^1D$, $4s^3S$–$4p^3P^o$, etc), proper estimate is Cowley-like:

$$\omega_{E1} = 3.438 \cdot 10^{-24} N_e \lambda^2 \frac{n_+^4 + n_-^4}{Z^2(2l_> - 1)^{-\frac{3}{4}}} f(T) \tag{5}$$

2. For a type II of transitions: nl–$n'l'$, $L = l, L' = l'$ (for example, $2p^3 P^o$–$3s^3 S$, $4p^2 P^o$–$5d^2 D$, $4d^2 D$–$5f^2 F^o$, $4d^2 D - 6f^2 F^o$, etc), proper estimate is Purić-like:

$$\omega_{E2} = 0.808 \cdot 10^{-25} N_e \lambda^2 \frac{n_+^6 + n_-^6}{Z^2 (2l_> - 1)^{-\frac{1}{5}}} f(T) \tag{6}$$

Here $f(T)$ is chosen temperature function (which will be explained later), while $l_> = max(l_{upper}, l_{lower})$, where l_{upper} and l_{lower} are orbital quantum numbers for upper and lower level respectively.

3. For all other types of these simplest transitions (type III), like nl–nl', $L \neq l$, $L' \neq l'$ and nl–$n'l'$, $L \neq l$, $L' \neq l'$ (for example, $3s^1 P^o$–$3p^1 D$, $3s^4 P^o$–$3p^4 P$, $3p^5 D^o$–$3d^5 F$, $3d^1 F^o$–$4p^1 D$, etc.), a well known general expression, valid also for the first two types, can be used to obtain width for particular lines within a multiplet from an average width as a whole:

$$\omega_{E3} = \left(\frac{\lambda_{E3}}{\lambda_0} \right)^2 \omega_0 \tag{7}$$

where ω_{E3} and ω_0 are estimates of uknown Stark widths and a Stark width obtained with estimates (5) or (6), while λ_{E3} and λ_0 are corresponding wavelengths respectively.

After optimizing the number of parameters in these estimates according to minimum description length properties (see, for example, Grünwald, 2004), and keeping in mind that all models are uncertain, idealizing reality (Wit et al., 2012) and that sample is not equal to population, we rounded exponents in (5) and (6) on the closest integer or rational number, to avoid physically meaningless results (for example, $\lambda^{1.74}$ is replaced with λ^2, $Z^{1.95}$ with Z^2, etc.) and to approach enough to probable statistical model ideally concerning about population.

From interpolation of analysed data, new temperature function is suggested:

$$f(T) = \frac{1 - \beta}{\sqrt{T}} + \beta \frac{\ln T}{\sqrt{T}} \tag{8}$$

where β is the linear function of temperature defined as:

$$\beta = AT + B \tag{9}$$

Numerical constants A and B are estimated to be A $= 9.62 \cdot 10^{-7}$ and B $= -4.167 \cdot 10^{-2}$ from the values of lower temperature limit for all considered Stark widths. Lower temperature limit for most of considered Stark widths lies in a range 15000 – 70000 K which corresponds to range of distance between perturbing and perturbed levels used in all considered Stark width calculations around cca 7500 – 38500 cm^{-1}. It is easy to see that relation $0 \leq \beta \leq 1$ is mostly valid for such choice of A and B, and that temperature function approximately

simulates both lower and upper temperature limit conditions when β reach to its limits, which is in a good agreement with some previous analyses of behavior of Stark width values for highest and lowest value of temperature (for example Sahal-Bréchot et al., 2014a).

Correlation between new estimates of full Stark width at half maximum (FWHM) obtained by using relations (5), (6) and (7), and existing MSE values for transition type I, type II and type III with corresponding regression lines are displayed in Figs. 1-3 respectively. To calculate correlation parameters for each estimate, we used the general symbol ω_{EST} instead of ω_{E1}, ω_{E2}, and ω_{E3}. Correlation coefficients corresponding to each estimate WEST are presented in Table 1. In the most idealistic scenario, for log-log regression equation $\log \omega_{EST} = C_1 + C_2 \log \omega_{MSE}$, should be valid C1 = 0, C2 = 1 and therefore $\omega_{EST} = \omega_{MSE}$. As the additional attemption to confirm a validation of this method, predicted Stark widths with estimates from above are compared with corresponding experimental values from references (Konjević et al., 1984, 2002). Result of this comparison is presented in Fig. 4.

Table 1. Correlation parameters for log-log regression equation $\log \omega_{EST} = C_1 + C_2 \log \omega_{MSE}$, between results of estimates (5), (6) and (7) respectively, and MSE values of FWHM Stark widths from analysed sample.

Transition type	C_1	C_2	$ErrC_1$	$ErrC_2$	St. dev.	R_{corr}
I	-1.45E-5	0.9126	0.0325	0.0336	0.13	97.76
II	-.28E-5	1.0266	0.0473	0.0262	0.19	99.32
III	-0.0334	0.84	0.025	0.029	0.064	97.23

2.2. Machine learning methods and RF algorithm

As machine learning represents a very popular tool for different types of problems encountered in science, here it was applied on the study of regularities of Stark broadening. Machine learning model based on Random Forest algorithm was developed and described in detail in reference (Tapalaga et al., 2022), so here it would be briefly described for the sake of completeness. Before developing the model, we needed to develop and create a database for training and testing of the future models. This database was created as a combination of two databases, namely NIST atomic database (Kramida et al., 2022), from which we took atomic parameters of interest for every transition and Stark B database (Sahal-Bréchot et al., 2015) from which we took Stark width and plasma parameters for each calculated width. After the completion of this database, it contained around 53 000 lines. Features selected for this research were: Plasma electron density, electron temperature, atomic number, charge of the emitter, energies of both upper and lower levels, total angular momentum of both upper and lower levels, principal and orbital quantum numbers for initial and final of corresponding transitions.
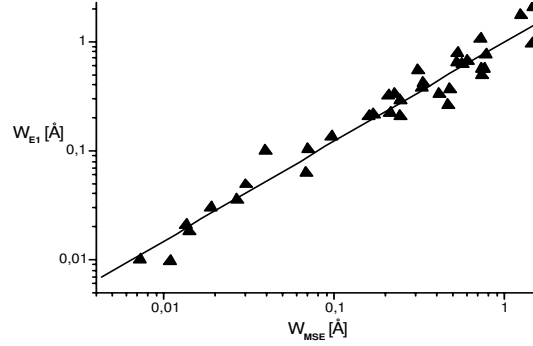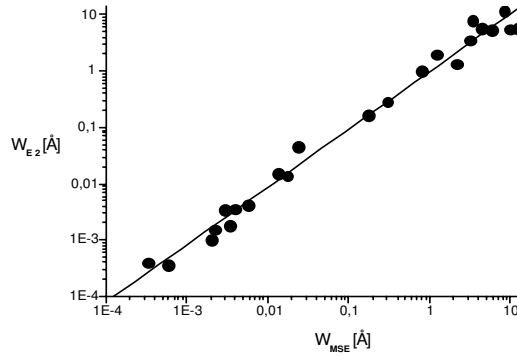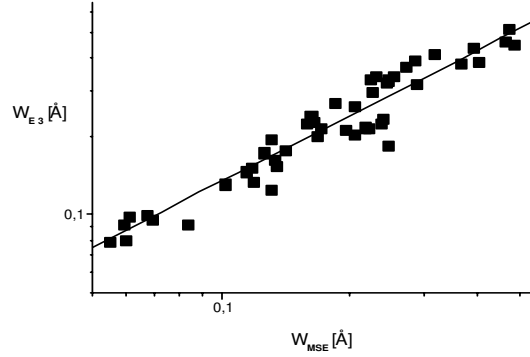
Figure 1. Log-log correlation between FWHM Stark width values obtained by using estimates from multiple regression analysis (ω_{E1}) and MSE values (ω_{MSE}), with corresponding regression line.

Figure 2. Log-log correlation between FWHM Stark width values obtained by using estimates from multiple regression analysis (ω_{E2}) and MSE values (ω_{MSE}), with corresponding regression line.

Additionaly, ionization energy and quantity called upper level effective potential after (Purić, Šćepanović, 1999) were taken into a set of input parameters, which provides a label data comparison. Data outliers were removed as data having higher energy of lower level than upper level. Finally, the analysis was constrained to the following plasma parameters: $N \leq 10^{17}$ cm^{-3}, $T_e \leq 150\,000$ K and $E_{upper} \leq 500$ eV. This restriction left us with around 32 000 available transitions for further analysis. To choose the best model and corresponding parameters, GridSearchCV (Grid Search Cross Validation) technique was applied. Here for every set of model parameters, model is trained and tested on

Figure 3. Log-log correlation between FWHM Stark width values obtained by using estimates from multiple regression analysis (ω_{E3}) and MSE values (ω_{MSE}), with corresponding regression line.
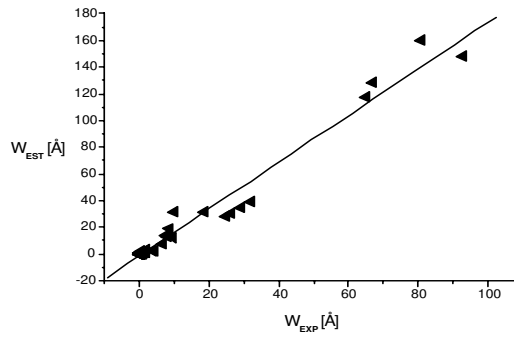

Figure 4. Linear correlation between FWHM Stark width values obtained by using estimates from multiple regression analysis (ω_{EST}) and corresponding experimental values (ω_{EXP}), with corresponding regression line.

given dataset, and best performance is reported. Along with best performance, algorithm reports with which parameters has been obtained. Three models were tested: Decission Tree, Random Forest and Gradient Boosting Regressor. Performances of the model are reported in table 2.

It can be seen that the best results were obtained with Random Forest for the following parameters: maximal depth of the tree equal to 10, minimal samples at one leaf set to 3 and number of estimators equal to 200. As in the case of multiple regression method, Stark widths predicted with using RF algorithm were compared with corresponding experimental widths from the same refer-

Table 2. Comparison of preformances for three learning machine models used in analysis.

Model	Parameters	R^2 score
Decision tree	max_depth = 5	0.9
Random Forest	max_depth = 10 min_samples_leaf = 3 n_estimators = 200	0.97
Gradient Boosting Regressor	max_depth = 10 min_samples_leaf = 2 n_estimators = 200	0.96

ences as before (Konjević et al., 1984, 2002). Results of this comparison are shown in Fig. 5 and Fig. 6. As we can see on figure 5, RF model preforms well, except of few points that are estimated badly. Also, from the figure 6 it can be concluded that RF method performs better in visible part than in the ultra violet or infrared part of the spectrum.
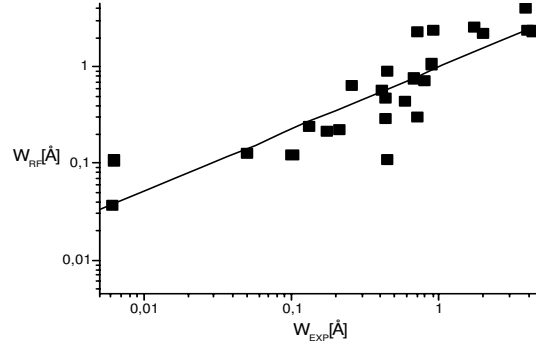
Figure 5. Log-log correlation between FWHM Stark width values obtained by using RF algorithm (ω_{RF}) and corresponding experimental values (ω_{EXP}), with corresponding regression line.

To improve the model and to test whether we could reduce the number of features in the dataset while keeping the accuracy of the model, permutation importance test was performed. This method permutes each feature randomly within dataset, and calculate the decrease in performance of the already trained model. Greater the decrease, more important is the feature. Results of this analysis are given in table 3.
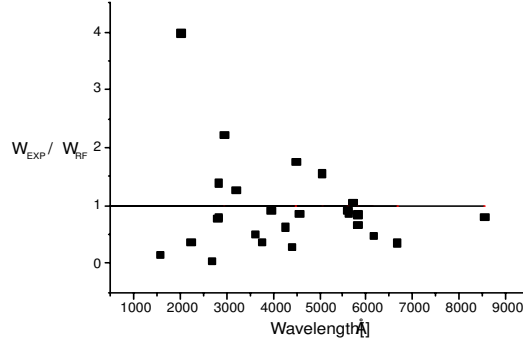
Figure 6. Dependence of ratio between experimental FWHM Stark widths (ω_{EXP}) and corresponding values obtained by using RF algorithm (ω_{RF}) on wavelength of spectral lines for which Stark widths are calculated.

Table 3. Feature importance test results for RF model.

Feature	Importance score
Electron density N_e	5.9 ± 0.2
Upper - level principal quantum number n_i	3.50 ± 0.12
Charge of emitter q	1.04 ± 0.04
Upper-level effective potential χ	0.37 ± 0.04
Emitter Z	0.31 ± 0.03
Upper-level orbital quantum number l_i	0.19 ± 0.02
Energy of upper level E_{upper}	0.11 ± 0.02
Lower-level principal quantum number n_f	0.11 ± 0.01
Energy of lower level E_{lower}	0.048 ± 0.005
Lower-level orbital quantum number l_f	0.029 ± 0.004
Lower-level total angular momentum quantum number J_{upper}	0.029 ± 0.007
Upper-level total angular momentum quantum number J_{lower}	0.021 ± 0.005
T_e	0.017 ± 0.003
E_i	0.002 ± 0.001

Results in table 3 indicate that electron density is most important feature as expected, while other important features are naturally emitter, its charge, principal and orbital quantum numbers of upper level and upper-level effective potential χ. Other parameters were removed from analysis, as upper level is included in definition of χ, and model was retrained. As expected, model gave very similar results as those reported in this work, which just confirms that model didn't got confused with some redundant data in initial run.

3. Discussion

For Type I, ratios between estimates and MSE values vary between 0.5 and 2.6, for type II between 0.4 and 1.7, and for type III between 0.7 and 2.0. so we can say that accuracy of our estimates according to MSE values are mostly between –50% and +160%. Including predicted accuracy of MSE results, which is ±50%, we expect that global accuracy of our estimates, according to statistical sample we used, should lie between ±50% and ±100% e.g. comparable with the old Griem's semiempirical theory (Griem, 1968).

Despite of several exceptions, ratio between most of new calculated estimates and corresponding experimental Stark widths from references (Konjević et al., 1984, 2002), lies between 0.2 and 2 (see Tab. 3), which leads to conclusion that our estimates are usually accurate in a range of ±100%, in accordance with our expectations. On the other hand, average value of this ratio for comparison of estimates with experimental Stark widths is 1.38 ± 0.11, resulting with accuracy in a range between ±30% and ±50%, which is even better than theoretically predicted accuracy for modified semiempirical theory by Dimitrijević and Konjević (1981).

Ratios between Stark widths predicted by using RF algorithm and corresponding experimental Stark widths taken from the same references mentioned above (Konjević et al., 1984, 2002), with the exception of two extreme values 0.06 and 4, lie between 0.16 and 2.23, but average ratio of these values is 0.96 ± 0.16, leading to an accuracy of around ±20%, which is much better than accuracy of predicted results obtained by using classical statistical method. To express the accuracy for both methods, as it is usual in statistics, we used arithmetical mean as the average value of analysed data, while the standard deviation is used as a measure of data dispersion. As a final proof that both of presented methods could be valid, in Fig. 7 we presented results obtained from mutual comparison of Stark width values predicted with these two different approaches. Linear regression equation which expresses dependence between Stark widths predicted with RF method ω_{RF} and those predicted by using estimates WEST obtained by using formulae (5), (6) and (7) is found to be $\omega_{RF} = 0.0523 + 1.0563\ \omega_{EST}$ with correlation coefficient $R_{CORR} = 91.05\%$. Figure 7 and values of correlation parameters show that both of these two methods are equivalent, e. g. the results of the estimates with RF model and classical multiple regression statistical method are almost the same. Although it is feeded with results obtained by using semiclassical perturbation method (see for example Sahal-Bréchot et al., 2014a), RF algorthm is shown to be a good predictor, despite of a theoretical method used to calculate analysed Stark width data, because it gives results comparable with estimates based on set of calculations obtained by using modified semiempirical method.
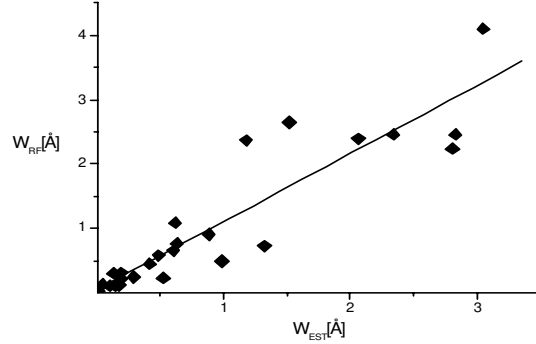
Figure 7. Linear correlation between FWHM Stark width values obtained by using estimates from multiple regression analysis (ω_{EST}) and corresponding values obtained by using RF algorithm (ω_{RF}) , with corresponding regression line.

4. Conclusion

Both of the methods used in this study have some advantages and disadvantages. In general, the advantage of ML models is that they are faster and easier to perform with the proper knowledge of computer programming. On the other hand, any of ML algorithms is some kind of black box, e. g. we finally don't know how input and output parameters are connected. If we want to find out the relationship between Stark width values and atomic and plasma parameters presented in a form of simple formula, we have to continue to investigate regularities and systematic trends of Stark widths using the estimates as, for example, were obtained here (equations (5)-(7)). If we don't need to know this connection, using of some ML algorithm is probably the best solution. Results of predictions using RF model show that, if some general estimate really exists, according to previous vision of Jagoš Purić, it should be the function of 14 variables. In this case, number of input atomic and plasma parameters we used before in a group of equations (1) to find systematic trends among the Stark width value, should be enlarged. We proved that, with additional two parameters (upper and lower orbital quantum number) and considering transition type into analysis, strongly affect on result of estimate, as it is assumed, for example, in (Majlinger et al., 2017b).

However, it is very important to stress that the estimates obtained in this work should be valid under the assumption that they can be applied on simple type of spectra, as they have been analysed in this case (for example, where for all transtitions in a whole spectrum parent term remains the same). For more complex spectra, these estimates should be improved, or some other methods are welcome to be used. Furthermore, although RF model shows very strong potential to be applied on RST analysis in future, it is tested only in the sample

of Stark broadening parameters related to simple spectra described here, and in the case of Li I spectral lines (Tapalaga et al., 2022), so it should also be confirmed in a greater sample to make us sure that this method can be applied generally in prediction of new Stark widths despite of complexity of a spectrum we investigate.For the application of these methods to study regularities and systematic trends among the Stark broadening parameters of lines in more complex spectra, additional investigations are needed, and development of both of these method are neccessary. Created database used in this and previous study is published online and it is available for use. It can be found on the link https://github.com/ivantraparic/StarkBroadeningMLApproach.

References

Aggarval, C., V., R. C. 2014, *Data Clustering* (Taylor and Francis Group)

Alwadie, N., Almodlej, A., Ben Nessib, N., Dimitrijević, M. 2020, *Contrib. Astron. Obs. Skalnaté Pleso*, **50**, 86

Chatterjee, S., Simonoff, J. S. 2014, *Handbook of Regression Analysis* (John Wiley and Sons)

Cowley, C. 1971, *The Observatory*, **91**, 139

Dimitrijević, M., Konjević, N. 1987, *J. Quant. Spectrosc. Radiat. Transfer*, **20**, 223

Dimitrijević, M. S., Konjević, N. 1981, *Spectral Line Shapes* (Walter de Gruyter and Co.), 211

Djeniže, S. 1999, *J. Res. Phys.*, **28**, 231

Djeniže, S., Srećković, A., Kalezić, S. 2001, *Serb. Astron. J.*, **164**, 21

Dojčinović, I. P., Tapalaga, I., Purić, J. 2011, *Pub. Astron. Soc. Australia*, **28**, 281

Dojčinović, I. P., Tapalaga, I., Purić, J. 2012, *Mon. Not. R. Astron. Soc.*, **419**, 904

Dojčinović, I. P., Tapalaga, I., Purić, J. 2013a, *Bull. Astron. Soc. India*, **41**, 281

Dojčinović, I. P., Tapalaga, I., Purić, J. 2013b, *Mon. Not. R. Astron. Soc.*, **429**, 2400

Griem, H. R. 1968, *Phys. Rev.*, **165**, 258

Grünwald, P. D., A tutorial introduction to the minimum description length principle. 2004, *ArXiv*, **math.ST/0406077**

Holtsmark, J. 1919, *Annalen der Physik*, **363**, 577

Jevtić, D., Dojčinović, I. P., Tapalaga, I., Purić, J. 2012, *Bull. Astron. Soc. India*, **40**, 151

Killian, J., Montenbruck, O., Nissen, P. 1991, *Astron. Astrophys. Suppl.*, **88**, 101

Konjević, N., Dimitrijević, M. S., Wiese, W. L. 1984, *J. Phys. Chem. Ref. Data*, **13**, 649

Konjević, N., Lessage, A., Fuhr, J. R., Wiese, W. L. 2002, *J. Phys. Chem. Ref. Data*, **31**, 819

Kramida, A., Ralchenko, Y., Reader, J., NIST ASD Team. 2022, NIST Atomic Spectra Database (version 5.10), https://physics.nist.gov/asd, accessed: September 2023

Majlinger, Z., Dimitrijević, M. S., Srećković, V. A. 2020a, *Mon. Not. R. Astron. Soc.*, **496**, 5584

Majlinger, Z., Dimitrijević, M. S., Srećković, V. A. 2020b, *Contrib. Astron. Obs. Skalnaté Pleso*, **50**, 164

Majlinger, Z., Dimitrijević, M. S., Simić, Z. 2017a, *Atoms*, **5**, 49

Majlinger, Z., Simić, Z., Dimitrijević, M. S. 2015, *Astron. Astrophys*, **36**, 671

Majlinger, Z., Simić, Z., Dimitrijević, M. S. 2017b, *Mon. Not. R. Astron. Soc.*, **470**, 1911

Miller, M. H., Lessage, A., Purić, J. 1980, *Astrophys. J.*, **239**, 410

Popović, L. C., Dimitrijević, M. S. 1998, *Contrib. Astron. Obs. Skalnaté Pleso*, **27**, 353

Purić, J., Dimitrijević, M. S., Lakićević, I. S. 1978, *Physics Letters A*, **67**, 189

Purić, J., Dojčinović, I. P., Nikolić, M., et al. 2008, *Astrophys. J.*, **680**, 803

Purić, J., Šćepanović, M. 1999, *Astrophys. J.*, **521**, 490

Purić, J., Šćepanović, M., Milosavljević, V., Ćuk, M., XXIII ICPIG (Toulouse, France). 1997, V − 48

Purić, J., Ćirković, L., XI ICPIG. 1973, 398

Purić, J., Miller, H., Lessage, A. 1993, *Astrophys. J.*, **416**, 825

Sahal-Bréchot, S., Dimitrijević, M., Ben Nessib, N. 2014a, *Atoms*, **2**, 225

Sahal-Bréchot, S., Dimitrijević, M. S., Moreau, N. 2015, STARK-B database, http://stark-b.obspm.fr, accessed: September 2023

Sahal-Bréchot, S., Dimitrijević, M. S., Moreau, N., Ben Nessib, N., SF2A Conf. 2014b, 515

Scepanovic, M., Puric, J. 2013, *Rom. Rep. Phys.*, **65**, 1275

Tapalaga, I., Dojčinović, I. P., Purić, J. 2011, *Mon. Not. R. Astron. Soc.*, **415**, 503

Tapalaga, I., Dojčinović, I. P., Purić, J. 2018, *Mon. Not. R. Astron. Soc.*, **474**, 5479

Tapalaga, I., Traparić, I., Trklja Boca, N., et al. 2022, *Neural Comput. Applic.*, **34**, 6349

Trklja, N., Dojčinović, I. P., Tapalaga, I., Purić, J. 2019a, *Atoms*, **7**, 99

Trklja, N., Tapalaga, I., Dojčinović, I. P., Purić, J. 2019b, *New Astron*, **59**, 54

Wiese, W., Konjevic, N. 1982, *J. Quant. Spectrosc. Radiat. Transfer*, **28**, 185

Wit, E., van den Heuvel, E., Romeijn, J. 2012, *Statistica Neerlandica*, **66**, 217

Spectroscopy of adiabatic dark states under two-photon excitation of sodium atoms

Arturs Cinins[1] , **Milan S. Dimitrijević**[2,3] , **Vladimir A. Srećković**[4] ,

Martins Bruvelis[5] , **Kaspars Miculis**[1,6] , **Nikolai N. Bezuglov**[7,8] **and**

Aigars Ekers[5]

[1] *Institute of Atomic Physics and Spectroscopy, University of Latvia,*
LV-1004 Riga, Latvia, (E-mail: arturs.cinins@lu.lv)

[2] *Astronomical Observatory, Volgina 7, 11060 Belgrade, Serbia,*
(E-mail: mdimitrijevic@aob.rs)

[3] *LERMA, Observatoire de Paris, Université PSL, CNRS, Sorbonne*
Université, F-92190 Meudon, France

[4] *Institute of physics Belgrade, University of Belgrade, P.O. Box 57, Belgrade,*
11001, Serbia, (E-mail: vlada@ipb.ac.rs)

[5] *King Abdullah University of Science and Technology (KAUST), Computer,*
Electrical and Mathematical Sciences and Engineering Division (CEMSE),
Thuwal 23955-6900, Saudi Arabia, (E-mail: martins.bruvelis@gmail.com)

[6] *National Research Nuclear University MEPhI, Moscow, 115409 Russia,*
(E-mail: kaspars.miculis2@lu.lv)

[7] *Sankt-Petersburg State University, 199034 St. Petersburg, Russia,*
(E-mail: nikolay.bezuglov@gmail.com)

[8] *Rzhanov Institute of Semiconductor Physics SB RAS, Novosibirsk, Russia*

Abstract. This work focuses on visualization of dark states arising in systems of hyperfine states upon two-photon excitation. In our experiment, levels $3S_{1/2}$ and $3P_{1/2}$ of sodium atoms are coupled by a strong S-laser field forming the laser-dressed adiabatic states, which are then monitored by scanning a weak probe P-field across the $3P_{1/2} \rightarrow 7D_{3/2}$ transition. The excitation spectrum of the $7D_{3/2}$ state exhibits one main peak and several side peaks. The latter shift farther apart with increasing S-laser intensity, while the position of the main peak is hardly affected, which associates its origin with a class of dark states decoupled from laser interactions. The results of numerical simulation of the observed spectra based on the solution of the optical Bloch equations are in good agreement with the experimental data. The results are of interest for atomic and laser physics.

Key words: laser excitation – optical adiabatic states – Na spectra – dark state peaks

1. Introduction

Adiabatic processes are observed in many fundamental and applied issues of natural science, having a wide range of applications depending on the characteristics of the problems. The quantum-mechanical theory has added its own specific approaches to the traditional methods of studying adiabatic phenomena in the classical sections of physical kinetics of gaseous geo- and space media (including plasma). These approaches include the formalism of adiabatic states, introduced as eigenfunctions ψ_κ

$$\widehat{H}(I)\psi_\kappa(I) = \varepsilon_\kappa(I)\psi_\kappa(I) \tag{1}$$

of a non-stationary Hamiltonian $\widehat{H}(I)$, which depends on slowly varying external parameters $I(t)$ (Landau, Lifshitz, 1981; Schiff, 1968). When studying dynamics of atomic or molecular formations, the parameters I are represented by internuclear distances R (Nikitin, Umanskii, 1984).

In contemporary problems of controlling atomic/molecular multilevel systems, the particles are subjected to optical coupling by pulsed laser fields. For quasi-resonant dipole transitions between energy levels, the field amplitudes are conventionally incorporated into the so-called Rabi frequencies $\Omega(t)$ (Shore, 2017). The corresponding adiabatic states ψ_κ (termed laser-dressed states in quantum optics (Shore, 2017; Vitanov $et\ al.$, 2017), with Rabi frequencies Ω as parameters I are classified into three categories - Dark, Bright, and Chameleon states (Shore, 2017; Kirova $et\ al.$, 2017). Dark states are completely decoupled from the laser-atomic interaction. Therefore, they do not directly contribute to the fluorescence spectra, while their adiabatic "dark" energies $\varepsilon_\kappa^{(D)}$ (AC Stark shifts) are inherently insensitive to changes in Ω. Bright states, on the contrary, are responsible for the interaction with laser fields and, therefore, participate in the absorption spectra formation, while the associated adiabatic "bright" energies $\varepsilon_\kappa^{(Br)}$ experience strong Stark shifts. Chameleon states are endowed with the properties of both dark states, due to the fact that they are not directly involved in the excitation of the atomic system (Kirova $et\ al.$, 2017), and bright states, since their energies also significantly depend on Rabi frequencies (Cinins $et\ al.$, 2022 a).

Noteworthy, the dark states emerge from a coherent mixture of stable sublevels (belonging to HF or Zeeman structures) of the system ground state, i.e. they turn out to be little susceptible to various dephasing effects that are inherent in excited states due to the processes of radiative decay or strong interatomic interaction (Van Der Waals, dipole-dipole, etc.). For this reason the dark states are widely used in quantum optics for design and subsequent practical implementations of new phenomena or quantum formations (such as electromagneticaly induced transparency (Fleischhauer $et\ al.$, 2005) or polaritons - a coherent composition of photonic and atomic states (Fleischhauer, Juzeliūnas, 2016), as well as to find highly efficient algorithms for performing quantum operations based on adiabatic passage processes (Rousseaux $et\ al.$, 2013; Cinins

et al., 2022 b). In this context, real-time monitoring and control of the evolution of dark states presents a challenging practical task. Here we present an experimental scheme for optical diagnostics of dark states, based on the nontrivial possibility of their manifestation in absorption spectra upon two-photon excitation of sodium atoms.

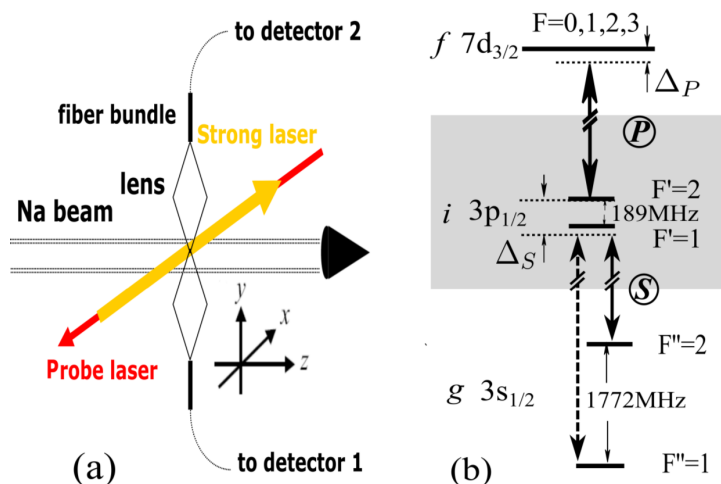In what follows, the principal quantum numbers and the orbital, electronic, and total angular momenta of atoms are denoted by $n, L, J,$ and F, respectively.

Figure 1. (**a**) Geometry of the experiment with a supersonic beam of Na atoms and (**b**) the corresponding ladder excitation scheme. The two S- and P-laser beams counter propagate along the x-axis. The lasers linear polarization vectors and the atomic beam axis are parallel to the z axis, which is also chosen as the quantization axis.

2. Experiment

2.1. Experimental setup

The experiment was performed in a supersonic beam of Na atoms with a mean flow velocity $v_f = 1160$ m/s. Two skimmers and a 2-mm entrance aperture of the excitation zone colimate the beam to the divergence angle of $0.67° \pm 0.02°$, which corresponds to the residual FWHM Doppler widths of 11.2 MHz and 14.7 MHz for one-photon excitation wavelengths of 589 and 450 nm, respectively.

The Na atoms are excited and probed upon crossing at a right angle two mutually collinear, anti-parallel laser beams S and P (see Fig. 1 (a)). The strong S-laser beam from a single-mode Coherent CR-699-21 ring dye laser couples a hyperfine component of sodium D_1 line at 589.5 nm, and the weaker probe P-laser beam from a TOPTICA TA-SHG 110 semiconductor laser couples the

second transition between $3p_{1/2}$ and $7d_{3/2}$ near 449.4 nm. Both lasers have narrow line with below 1 Mhz, and they are linearly polarized in the direction $\mathbf{e}_z$ of the atomic beam axis z, which serves as the quantization axis. The number density of atoms in the laser excitation region was chosen sufficiently low ($\leq 10^{10}\text{cm}^{-3}$), ensuring that the effects of radiation trapping and reabsorption (Bezuglov *et al.*, 2003) can be safely neglected.

The two-photon excitation $3s_{1/2}, F'' \to 3p_{1/2} \to 7d_{3/2}$ of Na shown in Fig. 1 (b) implies a two-step process. At the first step, the S-laser (strong laser) provides strong coupling of Zeeman sublevels M'' from one of the ground hyperfine (HF) g-component F'' and F', M'-sublevels of the first excited (intermediate) i-state $3p_{1/2}$. The laser-dressed (adiabatic) states, arising in the strongly coupled multilevel $g-i$ system, are probed by weak coupling by P-laser to the final excited f-state $7d_{3/2}$. Detunings $\Delta_{P,S}$ of the laser fields with frequencies $\omega_{P,S}$ are defined relative to the resonance (Bohr) frequencies of the respective HF transitions between components with $F'' = 1, 2$ and $F' = 2$ in the case of S-laser, and between $F' = 2$ and $F = 2$ for P-laser. The linear polarizations of both lasers imply that the total atomic angular momentum projection is conserved in both transitions, i.e. $\Delta M_{g \to i, i \to f} = 0$.

The fluorescence emitted by Na atoms is collected by lenses into two fiber bundles at a right angles with respect to both atom beam and laser beams axes. The collected light is then guided via spectral filters into two photomultipliers. Photocurrent signals are accumulated using a SRS SR400 photon counter. We record the total fluorescence from the level f (by detector 2) as a function of the P-laser detuning Δ_P for a fixed S-laser detuning Δ_S and refer to this signal as a spectral profile. In addition, auxiliary detector 1 registers photons emitted by the i-levels. Both signals are proportional to the integral (over excitation volume and HF sublevels) populations of the respective excited states.

2.2. Experimental parameters

The use of counterpropagating laser beams in the ladder excitation scheme corresponds to a typical Doppler-free setting of the experiment in atomic-molecular spectroscopy (Vitanov*et al.*, 2017; Bruvelis *et al.*, 2012). The P,S-beams are focused using cylindrical lenses such that the long axis of the focus is perpendicular to the atomic beam axis. The chosen here typical in our experiments beam waists $\varpi_S = 20.5 \mu m$ of the S- (strong) and $\varpi_P = 70 \mu m$ of the P- (probe) laser beams allows safely ignoring the effects of laser wave-front curvatures (Bruvelis *et al.*, 2012). The relatively small waist of strong S-laser reduces the effects of optical pumping (Sydoryk *et al.*, 2008; Porfido *et al.*, 2015).

The laser spatial intensity profiles are Gaussian and along z-axis is $I_j(z) \sim \exp(-z^2/\varpi_j^2)$ ($j = P, S$). The mean flow velocity v_f of atoms is 1160 m/s, so that the transit times (Sydoryk *et al.*, 2008) $\tau_j = 2\varpi_j/v_f$ of atoms through the laser beams are $\tau_S = 37ns$ and $\tau_P = 126ns$ for S- and P-lasers respectively. The above distributions $I_j(z)$ result in the Gaussian time variations

$$I_j(t) = I_j^{(0)} \exp(-4t^2/\tau_j^2); \qquad j = P, S \tag{2}$$

of laser intensities in the moving frame of an atom ($t = z/v_f$).

In the rotating-wave approximation (RWA) (Shore, 2011), the atom-light interaction is determined by slowly varying vector amplitudes $\mathbf{E}_j(t) \sim \sqrt{I_j(t)}$ of the laser electric fields. The corresponding field operators $\hat{V}_j = -0.5\hat{\mathbf{d}}\mathbf{E}_j$ describe the coupling of the atomic electric dipole moment $\hat{\mathbf{d}}$ with P- and S-laser fields $\mathbf{E}_j = E_j\mathbf{e}_z$ linearly polarized along the quantization axis z, that is

$$\hat{V}_{S,P}(t) = -0.5\hat{d}_z E_{S,P}(t) \tag{3}$$

It is convenient to describe the laser induced couplings using the characteristic Rabi frequencies $\Omega_{P,S}$ (the so called reduced Rabi frequencies) that drive the transitions $3s-3p$ and $3p-7d$ (Sydoryk *et al.*, 2008):

$$\begin{aligned}
\Omega_S &= E_S(z=0) \cdot |(3s \parallel D \parallel 3p)|/\hbar; \\
\Omega_P &= E_P(z=0) \cdot |(3p \parallel D \parallel 7d)|/\hbar.
\end{aligned} \tag{4}$$

Here $(\tilde{n}\tilde{l} \parallel D \parallel nl)$ are the corresponding reduced matrix elements for the discussed transitions, considered unresolved with respect to fine and hyperfine structure (Sobelman, 1992).

Equation (4) defines the reduced Rabi frequencies Ω_j via maximum values $E_j^{(0)} \equiv E_j(z=0)$ of the laser electrical field amplitudes at the center parts $z = 0$ of the laser beams. Practically more convenient is the relation (Sydoryk *et al.*, 2008; Metcalf, van der Straten, 1999):

$$\Omega_j^2 = g_j A_j \frac{3\lambda_j^3}{4\pi^2\hbar c} I_j^{(0)}; \qquad W_j = \pi I_j^{(0)} \varpi_j^2 \tag{5}$$

between the reduced frequencies Ω_j and intensities $I_j^{(0)}$ entering Eq. (2) which are easily found from the measured laser powers W_j. Here λ_j and A_j are the wavelength and the Einstein coefficient of the j-transition $\tilde{n}\tilde{l} - nl$, and $g_j = 2l+1$ is the the statistical weight of the transition upper level nl.

3. Results and discussion

The fluorescence signal S_f observed in the experiment is proportional to the integral population $\overline{n}_f$ of the final $7d_{3/2}$ state of an atom. This population can be found in terms of the total number of photons N_f emitted by the corresponding HF and Zeeman components F, M having the partial populations $n_{FM}^{(f)}(t)$ at the time t in the moving frame of an atom:

$$S_f \sim N_f = A_f\overline{n}_f; \qquad \overline{n}_f = \int_{-\infty}^{\infty} \sum_{FM} n_{FM}^{(f)}(t)dt, \tag{6}$$

where A_f is a natural width of the f-state.

3.1. Numerical modeling

For obtaining the emitted photon number N_f one should solve the modified Optical Bloch equations (Shore, 2011)

$$\frac{d\rho}{dt} = -i\left[\hat{H}\rho\right] + \hat{R}\rho. \tag{7}$$

for atomic density matrix ρ of the sodium atoms ensemble under study. The total Hamiltonian $\hat{H}$ of the atom-laser system in RWA

$$\hat{H}_{RW} = \hat{H}^{(a)} + \hat{H}^{(hf)} + \hat{V}_S(t) + \hat{V}_P(t) \tag{8}$$

describes interaction of Na atoms with external electromagnetic fields. The atomic Hamiltonian $\hat{H}^{(a)}$ that includes the fine structure interaction along with the HF operator $\hat{H}^{(hf)}$ give the energy structure of the diabatic (bare) states of isolated atoms. The field operators $\hat{V}_{S,V}$ (3) are responsible for the laser-atom interaction which is depicted in Figs. 1(b). The term $\hat{R}$ deals with relaxation processes caused by spontaneous emission and the finite laser linewidths. The diagonal elements $\rho_{\kappa,\kappa}$ of the matrix ρ give the population n_κ of quantum state $|\kappa\rangle$, while the off-diagonal elements $\rho_{\kappa,\kappa'}$ belong to the so-called coherences.
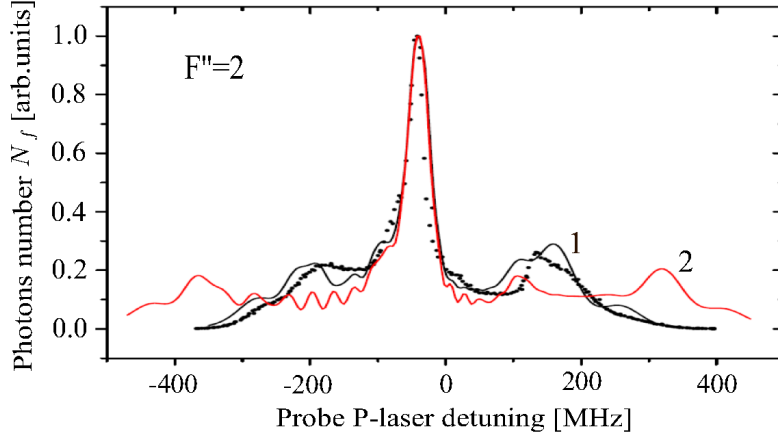

Figure 2. The total number N_f of photons emitted by the final $7d_{3/2}$ state of Na atoms vs probe P-laser detuning Δ_P for the $3s_{1/2}(F'' = 2) \rightarrow 3p_{1/2} \rightarrow 4d_{3/2}$ excitation sequences with HF ground state component $F'' = 2$. The experimental (dot curve) and the theoretical (solid curve 1) profiles correspond to S-laser reduced Rabi frequency (4) $\Omega_S = 1200$MHz while theoretical profile 2 (red solid curve) is calculated for $\Omega_S = 2000$MHz. The probe P-laser reduced Rabi frequency (4) $\Omega_P = 7$MHz. The strong S-laser detuning $\Delta_S = -120$MHz.

Matrix elements of the field operators describe a variety of stimulated transitions among the HF and Zeeman sublevels. The absolute strengths of the transitions are connected with the reduced Rabi frequencies (4). Rabi frequencies of individual fine $LJ \to \widetilde{L}\widetilde{J}$ and HF $LJF \to \widetilde{L}\widetilde{J}\widetilde{F}$ transitions are then defined by the tabulated line strength values (Sobelman, 1992). The Rabi frequencies for individual transitions $LJFM \to \widetilde{L}\widetilde{J}\widetilde{F}\widetilde{M}$ between Zeeman sublevels M in the case of linearly polarized excitation are obtained using the formulas provided in (Sobelman, 1992; Auzinsh *et al.*, 2010), and the respective values can be found in (Sydoryk *et al.*, 2008; Bruvelis *et al.*, 2012).

Here we employ a numerical algorithm akin to our previous works (Cinins *et al.*, 2022 a; Sydoryk *et al.*, 2008; Bruvelis *et al.*, 2012), i.e. an algorithm based on the split operator technique. The latter has increased stability of sympletic numerical integration schemes (Hairer *et al.*, 2006) and is successfully used to solve a wide range of problems in the theory of radiation transfer in dense absorbing media (Kazansky *et al.*, 2001), laser spectroscopy (Kirova *et al.*, 2017), and in the analysis of the dynamic chaos regime in Hamiltonian systems (Efimov *et al.*, 2014).
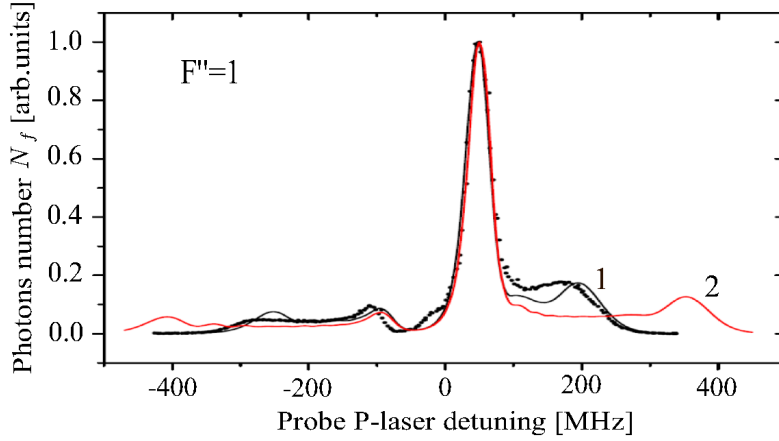

Figure 3. The same as in Fig. 2 in the case of the the initially populated HF component $F'' = 1$ and the strong S-laser detuning $\Delta_S = -178$MHz.

3.2. Experimental and numerical results

Figures 2 and 3 show excitation fluorescence from the upper f-level as a function of the S-laser detaining Δ_S for several values of both P-laser detuning Δ_P and the initially populated HF component F'' of the ground $3s_{1/2}$ state. The circles correspond to experimental values and the solid lines are results of numerical calculations discussed above. In the following subsections, we will provide a detailed interpretation of the obtained spectra.

3.3. Discussion

Upon coupling with linearly polarized photons, the atomic magnetic (Zeeman) quantum number M is an exact invariant (Landau, Lifshitz, 1981), i.e. atomic system in Fig. 1(b) is decomposed into a set of independent (mutually orthogonal) partial excitation ladders (M-ladders) whose levels are labeled only by the HF quantum numbers F, as shown in Fig. 4(a).

Qualitative interpretation of the excitation spectra exhibited in Figs. 2-3 is based on the concept of adiabatic (dressed) states for strongly coupled sub-levels of (g-i) system. Let us first introduce a somewhat idealized atomic model to provide an illustrative explanation of the observed spectra features, in particular, the existence of central peaks without any noticeable influence of the S-laser intensity on them. We accept the following two main simplifications. (i) All atoms move at the same flow velocity v_f (i.e. one disregards Doppler broadening); (ii) The HF splitting between the HF components $F' = 1, 2$ of $3p_{1/2}$ i-state can be neglected in the first approximation (the final state $7d_{3/2}$ fully meets this requirement). The second assumption means that the partial simplified excitation ladders have a non-degenerate lower state (F''), a doubly degenerate i-state $(F' = 1, 2)$, and a triply degenerate f-state (due to the selection rule $\Delta F = 0, \pm$).
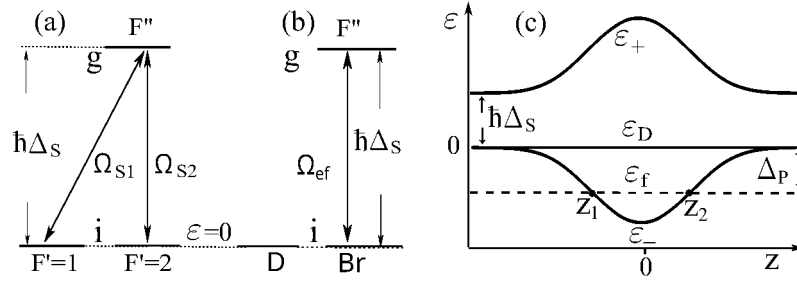

Figure 4. (a) The first (g-i) excitation step with some fixed value of Zeeman quantum number M under the rotating-wave approximation (RWA) and in neglecting the HF interaction for the $3p_{1/2}$ i-state. (b) The same excitation scheme as in frame (a) in the Dark-Bright basis. (c) Atomic energy level diagram of laser-dressed states with beam axis coordinate $z = v_f \cdot t$ as a parameter. The excitation of the final f-state $7d_{3/2}$ occurs at the intersection (Landau-Zener) points $z_{1,2}$.

The main features of fluoresce signals are determined by the atomic adiabatic (dressed) states ψ_κ (more precisely, by their energies ε_κ) formed by strong S-laser at the first excitation step shown in Fig. 4(a) for M-ladder. This step turns out to be a conventional Lambda-excitation scheme with the following parameters. We choose as zero the atomic energy ε of the diabatic HF component $\psi_{F'1} \equiv |iF'{=}2\rangle$ of $3p_{1/2}$ i-state, i.e. under the simplified model $\varepsilon_{F'=1,2} = 0$. In RWA, the

diabatic energies of g-,f-states are defined by the corresponding laser detunings: $\varepsilon_{F''} = \hbar\Delta_S$ and $\varepsilon_F = -\hbar\Delta_P$ as seen in Fig. 4(a). The partial Rabi frequencies $\Omega_{S1,2}$ are proportional to the reduced S-frequency Ω_S (4) with coefficients of proportionality ~ 0.2 depending on the quantum numbers M, F'', F' via 6j- and 3j-symbols (Sydoryk *et al.*, 2008; Sobelman, 1992).

The algorithm for obtaining the adiabatic states ψ_κ for Lambda-schemes is well known and includes two sequential actions (Vitanov *et al.*, 2017; Shore, 2011; Cinins *et al.*, 2023). (i) First, two new mutually orthogonal wave vectors ψ_D and ψ_{Br} are constructed

$$\psi_D = \frac{\Omega_{S1}}{\Omega_{ef}}\psi_{F'2} - \frac{\Omega_{S2}}{\Omega_{ef}}\psi_{F'1}; \ \ \psi_{Br} = \frac{\Omega_{S2}}{\Omega_{S1}}\psi_{F'1} + \frac{\Omega_{S1}}{\Omega_{ef}}\psi_{F'2}; \quad \Omega_{ef} = \sqrt{\Omega_{S1}^2 + \Omega_{S2}^2}. \tag{9}$$

Vectors $\psi_{D,Br}$ differently relate to the RWA g-sublevels $\psi_{F''} \equiv |gF''\rangle$: completely decoupled D-vector ψ_D (termed "Dark") and Br-vector ψ_{Br} (termed "Bright") with coupling Rabi frequency Ω_{ef} (see Fig. 4(b)). (ii) Second, linear combination of a coupled pair of diabatic vectors $\psi_{Br}, \psi_{F''}$ provides two new adiabatic states (eigenstates) $\psi_\pm$

$$\psi_+ = \cos\theta\psi_{F''} + \sin\theta\psi_{Br}; \quad \psi_- = -\sin\theta\psi_{F''} + \cos\theta\psi_{Br}, \tag{10}$$

with newly acquired repulsive adiabatic energies

$$\varepsilon_\pm(z) = \frac{\hbar}{2}\Delta_S \pm \frac{\hbar}{2}\sqrt{\Delta_S^2 + \Omega_{ef}(z)^2}; \quad z = v_f \cdot t, \tag{11}$$

due to ac Stark shift (Delone, Krainov, 1999) stimulated by the coupling frequency Ω_{ef}(9). The mixing angle $2\theta = \arctan(-2\Omega_{ef}/\Delta S)$ $(0 \leq \theta \leq \pi/2)$ in Eq. (10) defines a measure of amplitudes sharing between the diabatic vectors $\psi_{F''}, \psi_{Br}$.

Importantly, in the moving frame of the atom the Rabi frequencies $\Omega_j(z)$

$$\Omega_j \to \Omega_j(z) = \Omega_j(z=0) \cdot \exp(-z^2/2\varpi_j^2)); \tag{12}$$

along with ac Stark shifts $\varepsilon_\pm$ (9) become z- and time-dependent (see Fig. 4(c)). The energy ε_D of the dark state, on the contrary, since it is not involved into the light-atom interaction, always remains equal to diabatic zero value $\varepsilon_D = 0$, as depicted in Fig. 4(c).

Probing the spatially varying energies $\varepsilon_\pm, \varepsilon_D$ of the dressed adiabatic states at the second stage of the ladder scheme using a weak P-probe laser has a number of interesting features. Due to the different spatial behavior of $\varepsilon_\pm$ and ε_D, the bright and dark states are responsible for the formation of different parts of the N_f (6) fluorescence signal as a function on P-laser detuning Δ_P.

(i) In the case of $\psi_\pm$ vectors, they coherently share the population with the ground state $\psi_{F''}$ (see Eq. (10)) and can transfer it to f-states only at two

Landau-Zener resonance points $z_{1,2}$, shown in Fig. 4(c). The maximum probability of population transfer occurs at point $z = 0$, i.e. the intersections of the horizontal lines $\varepsilon = \hbar\Delta_P$ with curves $\varepsilon = \varepsilon_{\pm}$ provides a wide fluorescence signal background with width $\Delta\omega_f \approx (\varepsilon_+ + |\varepsilon_-|) \sim \Omega_S$. These findings of ours correlate well with the data presented in Fig. 2,3.

(ii) The dark state ψ_D (9), completely decoupled from the laser-atom interaction, cannot be excited by the S-laser and, at first glance, does not contribute to the N_f signal. There is, however, another way of its excitation, namely due to HF splitting $\Delta_{HF} = 189$MHz between $F' = 1$ and $F' = 2$ HF components of $3p_{1/2}$ i-state. As mentioned in (Shore, 2017; Vitanov *et al.*, 2017; Auzinsh *et al.*, 2008), the splitting Δ_{HF}, often called the double-photon detuning, opens a pathway for population flow from ψ_{Br} to ψ_D states. Since the potential curves $\varepsilon_{D,f}$ of D- and f-states intersect in our simplified model only at $\Delta_P = 0$, the D-state manifests itself in the $N_f(\Delta_P)$ signal as a central peak blurred and shifted from resonance $\Delta_P = 0$ by HF interaction. The characteristics of this "Dark" peak, determined solely by Δ_{HF}, should be slightly affected by the intensity of the S-laser, which is consistent with the spectral profiles in Fig. 2,3.

4. Conclusions

In this work, the processes of formation of laser-dressed states on the hyperfine (HF) sublevels of sodium atoms are experimentally and theoretically studied using two-photon laser spectroscopy. A supersonic beam of sodium atoms is excited near the frequency of the D_1 line by a strong S-laser, which induces formation of a system of bright and dark adiabatic states from the HF components of the $3p_{1/2}$ state. Probing the $3p_{1/2} \rightarrow 7d_{3/2}$ transition with a weak P-laser allows to diagnose the dressed state parameters based on the features of the $7d_{3/2}$ state emission spectrum. Numerical calculations, which describe well the experimental data, followed by their qualitative analysis, made it possible to explain the presence of two characteristic structural parts of the spectra. The first of them, which has a large spectral extent with a width proportional to the S-laser intensity, is formed by bright states since the associated adiabatic energies alter along the atomic beam axis in the laser excitation zone. The second region, presented in the spectra as a relatively narrow central peak, weakly responds to the excitation intensity and, as analysis shows, is formed by transferring the population of the bright state to the dark one due to their mixing by the HF interaction operator. Thus, we have proposed and implemented an experimental scheme for optical diagnostics of dark states, based on their visualization in two-photon absorption spectra of sodium atoms. The results are of interest for atomic and laser physics.

References

Auzinsh, M., Bezuglov, N.N., Miculis, K.: 2008, *Phys. Rev. A*, **78**, 053415

Auzinsh, M., Budker, D., Rochester, S.: 2010, *Optically Polarized Atoms: Understanding Light-atom Interactions*, OUP Oxford

Bezuglov, N.N., Ekers, A., Kaufmann, O., Bergmann, K., Fuso, F., Allegrini, M.: 2003, *Journal of Chemical Physics*, **119**, 7094

Bruvelis, M., Ulmanis, J., Bezuglov, N.N., Miculis, K., Andreeva, C., Mahrov, B., Tretyakov, D., Ekers, A.: 2012, *Phys. Rev. A*, **86**, 012501

Cinins, A., Bruvelis, M., Bezuglov, N.N.: 2022 a, *Journal of Physics B: Atomic, Molecular and Optical Physics*, **55**, 234003

Cinins, A., Bruvelis, M., Dimitrijević, M.S., Srećković, V.A., Efimov, D.K., Miculis, K., Bezuglov, N.N., Ekers, A.: 2022 b, *Astronomische Nachrichten*, **343**, e210081

Cinins, A., Dimitrijević, M.S., Srećković, V.A., Miculis, K., Bezuglov, N.N.: 2023, *The European Physical Journal D*, **77**, 87

Delone, N.B., Krainov, V.P.: 1999, *Physics-Uspekhi*, **42**, 669

Efimov, D.K., Bezuglov, N.N., Klyucharev, A.N., Gnedin, Y.N., Miculis, K., Ekers, A.: 2014, *Optics and Spectroscopy*, **117**, 8

Fleischhauer, M., Imamoglu, A., Marangos, J.P.: 2005, *Rev. Mod. Phys.*, **77**, 633

Fleischhauer, M., Juzeliūnas, G.: 2016, Slow, stored and stationary light, in: *Optics in Our Time*, 359

Hairer, E., Wanner, G., Lubich, C.: 2006, *Geometric Numerical Integration: Structure-Preserving Algorithms for Ordinary Differential Equations*, Springer Berlin Heidelberg: Berlin, Heidelberg

Kazansky, A.K., Bezuglov, N.N., Molisch, A.F., Fuso, F., Allegrini, M.: 2001, *Phys. Rev. A*, **64**, 022719

Kirova, T., Cinins, A., Efimov, D.K., Bruvelis, M., Miculis, K., Bezuglov, N.N., Auzinsh, M., Ryabtsev, I.I., Ekers, A.: 2017, *Phys. Rev. A*, **96**, 043421

Landau, L., Lifshitz, E.: 1981, *Quantum Mechanics: Non-Relativistic Theory, Course of Theoretical Physics*, Butterworth-Heinemann: Oxford

Metcalf, H.J., van der Straten, P.: 1999, *Laser Cooling and Trapping*, Springer New York: New York, NY

Nikitin, E.E., Umanskii, S.Y.: 1984, *Theory of Slow Atomic Collisions*, Springer Berlin Heidelberg: Berlin, Heidelberg

Porfido, N., Bezuglov, N.N., Bruvelis, M., Shayeganrad, G., Birindelli, S., Tantussi, F., Guerri, I., Viteau, M., Fioretti, A., Ciampini, D., Allegrini, M.,

Comparat, D., Arimondo, E., Ekers, A., Fusoet, F.: 2015, *Phys. Rev. A*, **92**, 043408

Rousseaux, B., Guérin, S., Vitanov, N.V.: 2013, *Phys. Rev. A*, **87**, 032328

Schiff, L.I.: 1968, *Quantum Mechanics*, third ed., McGraw-Hill: New York

Shore, B.W.: 2011, *Manipulating Quantum Structures Using Laser Pulses*, Cambridge University Press

Shore, B.W.: 2017, *Adv. Opt. Photon*, **9**, 563

Sobelman, I.I.: 1992, *Atomic Spectra and Radiative Transitions*, Springer

Sydoryk, I., Bezuglov, N.N., Beterov, I.I., Miculis, K., Saks, E., Janovs, A., Spels, P., Ekers, A.: 2008, *Phys. Rev. A*, **77**, 042511

Vitanov, N.V., Rangelov, A.A., Shore, B.W., Bergmann, K.: 2017, *Reviews of Modern Physics*, **89**, 015006

On the Stark broadening of N VI spectral lines

**Magdalena D. Christova[1], Milan S. Dimitrijević[2,3] and
Sylvie Sahal-Bréchot[3]**

[1] *Department of Applied Physics, Technical University of Sofia, 1000 Sofia,
Bulgaria, (E-mail: mchristo@tu-sofia.bg)*

[2] *Astronomical Observatory, Volgina 7, 11060 Belgrade, Serbia,
(E-mail: mdimitrijevic@aob.rs)*

[3] *LERMA, Observatoire de Paris, Université PSL, CNRS, Sorbonne
Université, F-92190 Meudon, France*

Abstract. Results for the Stark broadening parameters for spectral lines within one spectral series of N VI 2s-np (n = 2 – 4) triplet transitions are included. Plasma conditions of interest cover temperatures from 50 000 K to 2 000 000 K, perturber density is 10^{17} cm^{-3}, and electrons, and boron ions (B III, B IV, B V and B VI) are perturbers. These conditions correspond to those in laser driven plasma for proton boron fusion reaction. The contribution in Stark width and shift of different types of perturbers is analyzed. The width versus principal quantum number is presented.

Key words: Stark broadening – spectral line shapes – atomic data – N VI – proton-boron fusion

1. Introduction

Stark broadening data, or data for broadening by collisions with charged particles, are of interest in many research topics. They are particularly needed for astrophysical plasma research, but also for laboratory plasma diagnostics, for fusion plasma, laser research and for various plasmas in technology.

Data for Stark broadening of five times charged nitrogen ion (N VI) spectral lines are important particularly for investigation of white dwarfs where N VI lines are present (see e.g. Rauch 2007) and Stark broadening is the dominant pressure broadening mechanism. Reliable data for Stark broadening of N VI are also of interest for proton-boron fusion plasma since in a number of investigations (see e,g, Margarone *et al.*, 2015; Giuffrida *et al.*, 2020; Istokskaia *et al.*, 2023) the target is boron nitride (BN).

Fusion reaction is known in the universe as the dominant energy source that occurs in the stellar interiors. Several international and national projects as the International Thermonuclear Energy Reactor (ITER), and the National Ignition Facility (NIF) perform continuous efforts to obtain controlled fusion reaction device in laboratory.

Using the semiclassical perturbation theory (see for example Sahal-Bréchot *et al.*, 2014 and references therein), we calculated Stark widths and shifts, determining line profile, for 15 multiplets containing 33 spectral lines of N VI broadened by collisions with the most important charged constituents of stellar and proton-boron fusion plasma: electrons, protons, alpha particles, B III, B IV, B V and B VI ions. Calculations have been performed for a grid of temperatures and perturber densities. The obtained results will be also prepared in VO (Virtual Observatory) and XSAMS (XML Schema for Atomic, Molecular and Solid Data) format for the implementation of results in the international, on-line database STARK-B (Sahal-Bréchot *et al.* 2015 - https://stark-b.obspm.fr/) a part of VAMDC (Virtual Atomic and Molecular Data Center, Dubernet *et al.*, 2010), after the publication of the main article.

In this contribution we will present and discuss a part of the results which will be published in entirety elsewhere (Dimitrijević, Christova and Sahal-Bréchot, 2023).

2. The impact semiclassical perturbation method

Spectral line profiles of detected emitted or absorbed spectral lines ensure important data for the interactions between emitters and surrounding particles. As a result of these interactions in the plasma environment, the profiles are broadened and shifted. The degree of profile's change depends on temperature and density. This plasma phenomenon is known in the theory as pressure broadening mechanism. Pressure broadening can be provoked by interactions with charged particles and due to interactions with neutral atoms. In the case of interactions between emitters and charged particles (electrons, protons, ions), pressure broadening is named Stark broadening. In this work, we investigate Stark broadening parameters of several spectral lines belonging to N VI transitions. This study is first of all oriented for application in laser driven proton boron plasma, but also and for astrophysical purposes. The semiclassical perturbation theory (Sahal-Bréchot, 1969 a,b) is applied. This theory is developed for the case of an isolated, non-hydrogenic spectral line which full width at half maximum (FWHM) and shift are expressed as:

$$W = N \int v f(v) dv \left(\sum_{i' \neq i} \sigma_{ii'}(v) + \sum_{f' \neq f} \sigma_{ff'}(v) + \sigma_{el} \right)$$

$$d = N \int v f(v) dv \int_{R_3}^{R_D} 2\pi \rho d\rho \sin(2\varphi_p). \tag{1}$$

where the indexes i and f concern the initial and final level of a given transition; i' and f' are the corresponding perturbing levels, respectively. N is electron density, v perturber velocity, f(v) represents the Maxwellian distribution of electron velocities, and ρ is the perturber's impact parameter.

The cross sections for inelastic collisions $\sigma_{kk'}(v)$, $k = i, f$, could be written by an integration of the transition probability $P_{kk'}(\rho, v)$, over the impact parameter ρ :

$$\sum_{k' \neq k} \sigma_{kk'}(v) = \frac{1}{2}\pi R_1^2 + \int_{R_1}^{R_D} 2\pi\rho d\rho \sum_{k' \neq k} P_{kk'}(\rho, v). \tag{2}$$

The following two equations estimate the cross section of elastic collisions between emitters and charged particles:

$$\sigma_{el} = 2\pi R_2^2 + \int_{R_2}^{R_D} 2\pi\rho d\rho \sin^2 \delta + \sigma_r,$$

$$\delta = (\varphi_p^2 + \varphi_q^2)^{\frac{1}{2}}. \tag{3}$$

where δ denotes the phase shift due to polarization ($\varphi_p \ (r^{-4})$) and quadrupole ($\varphi_q \ (r^{-3})$) potentials for atom-perturber elastic interactions. The details for cut-off parameters R_1, R_2, R_3, the Debye cut-off R_D and the symmetrization are explained in Sahal–Bréchot (1969 b) (Section 1 of Chapter 3). The term σ_r gives the contribution of Feshbach resonances (Sahal–Bréchot, 2021).

3. Results and Discussion

Two main research fields where Stark broadening data for N VI spectral lines are needed are first of all white dwarfs, where Stark broadening is the dominant pressure broadening mechanism and N VI lines are present in their spectra. The other research field is the proton-boron fusion experiments, where nitrogen is an important target. In order to satisfy the needs of both fields, we have calculated, using the semiclassical perturation method (Sahal-Bréchot, 1969 a, b; Sahal-Bréchot *et al.*, 2014), Stark broadening of spectral lines within 15 multiplets of N VI. The temperature values are in a wide interval from 50 000 K to 2 000 000 K and perturber densities from 10^{17} cm^{-3} to 10^{24} cm^{-3}. Broadening due to collisions with electrons, protons, alpha particles and boron ions in different degrees of ionization (B III, B IV, B V and B VI), charged particles of interest for white dwarfs and proton-boron fusion, are examined. The complete results will be published in entirety elsewhere (Dimitrijević, Christova and Sahal-Bréchot, 2023). Here, in Tables 1-2 are presented line widths and in Tables 3-4 shifts of three lines within one spectral series, for all examined temperatures and for perturber density 10^{17} cm^{-3}. These lines belong to triplets N VI 2s-2p, 1901.5 Å; N VI 2s-3p, 161.2 Å; N VI 2s-4p, 122.4 Å. These results are used for discussion of systematic trend of Stark widths within a spectral series and for comparison and analysis of the influence of different perturbers. The parameter C (Dimitrijević, Sahal-Bréchot, 1984), provided in Tables 1-4, when divided by the corresonding width (W), gives the maximal perturber density for which the line may be considered as isolated.

Table 1. Stark full widths (Å) at half intensity maximum of N VI spectral lines due to interactions with electrons, B III and B IV ions. The presented lines belong to triplets within one spectral series. The perturber density is 10^{17} cm^{-3}.

Transition	T[K]	We	WBIII	WBIV
N VI 2s-2p	50000.	0.730E-02	0.205E-04	0.206E-04
1901.5 A	100000.	0.523E-02	0.729E-04	0.780E-04
C= 0.19E+21	300000.	0.321E-02	0.365E-03	0.483E-03
	500000.	0.259E-02	0.549E-03	0.790E-03
	1000000.	0.198E-02	0.852E-03	0.136E-02
	2000000.	0.155E-02	0.111E-02	0.178E-02
N VI 2s-3p	50000.	0.199E-03	0.500E-05	0.552E-05
161.2 A	100000.	0.147E-03	0.113E-04	0.140E-04
C= 0.19E+18	300000.	0.959E-04	0.241E-04	0.352E-04
	500000.	0.800E-04	0.289E-04	0.442E-04
	1000000.	0.634E-04	0.350E-04	0.560E-04
	2000000.	0.511E-04	0.405E-04	0.679E-04
N VI 2s-4p	50000.	0.337E-03	0.295E-04	0.394E-04
122.4 A	100000.	0.258E-03	0.480E-04	0.694E-04
C= 0.48E+17	300000.	0.177E-03	0.743E-04	0.120E-03
	500000.	0.150E-03	0.854E-04	0.141E-03
	1000000.	0.121E-03	0.105E-03	0.174E-03
	2000000.	0.979E-04	0.124E-03	0.193E-03

To investigate the width's behavior in the spectral series we give Stark widths *versus* principal quantum number. To eliminate the influence of the wavelength, the broadening is given in angular frequency units in Fig. 1 for 300 000 K and electron density 10^{20} cm^{-3}. This dependence is in accordance with the theory that spectral lines originated from higher transitions are more broadened. This systematic trend could be useful to roughly estimate by extrapolation, Stark width due to interactions with electrons for other spectral lines from the same series.

In the next two figures we present Stark broadening parameters due to different perturbers for spectral line with wavelength 9624.6 Å – transition (singlet) N VI 3s-3p. The perturber density is 10^{16} cm^{-3}. The case of Stark width is illustrated in Fig. 2. The width due to collisions with electrons decreases with temperature and dominates for temperatures up to 200 000 K, while those due to protons, alpha particles, and boron ions with different degrees of ionization increase with T. The broadening is larger with the increasing of the electric charge of the perturber. The lowest values are obtained for protons and highest for boron ions B VI. All curves are well separated and distinguishable. The corresponding Stark shift values are shown in Fig. 3. They are all negative (towards the blue). The smallest shifts of the spectral line are obtained for N VI-electron
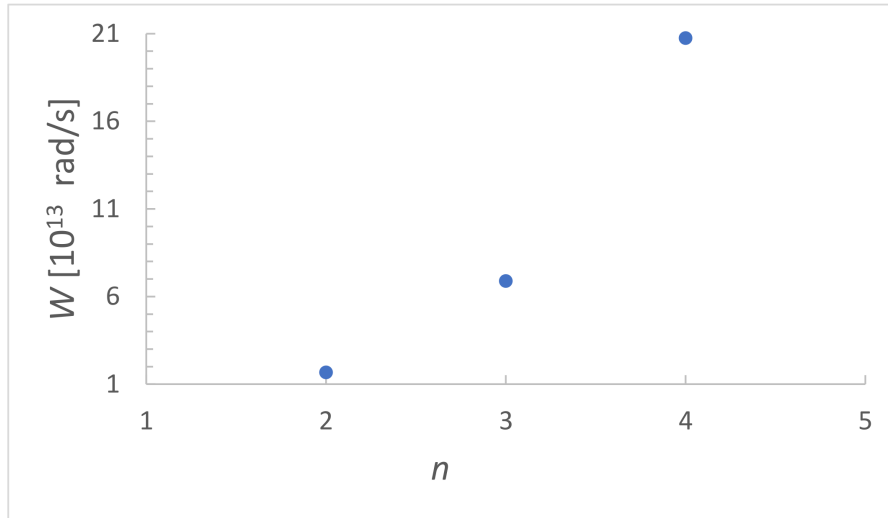
Figure 1. Stark widths due to interactions with electrons *versus* principal quantum number for spectral lines within one spectral series corresponding to N VI 2s-np (n = 2 − 4) triplets. The temperature is 300 000 K and the perturber density 10^{20} cm^{-3}.
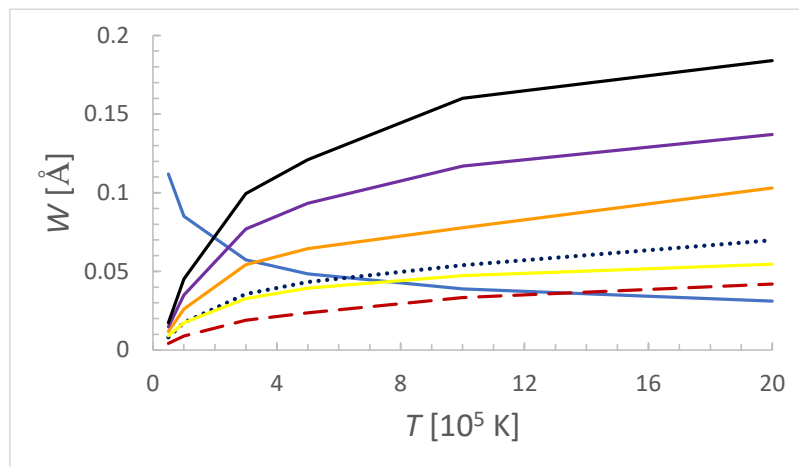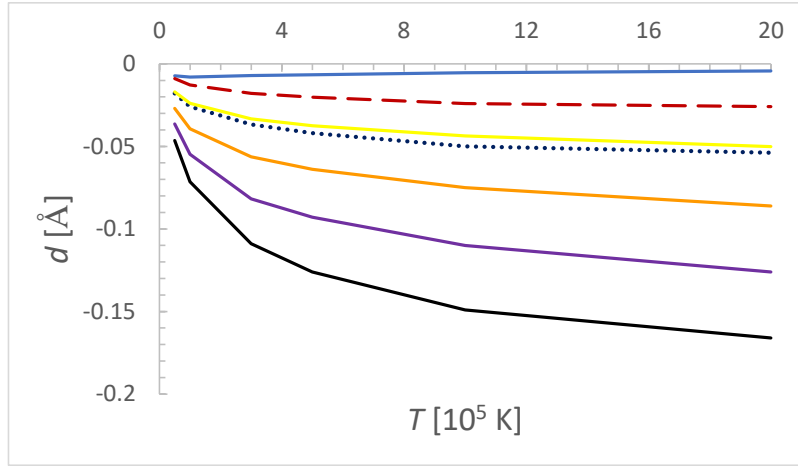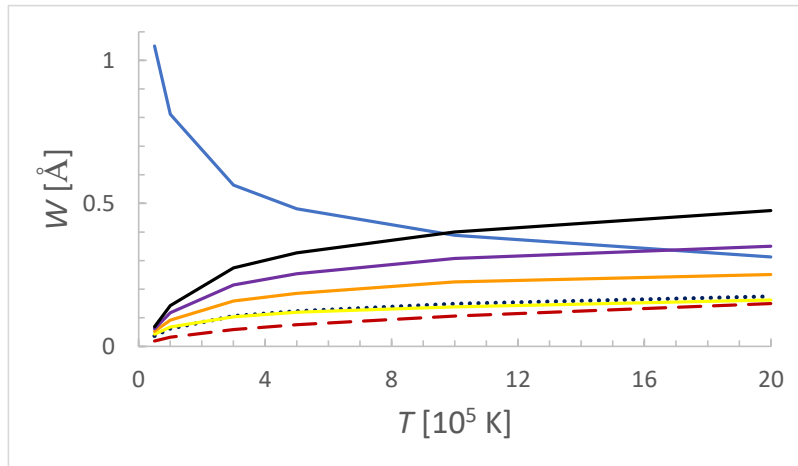

Figure 2. Stark width due to interactions with electrons (blue solid line), protons (red dashes), alpha particles (dark blue dots) and ions: B III (yellow solid line), B IV (orange solid line), B V (purple solid line), and B VI (black solid line) ions *versus* temperature. Spectral line corresponds to N VI 3s-3p singlet transition with $\lambda = 9624.6$ Å. The perturber density is 10^{16} cm^{-3}.

Figure 3. Stark shift due to interactions with electrons (blue solid line), protons (red dashes), alpha particles (dark blue dots) and ions: B III (yellow solid line), B IV (orange solid line), B V (purple solid line), and B VI (black solid line) ions *versus* temperature. Spectral line corresponds to N VI 3s-3p singlet transition with $\lambda = 9624.6$ Å. The perturber density is 10^{16} cm^{-3}.

Figure 4. Stark width due to interactions with electrons (blue solid line), protons (red dashes), alpha particles (dark blue dots) and ions: B III (yellow solid line), B IV (orange solid line), B V (purple solid line), and B VI (black solid line) ions *versus* temperature. Spectral line corresponds to N VI 4s-4p singlet transition with $\lambda = 17182$ Å. The perturber density is 10^{16} cm^{-3}.

Table 2. Stark full widths (Å) at half intensity maximum of N VI spectral lines due to interactions with B V and B VI ions. The presented lines belong to triplets within one spectral series. The perturber density is 10^{17} cm^{-3}.

Transition	T[K]	WBV	WBVI
N VI 2s-2p	50000.	0.206E-04	0.206E-04
1901.5 A	100000.	0.808E-04	0.824E-04
C= 0.19E+21	300000.	0.574E-03	0.673E-03
	500000.	0.107E-02	0.134E-02
	1000000.	0.185E-02	0.232E-02
	2000000.	0.251E-02	0.328E-02
N VI 2s-3p	50000.	0.581E-05	0.598E-05
161.2 A	100000.	0.165E-04	0.185E-04
C= 0.19E+18	300000.	0.451E-04	0.557E-04
	500000.	0.616E-04	0.788E-04
	1000000.	0.781E-04	0.101E-03
	2000000.	0.923E-04	0.127E-03
N VI 2s-4p	50000.	0.465E-04	0.531E-04
122.4 A	100000.	0.905E-04	0.110E-03
C= 0.48E+17	300000.	0.169E-03	0.220E-03
	500000.	0.169E-03	0.257E-03
	1000000.	0.234E-03	0.326E-03
	2000000.	0.304E-03	0.383E-03

interactions and the largest – for N VI-B VI ion interactions. All shifts increase with temperature and the T-gradient increases with electric charge of the perturbing particle.

The similar dependencies of Stark broadening parameters for N VI 4s-4p singlet transition are given in Fig. 4 and Fig. 5, respectively. The perturber density is 10^{16} cm^{-3}. In the case of Stark width (Fig. 4), the electron width is largest for temperatures up to 1 000 000 K. Even that then it slowly decreases, it stays significant for the rest of the examined temperature interval. As for the previous line, the broadening due to other perturbers increases with their electric charge. Here, the separations between different curves are smaller, they increase with the electric charge, also. Concerning line shift (Fig. 5), all components are negative and increase with temperature. The different curves are well separated from each other. Perturbers with large electric charges are more effective in the case of shift of the considered spectral line. The presented results for all spectral lines in this study could be used for spectroscopic diagnostics of astrophysical objects, laser driven plasmas in proton-boron fusion experiments with nitrogen target, and other high temperature laboratory and industrial plasma environment.

Table 3. Stark shifts (Å) of the intensity maximum of N VI spectral lines due to interactions with electrons, B III and B IV ions. The presented lines belong to triplets within one spectral series. The perturber density is 10^{17} cm^{-3}.

Transition	T[K]	de	dBIII	dBIV
N VI 2s-2p	50000.	-0.518E-04	-0.110E-03	-0.161E-03
1901.5 A	100000.	-0.155E-03	-0.226E-03	-0.337E-03
C= 0.19E+21	300000.	-0.176E-03	-0.522E-03	-0.839E-03
	500000.	-0.165E-03	-0.668E-03	-0.108E-02
	1000000.	-0.155E-03	-0.844E-03	-0.144E-02
	2000000.	-0.140E-03	-0.102E-02	-0.172E-02
N VI 2s-3p	50000.	0.114E-05	0.669E-05	0.993E-05
161.2 A	100000.	0.194E-05	0.119E-04	0.184E-04
C= 0.19E+18	300000.	0.152E-05	0.206E-04	0.341E-04
	500000.	0.157E-05	0.237E-04	0.395E-04
	1000000.	0.114E-05	0.281E-04	0.476E-04
	2000000.	0.892E-06	0.329E-04	0.561E-04
N VI 2s-4p	50000.	0.949E-05	0.325E-04	0.510E-04
122.4 A	100000.	0.908E-05	0.473E-04	0.756E-04
C= 0.48E+17	300000.	0.805E-05	0.651E-04	0.110E-03
	500000.	0.685E-05	0.740E-04	0.127E-03
	1000000.	0.542E-05	0.853E-04	0.143E-03
	2000000.	0.443E-05	0.991E-04	0.166E-03

4. Conclusions

New calculated results for Stark broadening parameters of N VI spectral lines are obtained. Conditions of interest include temperatures and densities corresponding to the white dwarfs and to the laser driven proton-boron plasma for fusion reaction. Stark width dependence *versus* principal quantum number is presented for spectral lines from triplet transitions within one spectral series N VI 2s - np (n = 2 − 4). The result is in accordance with the theory. The role of different perturbers in the Stark broadening of two spectral lines belonging to singlet transitions (N VI 3s-3p and N VI 4s-4p) is investigated. More effective in the broadening and shifting of spectral lines are perturbers with larger electric charge. The shifts are negative, the spectral lines are shifted towards high frequencies (towards blue). Obtained new results for Stark broadening parameters of N VI spectral lines will be included in the Stark-B database (Sahal-Bréchot *et al.* 2015 - https://stark-b.obspm.fr/), part of Virtual Atomic and Molecular Data Center (VAMDC – Dubernet *et al.*, 2010). Additionally, there is a link to Stark-B on the website of Serbian Virtual Observatory (SerVO, http://servo.aob.rs).

The results obtained in this work will be of interest for example for investigation of white dwarfs, stellar subphotospheric layers, laser driven plasma in

Table 4. Stark shifts (Å) of N VI spectral lines due to interactions with B V and B VI ions. The presented lines belong to triplets within one spectral series. The perturber density is 10^{17} cm^{-3}.

Transition	T[K]	dBV	dBVI
N VI 2s-2p	50000.	-0.209E-03	-0.254E-03
1901.5 A	100000.	-0.448E-03	-0.556E-03
C= 0.19E+21	300000.	-0.116E-02	-0.148E-02
	500000.	-0.153E-02	-0.201E-02
	1000000.	-0.209E-02	-0.277E-02
	2000000.	-0.250E-02	-0.333E-02
N VI 2s-3p	50000.	0.0130E-04	0.159E-04
161.2 A	100000.	0.252E-04	0.320E-04
C= 0.19E+18	300000.	0.482E-04	0.635E-04
	500000.	0.576E-04	0.772E-04
	1000000.	0.691E-04	0.921E-04
	2000000.	0.819E-04	0.111E-03
N VI 2s-4p	50000.	0.848E-04	0.681E-04
122.4 A	100000.	0.136E-03	0.106E-03
C= 0.48E+17	300000.	0.214E-03	0.161E-03
	500000.	0.243E-03	0.182E-03
	1000000.	0.288E-03	0.213E-03
	2000000.	0.331E-03	0.247E-03
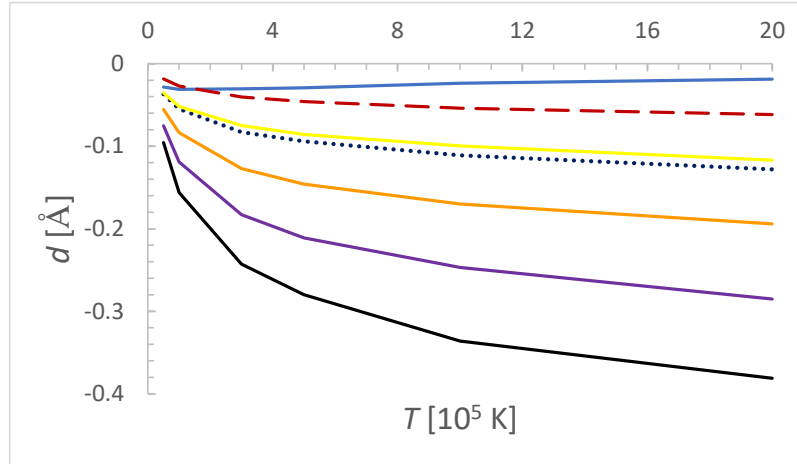
Figure 5. Stark shift due to interactions with electrons (blue solid line), protons (red dashes), alpha particles (dark blue dots) and ions: B III (yellow solid line), B IV (orange solid line), B V (purple solid line), and B VI (black solid line) ions *versus* temperature. Spectral line corresponds to N VI 4s-4p singlet transition with $\lambda = 17182$ Å. The perturber density is 10^{16} cm^{-3}.

proton-boron fusion experiments, laboratory plasmas and other topics in astrophysics and plasma physics.

References

Dimitrijević, M.S., Christova, M.D., Sahal-Bréchot, S.: 2023, to be submitted

Dimitrijević, M. S.; Sahal-Bréchot, S.: 1984, *J. Quant. Spectrosc. Radiat. Transfer*, **31**, 301

Dubernet, M. L.; Boudon, V.; Culhane, J. L.; Dimitrijevic, M. S.; Fazliev, A. Z.; Joblin, C.; Kupka, F.; Leto, G.; Le Sidaner, P.; Loboda, P. A.; Mason, H. E.; Mason, N. J.; Mendoza, C.; Mulas, G.; Millar, T. J.; Nuñez, L. A.; Perevalov, V. I.; Piskunov, N.; Ralchenko, Y.; Rixon, G.; Rothman, L. S.; Roueff, E.; Ryabchikova, T. A.; Ryabtsev, A.; Sahal-Bréchot, S.; Schmitt, B.; Schlemmer, S.; Tennyson, J.; Tyuterev, V. G.; Walton, N. A.; Wakelam, V.; Zeippen, C. J.: 2010, *J. Quant. Spectrosc. Radiat. Transfer*, **111**, 2151

Giuffrida, L.; Belloni, F.; Margarone, D.; Petringa, G.; Milluzzo, G.; Scuderi, V.; Velyhan, A.; Rosinski, M.; Picciotto, A.; Kucharik, M.; Dostal, J.; Dudzak, R.; Krasa, J.; Istokskaia, V.; Catalano, R.; Tudisco, S.; Verona, C.; Jungwirth, K.; Bellutti, P.; Korn, G.; Cirrone, G. A. P.: 2020, *Phys. Rev.E*, **101**, 013204

Istokskaia, V.; Tosca, M.; Giuf frida, L.; Psikal, J.; Grepl, F.; Kantarelou, V.; Stancek, S.; Di Siena, S.; Hadjikyriacou, A.; McIlvenny, A.; Levy, Y.; Huynh, J.; Cimrman, M.; Pleskunov, P.; Nikitin, D.; Choukourov, A.; Belloni, F.; Picciotto, A.; Kar, S.; Borghesi, M.; Lucianetti, A.; Mocek, T.; Margarone, D.: 2023, *Communications Physics*, **6**, 27

Margarone, D.; Picciotto, A.; Velyhan, A.; Krasa, J.; Kucharik, M,; Mangione, A.; Szydlowsky, A.; Malinowska, A.; Bertuccio, G.; Shi, Y.; Crivellari, M.; Ullschmied, J.; Bellutti, P.; Korn, G.: 2015, *Plasma Phys. Control. Fusion*, **57**, 014030

Rauch, T.: 2007, *Astron. Astrophys.*, **470**, 317

Sahal–Bréchot, S.: 1969 a, *Astron. Astrophys.*, **1**, 91

Sahal–Bréchot, S.: 1969 b, *Astron. Astrophys.*, **2**, 322

Sahal–Bréchot, S.: 2021, *Atoms*, **9**, 29

Sahal–Bréchot, S., Dimitrijević, M.S., Ben Nessib, N.: 2014, *Atoms*, **2**, 225

Sahal-Bréchot, S., Dimitrijević, M. S., Moreau, N., Ben Nessib N.: 2015, *Phys. Scr.*, **90**, 054008

Chemi-recombination processes in astrophysical and low-temperature laboratory plasmas: the case of potassium

V.A. Srećković [ID] **and L.M. Ignjatović** [ID]

Institute of Physics Belgrade, University of Belgrade, Pregrevica 118,
11080 Belgrade, Serbia, (E-mail: vlada@ipb.ac.rs)

Abstract. In this manuscript, the chemi-recombination (CR) processes i.e. electron driven collisions are examined. We obtained the rate coefficients for CR processes in potassium collisions for principal quantum numbers $n \geq 6$ and temperatures from 500 K to 5 000 K. The data presented here could help enhance the investigation and modeling of weakly ionized layers in various atmospheres and cosmic objects, including geocosmical ones.
Key words: atomic and molecular data – molecular ions – astrophysical plasma – spectroscopy – plasma diagnostics

1. Introduction

As referred over the recent years the collisional processes are of great interest to the scientists (Iacob et al., 2019; Ignjatović et al., 2019; Mihajlov et al., 2012). The reason for this is that they have an effect on the spectral properties of astrophysical and laboratory plasmas (see papers Tielens, 2013; Beuc et al., 2018a,b; Srećković et al., 2014; Ignjatović et al., 2020). Collisional processes involving various species including alkali atoms, ions, and small molecule ions can have an impact on the ionization level, atom excited-state populations, and optical properties (Mihajlov et al., 2011; Srećković et al., 2017). In low-temperature plasma astrophysics, collisional events are commonly acknowledged as an effective conduit for the creation/destruction of corresponding molecular ions (Iacob et al., 2019; Srećković et al., 2022; Pop et al., 2021; Epée Epée et al., 2022, and references therein).

It should be noted that potassium and its molecules are important in the study of cool brown dwarf atmospheres (see Allard et al., 2007). For instance, Allard et al. (2016) emphasize that for cool brown dwarfs, the wings of the alkali resonance lines—particularly the K I resonance doublet—dominate the opacity in the red optical to near-IR region. The corresponding data could be useful for modeling and investigation of potassium-containing chemical processes in Europa's atmosphere, as well as cometary gas tails and cool stars (see, e.g.

Fegley & Zolotov, 2000). Potassium atoms have been found in exospheres of Mercury and Moon, and also in circumstellar envelopes (see Valiev et al., 2020, and references therein) . Additionally, certain technological applications and laboratory tests involve the use of potassium collisional processes (Beuc et al., 2018b; Albert et al., 2020; Marinković et al., 2017; Srećković et al., 2021).

In this study, we obtained rate coefficients for potassium collisional symmetric chemi-recombination (CR) processes important for modeling planetary atmospheres, laboratory and geocosmic plasma. The collisional data are obtained for a wide range of temperatures 500 K $\leq T \leq$ 5 000 K and principal quantum numbers up to 20.

2. Theoretical remarks

2.1. Chemi-Recombination Processes

In this study, we investigated the electron driven collisional processes i.e. symmetric CR processes:

$$e + A_2^+ \Longrightarrow A^*(n) + A, \tag{1a}$$

$$e + A + A^+ \Longrightarrow A^*(n) + A, \tag{1b}$$
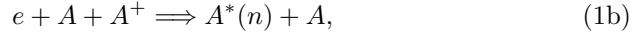
Here A denote potassium atoms in the ground states, $A^*(n)$ are corresponding Rydberg atoms, A_2^+ are the molecular ions in the ground electronic states. General symmetric CR processes (1) consist of two channels "a" (1a) and "b" (1a).

The calculations were carried out using the so-called dipole resonant mechanism (DRM), which is how the collisional reactions (1) were handled. The study in Mihajlov et al. (2003); Mihajlov et al. (2012) provides a complete and extensive overview. We offer a brief summary of the method together with the underlying theory in this section.

The DRM is used to calculate the rate coefficients for the principal quantum number $6 \leq n \leq 20$ with temperatures ranging from 500 K to 5000 K. Section 3 presents and discusses the data i.e. findings in depth.

2.2. Rate Coefficients

Rate coefficients $K_r^{(a,b)}(n,T)$ for the both channels "a" (1a) and "b" (1b) of CR processes (1) can be presented by

$$K_r^{(a,b)}(n,T) = Q_n(T) \cdot \int_{R_{min}}^{R_n} \exp\left[\frac{U_{12}(R)}{kT} - \frac{U_1(R)}{kT}\right] \cdot X^{(a,b)}(R,T) \cdot \frac{R^4 dR}{a_0^5} \tag{2}$$

using the theory from the papers (Mihajlov et al., 2003, 2011). $U_{12}(R) = U_2(R) - U_1(R)$, $U_1(R)$ and $U_2(R)$ are the ground and first excited electronic states of the system i.e. molecular ion, and R is the internuclear distance. Here R_n can
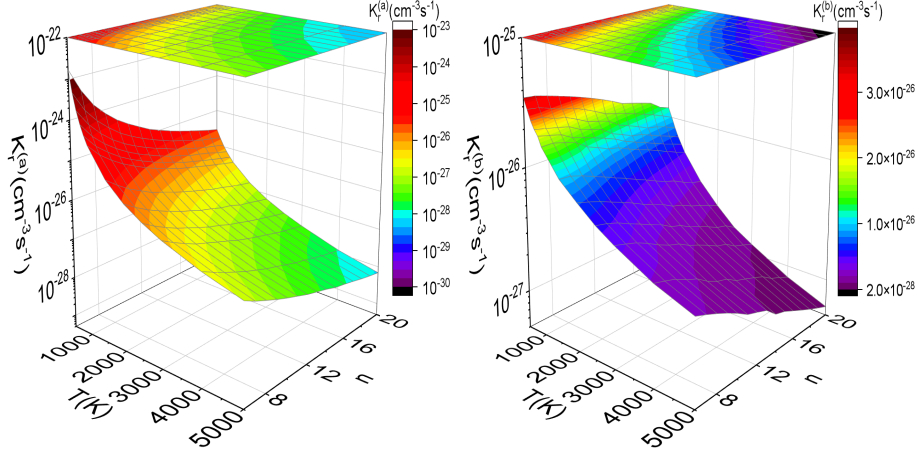
Figure 1. Left: Calculated values for rate coefficient $K_r^{(a)}$ (cm^3 s^{-1}) as a function of n and T for potassium case (A=K in Eq(1)); Right: Calculated values for rate coefficient $K_r^{(b)}$ (cm^3 s^{-1}) as a function of n and T for potassium case (A=K in Eq(1)).

be obtained by the equation $U_{12}(R) = I_n$ as the largest root, while R_{min} can be calculated as in Mihajlov et al. (2003). In (2) the needed quantity $Q_n(T)$ can be obtained by expression

$$Q_n(T) = \frac{(2\pi)^{5/2}}{3^{3/2}} \frac{(\hbar e a_0)^2}{(mkT)^{3/2}} n^{-3} \exp\left(\frac{I_n}{kT}\right), \tag{3}$$

where I_n is the excited atom ionization energy. $X^{(a)}$ parameter can be presented by:

$$X^{(a)}(R,T) = \begin{cases} \gamma\left(\frac{3}{2}; -\frac{U_1(R)}{kT}\right) / \Gamma\left(\frac{3}{2}\right) & U_1 < 0 \\ 0, & U_1 \geq 0 \end{cases} \tag{4}$$

Here γ and Γ are incomplete gamma functions. $X^{(b)}(R,T) = 1 - X^{(a)}(R,T)$. The total CR rate coefficient $K_r^{(ab)}(n,T)$ for the processes (2) is defined as

$$K_r^{(ab)}(n,T) = K_r^{(a)}(n,T) + K_r^{(b)}(n,T). \tag{5}$$

2.3. The Data

The rate coefficients are used as input parameters in many atmospheric models and spectrum synthesis software (Hauschildt & Baron, 2010). In order to be appropriately incorporated in codes and atomic and molecular (A&M) databases for modeling planetary atmospheres, early Universe chemistry, geocosmic plasma,
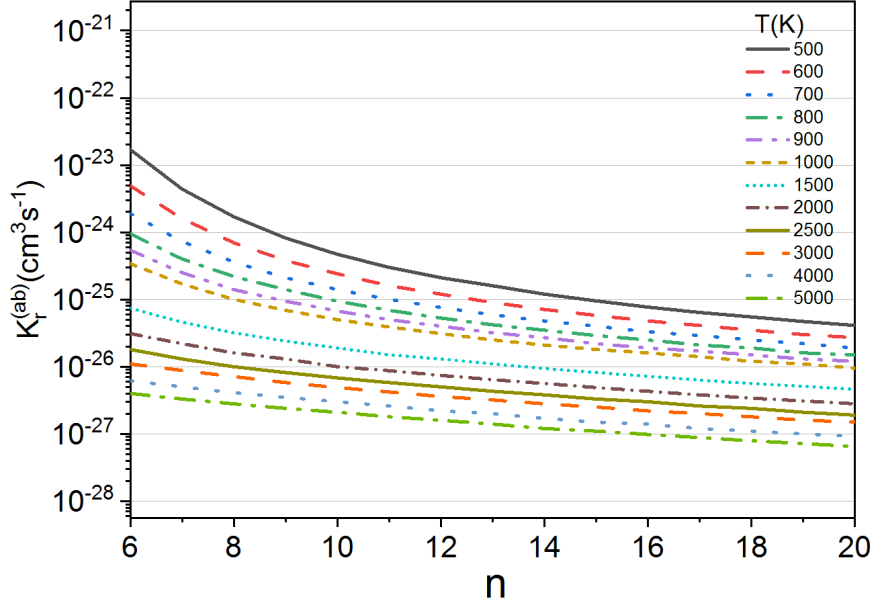
Figure 2. Calculated values for rate coefficient $K_r^{(ab)}$ (cm^3 s^{-1}) as a function of n and T for lithium case (A=K in Eq(1)).

etc., it is needed to establish good quality data (Albert et al., 2020; Marinković et al., 2017; Djuissi et al., 2020).

3. Results

The data i.e. the partial recombination rate coefficients $K_r^{(a,b)}(n, T)$, and total recombination rate coefficients $K_r^{(ab)}(n, T)$ obtained by Eqs. (2) and (5), for potassium are presented in figures 1 and 2.

The figs. 1a,b presents a 3D plot which covers the region $6 \leq n \leq 20$ and 500 K $\leq T \leq 5000$ K. One can see that the probability for "a" channel of dissociative recombination is higher for lower n and lower temperature. Similar behavior is for the case of channel "b". Therefore, it appears that in the examined environment, these collisions form one of the primary processes for the production of Rydberg atoms.

Our future objective is to obtain and provide a straightforward approximative formula for the rate coefficients in order to facilitate the use of calculated data. It would also be extremely beneficial to include data in an A&M database. We intend to add these datasets to VAMDC (vamdc.eu), a searchable A&M data

provider, by extending one of the VAMDC nodes hosted by Serbian Virtual Observatory at servo.aob.rs (Jevremović et al., 2020).

4. Summary

For the electron-impact processes involving the potassium atoms, ions, molecular cations, we have calculated the rate coefficients for the chemi-recombination in domains of principal quantum numbers $n \geq 6$ and temperatures from 500 K to 5 000 K in this paper.

The numerical results demonstrate that the processes under investigation could have influence on the atom excited-state populations, and consequently on the optical characteristics in the weakly ionized layers of atmospheres of different stars which contain potassium. Additionally, the provided collisional data could be useful in interstellar chemistry as well as in geo-cosmical and cold plasma investigation.

References

Albert, D., Antony, B. K., Ba, Y. A., et al., A Decade with VAMDC: Results and Ambitions. 2020, *Atoms*, **8**, 76, DOI: 10.3390/atoms8040076

Allard, F., Allard, N. F., Homeier, D., et al., K-H_2 quasi-molecular absorption detected in the T-dwarf Indi Ba. 2007, *Astron. Astrophys.*, **474**, L21, DOI: 10.1051/0004-6361:20078362

Allard, N. F., Spiegelman, F., & Kielkopf, J. F., K-H_2 line shapes for the spectra of cool brown dwarfs. 2016, *Astron. Astrophys.*, **589**, A21, DOI: 10.1051/0004-6361/201628270

Beuc, R., Movre, M., & Pichler, G., High Temperature Optical Spectra of Diatomic Molecules at Local Thermodynamic Equilibrium. 2018a, *Atoms*, **6**, 67, DOI: 10.3390/atoms6040067

Beuc, R., Peach, G., Movre, M., & Horvati, B., Lithium, sodium and potassium resonance lines pressure broadened by helium atoms. 2018b, *Astron. Astrophys. Trans.*, **3**, 315

Djuissi, E., Bogdan, R., Abdoulanziz, A., et al., Electron driven reactive processes involving H+2 and HD+ molecular cations in the Early Universe. 2020, *Rom. Astron. J.*, **30**, 101, DOI: 10.48550/arXiv.2203.01239

Epée Epée, M. D., Motapon, O., Pop, N., et al., Dissociative recombination and rotational transitions of D^+_2 in collisions with slow electrons. 2022, *Mon. Not. R. Astron. Soc.*, **512**, 424, DOI: 10.1093/mnras/stac501

Fegley, B. & Zolotov, M. Y., Chemistry of Sodium, Potassium, and Chlorine in Volcanic Gases on Io. 2000, *Icarus*, **148**, 193, DOI: 10.1006/icar.2000.6490

Hauschildt, P. H. & Baron, E., A 3D radiative transfer framework. VI. PHOENIX/3D example applications. 2010, *Astron. Astrophys.*, **509**, A36, DOI: 10.1051/0004-6361/200913064

Iacob, F., Pop, N., Mezei, J. Z., et al., Recombination and excitation of molecular cations with electrons: Application to, H^+_2 BeD$^+$ and BeT$^+$. 2019, in American Institute of Physics Conference Series, Vol. **2071**, *Tim 18 Physics Conference*, 020007

Ignjatović, L. M., Srećković, V. A., & Dimitrijević, M. S., The collisional atomic processes of Rydberg alkali atoms in geo-cosmical plasmas. 2019, *Mon. Not. R. Astron. Soc.*, **483**, 4202, DOI: 10.1093/mnras/sty3294

Ignjatović, L. M., Srećković, V. A., & Dimitrijević, M. S., Photoionization of the alkali molecular ions in geo-cosmical plasmas. 2020, *Contrib. Astron. Obs. Skaln. Pleso*, **50**, 187, DOI: 10.31577/caosp.2020.50.1.187

Jevremović, D., Srećković, V. A., Marinković, B. P., & Vujčić, V., Databases for collisional and radiative processes in small molecules needed for spectroscopy use in astrophysics. 2020, *Contrib. Astron. Obs. Skaln. Pleso*, **50**, 44, DOI: 10.31577/caosp.2020.50.1.44

Marinković, B. P., Jevremović, D., Srećković, V. A., et al., BEAMDB and MolD - databases for atomic and molecular collisional and radiative processes: Belgrade nodes of VAMDC. 2017, *Eur. Phys. J. D*, **71**, 158, DOI: 10.1140/epjd/e2017-70814-6

Mihajlov, A., Srećković, V., Ignjatović, L. M., & Klyucharev, A., The Chemi-Ionization Processes in Slow Collisions of Rydberg Atoms with Ground State Atoms: Mechanism and Applications. 2012, *J. Clust. Sci.*, **23**, 47, DOI: 10.1007/s10876-011-0438-7

Mihajlov, A. A., Ignjatović, L. M., Dimitrijević, M. S., & Djurić, Z., Symmetrical Chemi-Ionization and Chemi-Recombination Processes in Low-Temperature Layers of Helium-rich DB White Dwarf Atmospheres. 2003, *Astrophys. J., Suppl. Ser.*, **147**, 369, DOI: 10.1086/375621

Mihajlov, A. A., Ignjatović, L. M., Srećković, V. A., & Dimitrijević, M. S., Chemiionization in Solar Photosphere: Influence on the Hydrogen Atom Excited States Population. 2011, *Astrophys. J., Suppl. Ser.*, **193**, 2, DOI: 10.1088/0067-0049/193/1/2

Pop, N., Iacob, F., Niyonzima, S., et al., Reactive collisions between electrons and BeT+: Complete set of thermal rate coefficients up to 5000 K. 2021, *Atomic Data and Nuclear Data Tables*, **139**, 101414, DOI: 10.1016/j.adt.2021.101414

Srećković, V., Ignjatović, L., Jevremović, D., Vujčić, V., & Dimitrijević, M., Radiative and Collisional Molecular Data and Virtual Laboratory Astrophysics. 2017, *Atoms*, **5**, 31, DOI: 10.3390/atoms5030031

Srećković, V. A., Ignjatović, L. M., & Dimitrijević, M. S., Photodestruction of Diatomic Molecular Ions: Laboratory and Astrophysical Application. 2021, *Molecules*, **26**, 151, DOI: 10.3390/molecules26010151

Srećković, V. A., Ignjatović, L. M., & Dimitrijević, M. S., Electron-impact processes involving small molecular ions relevant for the astrochemistry. 2022, *Contrib. Astron. Obs. Skaln. Pleso*, **52**, 90, DOI: 10.31577/caosp.2022.52.3.90

Srećković, V. A., Mihajlov, A. A., Ignjatović, L. M., & Dimitrijević, M. S., Ion-atom radiative processes in the solar atmosphere: quiet Sun and sunspots. 2014, *Adv. Space Res.*, **54**, 1264, DOI: 10.1016/j.asr.2013.11.017

Tielens, A. G. G. M., The molecular universe. 2013, *Rev. Mod. Phys.*, **85**, 1021, DOI: 10.1103/RevModPhys.85.1021

Valiev, R. R., Berezhnoy, A. A., Gritsenko, I. S., et al., Photolysis of diatomic molecules as a source of atoms in planetary exospheres. 2020, *Astron. Astrophys.*, **633**, A39, DOI: 10.1051/0004-6361/201936230

The development of simplified approach in describing of the ionic field to emitter interaction in stellar and laboratory plasmas

N.M. Sakan[1] , **Z. Simić**[2] , **V.A. Srećković**[1] **and M. Dechev**[3]

[1] *University of Belgrade, Institute of Physics Belgrade, PO Box 57,*
(E-mail: nsakan@ipb.ac.rs)

[2] *Astronomical Observatory, Volgina 7, 11060 Belgrade, Serbia*

[3] *Institute of Astronomy and National Astronomical Observatory, Bulgarian*
Academy of Sciences, 72, Tsarigradsko chaussee Blvd. Sofia, Bulgaria

Abstract. Dense plasma of moderate and strong non-ideality is of growing interest in physics related to stellar and laboratory plasma. Up until now the optical parameter of hydrogen plasma of mid and moderately high nonideality parameter could be described successfully, thus enabling the modeling of optical properties. But the model potential used does not include the correct plasma interaction in it's basic form. The influence of dense packing ionic structure onto the form of potential is investigated in this paper. The presented results are a step towards the more precise description of ionic field influence onto the plasma microfield when the dynamic of the ionic structure is neglected and the dense packing assumed.

Key words: optical properties – dense plasma – bond states – pseudopotential – modelling

1. Introduction

Nowadays, modeling of the optical properties of dense plasma is of growing interest in both astrophysical as well as laboratory plasma (Chabrier et al., 2002; Bardet et al., 2003; Vitel, 2004; Sultana & Schlickeiser, 2018; Chabrier et al., 2006). Since the known models of plasma emitter interaction do not describe this case well enough and precise simulation models are extremely computing time consuming the need for this research is required (see e.g. Agranat et al., 2007; Mazevet et al., 2005).

In the dense plasma the inter-particle Coulomb interaction becomes dominant over the thermal kinetic energy (Fortov et al., 2006). In such conditions a coupled system of particles behaves partially like a crystal. The simplified version, for hydrogen case, of non-ideality parameter Γ is given by

$$\Gamma = \frac{E_p}{E_k} = \frac{e^2}{kTr_{WS}} \sim e^2 N_e^{1/3}\beta, \qquad \beta = 1/kT, \qquad r_{WS} = \left(\frac{3}{4\pi N_e}\right)^{1/3}. \quad (1)$$

The simplified screening model of Debye is used to investigate screening influence, although it is not ideal for dense plasma, $r_D = \left(\frac{\varepsilon_0 k_B T_e}{n_e q_e^2}\right)^{1/2}$.

Models used for describing dense plasma

The usage of Cut-off Coulomb model potential was applied in the fully quantum mechanical solution for determining the optical properties of dense hydrogen plasma. Up until now the results were presented and used for instance see Dimitrijević et al. (2018); Srećković et al. (2018); Mihajlov et al. (2015, 2011); Ignjatović et al. (2017); Ignjatović et al. (2009). Both Coulomb as well as cut-off Coulomb potential is presented in Eq. 2,

$$U(r) = -\frac{e^2}{r}, \qquad U_c(r) = \begin{cases} -\dfrac{e^2}{r} + \dfrac{e^2}{r_c}, & : \ 0 < r \le r_c, \\[2mm] 0, & : \ r_c < r < \infty \end{cases} \qquad (2)$$

The plasma-emitter interaction is roughly modeled by the cut-off radius r_c. The close vicinity of the emitter is described correctly by the shifted Coulomb potential in the vicinity of the emitter as well as constant plasma potential in the far field $r \gg r_c$.

2. Results and discussion

Since the strongly coupled Coulomb systems have small thermal mobility, the idea of was to use a dense packing of spheres to describe an influence of ionic field. The densest packing of the spheres is applied (see John Horton Conway, 1998). The calculations have been carried out to average a potential seen by the central particle of dense packing in accordance with the algorithm of integration on the sphere surface presented in Lebedev & Laikov (1999).

As first test a behavior of enlarging a number of charged ions layers is analyzed and presented in Fig. 1, in case of expected plasma parameters and then in model case of non-physical values of plasma density parameters and screening values (Fig. 2).

The influence of charged particle density as well as screening influence is shown in Fig. 3 and Fig. 4. It is expected to yield a semi-empirical form of describing plasma influence onto emitter potential and develop more precise plasma-emitter describing.

In order to describe the collective influence onto the emitter the ratio of the yielded potential and the Coulomb one is presented. It could be seen, from Fig. 1,
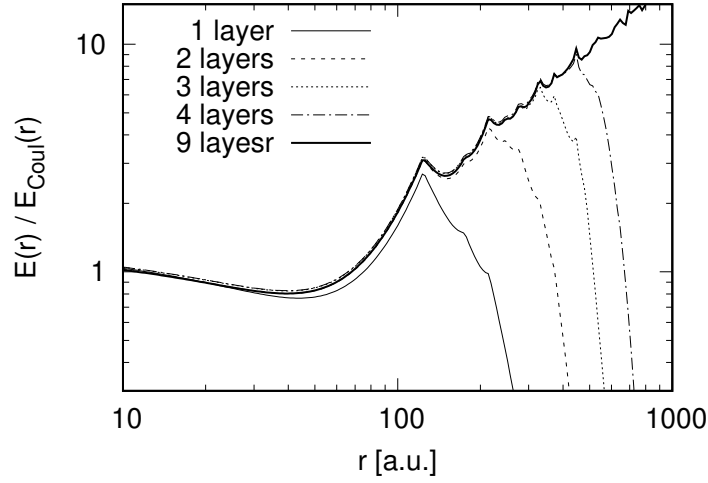
Figure 1. Investigation of the effect of number of layers of charged particles in realistic case, $N_e = 10^{19}$ cm^{-3}, $T = 10$ kK giving estimated values of $r_D = 54.4\,a.u.$ and $r_{WS} = 41.2\,a.u..$

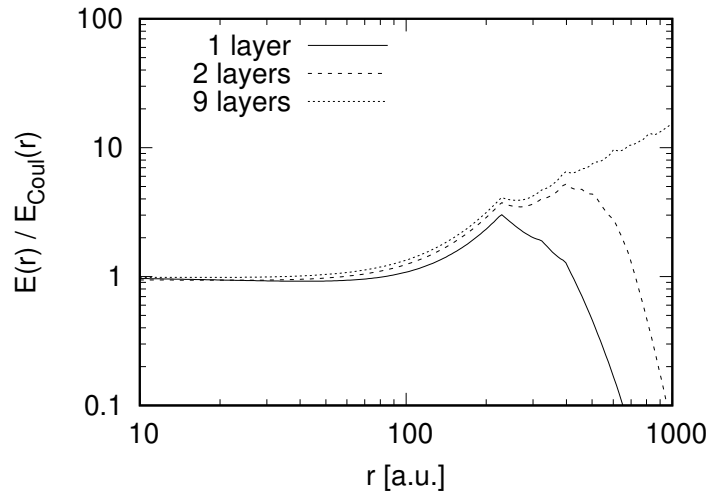**Figure 2.** Number of layers effect on modeled case $r_D = 100\,a.u.$ and $r_{WS} = 100\,a.u..$

and Fig. 2, that the enlargement of the charged particle layers lead to linear enlargement of the collective potential influence, the larger the layer count, the larger linear part is. So it is expected that in an ideal infinite case the linear enlargement of the collective potential could be a good candidate for

$r_D = 100$ a.u.
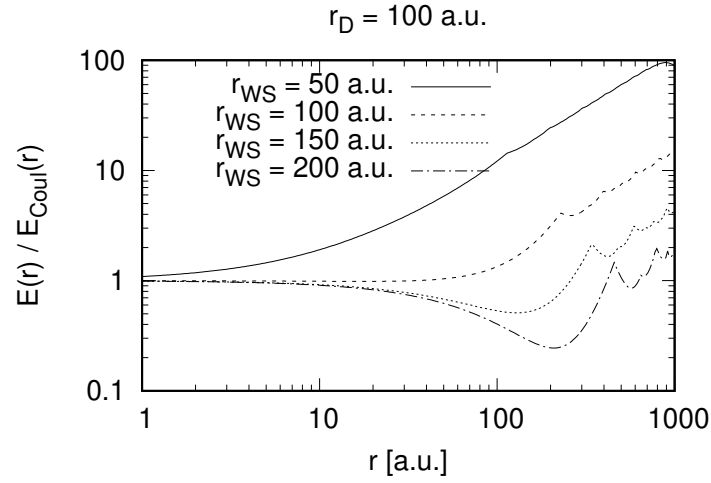
Figure 3. A modeling an effect of charged particle density variation, case of 9 layers.

$r_{WS} = 100$ a.u.
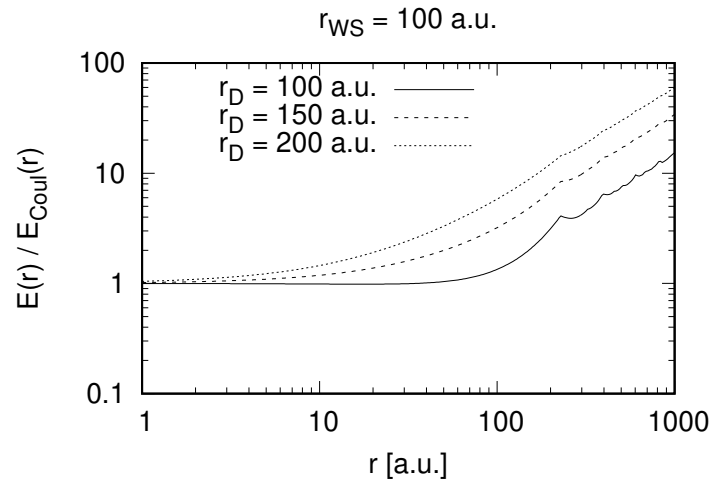
Figure 4. A modeling an effect of screening Debye-like parameter variation, case of 9 layers.

more precise description of the plasma influence onto the emitter. The inter-ionic distance influence is shown in Fig. 3, it is obvious that smaller inter-ionic distance is the faster plasma influence starts to be important, as expected. In Fig. 4 the screening influence is shown. It is expected that the plasma influence

could be modeled with some form of analytical or semi-analytical form of pseudo-potential. This enables a more acceptable mechanism of broadening of the bond levels.

3. Conclusions

The simplification of plasma-emitter influence is needed, since the detailed approach with molecular dynamic code coupled with quantum mechanical solver is computing power intense method. The presented results are a step towards the more precise description of ionic field influence onto the plasma microfield when the dynamic of the ionic structure is neglected and the dense packing assumed. Although this approach is not ideal it could lead to a model both satisfactory in precision as well as with numerical simplicity.

The results that were obtained may be relevant to some astrophysical plasmas, such as the plasma of the solar atmosphere's inner layers and the plasmas of some other star atmospheres (such as those of some DA and DB white dwarfs).

References

Agranat, M. B., Andreev, N. E., Ashitkov, S. I., et al., Determination of the transport and optical properties of a nonideal solid-density plasma produced by femtosecond laser pulses. 2007, *JETP Lett.*, **85**, 271, DOI: 10.1134/S0021364007060021

Bardet, J. P., Valognes, J. C., & Vitel, Y., Comparative study on Stark broadenings of neutral He(I) spectral lineshapes in dense cold plasmas. 2003, *J. Quant. Spectrosc. Radiat. Transf.*, **76**, 45, DOI: 10.1016/S0022-4073(02)00045-6

Chabrier, G., Douchin, F., & Potekhin, A. Y., Dense astrophysical plasmas. 2002, *J. Condens. Matter Phys.*, **14**, 9133, DOI: 10.1088/0953-8984/14/40/307

Chabrier, G., Saumon, D., & Potekhin, A. Y., Dense plasmas in astrophysics: from giant planets to neutron stars. 2006, *J. Phys. A*, **39**, 4411, DOI: 10.1088/0305-4470/39/17/S16

Dimitrijević, M. S., Srećković, V. A., Sakan, N. M., Bezuglov, N. N., & Klyucharev, A. N., Free-Free Absorption in Solar Atmosphere. 2018, *Geomagn. Aeron.*, **58**, 1067, DOI: 10.1134/S0016793218080054

Fortov, V., Iakubov, I., & Khrapak, A. 2006, *Physics of Strongly Coupled Plasma*, International Series of Monographs on Physics (OUP Oxford)

Ignjatović, L. M., Mihajlov, A. A., Sakan, N. M., Dimitrijević, M. S., & Metropoulos, A., The total and relative contribution of the relevant absorption processes to the opacity of DB white dwarf atmospheres in the UV and VUV regions. 2009, *Mon. Not. R. Astron. Soc.*, **396**, 2201, DOI: 10.1111/j.1365-2966.2009.14870.x

Ignjatović, L., Srećković, V., & Dimitrijević, M., The Screening Characteristics of the Dense Astrophysical Plasmas: The Three-Component Systems. 2017, *Atoms*, **5**, 42, DOI: 10.3390/atoms5040042

John Horton Conway, N. J. A. S. 1998, *Sphere Packings, Lattices and Groups, 3rd edn.*, Grundlehren der mathematischen Wissenschaften v. 290 (Springer)

Lebedev, V. I. & Laikov, D. N., A Quadrature Formula for the Sphere of the 131st Algebraic Order of Accuracy. 1999, *Doklady Mathematics*, **59**, 477

Mazevet, S., Desjarlais, M. P., Collins, L. A., Kress, J. D., & Magee, N. H., Simulations of the optical properties of warm dense aluminum. 2005, *Phys. Rev. E*, **71**, 016409, DOI: 10.1103/PhysRevE.71.016409

Mihajlov, A. A., Sakan, N. M., Srećković, V. A., & Vitel, Y., Modeling of continuous absorption of electromagnetic radiation in dense partially ionized plasmas. 2011, *J. Phys. A*, **44**, 095502, DOI: 10.1088/1751-8113/44/9/095502

Mihajlov, A. A., Srećković, V. A., & Sakan, N. M., Inverse Bremsstrahlung in Astrophysical Plasmas: The Absorption Coefficients and Gaunt Factors. 2015, *J. Astrophys. Astron.*, **36**, 0, DOI: 10.1007/s12036-015-9350-0

Srećković, V. A., Sakan, N., Šulić, D., et al., Free–free absorption coefficients and Gaunt factors for dense hydrogen-like stellar plasma. 2018, *Mon. Not. R. Astron. Soc.*, **475**, 1131, DOI: 10.1093/mnras/stx3237

Sultana, S. & Schlickeiser, R., Fully nonlinear heavy ion-acoustic solitary waves in astrophysical degenerate relativistic quantum plasmas. 2018, *Astrophys. Space Sci.*, **363**, 103, DOI: 10.1007/s10509-018-3317-y

Vitel, Y., Spectra of dense pure hydrogen plasma in Balmer area. 2004, *J. Quant. Spectrosc. Radiat. Transf.*, **83**, 387, DOI: 10.1016/S0022-4073(02)00380-1

The radiative processes involving some non-symmetric systems relevant for astrochemistry: data needed for modeling

V.A. Srećković[1] , **L.M. Ignjatović**[1] , **S. Tošić**[1] **and V. Vujčić**[2]

[1] *Institute of Physics Belgrade, University of Belgrade, Pregrevica 118,*
11080 Belgrade, Serbia, (E-mail: vlada@ipb.ac.rs)

[2] *Astronomical Observatory, Volgina 7, 11060 Belgrade, Serbia,*
(E-mail: veljko@aob.rs)

Abstract. The photo-association, charge-exchange, and photo-dissociation absorption processes in non-symmetric systems including hydrogen and calcium atoms, ions, molecules, and molecular-ions are investigated in this paper. For the current computation, we have calculated the data for molecules and molecular state characterizations. We obtained the cross-sections and corresponding spectral absorption rate coefficients - as the functions of wavelengths, and temperatures. The collected data has the potential for an impact on vast additional applications, such as modeling of laboratory plasmas and numerous astrophysical objects.

Key words: atomic and molecular data – astrophysical plasma – optical characteristics – absorption

1. Introduction

Due to the complexity of electron dynamics in molecules and the sophistication of most experimental setups used in this context, atomic and molecular (A&M) data and databases are an indispensable ingredient in new experimental approaches and accurate theoretical support (Hauschildt & Baron, 2010; Albert et al., 2020; Epée Epée et al., 2022; Srećković et al., 2021). Furthermore, one can observe the present importance of investigating the optical properties of numerous small molecules as well as the associated A&M data (Sansone et al., 2010; Djuissi et al., 2020; Iacob et al., 2019; Srećković et al., 2022; Mihajlov et al., 2011). Precision spectroscopy of molecular ions has applications in astrochemistry, quantum state controlled chemical reactions, and measurements of fundamental constants (Vázquez-Carson et al., 2022; Iacob, 2020; Brown et al., 2016; Ignjatović et al., 2020; Pop et al., 2021). Such precise spectroscopy measurements open the path for search for astrophysical presence of those small molecules like CaH^+, etc. (Khanyile et al., 2013).

Our aim is to obtain spectroscopic information, i.e., data, about such systems involving hydrogen and calcium atoms, ions, molecules and molecular-ions. For example, CaH$^+$ molecular ions are of great scientific interest due to possible applications to astrophysics and fundamental physics, similar to other alkaline earth hydride ions (Monteiro et al., 1988; Dutta et al., 2006; Kimura et al., 2011). Interstellar medium (ISM) and comets are believed to contain these hydrides. For such systems, we calculated spectral absorption rate coefficients and average cross-sections. These parameters cover a wide range of temperatures and EUV and UV region of wavelengths.

The outcomes, i.e. the obtained datasets, may be applied to important tasks, such as modelling or in PLEIADES SOLEIL synchrotron (Giuliani et al., 2014). Also, the collected data have the potential to have a high impact and vast applications, such as lasers, ultra-short lasers and laser physics, modeling of laboratory plasmas and numerous astrophysical objects (Canuto et al., 1993; Barklem & O'Mara, 1998; Brown et al., 2016). Also, for quality modelling accurate data is needed, which makes the research relevant and up to date.

Brief theory and calculated quantities are presented in section 2; section 3 describes and discusses the results. Finally, the section 4 is devoted to conclusions and future directions of research.

2. Theory

2.1. Processes

In this study, radiative processes are investigated in terms of their impact on the optical properties of weakly ionized astrophysical and laboratory plasmas. In particular, in the case of strongly non-symmetric systems, the processes of photo-association i.e. free-bound (fb), absorption charge-exchange i.e. free-free (ff) and photo-dissociation i.e. bound-free (bf) are investigated.

We shall investigate the processes that can be described as non-symmetric

$$\varepsilon_\lambda + AB^+ \Rightarrow A^+ + B, \tag{1}$$

$$\varepsilon_\lambda + A + B^+ \Rightarrow A^+ + B. \tag{2}$$

$$\varepsilon_\lambda + A + B^+ \Rightarrow (AB^+)^* \tag{3}$$
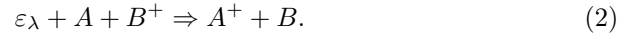
Here, B represents a calcium atom (Ca), and A=H. Molecular-ion in the ground electronic state HCa$^+$ is represented by the symbol AB^+, and molecular-ion in the first excited electronic state is represented by the symbol $(AB^+)^*$.

2.2. The spectral characteristics

As stated in Srećković et al. (2014), the free-free spectral rate coefficients $K_{(ff)}(\lambda, T)$ which described the processes (2) can be presented by relation:

$$K_{(ff)}(\lambda, T) = \int\limits_0^\infty \left(\frac{2E}{\mu} \right)^{\frac{1}{2}} \sigma_{(ff)}(\lambda, E) f(E) dE \qquad (4)$$

Here quantity $\sigma_{(ff)}(\lambda, E)$ denotes the cross section and $f(E)$ is the Maxwell energy distribution function

$$f(E) = \frac{2}{\pi^{1/2}(kT)^{3/2}} e^{-\frac{E}{k_B T}} E^{1/2} dE, \qquad (5)$$

where μ is the reduced mass of the considered system.

The free-free absorption cross section $\sigma_{(ff)}(\lambda, E)$ for radiative charge exchange processes can be represented as

$$\sigma_{(ff)}(\lambda, E) = \frac{g_1 g_2}{g_{1'} g_{2'}} \frac{8\pi^4 \hbar^2 \varepsilon_\lambda}{3c2\mu E} \cdot$$
$$\left[(J+1) \cdot |D_{J,E;J+1,E'_{imp}}|^2 + J \cdot |D_{J,E;J-1,E'_{imp}}|^2 \right], \qquad (6)$$

where $D_{J,E;J\pm1,E'_{imp}} = < in, J, E; R|D_{in,fin}(R)|fin, J \pm 1, E' >$. $D_{in;fin}(R)$ $= < in; R|\mathbf{D}(R)|fin; R >$ is the electronic dipole matrix element and $\mathbf{D}$ is the operator of the dipole moment of the investigated system. Detailed theory and definitions of all quantities can be found in Srećković et al. (2014).

The rate coefficient $K_{(fb)}(\lambda, T)$ for the free-bound processes (3) can be presented as in Ignjatović et al. (2014) by:

$$K_{(fb)}(\lambda, T) = \frac{(2\pi)^3}{3\hbar\lambda} \left(\frac{2\pi\hbar^2}{\mu kT} \right)^{3/2} \sum_{J',v'} \left(\frac{\mu}{2E} \right)^{1/2} e^{-\frac{E}{kT}} \cdot S_{J',v'}, \qquad (7)$$

where

$$S_{J',v'} = \frac{g_{12}}{g_1 g_2} \cdot [J'|D_{J'-1,E;J',v'}|^2 + (J'+1)|D_{J'+1,E;J',v'}|^2]. \qquad (8)$$

Here $D_{J'\pm1,E;J',v'} = < in, J' \pm 1, E; R|D_{in,fin}(R)|fin, J', v' >$. Detailed definitions of all quantities and theory can be found in papers Srećković et al. (2014); Ignjatović et al. (2014).

The (bf) i.e. photo-dissociation spectral rate coefficient for processes (1) can be presented by

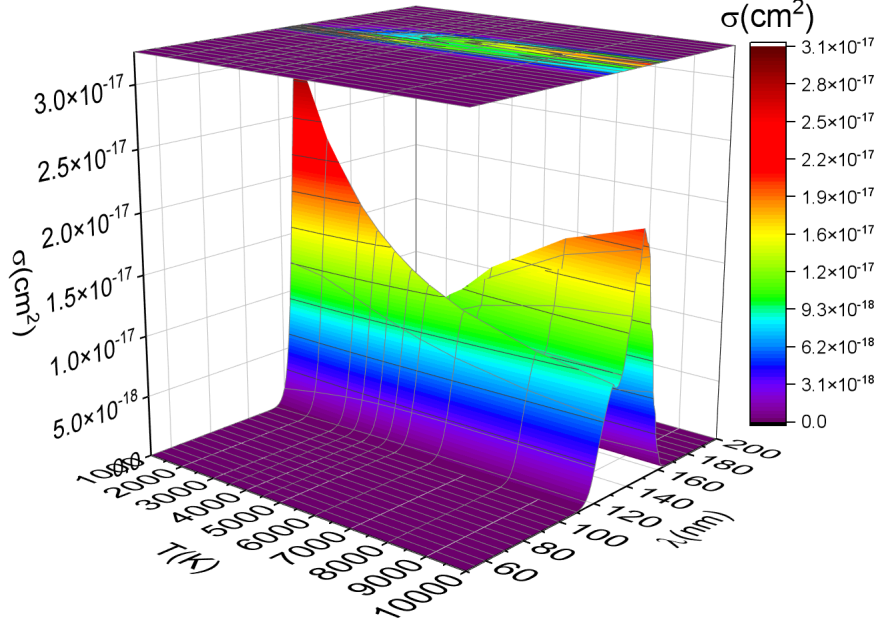$$K_{(bf)}(\lambda, T) = X^{-1}(T) \cdot \sigma_{(bf)}(\lambda, T). \qquad (9)$$

Figure 1. 3D plot of the mean thermal photo-dissociation cross- section for molecular-ion CaH+.

Here the X factor is given by

$$X(T) = \left(\frac{\mu k T}{2\pi\hbar^2}\right)^{\frac{3}{2}} \frac{g_1 g_2}{g_{12}} \cdot \frac{1}{\sum\limits_{J,v}(2J+1)e^{\frac{E_{dis}-E_{J,v}}{kT}}}. \tag{10}$$

The average thermal photo-dissociation cross section $\sigma_{(bf)}(\lambda, T)$ is:

$$\sigma_{(bf)}(\lambda, T) = \frac{\sum\limits_{J,v}(2J+1)e^{\frac{-E_{J,v}}{kT}} \cdot \sigma_{J,v}^{(bf)}(\lambda)}{\sum\limits_{J,v}(2J+1)e^{\frac{-E_{J,v}}{kT}}}. \tag{11}$$

The partial cross-sections $\sigma_{J,v}^{(bf)}(\lambda)$ can be presented with the expression:

$$\sigma_{J,v}^{(bf)}(\lambda) = \frac{8\pi^3}{3\lambda}\left[\frac{J+1}{2J+1}|D_{J,v;J+1,E'_{imp}}|^2 + \frac{J}{2J+1}|D_{J,v;J-1,E'_{imp}}|^2\right]. \tag{12}$$

All needed quantities and relations are given in detail in e.g. papers of Srećković et al. (2014); Srećković et al. (2021); Ignjatović et al. (2014).

3. Results and Discussion

The dataset i.e. results have been provided in tabulated form by Tabs. 1 - 3. In addition, the results are also illustrated in this section by Figure 1. The data cover the region 50 nm $\leq \lambda \leq$ 200 nm and 1000 K $\leq T \leq$ 10000 K. Data could be beneficial for laboratory plasma diagnostics, astrophysics and industrial plasma modeling.

Table 1. The spectral absorption coefficient $K_{(bf)}(\lambda, T)$ [cm^5] which characterizes absorption processes (1) for calcium hydride molecular ion as a function of wavelength λ [nm] and temperature T [K].

lambda/T	1000	2000	3000	4000	6000	8000	10000
50	1.16E-36	1.40E-41	6.05E-43	1.44E-43	3.43E-44	1.57E-44	9.26E-45
60	2.29E-36	6.82E-41	2.52E-42	4.91E-43	9.14E-44	3.68E-44	2.02E-44
70	2.40E-36	7.81E-41	3.15E-42	6.87E-43	1.52E-43	6.76E-44	3.94E-44
80	4.62E-36	1.60E-40	7.97E-42	1.97E-42	4.95E-43	2.35E-43	1.43E-43
90	9.37E-36	3.35E-40	1.73E-41	4.66E-42	1.31E-42	6.56E-43	4.10E-43
100	1.73E-35	4.02E-40	2.47E-41	7.67E-42	2.45E-42	1.29E-42	8.30E-43
110	2.40E-34	7.96E-39	4.49E-40	1.25E-40	3.57E-41	1.78E-41	1.11E-41
120	4.12E-31	4.04E-36	1.05E-37	1.79E-38	3.07E-39	1.21E-39	6.62E-40
130	8.04E-30	4.61E-35	7.87E-37	1.01E-37	1.24E-38	4.13E-39	2.04E-39
140	1.05E-32	3.32E-36	2.17E-37	5.40E-38	1.24E-38	5.45E-39	3.14E-39
150	4.71E-35	4.50E-37	8.59E-38	3.46E-38	1.22E-38	6.44E-39	4.10E-39
160	4.13E-38	6.29E-39	2.67E-39	1.54E-39	7.51E-40	4.62E-40	3.20E-40
165	5.80E-42	2.02E-42	1.10E-42	7.11E-43	3.86E-43	2.51E-43	1.79E-43

Table 2. The spectral absorption coefficient $K_{(ff)}(\lambda, T)$ [cm^5] which characterizes absorption processes (2) as a function of wavelength λ [nm] and temperature T [K].

lambda/T	1000	2000	3000	4000	6000	8000	10000
50	5.19E-45	1.49E-45	1.60E-45	1.67E-45	1.74E-45	1.90E-45	2.41E-45
60	2.04E-45	1.44E-45	1.89E-45	2.26E-45	2.89E-45	3.26E-45	3.93E-45
70	1.99E-44	1.74E-44	1.85E-44	1.96E-44	2.06E-44	2.34E-44	2.60E-44
80	1.94E-43	1.42E-43	1.54E-43	1.67E-43	1.91E-43	2.16E-43	2.37E-43
90	7.74E-43	6.30E-43	6.28E-43	6.37E-43	6.90E-43	7.40E-43	7.97E-43
100	1.94E-42	1.52E-42	1.51E-42	1.54E-42	1.64E-42	1.73E-42	1.85E-42
110	1.86E-41	1.07E-41	1.02E-41	9.63E-42	9.04E-42	8.54E-42	8.33E-42
120	2.58E-40	8.05E-41	8.53E-41	8.46E-41	7.65E-41	7.05E-41	7.81E-41
130	1.76E-40	6.19E-41	7.27E-41	8.04E-41	8.57E-41	8.81E-41	8.97E-41
140	2.92E-40	2.58E-40	2.86E-40	3.15E-40	3.52E-40	3.48E-40	4.39E-40
150	9.79E-40	6.34E-40	6.97E-40	7.46E-40	8.18E-40	8.52E-40	1.02E-39
160	5.08E-40	2.88E-40	3.16E-40	3.63E-40	3.86E-40	4.11E-40	5.01E-40
170	1.90E-41	7.52E-41	9.74E-41	1.10E-40	1.46E-40	1.63E-40	1.87E-40
180	1.34E-44	5.02E-43	1.74E-42	3.33E-42	7.45E-42	1.15E-41	1.68E-41
190	1.57E-48	4.58E-46	3.72E-45	9.59E-45	3.64E-44	8.86E-44	1.42E-43
200	2.01E-50	4.12E-47	4.71E-46	1.59E-45	5.19E-45	1.07E-44	1.62E-44

Figure 1 shows the results of calculations of the average thermal photo-dissociation cross-section $\sigma^{(bf)}_{\mathrm{CaH^+}}(\lambda;T)$ for the calcium hydride molecular ion over a wide range of temperatures and wavelengths. The 3D plot shows a complex dependence on wavelength and temperature with noticeable maxima in the wavelength region 100 nm-160 nm.

The absorption coefficients as functions of wavelength and temperature, which involves hydrogen and calcium atoms, ions, molecules and molecular-ions, are given. The data of the bound-free $K_{(bf)}(\lambda,T)$, free-free $K_{(ff)}(\lambda,T)$ and free-bound $K_{(fb)}(\lambda,T)$ spectral rate coefficient are given by the Tabs. 1, 2 and 3. The tables cover the region 50 nm $\leq \lambda \leq$ 200 nm and 1000 K $\leq T \leq$ 10000 K which enables potential modeling. These tables show that the values of all rate coefficients have maxima depending on temperature and wavelength.

Table 3. The spectral absorption coefficient $\mathrm{K}_{(fb)}(\lambda,T)$ [cm^5] which characterizes absorption processes (3) as a function of wavelength λ [nm] and temperature T [K].

lambda/T	1000	2000	3000	4000	6000	8000	10000
166	1.38E-41	5.54E-42	3.15E-42	2.09E-42	1.16E-42	7.64E-43	5.50E-43
170	1.06E-40	6.84E-41	4.64E-41	3.37E-41	2.06E-41	1.42E-41	1.05E-41
171	3.24E-40	2.39E-40	1.71E-40	1.28E-40	8.10E-41	5.67E-41	4.25E-41
175	2.06E-41	3.42E-41	3.29E-41	2.86E-41	2.10E-41	1.59E-41	1.25E-41
180	9.96E-45	3.93E-44	5.17E-44	5.29E-44	4.58E-44	3.76E-44	3.10E-44
185	5.57E-46	6.18E-45	1.12E-44	1.35E-44	1.37E-44	1.21E-44	1.05E-44
190	4.23E-47	1.42E-45	3.73E-45	5.38E-45	6.56E-45	6.39E-45	5.83E-45
195	4.13E-48	3.42E-46	1.22E-45	2.06E-45	2.94E-45	3.10E-45	2.97E-45
200	5.13E-49	9.99E-47	4.74E-46	9.20E-46	1.51E-45	1.71E-45	1.71E-45

4. Summary

In this contribution, we explored the absorption processes of photo-association, charge-exchange, and photo-dissociation for non-symmetric systems. We provide average cross-sections and also tabulated spectral rate coefficients for radiative processes involving calcium and hydrogen atoms, ions, molecules, and molecular ions in the wide region of temperatures in the EUV and VUV spectral region. The results have potential laboratory and astrophysical applications, such as in the spectroscopic investigation, synchrotron experiments, in the modeling of weakly ionized layers of the atmospheres of different stars and astronomical objects as well ISM.

The further step and our plan is to investigate absorption processes for other species in various environments. Also it would be very useful to include data in an A&M database. We plan to insert these datasets into a searchable A&M data provider - VAMDC (vamdc.eu), by extending one of the VAMDC nodes hosted by Serbian Virtual Observatory at servo.aob.rs.

References

Albert, D., Antony, B. K., Ba, Y. A., et al., A Decade with VAMDC: Results and Ambitions. 2020, *Atoms*, **8**, 76, DOI: 10.3390/atoms8040076

Barklem, P. S. & O'Mara, B. J., The broadening of strong lines of Ca$\hat{+}$, Mg$\hat{+}$ and Ba$\hat{+}$ by collisions with neutral hydrogen atoms. 1998, *Mon. Not. R. Astron. Soc.*, **300**, 863, DOI: 10.1046/j.1365-8711.1998.01942.x

Brown, K. R., Khanyile, N. B., Rugango, R., Shu, G., & Calvin, A., Single Molecular Ion Spectroscopy: Towards Precision Measurements on CaH$^+$. 2016, in *71st International Symposium on Molecular Spectroscopy*, TD09

Canuto, S., Castro, M. A., & Sinha, K., Theoretical determination of the spectroscopic constants of CaH$^+$. 1993, *Phys. Rev. A*, **48**, 2461, DOI: 10.1103/PhysRevA.48.2461

Djuissi, E., Bogdan, R., Abdoulanziz, A., et al., Electron driven reactive processes involving H+2 and HD+ molecular cations in the Early Universe. 2020, *Rom. Astron. J.*, **30**, 101

Dutta, C. M., Oubre, C., Nordlander, P., Kimura, M., & Dalgarno, A., Charge-transfer cross sections in collisions of ground-state Ca and H$^+$. 2006, *Phys. Rev. A*, **73**, 032714, DOI: 10.1103/PhysRevA.73.032714

Epée Epée, M. D., Motapon, O., Pop, N., et al., Dissociative recombination and rotational transitions of D$^+_2$ in collisions with slow electrons. 2022, *Mon. Not. R. Astron. Soc.*, **512**, 424, DOI: 10.1093/mnras/stac501

Giuliani, A., Milosavljević, A. R., Canon, F., & Nahon, L., Contribution of synchrotron radiation to photoactivation studies of biomolecular ions in the gas phase. 2014, *Mass Spectrom. Rev.*, **33**, 424, DOI: 10.1002/mas.21398

Hauschildt, P. H. & Baron, E., A 3D radiative transfer framework. VI. PHOENIX/3D example applications. 2010, *Astron. Astrophys.*, **509**, A36, DOI: 10.1051/0004-6361/200913064

Iacob, F., On the geometric quantization of the ro-vibrational motion of homonuclear diatomic molecules. 2020, *Phys. Lett. A*, **384**, 126888, DOI: 10.1016/j.physleta.2020.126888

Iacob, F., Pop, N., Mezei, J. Z., et al., Recombination and excitation of molecular cations with electrons: Application to, H$_2^+$ BeD$^+$ and BeT$^+$. 2019, in American Institute of Physics Conference Series, Vol. **2071**, *Tim 18 Physics Conference*, 020007

Ignjatović, L. M., Mihajlov, A. A., Srećković, V. A., & Dimitrijević, M. S., The ion-atom absorption processes as one of the factors of the influence on the sunspot opacity. 2014, *Mon. Not. R. Astron. Soc.*, **441**, 1504, DOI: 10.1093/mnras/stu638

Ignjatović, L. M., Srećković, V. A., & Dimitrijević, M. S., Photoionization of the alkali molecular ions in geo-cosmical plasmas. 2020, *Contrib. Astron. Obs. Skaln. Pleso*, **50**, 187, DOI: 10.31577/caosp.2020.50.1.187

Khanyile, N. B., Goeders, J. E., & Brown, K. R., Vibrational Spectroscopy of Sympathetically Cooled CaH$\hat{+}$ Molecular Ions. 2013, in *68th International Symposium on Molecular Spectroscopy*, ERB01

Kimura, N., Okada, K., Takayanagi, T., et al., Sympathetic crystallization of CaH$^+$ produced by a laser-induced reaction. 2011, *Phys. Rev. A*, **83**, 033422, DOI: 10.1103/PhysRevA.83.033422

Mihajlov, A. A., Sakan, N. M., Srećković, V. A., & Vitel, Y., Modeling of continuous absorption of electromagnetic radiation in dense partially ionized plasmas. 2011, *J. Phys. A*, **44**, 095502, DOI: 10.1088/1751-8113/44/9/095502

Monteiro, T. S., Danby, G., Cooper, I. L., Dickinson, A. S., & Lewis, E. L., Broadening of the Ca(+) and Mg(+) resonance lines by collision with atomic hydrogen. 1988, *J. Phys. B*, **21**, 4165, DOI: 10.1088/0953-4075/21/24/016

Pop, N., Iacob, F., Niyonzima, S., et al., Reactive collisions between electrons and BeT+: Complete set of thermal rate coefficients up to 5000 K. 2021, *At. Data Nucl. Data Tables*, **139**, 101414, DOI: 10.1016/j.adt.2021.101414

Sansone, G., Kelkensberg, F., Pérez-Torres, J. F., et al., Electron localization following attosecond molecular photoionization. 2010, *Nature*, **465**, 763, DOI: 10.1038/nature09084

Srećković, V. A., Mihajlov, A. A., Ignjatović, L. M., & Dimitrijević, M. S., Ion-atom radiative processes in the solar atmosphere: quiet Sun and sunspots. 2014, *Adv. Space Res.*, **54**, 1264, DOI: 10.1016/j.asr.2013.11.017

Srećković, V. A., Ignjatović, L. M., & Dimitrijević, M. S., Photodestruction of Diatomic Molecular Ions: Laboratory and Astrophysical Application. 2021, *Molecules*, **26**, 151, DOI: 10.3390/molecules26010151

Srećković, V. A., Ignjatović, L. M., Kolarski, A., et al., Data for Photodissociation of Some Small Molecular Ions Relevant for Astrochemistry and Laboratory Investigation. 2022, *Data*, **7**, 129, DOI: 10.3390/data7090129

Vázquez-Carson, S. F., Sun, Q., Dai, J., Mitra, D., & Zelevinsky, T., Direct laser cooling of calcium monohydride molecules. 2022, *New J. Phys.*, **24**, 083006, DOI: 10.1088/1367-2630/ac806c

Data of plasma velocity obtained from Streak image processing of laser-induced breakdown

M.S. Rabasovic[ID], **A. Dencevski**[ID], **M.D. Rabasovic**[ID] **and D. Sevic**[ID]

Institute of Physics Belgrade, University of Belgrade, Pregrevica 118,
11080 Zemun, Serbia, (E-mail: sevic@ipb.ac.rs)

Abstract. We present time resolved measurements of the laser induced plasma development in air. A Q-switched Nd:YAG laser is employed as the excitation source. The detection part of the acquisition system is based on a streak camera. We propose streak image processing technique based on a set of simple algorithms as a way to obtain estimations of plasma core and plasma plume instantaneous velocity. Using of the proposed technique enables us to obtain all data relevant for temporal analysis by a single shot excitation.

Key words: Laser induced breakdown spectroscopy – Streak camera – Image processing

1. Introduction

The formation of laser induced breakdown (LIB) refers to a plasma production by focusing an intense laser beam in a gas, liquid or solid target. Parameters of laser induced plasma depend on irradiation conditions, such as laser intensity, pulse duration, laser wavelength or ambient gas. To understand the process of laser induced breakdown it is required to obtain the detailed knowledge of the initial stages of various processes involving laser duration and irradiation, plasma formation and its expansion. The nanosecond laser pulse generates plasma through thermal and non-thermal mechanisms. Studying the plasma formation with a high temporal, spectral and spatial resolution is of a great interest and formation of laser induced breakdown plasma in air has been studied by many researchers Robledo-Martinez et al. (2008); Villagran-Muniz et al. (2001); Camacho et al. (2010); Kawahara et al. (2007); Pandey & Thareja (2010); Hori & Akamatsu (2008), including references therein. After the initial breakdown, plasma plume propagates towards the focusing lens Robledo-Martinez et al. (2008). The bright plasma core of the LIB plasma in open air is surrounded by a layer of cold, moderately ionized gas called the sheath Robledo-Martinez et al. (2008). Glow of plasma sheath, although fainter than the core, is also visible to the naked eye. An explosive plasma expansion induces optodynamic phenomena, i.e., the propagation of a shock, acoustical and ultrasonic waves. The optodynamic phenomena convey important information about the

laser-material interaction. On the other hand, optical lines emission due to the electron transitions in laser-induced plasma can be used to obtain the crucial information for elemental analysis of samples in all three states. Studying the plasma formation with a high temporal and spatial resolution is therefore of a great importance in a laser-induced material transfer Bohandy et al. (1986); Mattle et al. (2012); Feinaeugle et al. (2012), pulsed-laser deposition Lunney (1995); Sánchez-Aké et al. (2012); Guzmán et al. (2013), and various industrial applications Bilmes et al. (2006); Lackner et al. (2004). The velocity field measurement of LIB plasma plumes in air has been the subject of various experimental techniques in recent years Koll et al. (2020); Shi et al. (2019); Nishihara et al. (2020). The influence of the delay time between the subsequent plasma images along the different directions are investigated in Shi et al. (2019). In this paper we propose streak image processing technique as a way to obtain estimations of plasma core and plasma plume periphery instantaneous velocity. Studies with similar aims were presented in references Robledo-Martinez et al. (2008); Villagran-Muniz et al. (2001); Camacho et al. (2010); Kawahara et al. (2007), but our method of data processing is quite different. Using the picosecond temporal resolution of our streak camera we analyze the initial time period after the laser induced breakdown. There are many well known simple image processing algorithms but the answer to the question which simple algorithms should be selected for use and how to combine them to achieve the goal desired in our study is not simple at all. After some considerations we discarded several techniques which seemed at the first glance as obvious solution for our problem. Namely, common image processing techniques are usually intended to be used on images seen in nature by a human observer. Streak images look like images, but they have some specific characteristics. First of all, they are spatial only in one dimension, the other dimension being the time. So, for example, general gradient methods for image edge detection would be misused if applied here and we discarded them.

2. Methods

A schematic diagram of the experimental apparatus is shown in Fig. 1. Time resolved LIB system implemented in our laboratory is based on Nd:YAG laser and Optical Parametric Oscillator (OPO; Vibrant 266). The OPO system, pumped by a pulsed Q switched Nd:YAG laser (Brilliant B) includes the second and fourth harmonic generator (SHG and FHG). In our experiments we used all outputs of this laser system as the excitation sources, but in this paper only the fundamental output at 1064 nm (pulse energy up to 270 mJ, pulse duration of about 5 ns) is used to create an optical breakdown in ambient air. One of advantages of using the excitation at 1064 nm is the fact that, for any kind of temporal analysis, we do not need to perform deconvolution of the laser pulse signal from streak image of plasma emission. The delay generator (Stanford Re-

search Systems DG535) plays a significant role in the streak camera operation. Timing considerations regarding the laser pulse and streak camera synchronization are very important in our measurements Rabasovic et al. (2012, 2019), so we added a photodiode and digital oscilloscope to our experimental setup, Fig. 1. The plasma plume in air is obtained by focusing the laser beam using lens with the focal length of 40 mm. The OPO system is controlled by OPOTEK software installed on PC.
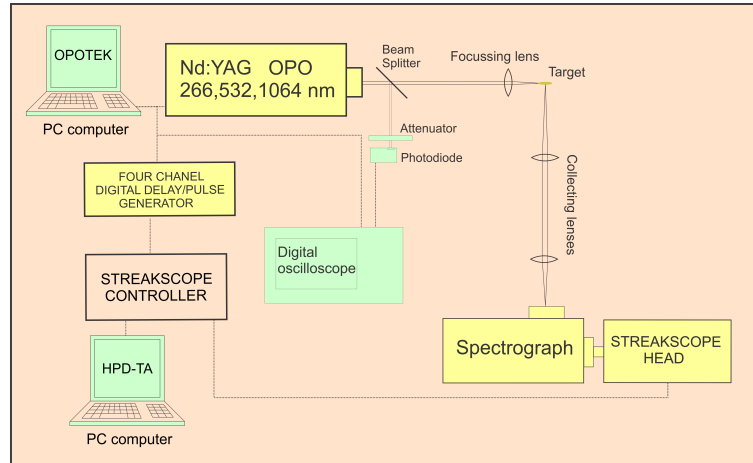

Figure 1. Setup for time-resolved laser induced breakdown measurements.

The optical emission from the plasma is collected by using a spectrograph (SpectraPro 2300i) and recorded with a Hamamatsu streak camera (model C4334) (Fig. 1). The streak images are time resolved thus enabling monitoring of temporal evolution of the ionic and atomic emission lines or spatial development of the plasma. The camera has the spectral range from 200 nm to 850 nm and time resolution up to 30 ps. The CCD chip has a resolution of 640 x 480 pixels. The data are acquired and analyzed using High Performance Digital Temporal Analyzer (HPD-TA) software, provided by Hamamatsu. Our earlier research of optical emission of plasma was limited so far to analysis of time resolved optical emission spectra acquired by the streak camera Sevic et al. (2011); Rabasovic et al. (2012, 2014). To make our study more comprehensive we saw the need for measuring the spatial distribution of plasma optical emission Rabasovic et al. (2019) and requirement for easy switching between the spectral and spatial measurement modes of our streak camera system soon became apparent to us. We performed a simple modification of our spectrograph that enables easy switching between the spectral and spatial measurement modes. Similar modification was already proposed and successfully used in the study of Siegel et al. (2005), where imaging device was ICCD camera. Our modifica-

tion is different in a sense that optical alignment of target area to the streak camera slit needs special consideration and careful procedure. The spectrograph contains the triple grating turret. The diffraction gratings of 50, 150 and 300 gr/mm were installed. In the place of the 150 gr/mm grating we mounted the plain mirror. Now, if grating of 150 gr/mm is selected by HPD-TA software, than spectromemer projects the image of entrance slit to the streak camera. At the same time, collecting lenses project the image of the target plasma to the spectrometer entrance slit. In this way, streak camera instead of the image of the optical spectrum takes the image of the spatial distribution of the optical emission of the laser induced breakdown. The spectrograph entrance slit should be fully open to utilize as much as possible of the CCD camera active area. For measurements presented here other optical parts of the acquisition system were chosen so to have overall optical magnification of 0.6. In this case, the calibration procedure shows that 1 mm on the target position corresponds to 72 pixels of the CCD camera.

3. Results and discussion

Single-shot laser induced breakdown plasma emission spatial images analyzed in this paper are acquired in the direction perpendicular to the laser beam, as shown in Fig. 1. The streak image of the laser induced plasma (excitation at 1064 nm, energy of 51 mJ, peak intensity of 1.3 10^{11} W/cm^2) is shown in Fig. 2. The time axis is vertical, with zero time on the top of the image. The spatial axis is horizontal. The development of the plasma is seen on the streak image as vertical development (corresponding to a passing of time) of a narrow horizontal section of plasma optical emission, seen through the camera slit, along the direction of propagation of the laser beam. In other words, two dimensional (2 D) streak image corresponds to only 1-D spatial image, represented by rows of image matrix, the other dimension being the time. The streak images are often presented in pseudo-color, where different intensities are coded as different colors. However, the edges on such images could be misunderstood by an observer, so we present streak image as grayscale. Red points indicate the edges and peak values of plasma brightness, detected by our image processing algorithm. The laser beam is incident from the right-hand side of the streak image. As expected Robledo-Martinez et al. (2008), plasma plume expands towards the laser beam.

Our streak image processing algorithm is effective and easy to implement. First, the rows of streak image are mean filtered, using nine neighboring pixels, two times iteratively.

$$Lout[x] = \frac{\sum_{x=-4}^{x=4} L[x]}{9.0} \tag{1}$$

where $L[x]$ denotes intensity of streak image pixel with coordinate x.
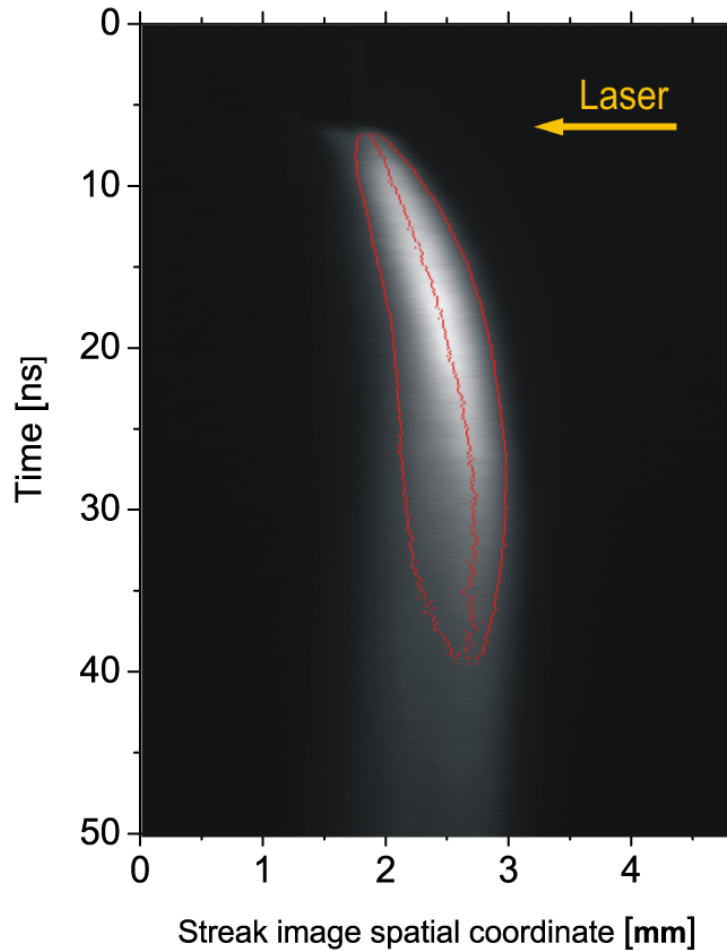
Figure 2. Streak image of the laser induced plasma (excitation at 1064 nm, energy of 51 mJ). Red points indicate the detected edges and peak values of brightness of the plasma plume.

The preliminary tests showed that mean filter is quite satisfying and simple method of filtering. We didn't use median filter because it is not suitable for Gaussian noise which is present on our streak images. It is generally true that median filter (often improved with several techniques like fuzzy logic, weighted coefficients, etc) performs better than mean filter. However, when there is too much Gaussian noise, a median filter blurs fine structures of an image and causes edge jitter and streaking Yang (1999). So, after some initial tries we have selected the mean filter which is simpler to implement than median. To alleviate effects of impulse noise, we introduced the following correcting rule:

if $((L[x] - mean) > threshold)$ then $L[x] = mean$
where *mean* is calculated as mean value of eight neighboring s:

$$mean = \frac{\sum_{x=-4}^{x=-1} L[x] + \sum_{x=1}^{x=4} L[x]}{8.0} \tag{2}$$

After some experimenting, The *threshold* was set to be 5 % of value of maximal pixel intensity of analyzed streak image.

The problem of streak image noise is typically solved by using some kind of cumulative or integrating measuring streak camera techniques, based on repetitive laser excitation. By using the proposed filtering method it is possible to use a single-shot laser excitation.

All our streak images of plasma development are of the similar shape and the plasma contour is similarly positioned on the image, so it is possible to use a simplified algorithm for edge detection, specialized for our purpose. Namely, it is assumed that the right edge of plasma plume is detected when pixel intensities exceeds certain threshold above the averaged background, testing iteratively through the row of pixels, starting from the right side of the image. The algorithm is similarly conducted for the left edge of plasma plume. It is supposed that the pixel or pixels with the peak value of brightness of plasma core are identified when the value of pixel is equal to the calculated value of peak of that row. We did not limit the peak to the only one pixel because it would make a fitting of curve indicating the moving of plasma core more difficult.

The time diagrams of position changes of left and right side edge of plasma plume, and of the peak of plasma brightness, corresponding to the movement of the center of plasma core, are shown in Fig. 3. Note that the time ranges in Figures 3 and 4 correspond to the part of streak image where plasma expands. The diagrams are obtained by transferring the coordinates of pixels corresponding to detected edges and peaks of rows of streak image from Fig. 2. Time dependence of instantaneous-velocity of edges of plasma plume and peak brightness were also calculated from the same data set and shown in Fig. 4. Data corresponding to fitted curves from Fig. 3 were used for calculation to avoid nonexistent velocity fluctuations. Because the plasma plume is expanding and moving to the right at the same time, the velocity of the right edge is greater than the velocity of the center of the core, as shown in Fig. 4. As the expansion of the plasma plume ceases (for excitation energy of 51 mJ after about 10 ns) the velocity of right edge of plasma plume decreases. The velocity of the left edge of the plasma plume is smallest, because the direction of the plasma expanding is opposite to the direction of the plasma moving (Fig. 4).
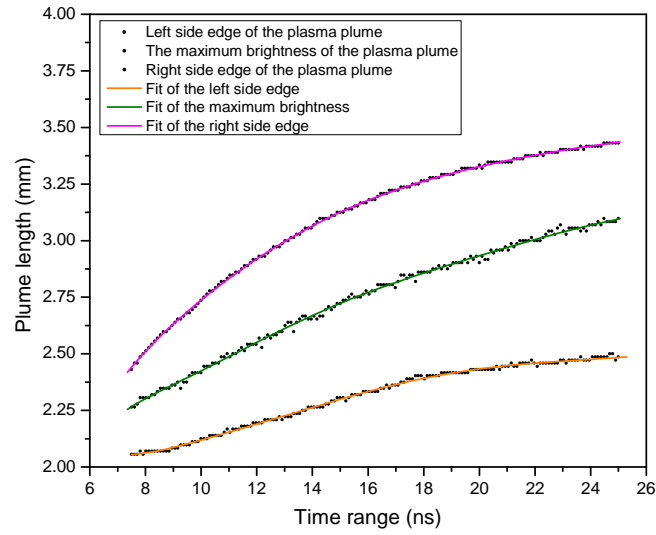
Figure 3. The time diagrams of moving of left side and right side edge of plasma plume, and of the peak of plasma brightness.
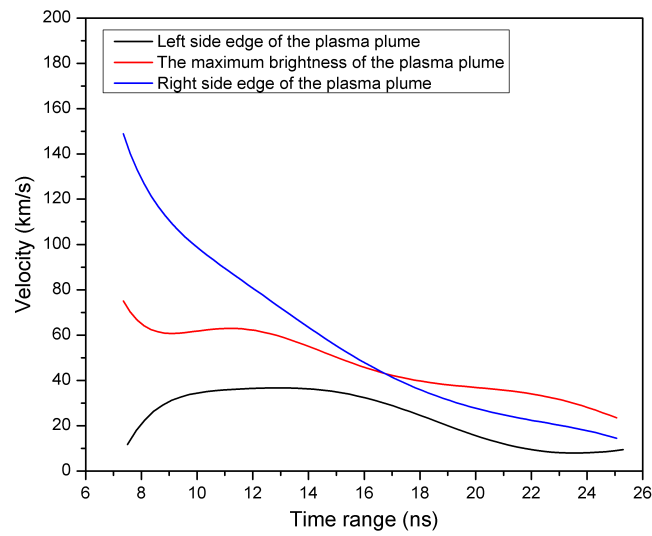

Figure 4. The time diagrams of instantaneous velocity of left side, right side (towards the laser beam) edge of plasma plume, and of the peak of plasma brightness.

Let us point out that, as stated in Introduction, our approach is quite different than the approaches in references describing investigations of laser produced plasma plume cited in our paper (before all, because their experimental equipment is more complex), so it is difficult to provide a quantitative comparison. There is no doubt that the results presented in cited references are more detailed and reliable, but similar investigations in cited references use fast framing cameras with two dimensional imaging, while our streak camera, although faster in time, has only one spatial dimension. Our study provides improved analysis of streak images based on image processing techniques.

It's important to highlight that the single-shot feature of our system has two dimensions: firstly, all the necessary data for calculating instantaneous velocity can be found within a single streak image, and secondly, the streak image can be acquired in a single shot thanks to the noise filtering method introduced in this paper.

4. Discussion and Conclusions

We have presented streak camera velocity measurements of the laser induced plasma development in air. We have described how to obtain estimations of plasma core and sheath instantaneous velocity by using streak image processing technique, based on image noise filtering and plasma sheet edge and plasma core peak brightness detection. So, we have provided, by data postprocessing techniques, alternative to much more complex experimental setups analyzing the laser produced plasma plume. All data relevant for temporal analysis were acquired by a single shot excitation. The presented method is suitable for plasma sheath velocity measurements from the very beginning of the laser induced breakdown by using a picosecond time resolution of our streak camera. For our future work we plan to include machine learning techniques for improving quality of streak images.

References

Bilmes, G. M., Orzi, D. J. O., Martínez, O. E., & Lencina, A., A real time method for surface cleanliness measurement. 2006, *Applied Physics B: Lasers and Optics*, **82**, 643, DOI: 10.1007/s00340-005-2096-7

Bohandy, J., Kim, B. F., & Adrian, F. J., Metal deposition from a supported metal film using an excimer laser. 1986, *Journal of Applied Physics*, **60**, 1538, DOI: 10.1063/1.337287

Camacho, J. J., Díaz, L., Santos, M., Juan, L. J., & Poyato, J. M. L., Time-resolved optical emission spectroscopy of laser-produced air plasma. 2010, *Journal of Applied Physics*, **107**, 083306, DOI: 10.1063/1.3382914

Feinaeugle, M., Alloncle, A. P., Delaporte, P., Sones, C. L., & Eason, R. W., Time-resolved shadowgraph imaging of femtosecond laser-induced forward transfer of solid materials. 2012, *Applied Surface Science*, **258**, 8475, DOI: 10.1016/j.apsusc.2012.04.101

Guzmán, F., Favre, M., Ruiz, H. M., et al., Pulsed laser deposition of thin carbon films in a neutral gas background. 2013, *Journal of Physics D Applied Physics*, **46**, 215202, DOI: 10.1088/0022-3727/46/21/215202

Hori, T. & Akamatsu, F., Laser-Induced Breakdown Plasma Observed using a Streak Camera. 2008, *Japanese Journal of Applied Physics*, **47**, 4759, DOI: 10.1143/JJAP.47.4759

Kawahara, N., Beduneau, J. L., Nakayama, T., Tomita, E., & Ikeda, Y., Spatially, temporally, and spectrally resolved measurement of laser-induced plasma in air. 2007, *Applied Physics B: Lasers and Optics*, **86**, 605, DOI: 10.1007/s00340-006-2531-4

Koll, M., Freund, J. B., & Elliott, G. S., Particle Image Velocimetry of a Nano-Second Laser-Induced Breakdown in Air. 2020, *AIAA Scitech 2020 Forum, Session: Other Topics in Fluid Dynamics III*, 1, DOI: 10.2514/6.2020-2047

Lackner, M., Charareh, S., Winter, F., et al., Investigation of the early stages in laser-induced ignition by Schlieren photography and laser-induced fluorescence spectroscopy. 2004, *Optics Express*, **12**, 4546, DOI: 10.1364/OPEX.12.004546

Lunney, J. G., Pulsed laser deposition of metal and metal multilayer films. 1995, *Applied Surface Science*, **86**, 79, DOI: 10.1016/0169-4332(94)00368-8

Mattle, T., Shaw-Stewart, J., Schneider, C. W., Lippert, T., & Wokaun, A., Laser induced forward transfer aluminum layers: Process investigation by time resolved imaging. 2012, *Applied Surface Science*, **258**, 9352, DOI: 10.1016/j.apsusc.2011.08.113

Nishihara, M., Freund, J. B., & Elliott, G. S., A study of velocity, temperature, and density in the plasma generated by laser-induced breakdowns. 2020, *Journal of Physics D Applied Physics*, **53**, 105203, DOI: 10.1088/1361-6463/ab5b26

Pandey, P. K. & Thareja, R. K., Plume dynamics of laser produced air plasma. 2010, in Journal of Physics Conference Series, Vol. **208**, *Journal of Physics Conference Series*, 012091

Rabasovic, M., Rabasovic, M., Marinkovic, B., & Sevic, D., Laser-Induced Plasma Measurements Using Nd:YAG Laser and Streak Camera: Timing Considerations. 2019, *Atoms*, **7**, 6, DOI: 10.3390/atoms7010006

Rabasovic, M. S., Marinkovic, B. P., & Sevic, D., Time-Resolved Optical Spectra of the Laser-Induced Indium Plasma Detected Using a Streak Camera. 2014, *IEEE Transactions on Plasma Science*, **42**, 2588, DOI: 10.1109/TPS.2014.2352400

Rabasovic, M. S., Sevic, D., Pejcev, V., & Marinkovic, B. P., Detecting indium spectral lines using electron and laser induced breakdown spectroscopy.

2012, *Nuclear Instruments and Methods in Physics Research B*, **279**, 58, DOI: 10.1016/j.nimb.2011.10.020

Robledo-Martinez, A., Sobral, H., Villagrán-Muniz, M., & Bredice, F., Light focusing from large refractive indices in ionized air. 2008, *Physics of Plasmas*, **15**, 093510, DOI: 10.1063/1.2988768

Sánchez-Aké, C., Camacho, R., & Moreno, L., Deposition and composition-control of Mn-doped ZnO thin films by combinatorial pulsed laser deposition using two delayed plasma plumes. 2012, *Journal of Applied Physics*, **112**, 044904, DOI: 10.1063/1.4747935

Sevic, D., Rabasovic, M., & Marinkovic, B. P., Time-Resolved LIBS Streak Spectrum Processing. 2011, *IEEE Transactions on Plasma Science*, **39**, 2782, DOI: 10.1109/TPS.2011.2158555

Shi, Z., Hardalupas, Y., & Taylor, A. M. K. P., Laser-induced plasma image velocimetry. 2019, *Experiments in Fluids*, **60**, 5, DOI: 10.1007/s00348-018-2649-2

Siegel, J., Epurescu, G., Perea, A., et al., High spatial resolution in laser-induced breakdown spectroscopy of expanding plasmas. 2005, *Spectrochimica Acta*, **60**, 915, DOI: 10.1016/j.sab.2005.05.020

Villagran-Muniz, M., Sobral, H., Sanchez Ake, C., Escobar, L., & Camps, E., Plasma ablation characterization by a laser beam deflection technique. 2001, in Society of Photo-Optical Instrumentation Engineers (SPIE) Conference Series, Vol. **4419**, *4th Iberoamerican Meeting on Optics and 7th Latin American Meeting on Optics, Lasers, and Their Applications*, ed. V. L. Brudny, S. A. Ledesma, & M. C. Marconi, 102–105

Yang, T. 1999, Advances in Imaging and Electron Physics, Vol. **109**, *Fuzzy Cellular Neural Networks and Their Applications to Image Processing*, ed. P. W. Hawkes (Elsevier), 265–446

Reduced mobility and rate coefficients for H_2^+ ions in H_2 gas

Ž.D. Nikitović and Z.M. Raspopović

Institute of Physics Belgrade, University of Belgrade,
Pregrevica 118, 11080 Belgrade, Serbia

Abstract. In this work, we present a complete cross sections set that describe the interaction between H_2^+ ions and H_2 molecules. Based on these cross sections, we have calculated the transport properties of H_2^+ ions in H_2 gas, depending on the reduced electric field. Ionic charge exchange reactions with molecules are indispensable elementary processes in the modeling of kinetics in terrestrial, industrial and astrophysical plasma in the detection of dark matter. A Monte Carlo simulation method is applied to accurately calculate transport parameters in hydrodynamic regime. We discuss new data for H_2^+ ions in H_2 gas where the mean energy the flux and bulk values of reduced mobility and other transport coefficients, are given as a function of low and moderate reduced electric fields.

Key words: H_2^+ ions – H_2 gas – Monte Carlo simulation – cross sections – transport parameters

1. Introduction

Transport properties of species in gas plasmas are of great importance in understanding the nature of molecular and ionic interactions in gas mixtures (Todd *et al.*, 2002; Mason, 1957; Golzar *et al.*, 2014). These properties include the mean energy, drift velocity, diffusion coefficients, ionization and chemical reaction coefficients, chemical reaction coefficients for ions and (rarely) excitation coefficients, and they are very useful in chemical industries for the design of many types of transport and process equipment.

H_2 gas is used in gaseous electronic multipliers for various imaging purposes (X-rays, charged particles, thermal neutrons and dark matter detection) (Fraga *et al.*, 2003; Kaboth *et al.* 2008). Hydrogen, is one of the most common elements on Earth and in its gaseous form is a fuel for obtaining energy. Hydrogen is a highly explosive gas and creates one of the highest flame temperatures.

We acknowledge the importance of the results obtained, which provide atomic and molecular data regarding ion transport properties in gases, depending on the reduced electric field, E/N (E-electric field, N-gas density). These data as essential input parameters for modeling various environments. Low temperature

can change the state of metals, gases, liquids and solids, cause damage to organisms depending on length of exposure, and change the functionality of mechanized processes. Quantum-mechanical calculation of a certain cross-section is a required task that requires knowledge of the surface potential energy of ions and molecules to be constructed from the structure of the reactants. Less intensive computational methods, such as the Denpoh-Nanbu theory (Denpoh & Nanbu, 1998; Nikitović *et al.* 2014; Petrović *et al.*, 2007), require knowledge of thermodynamic formation data and are applicable to a range of molecules.

Charge exchange reactions between molecular ions and the parent gas are important elementary processes in modeling kinetics in all types of plasma. In many cases, the cross section for these reactions is known to be the most significant part of the set. The cross-section set describes the total collision cross-section between an ion and a gas particle. The total collision cross-section between an ion and a gas particle is described at low energies using Langevin's cross-section and at higher energies using the collision of rigid spheres, as demonstrated in paper (Nikitović *et al.*, 2016; Nikitović *et al.*, 2019).

Transport parameters of H_2^+ ions in H_2 gas, such as ion energy probability functions, mean energy, drift velocity, reduced mobility, longitudinal and transverse diffusion coefficients, and rate coefficients, are calculated using Monte Carlo simulation. Calculated flux and bulk reduced mobilities exhibit significant differences in the region of moderate *E/N*. The novelty of the work is the first-ever detailed presentation of a set of cross-sections for the interaction of H_2^+ ions with an H_2 molecule, as well as the results of transport coefficients of H_2^+ ions in an H_2 gas.

2. Cross section sets

Transport properties needed for modeling H_2 discharges containing H_2^+ ions are calculated by the Monte Carlo method. A code that properly takes into account thermal collisions was used (Ristivojević & Petrović, 2012). For collisions of H_2^+ ions with H_2 molecules, at energies below 1 eV, the total cross-section is labeled as 'Langevin' in Figure 1 and includes anisotropic forward scatterings, an isotropic capture part, rotational excitations, as well as the charge exchange reaction. The transition from Langevin's cross-section to the collision of rigid spheres (labeled as σ HS in the figure) occurs at energies around 1 eV.

At low collision energies, below 1 eV, predominantly influenced by the induced dipole interaction between ions and molecules, an exothermic proton transfer reaction prevails. As energy increases, H_2^+ ions cease to be effectively captured by the induced dipole forces of H_2 molecules, leading to a observed cross-section displaying a $1/v^3$ trend (Krstić *et al.*, 2009), where v signifies the center-of-mass velocity. Beyond 1 eV, the cross-section for elastic momentum transfer corresponds to direct collisions involving rigid spheres. Initially, collisions of these rigid spheres at low energies may be perceived as isotropic. How-
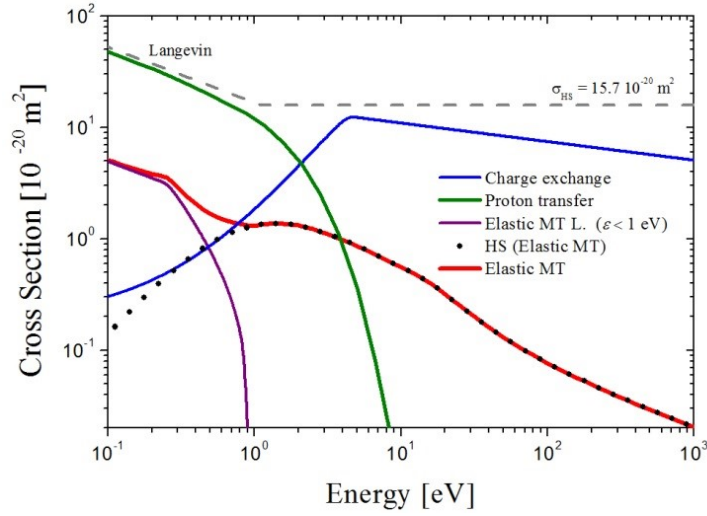
Figure 1. Elastic momentum transfer cross section for collisions between H_2^+ ions and H_2 molecules as a function of collision energy.
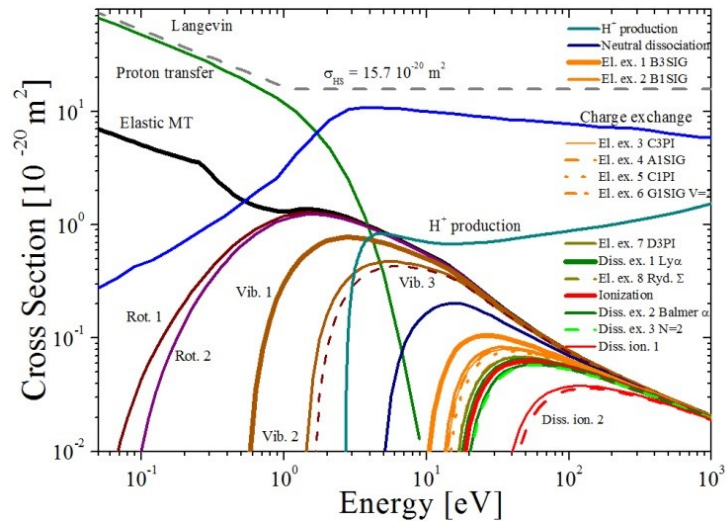

Figure 2. Complete set of cross sections for ion (H_2^+) and molecule (H_2) interactions as a function of collision energy.

ever, with escalating collision energy, their isotropic nature diminishes, progressively favoring forward-directed collisions. Consequently, the momentum transfer cross-section for rigid spheres diminishes with increasing collision energy.
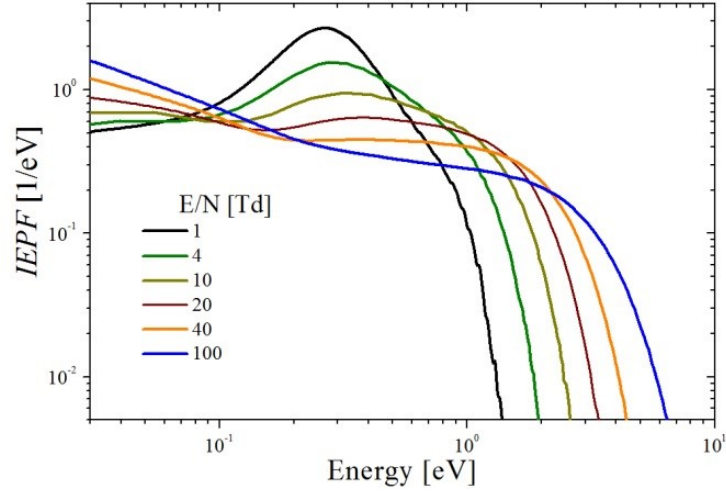
Figure 3. Ion energy probability functions from E/N = 1 Td to E/N = 100 Td.

This decrease is indicated by the black circles in Figure 1 and labeled as "HS (Elastic MT)," as proposed by Denpoh and Nanbu theory (Denpoh & Nanbu, 2022), relative to the total cross section of rigid spheres σ_{HS}. The elastic momentum transfer cross section used in the simulations presented in this study, labeled as 'Elastic MT' in the legend of Figure 1, is a superposition of two cross sections. The first one dominates at low energies and is caused by the induced dipole force between H_2^+ ions and H_2 molecules, denoted as 'Elastic MT L' in the legend. The second cross section results from their direct collision as rigid spheres and is labeled as 'HS (Elastic MT)' in the legend.

At low energies, the primary interaction between ions and gas particles is the induced dipole force, which depends on the collision energy (ε) and the polarizability (α) of the gas particle. The polarizability of H_2 molecules is assumed to be $\alpha = 0.803$ Å^3 (Radzig & Smirnov, 1986). This interaction gives rise to a momentum transfer cross section for collisions, commonly referred to as the Langevin cross section in the literature. Direct collisions between ions and molecules, ions captured by the induced dipole force of molecules resulting in direct collision, and collisions where ions only change direction due to the proximity of gas molecules are encompassed by the Langevin cross section.

At low energies, the primary exothermic reaction is $H_2^+ + H_2 \rightarrow H_3^+ + H$, which is labeled as "proton transfer" in Figure 1. The cross section for this
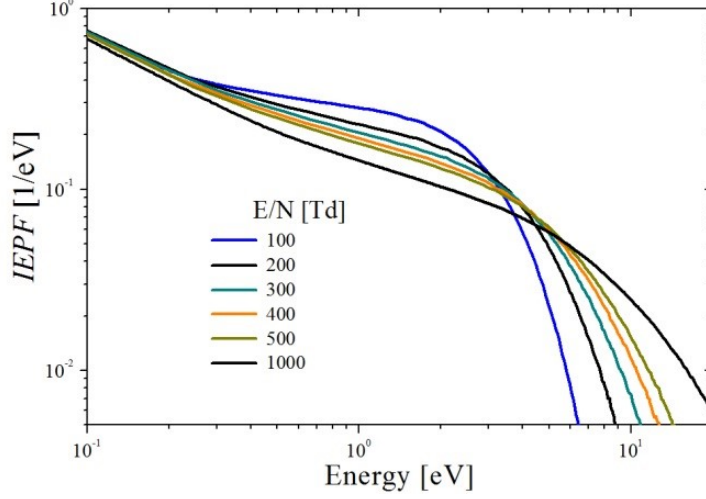
Figure 4. Ion energy probability functions from E/N = 100 Td to E/N = 1000 Td.

reaction is taken from the study by Phelps (1990), but scaled to match that of Denpoh and Nanbu theory (Denpoh & Nanbu, 2022) at an energy of 0.1 eV. The cross section for charge exchange, which refers to the formation of slow H_2^+ as labeled in the legend of Figure 1, was obtained from the study by (Phelps, 1990; Phelps, 2009). At energies below 5 eV, the charge-transfer cross section decreases as a result of competing with the formation of H_3^+.

The elastic momentum transfer cross section used in the simulations presented in this study, labeled as "Elastic MT" in the legend of Figure 1, comprising of two distinct components. Above 1 eV, it is represented by the "HS (Elastic MT)" cross section, while below 1 eV, it is the sum of the "HS (Elastic MT)" and the cross section denoted as "Elastic MT L." in the legend of Figure 1. The elastic momentum transfer cross section at low energies ($\varepsilon < 1$ eV), which originates from the induced dipole interaction (Elastic MT L.), was obtained by subtracting the cross sections of proton transfer, charge exchange reactions, and HS (Elastic MT) from the Langevin cross section. The cross section for this interaction decreases with increasing collision energy, and at 1 eV, it asymptotically approaches zero with a $1/v^3$ dependence.

Figure 2 presents a complete set of cross sections for ion-H_2 molecule interactions as a function of collision energy. The provided cross sections by (Denpoh & Nanbu, 2022) are presented, except for those for proton transfer, H+ production, and charge exchange, for which the cross sections were obtained from Phelps' work (Phelps, 1990; Phelps, 2011). The set includes elastic momentum transfer cross section denoted as "Elastic MT" in Figure 1. The set encompasses rotational ($H_2^+ + H_2$, Rot.), vibrational ($H_2^+ + H_2$, Vib.), electronic ($H_2^+ + H_2$,

El. ex.), and dissociative ($H_2^+ + 2H$, Diss. ex.) excitations, in addition to Neutral dissociation ($H_2^+ + 2H$, Neutral dissociation) and Ionization ($H_2^+ + H_2^+ + e$, Ionization), as well as dissociative ionization ($H_2^+ + H^+ + H + e$, Diss. Ionization) along with the other mentioned processes. The reaction products of $H_2^+ + H_2$ shown in parentheses, along with the corresponding labels on the Figure 2.

Non-elastic excitation processes are treated isotropically. In the case of ionization processes, the secondary ion H_2^+ is also tracked, which shares the incoming kinetic energy with the primary ion reduced by the reaction threshold. The partition of kinetic energy between the primary and secondary ions is determined randomly. In the case of proton transfer processes, the resulting ion H_3^+ is not tracked in the simulations, nor is the H^+ ion in the case of H^+ production.
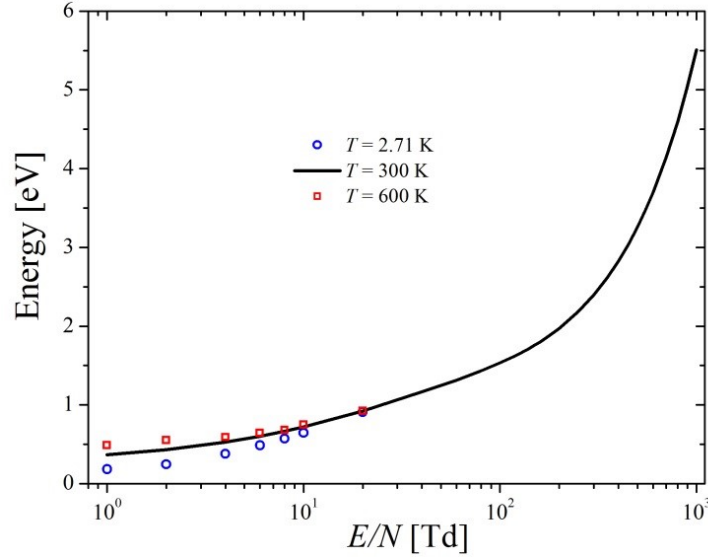
Figure 5. Mean energy of H_2^+ ions a function of E/N.

3. Results and discussion

During the relaxation of H_2^+ ions in H_2 molecules, an energy balance is established between the ion energy gains from the electric field and collisional energy losses. This leads to the appearance of ion energy probability functions (IEPF), as shown in Figure 3 for E/N values between 1 and 100 Td, and in Figure 4 for E/N values between 100 and 1000 Td.

The proton transfer reaction, responsible for the disappearance of H_2^+ ions from the swarm, is highly intense and even occurs at subthermal energies. As a
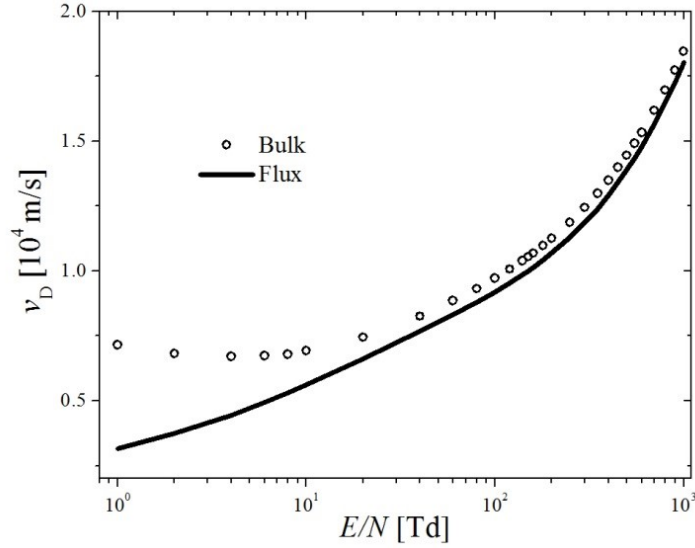
Figure 6. Bulk and flux drift velocity for H_2^+ in H_2 a function of E/N at 300 K.

result, the slow ion population is lacking in the 1-10 Td range, as observed in Figure 3. With increasing electric field intensity, more intense charge exchange reactions take place, leading to the production of slow H_2^+ ions and an increase in the probability of H_2^+ ions being at low energies, as depicted in Figures 3 and 4.

Overall, the ion energy probability function for the H_2^+ and H_2 system significantly deviates from the thermal Maxwell-Boltzmann distribution of ions by energy, for all electric field values.

After reaching steady-state values, the swarm parameters are plotted in Figures 5 to 9 as a function of reduced electric field. Proton transfer reactions deplete the swarm of low-energy H_2^+ ions, resulting in a mean ion energy of 0.37 eV at $E/N = 1$ Td, which is significantly higher than the thermal energy of H_2 molecules at T =300 K. The rise in mean energy is strongly resisted by charge exchange, rotational and vibrational excitation as the electric field increases. With increasing energy, the rate of charge exchange reactions decreases, allowing the mean energy to rise more quickly after E/N > 200 Td. Figure 5 displays not only the mean kinetic energy of ions at a reference temperature of 300 K but also includes data for the mean kinetic energy of ions at gas temperatures of 2.71 K and 600 K. The impact of gas temperatures on the mean kinetic energy of ions becomes noticeable for reduced field strengths below 20 Td.

Figure 6 depicts the drift velocities (Robson *et al.*, 2005; Ness & Robson, 1986; Nikitović *et al.*, 2018; Nikitović & Raspopović, 2021) obtained by simula-

tions using the Monte Carlo method in both real space (bulk) and velocity space (flux). Bulk values are computed as the center of mass displacement over time, $\Delta z_{c.m}/\Delta t$, while flux values correspond to the mean velocity of ions, $< v >$. Non-conservative processes are responsible for separating the bulk and flux values from the transport parameters. The reason for the significantly higher bulk drift velocity values compared to flux drift velocity values in Figure 6 is the decrease in the cross-section for proton transfer interactions with increasing energy. This leads to a greater depletion of H_2^+ ions from the swarm with energies lower than the mean energy value compared to those with higher energies. While the flux drift velocity increases, the slight decrease in bulk drift velocity observed as E/N increases from 1 to 10 Td indicates a reduction in the center of mass displacement over time as the electric field intensity increases. This reduction is due to the interplay between proton transfer reactions, in which slow H_2^+ ions predominantly disappear, and an increase in slow H_2^+ ions resulting from charge exchange reactions.

As a result, at reduced electric fields where ion energies reach the threshold for reaction and H^+ production, the disappearance of high-energy ions from the swarm begins. This results in decreasing differences between bulk and flux drift velocities with increasing E/N. When transitioning from Langevin's cross-section to the collision of rigid spheres, a significant decrease in the elastic momentum transfer cross-section is commonly observed, leading to the appearance of a maximum in the reduced mobility as a function of E/N (Nikitović *et al.*, 2016). In the case of the observed H_2^+ and H_2 system, although the elastic momentum transfer cross-section shows a sharp drop as the energy approaches 1 eV (Figures 1 and 2), it is small and overshadowed by the much more intense proton transfer process. Therefore, in this system, there is no maximum observed in either bulk or flux reduced mobility (Figure 7), and these values monotonically decrease with increasing electric field. The bulk reduced mobility value is higher than the flux reduced mobility value, just as the bulk drift velocity is higher than the flux drift velocity.

In Figure 8, the bulk and flux values of longitudinal and transverse diffusion coefficients, multiplied by the gas concentration, are shown as a function of E/N. The bulk diffusion coefficient values are calculated as

$D_L^B = 0.5\Delta(\langle z^2 \rangle - \langle z \rangle^2)/\Delta t$,
$D_T^B = 0.25(\Delta\langle x^2 \rangle/\Delta t + \langle y^2 \rangle/\Delta t)$,
while the flux diffusion coefficient values are calculated as
$D_L^F = \langle v_z z \rangle - \langle v_z \rangle\langle z \rangle$,
$D_T^F = 0.5(\langle v_x x \rangle + \langle v_y y \rangle)$.

For $E/N < 100$ Td, the significantly lower D_L than D_T indicates highly anisotropic diffusion of the swarm, which spreads four times slower in the direction of the field, deforming the swarm's spherical shape into a highly ellipsoidal shape.

The reduction of diffusion coefficients with increasing E/N is attributed to the rising number of charge exchange reactions with energy that produce slow
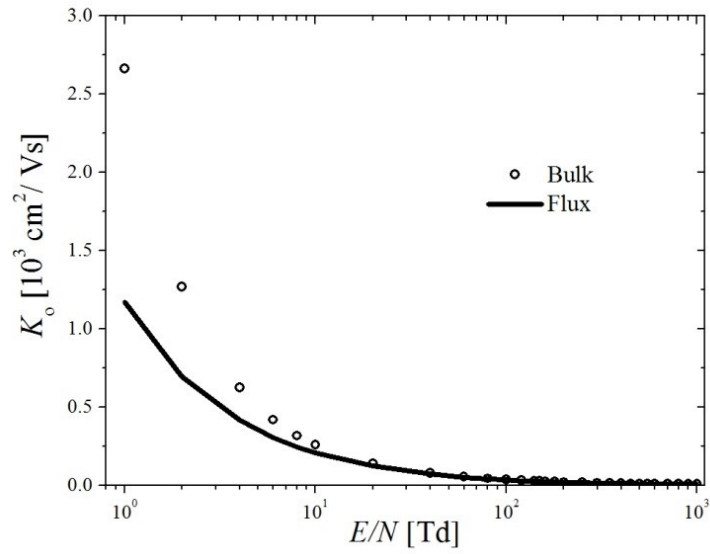
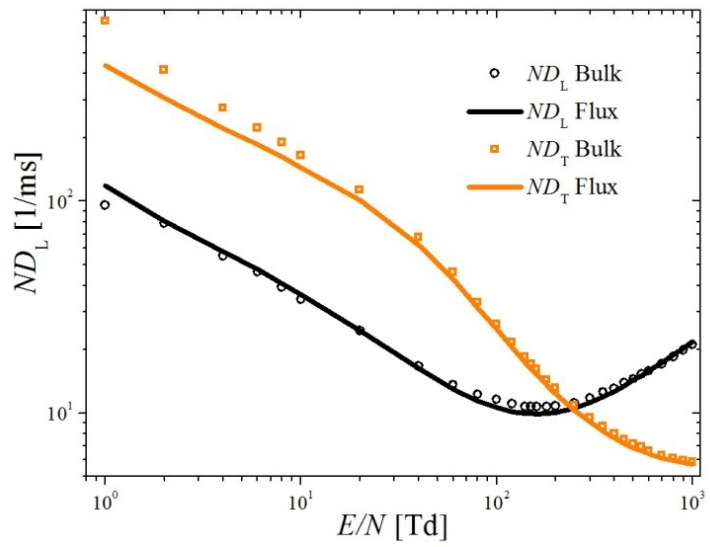**Figure 7.** Bulk and flux reduced mobility for H_2^+ in H_2 a function of E/N at 300 K.

Figure 8. Bulk and flux longitudinal and transverse diffusion coefficients as a function of E/N at 300K.

H_2^+ ions. Consequently, as the electric field intensifies, the population of slow H_2^+ ions also increase (as depicted in Figures 2 and 3), significantly impeding longitudinal diffusion. While there are minor differences between the bulk and flux values of diffusion coefficients, as evident in Figure 8, except for transverse diffusion at low fields, where the bulk values surpass the flux values.

From Figure 9, it is evident that the rate coefficients for rotational and vibrational excitations (denoted in the figure as RE1, RE2, Vib1, Vib2, and Vib3) exhibit an upward trend as the electric field strength increases. This trend is attributed to the increased overlap between the Ion energy probability functions (depicted in Figure 3 and Figure 4) and the respective collision frequencies for excitations, which depend on the energy level.
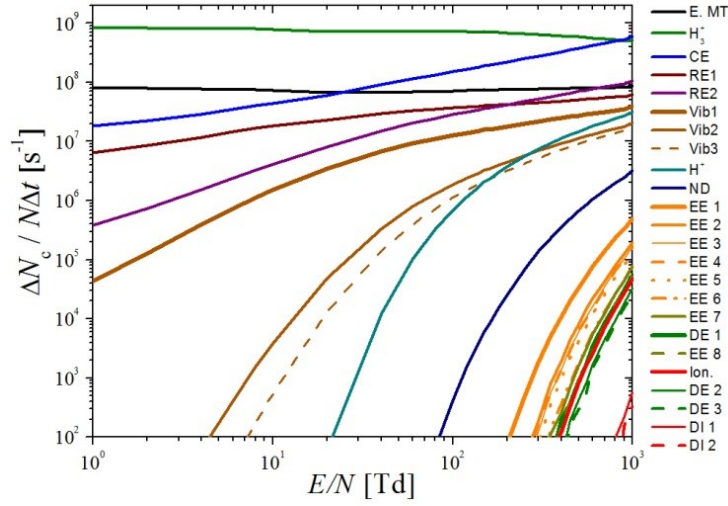
Figure 9. Rate coefficients for H_2^+ in H_2 a function of E/N at 300 K. The lines representing the rate coefficients correspond to the lines for the corresponding cross-sections shown in Figure 2.

4. Conclusion

In this paper we have determined the cross section of elastic moment transport as a function of energy for H_2^+ scattering on H_2 that can be used in modeling H_2^+ transport in H_2 gas. We used the data for a simple theoretical cross-section of the transmission of the total moment and obtained the cross-section of the transmission of the elastic moment by deduction of all experimentally obtained cross-sections of the charge exchange. In doing so, we assumed that the measured cross-sections of the charge exchange were collisions with the highest probability. Thus, in this paper, we have estimated the set of cross sections for H_2^+ ions in H_2

that can be used as an independent input in modeling H_2^+ ion transport. This estimation was performed using measured cross-sections of charge exchange.

Since, according to our knowledge, there is no direct information in the literature on how the mobility of high recombination energy ions, such as H_2^+ ions, behave in H_2 gas, we calculated transport parameters using the Monte Carlo simulation method (Nikitović *et al.*, 2014; Nikitović *et al.*, 2019).

In this work, we obtained and considered data on mean energy, drift velocity, longitudinal and transversal diffusion coefficients, bulk and flux reduced mobility and rate coefficients. Data on swarm coefficients for positive and negative ions are required for hybrid and fluid codes (White *et al.*, 2014; Marjanović *et al.*, 2016) and the current focus on liquids or liquids in rare gas mixtures dictates the need to produce data compatible with these models. Given the current interest in liquid and / or liquid models in mixtures with rare gases, data on swarm coefficients for positive and negative ions for hybrid and fluid codes are needed.

References

Denpoh K. and Nanbu K.: Comprehensive ion-molecule reactive collision model for processing plasmas, 2022, *Journal of Vacuum Science & Technology Å 40* **063007**, doi: 10.1116/6.0002098

Denpoh K. and Nanbu K.: Self-consistent particle simulation of radio-frequency CF_4 discharge with implementation of all ion–neutral reactive collisions, 1998, *J. Vac. Sci. Technol. A* **16**, 1201, DOI: doi.org/10.1116/1.581259

Fraga M.M.F.R., Fraga F.A.F., Fetal S.T.G., Margato L.M.S., Ferreira Marques R., Policarpo A.J.P.L.: The GEM scintillation in He–CF_4, Ar–CF_4, Ar–TEA and Xe–TEA mixtures, 2003, *Nucl. Instrum. Meth. in Phys. Res. A* **504**, 88, DOI: doi.org/10.1016/S0168-9002(03)00758-7

Golzar K., Amjad-Iranagh S., Amani M., Modarress H.: Molecular simulation study of penetrant gas transport properties into the pure and nanosized silica particles filled polysulfone membranes, 2014, *J. Membrane Science* **451**, 117 https://doi.org/10.1016/j.memsci.2013.09.056

Kaboth A., Monroe J., Ahlen S., Dujmić D., Henderson S., Kohse G., Lanza R., Lewandowska M., Roccaro A., Sciolla G., Skvorodnev N., Tomita H., Vanderspek R., Wellenstein H., Yamamoto R., Fisher P.: A measurement of photon production in electron avalanches in CF_4, 2008, *Nucl. Instrum. Meth. in Phys. Res. A* **592**, 63, DOI: doi.org/10.1016/j.nima.2008.03.120

Krstić P. S. and Schultz D. R.: Elastic and related transport cross sections for singly charged ion–atom scattering of light metals (Li, Be, B) and hydrogen, 2009, *J. Phys. B: At. Mol. Opt. Phys.* **42**, 065207
DOI 10.1088/0953-4075/42/6/065207

Mason E.: Scattering of Low-Velocity Molecular Beams in Gases, 1957, *J. Chem. Phys.* **27**, 782
https://doi.org/10.1063/1.1743829

Marjanović S., Banković, D. Cassidy A., Cooper B., Deller A., Dujko S. and Petrović Z. Lj.: A CF4 based positron trap, 2016, *J. Phys. B: At. Mol. Opt. Phys.* **49**, 215001
10.1088/0953-4075/49/21/215001

Ness K. F. and Robson R. E.: Velocity distribution function and transport coefficients of electron swarms in gases. II. Moment equations and applications, 1986, *Phys. Rev. A* **34**, 2185, DOI: doi.org/10.1103/PhysRevA.34.2185

Nikitović Ž., Raspopović Z. and Stojanović V.: Cross sections set and transport coefficients for Ar^+ in Ar/CF_4 mixtures, 2018, *Eur. Phys. J. D* **72**, 168, DOI: doi.org/10.1140/epjd/e2018-90059-1

Nikitović Ž., Raspopović Z.: Rate coefficients for Ar^+ in Ar/BF_3 mixtures, 2021, *Eur. Phys. J. D* **75**, 118, DOI:10.1140/epjd/s10053-021-00061-3

Nikitović Ž., Raspopović Z., Stojanović V. and Jovanović J.: Transport parameters of F-ions in Ar/BF_3 mixtures, 2014, *EPL* **108**, 35004, DOI:10.1209/0295-5075/108/35004

Nikitović Ž. D., Stojanović V. D. and Raspopović Z. M.: Modeling elastic momentum transfer cross-sections from mobility data, 2016, *EPL* **114**, 25001, DOI:10.1209/0295-5075/114/25001

Nikitović Ž., Raspopović Z. and Stojanović V.: Reduced mobility of Ar^+ in Ar/BF_3 mixtures, 2019, *EPL* **128**, 15001, DOI:10.1209/0295-5075/128/15001

Petrović Z. Lj., Raspopović Z. M., Stojanović V. D., Jovanović J. V., Malović G., Makabe T. and de Urquijo J.: Data and modeling of negative ion transport in gases of interest for production of integrated circuits and nanotechnologies, 2007, *J. Appl. Surf. Sci.* **253**, 6619
https://doi.org/10.1016/j.apsusc.2007.02.005

Phelps A. V.: Cross Sections and Swarm Coefficients for H^+, H_2^+, H_3^+, H, H_2, and H_- in H_2 for Energies from 0.1 eV to 10 keV, 1990, *J. Phys. Chem. Ref. Data* **19**, 653
doi.org/10.1063/1.555858

Phelps A. V.: Energetic ion, atom, and molecule reactions and excitation in low-current H_2 discharges:Model 2009, *Phys. Rev. E* **79**, 066401
https://doi.org/10.1103/PhysRevE.79.066401

Phelps A. V.: Collisional kinetics of non-uniform electric field, low-pressure, direct-current discharges in H_2, 2011, *Plasma Sources Sci. Technol.* **20**, 043001
DOI 10.1088/0963-0252/20/4/043001

Ristivojević Z. and Petrović Z. Lj.: A Monte Carlo simulation of ion transport at finite temperatures, 2012, *Plasma Sources Sci. Technol.* **21**, 035001
DOI 10.1088/0963-0252/21/3/035001

Radzig A. A. and Smirnov B. M.: Reference Data on Atoms, Molecules, and Ions, (Springer, New York, 1985), *p. 444* **ISBN 10: 3540124152**, ISBN 13: 9783540124153

Robson R. E., White R. D., Petrovic Z. Lj.: Colloquium: Physically based fluid modeling of collisionally dominated low-temperature plasmas, 2005, *Rev. Mod. Phys.* **77**, 1303, DOI:10.1103/RevModPhys.77.1303

Todd B., Young J. B.: Thermodynamic and transport properties of gases for use in solid oxide fuel cell modelling, 2002, *J. Power Sources* **110**, 186 https://doi.org/10.1016/S0378-7753(02)00277-X

White R. D., Tattersall W., Boyle G., Robson R. E., Dujko S., Petrović Z. Lj., Banković A., Brunger M. J., Sullivan J. P., Buckman S. J. and Garcia G.: Low-energy electron and positron transport in gases and soft-condensed systems of biological relevance, 2014, *Applied Radiation and Isotopes* **83**, 77, DOI: doi.org/10.1016/j.apradiso.2013.01.008

Energetic solar flare events in relation with subionospheric impact on 6-10 September 2017: data and modeling

A. Kolarski, V. A. Srećković [iD], M. Langović and F. Arnaut

*Institute of Physics Belgrade, University of Belgrade, Pregrevica 118,
11080 Belgrade, Serbia, (E-mail: aleksandra.kolarski@ipb.ac.rs)*

Abstract. Solar flares are among main extraterrestrial events that are well known to severely affect both space weather and near-Earth surrounding conditions. Under incident X-ray solar flare radiation, ionospheric plasma undergoes perturbations clearly and distinctly observable on ground-based monitoring systems' recordings. Mid-latitude lower ionosphere under influence of energetic solar flare events was examined by employing different numerical modeling procedures, including Machine Learning, relying on ground-based Very Low Frequency (VLF) radio signal recordings from Belgrade VLF database and solar soft X-ray irradiance satellite measurements taken from Geostationary Operational Environmental Satellite (GOES) database.

Key words: Solar activity – Solar X-ray flares – radio signal perturbations – GOES – data – modeling

1. Introduction

Through complex solar–terrestrial interactions, Earth is continually under Sun's emitted radiation influences, both of the electromagnetic and corpuscular nature (Kelly, 2009). As the major source of numerous and diverse driving agents related with Earth's magnetospheric and ionospheric perturbations, Sun's varying activity is under ongoing increasingly extensive research (see Hayes et al., 2021; Rycroft et al., 2000, and references therein). As modern society progressively becomes more and more dependent on complex technological systems including satellite, telecommunication and power grid networks, solar activity as potentially hazardous to these systems and consequently potentially threatening to an urban way of life, gained also in recent years more attention outside pure scientific community (Yasyukevich et al., 2018).

As still reliably unpredictable to current knowledge, solar activity especially in terms of high and extreme energetic solar events' occurrences, such as e.g. energetic eruptions of high class solar flare (SF) events and coronal mass ejections (CMEs) and their interactions, is often presented through analyses of separate events which make case studies very important in the sense of a comprehensive

overview of evolution of such complex natural phenomena and their impacts on near Earth's surroundings (Srećković et al., 2021a; Kolarski et al., 2023). Here, solar activity during the most active period of the descending branch of the solar cycle (SC) 24, with the respect of high class X-ray solar flare events with geo-effective implications, is presented as a case study of solar conditions throughout a period enclosing the strongest SF events in September 2017, as observed by ground-based systems located in Belgrade (Serbia) at the Institute of physics Belgrade (44.85^{o}N; 20.38^{o}E), through subionospheric Very Low Frequency (VLF) propagation disturbances (e.g. Šulić et al., 2016) recorded on signal emitted from UK, employing four numerical techniques developed for retrieving lower ionospheric plasma parameters (Silber & Price, 2017; Arnaut et al., 2023).

Table 1. X-class SFs from September 2017, from GOES15 database.

Fare date	Class	Region	Time UT			Ix^{max}
			Start	Max.	End	(10^{-4} Wm^{-2})
6 September 2017	X2.2	2673	08:57	09:10	09:17	2.2658*
6 September 2017	X9.3	2673	11:53	12:02	12:10	9.3293
7 September 2017	X1.3	2673	14:20	14:36	14:55	1.3880
10 September 2017	X8.2	2673	15:35	16:06	16:31	8.2808

* GOES13 data

2. Observations

Year of 2017 belongs to the descending branch of the SC 24, the cycle characterized by morphology notably decreased compared to several previous cycles, and with the intensity that is fourth smallest since the solar cycle 1 (Kolarski et al., 2022; Grodji et al., 2022). Even though it is placed close to the solar minimum between SCs 24 and 25, regarding solar flare activity year of 2017 stands out from other surrounding years from this descending branch, especially taking into consideration very active periods during months of September (when in total 99 SFs occurred, with 27 M-class and 4 X-class events, from which 2 of them were the strongest of SC 24) and April (when in total 52 SFs occurred, with 7 M-class and without X-class events). Solar conditions during September 2017 are mainly related to active region 2673 (AR12673) from which the strongest, 4 X-class SFs of intensity in range X1.3-X9.3 occurred during days of 06, 07 and 10 September (with X2.2 & X9.3 on 06 September, X1.3 on 07 September and X8.2 on 10 September). This active region with complex evolution appeared on 29 August on the south-eastern limb of the Sun and on 11 September disappeared from the Earth-view of the Sun, producing in total 77 SFs, of which 1 B (B9.8), 45 C in range C1-C9.8, 27 M in range M1-M8.1 and 4 X-class flares in range X1.3-X9.3. It is important to note that all M- and X-class SFs from September 2017 are related to this active region. Regarding the rest of the September, only
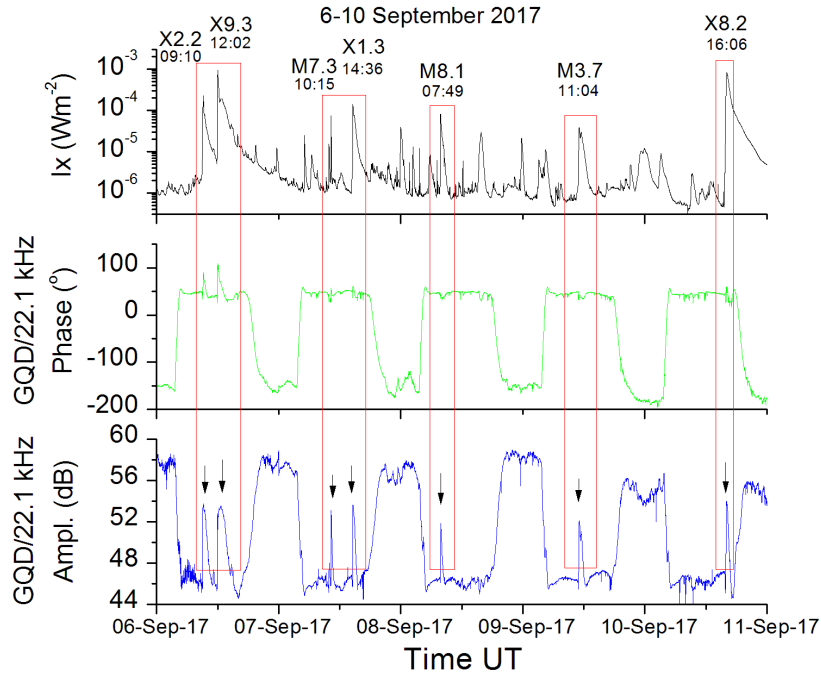
Figure 1. GQD signal perturbations registered in Belgrade during period of high solar activity from 06-10 September 2017 and GOES solar X-ray flux data as shown in the panels from lower to upper, respectively. Detected strong solar flares are marked with red rectangle.

weak flare activity of B- and C-class related to active regions 2677, 2680, 2681, 2682 (re-designated former active region 2673 which reappeared on 24 September and became again visible at the eastern limb of the Sun) and 2683 was reported, with total of 38 SFs in range B1-C3, with just 5 B-class SFs in range B2.2-B4.2 from active region 2682. There were also some days without reported flare activity, of which 6 days in a row 14-19 September and 2 days of 21-22 September. Main characteristics of X-class SFs from September 2017 are given in Table 1, with solar soft X-ray flux (0.1-0.8 nm) taken from Geostationary Operational Environmental Satellite (GOES) archive database (https://satdat. ngdc.noaa.gov/sem/goes/data/avg/).

Solar flare event of class X9.3, that occurred during solar cycle's declining branch relatively close to the solar minimum, particularly is interesting since event of X-class was not occurred as far back as on 05 May 2015 (X2.7), and of similar strength as far back as on 05 December 2006 (X9). If we exclude some weaker X-class SFs (e.g. as on 06 August 2011 (X6.9), 06 December 2006 (X6.5), 09 September 2005 (X6.2) and 08 September 2005 (X5.4)) and some significantly stronger SFs (e.g. as on 07 September 2005 (X17+), 04 November
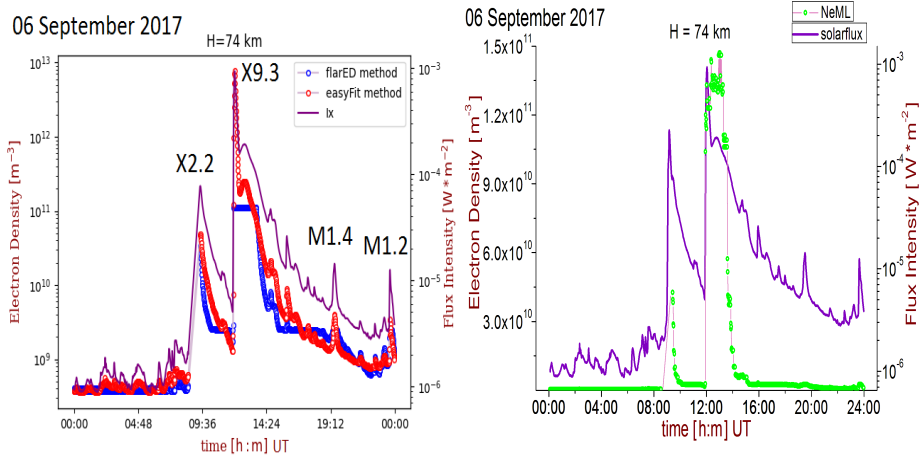
Figure 2. Variations of GOES X-ray flux (in violet) and Ne ($h = 74$ km) in function of UT on 06 September 2017 obtained by FlarED and easyFit methods (in blue and red, respectively) on the left and from ML method (in green) on the right.
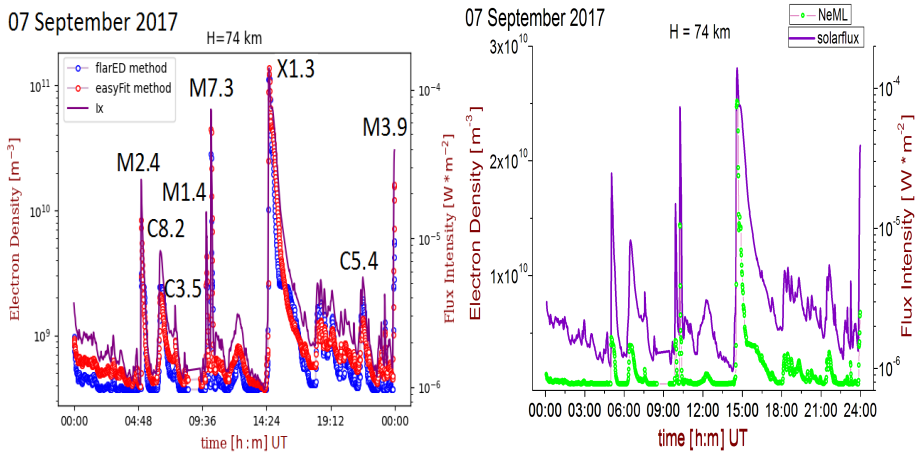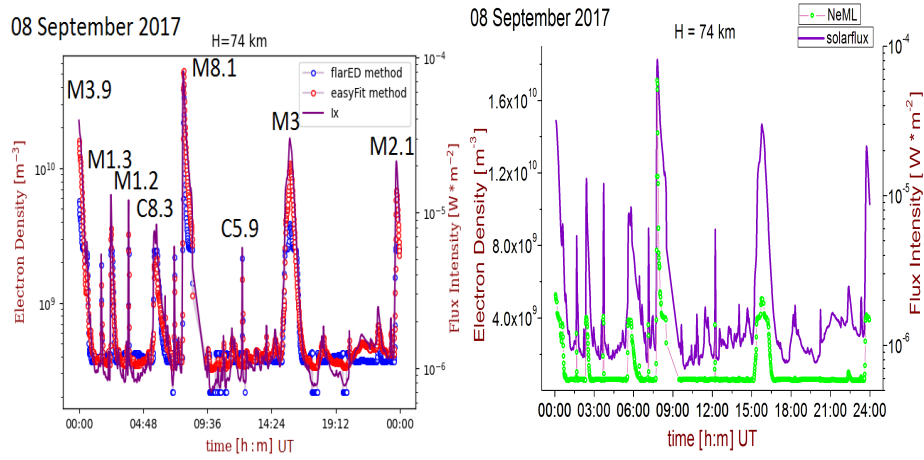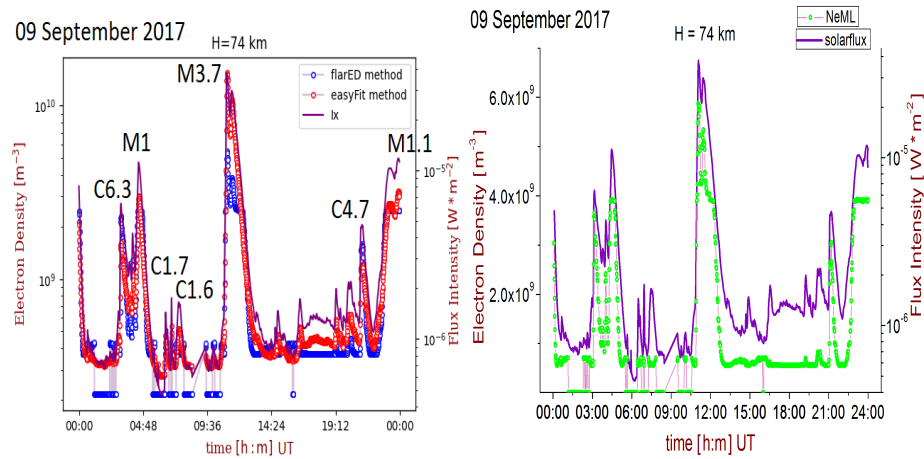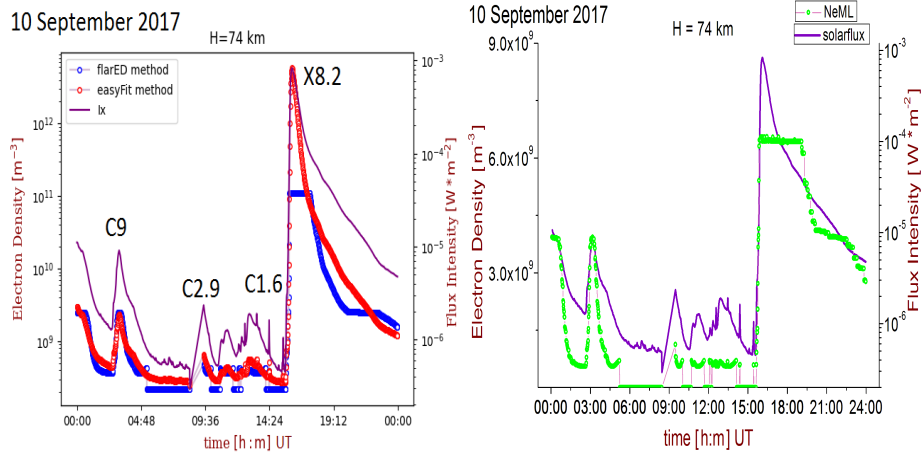

Figure 3. Variations of GOES X-ray flux (in violet) and Ne ($h = 74$ km) in function of UT on 07 September 2017 obtained by FlarED and easyFit methods (in blue and red, respectively) on the left and from ML method (in green) on the right.

Figure 4. Variations of GOES X-ray flux (in violet) and *Ne* (*h* = 74 km) in function of UT on 08 September 2017 obtained by FlarED and easyFit methods (in blue and red, respectively) on the left and from ML method (in green) on the right.

Figure 5. Variations of GOES X-ray flux (in violet) and *Ne* (*h* = 74 km) in function of UT on 09 September 2017 obtained by FlarED and easyFit methods (in blue and red, respectively) on the left and from ML method (in green) on the right.

Figure 6. Variations of GOES X-ray flux (in violet) and Ne ($h = 74$ km) in function of UT on 10 September 2017 obtained by FlarED and easyFit methods (in blue and red, respectively) on the left and from ML method (in green) on the right.

2003 (X28+), 28 October 2003 (X17.2+), 02 April 2001 (X20+) and 15 April 2001 (X14.4)), SF of similar strength as X9.3 from September 2017 occurred about two decades in the past i.e. on 06 November 1997 (X9.4). During 06, 07 and 10 September R3 radio blackouts related to X-class SFs were reported.

3. Results and discussion

VLF signal's response to strong solar X-ray flare events from September 2017 was monitored in Belgrade (44.85°N; 20.38°E) on signal transmitted from UK (GQD/22.1 kHz), using recordings from BEL AWESOME (Atmospheric Weather Electromagnetic System for Observation Modeling and Education) receiving system operating in narrow-band mode (Šulić et al., 2016). Response of GQD signal to these X-class SF together with corresponding solar X-ray irradiances during the most active days in September 2017 are given in Figure 1. Under strong solar X-ray radiation in soft range, GQD signal's amplitude and phase responded by following incident X-ray flux with time delay corresponding to the sluggishness (e.g. Mitra, 1974; Hayes et al., 2021; Žigman et al., 2023), with perturbations of complex morphology, characteristic for this signal as recorded in Belgrade (Kolarski & Grubor, 2014; Grubor et al., 2008). Amplitude and phase perturbations induced by these 4 X-class SFs reached up to 8 dB in amplitude and up to a few tens of degrees in phase, compared to unperturbed ionospheric conditions. Based on recorded GQD signal's amplitude and phase perturbations, modeling of propagation parameters (Wait & Spies, 1964) was conducted using Long Wave Propagation Capability (LWPC) software (Ferguson, 1998), with

goal that modeled and real conditions within waveguides match as close as possible. Aside LWPC, for obtaining lower ionospheric plasma parameters, three other numerical techniques were applied: FlareED and easyFit (Srećković et al., 2021a,b) and also novel method based on Machine Learning (ML) approach.

Table 2. Analyzed intense SF events from September 2017.

(dd/mm/yy) Class Ix^{max} time (UT)	Ne_{LWPC} (m^{-3})	$Ne_{easyFit}$ (m^{-3})	Ne_{FlarED} (m^{-3})	Ne_{ML} (m^{-3})
06/09/17 X2.2 09:10	$2.06 \cdot 10^{11}$	$3.49 \cdot 10^{11}$	$1.12 \cdot 10^{11}$	$1.23 \cdot 10^{11}$
06/09/17 X9.3 12:02	$1.15 \cdot 10^{12}$	$7.67 \cdot 10^{12}$	$1.12 \cdot 10^{11}**$	$1.33 \cdot 10^{11}*$
07/09/17 M7.3 10:15	$1.11 \cdot 10^{11}$	$4.45 \cdot 10^{10}$	$2.85 \cdot 10^{10}$	$1.44 \cdot 10^{10}$
07/09/17 X1.3 14:36	$1.76 \cdot 10^{10}$	$1.37 \cdot 10^{11}$	$1.12 \cdot 10^{11}$	$2.52 \cdot 10^{10}$
08/09/17 M8.1 07:49	$6.59 \cdot 10^{10}$	$5.25 \cdot 10^{10}$	$4.17 \cdot 10^{10}$	$1.66 \cdot 10^{10}$
10/09/17 X8.2 16:06	$2.12 \cdot 10^{11}*$	$5.79 \cdot 10^{12}$	$1.12 \cdot 10^{11}**$	$6.44 \cdot 10^{9}*$

*Unreliable result
***Saturation

In contrast to other energetic SFs reported within this active period, which were directed towards the Earth, main difference of X8.2 SF is in terms of geo-effective potential, since this event was the only one SF that erupted almost on the far side of the Sun's surface and did not directly affected the Earth. However, since this event was highly energetic, Earth was still affected in great deal, which can be clearly seen in perturbations of subionosphericaly propagating GQD signal. Another specific feature related to this event is that during the occurrence of X8.2 SF on GQD signal recorded in Belgrade there was a transition period from stable daytime to stable nighttime ionospheric conditions related to terminator period of sunset. Although process of modeling lower ionospheric response related to high class SFs based on VLF parameters is challenging by itself, some special circumstances, such as e.g. SF's occurrence during stable

daytime ionospheric conditions (such in case of e.g. X2.2 SF) and relatively not so high absolute amount of amplitude and/or phase perturbations (such in cases of some mid class SFs) etc., can go in favor especially when classical approach using LWPC software is employed. However, in conditions related to terminator periods modeling of SFs is especially challenging, which is emphasized in much greater deal when energetic ones are processed. Since classical approach in cases like X8.2 SF event is far from an ideal choice giving unreliable results, application of other numerical techniques, such as e.g. FlareED and easyFit methods, can be beneficial providing needed data.

FlareED and easyFit methods are already proven as efficient both in cases of moderate and high-class SF events (Barta et al., 2022; Kolarski et al., 2023). Together with this two methods, a novel technique employing ML procedures is developed and applied to the same cases of chosen energetic SFs from inspected period 06-10 September 2017, with aim to be tested and verified in conditions of strong solar X-ray radiation. Output results from FlareED and easyFit methods of electron density variations (at the arbitrary reference height of 74 km) covering entire days including cases of energetic SFs from inspected period 06-10 September 2017 are given on the left in Figures 2-6, with soft X-ray flux in violet and electron densities in blue and red for FlareED and easyFit methods, respectively. Results from novel technique relying on ML procedures are presented on the right in Figures 2-6, with soft X-ray flux in violet and electron density variations in green. Both FlareED and easyFit methods are sensitive to X-ray flux variations related to moderate and high-class SF events, with main difference that in case of very energetic SFs, like X9.3 and X8.2, FlareED method gave electron density that went into saturation, compared to output from easyFit method that successfully mimics input X-ray irradiance and gives much higher electron density values as well. Method relying on ML has also proven itself to be an efficient in cases of strong SFs, as other two methods, but also gave some results that went into saturation (especially related to X8.2 and in some sense to X9.3). Comparison between results, in cases of strongest SFs from inspected active period, obtained with applied different numerical methods is given in Table 2.

EasyFit method (Srećković et al., 2021a) gave electron densities higher than FlarED (Srećković et al., 2021b), while ML results are closer to these from FlarED than to easyFit. When compared to LWPC results, it can be said that easyFit method works better than other applied methods, except in the cases of X1.3 where results differ for about an order of magnitude and M7.3 about half an order of magnitude. Unfortunately in the case of M8.2 results from LWPC approach are not reliable, while results from FlarED and ML methods both went into saturation, just as in the case of X9.3, so only available result is from easyFit method. EasyFit gave result for X8.2 of the same order of magnitude but slightly lower than in the case of X9.3. In general, technique relying on ML procedures gives promising results, but also requires some further adjustments in order to provide correct output especially in cases of very strong SF events, like X9.3 and

X8.2. Developing novel numerical techniques that successfully represent lower ionospheric responses especially in cases of very strong SF events is of great importance since classical techniques such as LWPC has model limitations on one hand and VLF parameters are not always favourable on the other.

4. Conclusions and future studies

In this contribution numerical modeling of lower ionospheric response to energetic SF events during September 2017, in relation to subionospheric VLF propagation perturbations with analyzed GQD signal recordings from BEL VLF station, was conducted by employing four different numerical procedures: by classical approach using LWPC software, by approximate FlareED and easyFit methods and by novel procedure relying on ML techniques. Focus was on period 06-10 September 2017 covering especially active solar conditions with 4 X-class SFs in range X1.3-X9.3 and also including 2 strongest M-class SFs, of intensity M7.3 and M8.1, from September 2017. Results related to electron density variations obtained by FlareED, easyFit and ML methods are compared to each other and to these from classical approach using LWPC software. In general, when compared with LWPC output electron densities, best results were obtained by easyFit method. ML procedures gave promising results, but further work is necessary in order to provide better results just in cases of very energetic SFs, like these X9.3 and X8.2.

References

Arnaut, F., Kolarski, A., & Srećković, V. A., Random Forest Classification and Ionospheric Response to Solar Flares: Analysis and Validation. 2023, *Universe*, **9**, DOI: 10.3390/universe9100436

Barta, V., Natras, R., Srećković, V., et al., Multi-instrumental investigation of the solar flares impact on the ionosphere on 05–06 December 2006. 2022, *Frontiers in Environmental Science*, **10**, DOI: 10.3389/fenvs.2022.904335

Ferguson, J. 1998, Computer programs for assessment of long-wavelength radio communications, version 2.0: User's guide and source files, Tech. rep., Space and naval warfare systems center San Diego CA

Grodji, O. D. F., Doumbia, V., Amaechi, P. O., et al., A Study of Solar Flare Effects on the Geomagnetic Field Components during Solar Cycles 23 and 24. 2022, *Atmosphere*, **13**, DOI: 10.3390/atmos13010069

Grubor, D., Šulić, D., & Žigman, V., Classification of X-ray solar flares regarding their effects on the lower ionosphere electron density profile. 2008, *Annales Geophysicae*, **26**, 1731, DOI: 10.5194/angeo-26-1731-2008

Hayes, L. A., O'Hara, O. S. D., Murray, S. A., & Gallagher, P. T., Solar Flare Effects on the Earth's Lower Ionosphere. 2021, *Solar Physics*, **296**, 157, DOI: 10.1007/s11207-021-01898-y

Kelly, M. C. 2009, *The Earth's Ionosphere: Plasma Physics and Electrodynamics, Second Edition*

Kolarski, A. & Grubor, D., Sensing the Earth's low ionosphere during solar flares using VLF signals and goes solar X-ray data. 2014, *Advances in space research*, **53**, 1595, DOI: 10.1016/j.asr.2014.02.022

Kolarski, A., Srećković, V. A., & Mijić, Z. R., Monitoring solar activity during 23/24 solar cycle minimum through VLF radio signals. 2022, *Contributions of the Astronomical Observatory Skalnate Pleso*, **52**, 105, DOI: 10.31577/caosp.2022.52.3.105

Kolarski, A., Veselinović, N., Srećković, V. A., et al., Impacts of Extreme Space Weather Events on September 6th, 2017 on Ionosphere and Primary Cosmic Rays. 2023, *Remote Sensing*, **15**, 1403, DOI: 10.3390/rs15051403

Mitra, A. P. 1974, *Ionospheric effects of solar flares* (Springer, Berlin/Heidelberg)

Rycroft, M., Israelsson, S., & Price, C., The global atmospheric electric circuit, solar activity and climate change. 2000, *Journal of Atmospheric and Solar-Terrestrial Physics*, **62**, 1563, DOI: https://doi.org/10.1016/S1364-6826(00)00112-7

Silber, I. & Price, C., On the use of VLF narrowband measurements to study the lower ionosphere and the mesosphere–lower thermosphere. 2017, *Surveys in Geophysics*, **38**, 407, DOI: 10.1007/s10712-016-9396-9

Srećković, V. A., Šulić, D. M., Ignjatović, L., & Vujčić, V., Low Ionosphere under Influence of Strong Solar Radiation: Diagnostics and Modeling. 2021a, *Applied Sciences*, **11**, 7194, DOI: 10.3390/app11167194

Srećković, V. A., Šulić, D. M., Vujčić, V., Mijić, Z. R., & Ignjatović, L. M., Novel Modelling Approach for Obtaining the Parameters of Low Ionosphere under Extreme Radiation in X-Spectral Range. 2021b, *Applied Sciences*, **11**, 11574, DOI: 10.3390/app112311574

Šulić, D. M., Srećković, V. A., & Mihajlov, A. A., A study of VLF signals variations associated with the changes of ionization level in the D-region in consequence of solar conditions. 2016, *Advances in Space Research*, **57**, 1029, DOI: 10.1016/j.asr.2015.12.025

Žigman, V., Dominique, M., Grubor, D., Rodger, C. J., & Clilverd, M. A., Lower-ionosphere electron density and effective recombination coefficients from multi-instrument space observations and ground VLF measurements during solar flares. 2023, *Journal of Atmospheric and Solar-Terrestrial Physics*, **247**, 106074, DOI: 10.1016/j.jastp.2023.106074

Wait, J. R. & Spies, K. P. 1964, *Characteristics of the Earth-ionosphere waveguide for VLF radio waves* (US Department of Commerce, National Bureau of Standards, Boulder, CO, USA)

Yasyukevich, Y., Astafyeva, E., Padokhin, A., et al., The 6 September 2017 X-Class Solar Flares and Their Impacts on the Ionosphere, GNSS, and HF Radio Wave Propagation. 2018, *Space Weather*, **16**, 1013, DOI: 10.1029/2018SW001932

Analyzing solar activity with Belgrade muon station: case study of 2021 November 4th Forbush decrease

N.B. Veselinović[ID], M.B. Savić, D.M. Maletić, A.L. Dragić, R.M. Banjanac, D.R. Joković, D. Knežević, M. Travar and V.I. Udovičić

Institute of Physics Belgrade, University of Belgrade, Pregrevica 118, 11080 Belgrade, Serbia, (E-mail: veselinovic@ipb.ac.rs)

Abstract. The first significant Forbush decrease of the solar cycle 25 was recorded on November 4th, 2021. The Forbush decrease was observed with numerous ground based cosmic rays stations including Belgrade cosmic rays muons' station. Series of coronal mass ejections during October 28–November 4 2021. produce conditions for this Forbush decrease. We discuss here the variation of cosmic rays' flux detected with ground-based detectors and connection with conditions, measured in-situ, in interplanetary space around Earth, flux of solar wind protons measured with SOHO probe to assess implication for solar-terrestrial coupling processes.

Key words: Cosmic rays – Forbush decrease – Space weather – muon detector

1. Introduction

One of the methods of researching solar-terrestrial coupling processes is observing the response of the flux of cosmic rays (CR) to various types of disturbances (or drivers) in the heliosphere. Transient phenomena detected in CR flux due to modulation in the heliosphere is the Forbush decrease: a sudden drop in CR flux followed by a gradual return to the previous level. It occurs as CR interact with irregularities in the interplanetary magnetic field (IMF), usually connected with the emission of coronal plasma known as a coronal mass ejection (CME) and its interplanetary counterpart (ICME) (Yermolaev et al., 2021). In recent decades, space probes have measured IMF parameters in-situ as well as particle flux. The detected particles can be fast-moving particles, known as solar energetic particles (SEPs), related to violent eruptions from the Sun that can cause a sudden increase in measured CR flux at the surface - a ground level enhancement (GLE). The other particles detected with probes, aside from solar wind particles and SEPs, are energetic storm particles (ESP) accelerated locally by shocks driven by fast ICMEs (Desai & Giacalone, 2016) and low-energy CR

(Veselinović et al., 2021). It has been shown (Koldobskiy et al., 2019; Savić et al., 2023; Kolarski et al., 2023) that parameters measured in-situ correlate with the magnitude and time evolution of FD. The end of October and the beginning of November 2021 marked extreme activity with a strong X-class solar flare (CIT), accompanied by the first Ground Level Enhancement (GLE) event in this cycle on October 28th, measured by several ground stations (Papaioannou, A. et al., 2022). There were several typical CMEs during this period. Most pronounced were two halo CMEs on October 28th and November 2nd. The second halo CME, due to its speed, caught up with previous ICMEs and produced a CME-CME interaction (Li et al., 2022).These disturbances created additional modulation of CR, producing the first strong FD in the present solar cycle, detected by multiple ground stations around the globe (Chilingarian et al., 2022).

The present case-study combines in-situ measurements of solar wind parameters and proton flux in near-Earth space with measurements on the ground to analyze how these parameters affect parameters of the FD detected on November 4th, 2021.

2. Ground level cosmic ray observations

The most widely method of detecting CR use detectors that are part of the worldwide network of Neutron Monitors (NM) (`https://www.nmdb.eu/nest/`). One of the other species of these secondary CR that can be detected and used for monitoring primary CR are muons.

2.1. Belgrade muon detector

The ground level Belgrade muon station (GLL) is a part of the Low-Background Laboratory for Nuclear Physics at the Institute of Physics, Belgrade, Serbia. The energy range of the observed primary CR extends and complements the energy ranges detected by the NM network, but is still sensitive to CR modulation of the heliosphere. Details of the experimental setup, as well as the calculated response function of the detectors, are presented in (Veselinović et al., 2017).

2.2. Ground level data analysis

Both NM and muon detectors measure integral flux over different energy ranges, so the median energy of the detected primary CR is used in the analysis of the measured data. Another property of the detector system is Cut-off rigidity, the minimal magnetic rigidity that the CR must have in order to penetrate the IMF and geomagnetic field. To determine the amplitude of the FD for each station, which differs in median energy and asymptotic direction, a baseline was established using the average hourly count rate during mid-October 2021 when solar activity was low. For this study, we utilized 1-hour time series of CR flux detected at 17 NM stations and GLL data (Table 1).

Table 1. Cut-off rigidity (R_c) and median energy (E_m) of primary CR for several stations.

Stations	R_c (GV)	E_m (GeV)	Stations	R_c (GV)	E_m (GeV)
Belgrade	5.3	63	Kerguelen	1.14	10.4
Athens	8.53	17.8	Oulu	0.8	10.3
Guadalajara	6.95	15.4	Apatity	0.65	10.3
Baksan	5.6	13.7	Norilsk	0.63	10.3
Jungfraujoch	4.5	12.6	Tixie Bay	0.5	10.2
Lomnicky stít	3.84	12	Fort Smith	0.3	10.2
Dourbes	3.18	11.5	Inuvik	0.3	10.2
Kiel	2.36	11	S. Pole bare	0.1	10.1
Yakutsk	1.65	10.6	S. Pole	0.1	10.1

Median energy for NM was found using formula given in Li et al. (2023) and median energy for GLL was found using Monte Carlo method of CR transport. Dependence of FD amplitude on CR median energy is given by power law (Cane, 2000)

$$\frac{\Delta N}{N} = E^{-a} \tag{1}$$

Here N is CR flux, E is median energy and a is power exponent that depends on heliospheric conditions.

A scatter plot of the selected event is given (Figure 1) plotted in log-log scale and it show clear median rigidity dependence of the amplitude of FD.

Steeper spectrum during this event shows greater modulation of primary CR. If GLL data is included in the plot, the power exponent is not so large so that can be interpreted as stronger modulation of the lower energy CR due to CME-CME interaction. Linear regression is performed to found power indices correspond to November 2021 event. Power index for NM only is 1.23±0.22 and for NM and GLL power index is 0.62±0.10. This is, in general, in good agreement with some previous studies (Lingri et al. (2016) and references within).

3. Relation to in-situ measured data

In this study we used measured in-situ parameters relevant for heliospheric studies which are available at GSFC/Space Physics Data Facility, in the form of 1-hour resolution OMNI data (https://spdf.gsfc.nasa.gov/pub/data/omni/lowresomni/). Also we used proton flux date gathered by SOHO probe with two detectors, ERNE and EPHIN, onboard SOHO probe (Torsti et al., 2000; Kühl & Heber, 2019) at Lagrange point 1 in vicinity of Earth. Comparison between 1-hour time series of selected parameters of IMF from OMNI data and
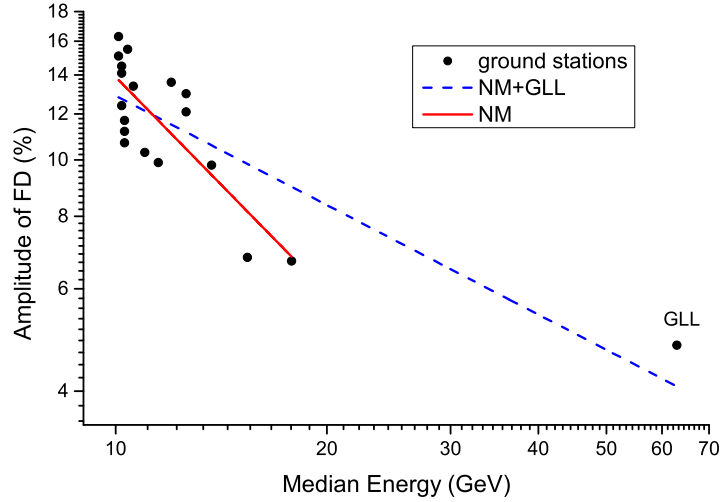
Figure 1. Rigidity spectrum of FD from November 4th 2021. Points represent the amplitude of the Forbush decrease as seen by 18 NMs and Belgrade GLL muon station.

relative detected CR flux of NM with low cut-off rigidity at South Pole and Belgrade muon detector and similar comparison for the same time interval between CR flux detected with two ground level detectors and selected channels of SOHO/ERNE and SOHO/EPHIN proton flux data is shown in Figure 2.

The discrepancies between time series of CR flux detected with ground stations and parameters of the IMF shows that CR was influenced by complex interactions in the heliosphere where low energy proton flux detected in-situ with detectors on board SOHO does not contribute substantially either to condition in heliosphere or CR flux.Increase of SEP flux, apparent in all detected proton flux from SOHO/ERNE and SOHO/EPHIN, produce GLE event detected with NM with low cut-off rigidity. Shape of detected FD on different stations varied, as expected due to difference cut-off rigidity, median energy, detector design, and sensitivity.

Correlation between respective time series was found using Pearson correlation coefficient using 2-tail test for significance is given at Table 2.

As expected correlation of CR flux is greater for NM detector at South Pole due to lower energy of detected CR which are more sensitive to disturbances of IMF. Inverse correlation of average magnetic field and solar wind plasma speed with CR flux is expected due to scattering of CR on turbulent magnetic field that produce a decrease in detected CR flux. The lack of correlation between proton fluxes and higher energy CR flux detected with GLL shown that monitor only some of the proton energy channel is not sufficient to model FD over range of CR energies during complex event with CME-CME interaction. Modeling of
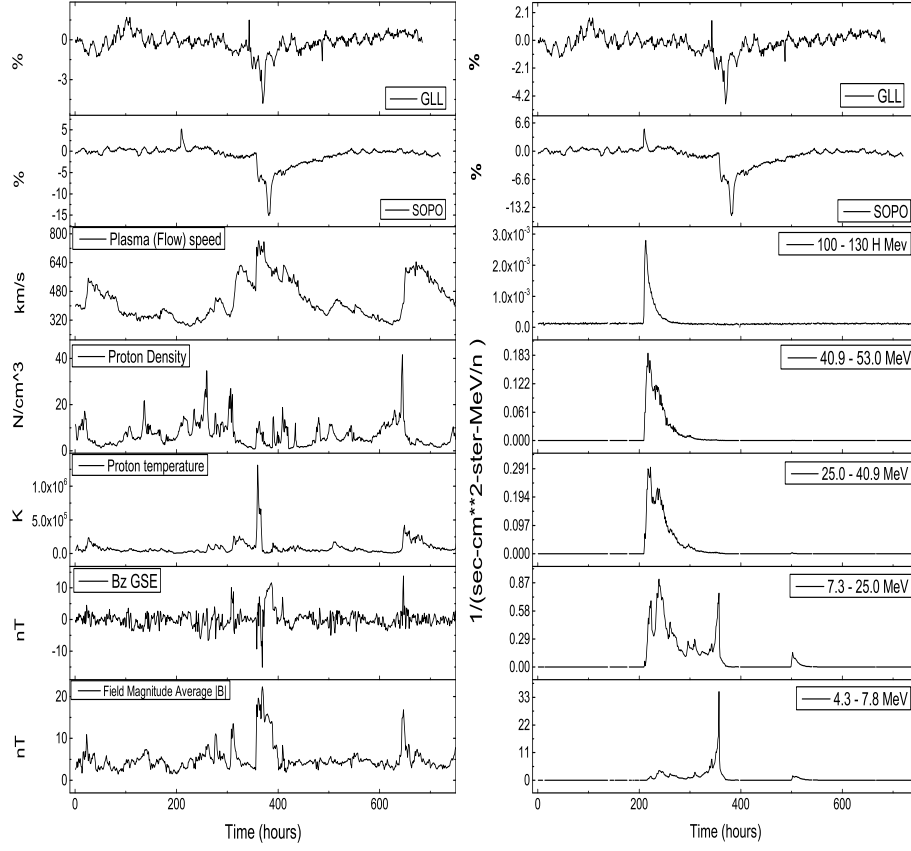
Figure 2. Left: Time series for plasma parameters (taken from OMNI database) and cosmic ray flux (measured at South Pole NM and GLL) from October 20th until November 20th, 2021. Right: Hourly time series for different proton energy channels from SOHO/ERNE and SOHO/EPHIN and two CR detectors time series for the same period.

this complicated shock-associated ICME disturbance where multiple shocks and transient flows merged is challenging and other studies (Zhao & Zhang, 2016; Werner et al., 2019) showed similar complex dependence of CR flux on different parameters of the IMF condition.

4. Summary

In this work we studied the FD occurred in November 4th, 2021, using data from Belgrade muon station and other multiple sources. Increased solar activity at the begging of the November 2021 had a measurable effect on CR, observed as a

Table 2. Pearson correlation coefficients for the correlation between CR flux detected at Belgrade CR station (GLL), at South pole (SOPO), flux of protons of different energies from SOHO/ERNE and SOHO/EPHIN and plasma parameters (from OMNI database) for the period from October 20th until November 20th, 2021.

	SOPO		GLL	
	Pearson Corr.	p-value	Pearson Corr.	p-value
SOPO	1		0.52	$<10^{-5}$
GLL	0.52	$<10^{-5}$	1	
|B| Average	-0.55	$<10^{-5}$	-0.48	$<10^{-5}$
Bz	-0.4	$<10^{-5}$	-0.15	$<10^{-4}$
Proton temperature	-0.18	$<10^{-5}$	-0.23	$<10^{-5}$
Proton Density	0.23	$<10^{-5}$	0.14	$<10^{-4}$
Plasma (Flow) speed	-0.61	$<10^{-5}$	-0.53	$<10^{-5}$
7.3-25.0 MeV p	0.17	$<10^{-5}$	-0.12	0.002
4.3-7.8 MeV p	0.01	0.67	-0.29	$<10^{-5}$
25.0-40.9 MeV p	0.21	$<10^{-5}$	0.02	0.5
40.9-53.0 MeV p	0.21	$<10^{-5}$	0.03	0.45
80-100 H Mev p	0.22	$<10^{-5}$	0.03	0.37

decrease in measured flux by all relevant CR stations. Energy range of affected primary CR was wide enough so effect was detected by neutron monitors but also muon detectors. Rapid decrease was detected with CR detectors around the world and it was one of the consequence, along with the strong G3-class geomagnetic storm, auroras and GLE event, of series of overlapping CMEs. We showed that based on measured amplitude of FD of the range of ground station that higher energy CR was less affected with heliospheric disturbance. Cross correlations between time series of CR flux and IMF and solar wind characteristics during these strongly disturbed heliospheric conditions were presented. Lack of strong correlation is also apparent for higher energy CR flux time series and time series of the heliospheric parameters and proton flux of certain energy ranges. This proves that, in order to better understand solar-terrestrial coupling processes, particularly its effect for higher energy particles requires more data from various sources and various probes and this analysis can be done in the future.

References

Cane, H. V., Coronal Mass Ejections and Forbush Decreases. 2000, *Space Science Reviews*, **93**, 55, DOI: 10.1023/A:1026532125747

Chilingarian, A., Hovsepyan, G., Martoyan, H., et al. 2022, Forbush decrease observed by SEVAN particle detector network on November 4, 2021

Desai, M. & Giacalone, J., Large gradual solar energetic particle events. 2016, *Living Reviews in Solar Physics*, **13**, 3, DOI: 10.1007/s41116-016-0002-5

Kühl, P. & Heber, B., Revising More Than 20 Years of EPHIN Ion Flux Data-A New Data Product for Space Weather Applications. 2019, *Space Weather*, **17**, 84, DOI: https://doi.org/10.1029/2018SW002114

Kolarski, A., Veselinović, N., Srećković, V. A., et al., Impacts of Extreme Space Weather Events on September 6th, 2017 on Ionosphere and Primary Cosmic Rays. 2023, *Remote Sensing*, **15**, DOI: 10.3390/rs15051403

Koldobskiy, S. A., Bindi, V., Corti, C., Kovaltsov, G. A., & Usoskin, I. G., Validation of the Neutron Monitor Yield Function Using Data From AMS-02 Experiment, 2011-2017. 2019, *Journal of Geophysical Research: Space Physics*, **124**, 2367, DOI: https://doi.org/10.1029/2018JA026340

Li, W.-h. et al., A study of Forbush Decreases effects with DAMPE experiment. 2023, *PoS*, **ICRC2023**, 1311, DOI: 10.22323/1.444.1311

Li, X., Wang, Y., Guo, J., & Lyu, S., Solar Energetic Particles Produced during Two Fast Coronal Mass Ejections. 2022, *The Astrophysical Journal Letters*, **928**, L6, DOI: 10.3847/2041-8213/ac5b72

Lingri, D., Mavromichalaki, H., Belov, A., et al., Solar Activity Parameters and Associated Forbush Decreases During the Minimum Between Cycles 23 and 24 and the Ascending Phase of Cycle 24. 2016, *Solar Physics*, **291**, 1025, DOI: 10.1007/s11207-016-0863-8

Papaioannou, A., Kouloumvakos, A., Mishev, A., et al., The first ground-level enhancement of solar cycle 25 on 28 October 2021. 2022, *A&A*, **660**, L5, DOI: 10.1051/0004-6361/202142855

Savić, M., Veselinović, N., Dragić, A., et al., New insights from cross-correlation studies between solar activity indices and cosmic-ray flux during Forbush decrease events. 2023, *Advances in Space Research*, **71**, 2006, DOI: https://doi.org/10.1016/j.asr.2022.09.057, recent progress in the physics of the Sun and heliosphere

Torsti, J., Mäkelä, P., Teittinen, M., & Laivola, J., SOHO/Energetic and Relativistic Nucleon and Electron Experiment Measurements of Energetic H, He, O, and Fe Fluxes during the 1997 November 6 Solar Event. 2000, *The Astrophysical Journal*, **544**, 1169, DOI: 10.1086/317219

Veselinović, N., Dragić, A., Savić, M., et al., An underground laboratory as a facility for studies of cosmic-ray solar modulation. 2017, *Nuclear Instruments and Methods in Physics Research Section A: Accelerators, Spectrometers, Detectors and Associated Equipment*, **875**, 10, DOI: https://doi.org/10.1016/j.nima.2017.09.008

Veselinović, N., Savić, M., Dragić , A., et al., Correlation analysis of solar energetic particles and secondary cosmic ray flux. 2021, *The European Physical Journal D*, **75**, 173, DOI: 10.1140/epjd/s10053-021-00172-x

Werner, A. L. E., Yordanova, E., Dimmock, A. P., & Temmer, M., Modeling the Multiple CME Interaction Event on 6–9 September 2017 with WSA-ENLIL+Cone. 2019, *Space Weather*, **17**, 357, DOI: https://doi.org/10.1029/2018SW001993

Yermolaev, Y. I., Lodkina, I. G., Dremukhina, L. A., Yermolaev, M. Y., & Khokhlachev, A. A., What Solar-Terrestrial Link Researchers Should Know about Interplanetary Drivers. 2021, *Universe*, **7**, DOI: 10.3390/universe7050138

Zhao, L.-L. & Zhang, H., Transient galactic cosmic-ray modulation during solar cycle 24: A comparative study of two prominent Forbush decrease events. 2016, *The Astrophysical Journal*, **827**, 13, DOI: 10.3847/0004-637X/827/1/13

Forbush decrease events associated with coronal mass ejections: Classification using machine learning

M.R. Savić[ID], N.B. Veselinović, A.L. Dragić, D.M. Maletić, R.M. Banjanac, D.R. Joković, D.Knežević, M.Travar and V.I. Udovičić

Institute of Physics Belgrade, University of Belgrade, Pregrevica 118, 11080 Belgrade, Serbia (E-mail: msavic@ipb.ac.rs)

Abstract. In presented work we further explore previously indicated possibility of the existence of two classes of Forbush decrease events, established by the prior analysis of the correlation between the shape of energetic proton fluence spectra and Forbush decrease properties. In an attempt to increase statistical robustness of the analysis and potentially reduce the uncertainties, we have developed an alternative classification procedure that employs machine learning and utilizes space weather parameters as input variables. Based on the overall performance, efficiency and flexibility of different machine learning methods we selected the best performing algorithm and established the optimal boundary value of Forbush decrease intensity to be used for class separation. A subset of good input variables was selected based on their predictive power.

Key words: cosmic rays – Forbush decrease – coronal mass ejection – solar energetic particles

1. Introduction

The dynamic activity of the Sun's coronal magnetic field can give rise to complex space weather events. These events may include solar flares (SFs), coronal mass ejections (CMEs), their interplanetary counterparts known as interplanetary coronal mass ejections (ICMEs), the emission of solar energetic particles (SEPs), and similar phenomena (Kahler, 1992; Yashiro & Gopalswamy, 2008; Gopalswamy, 2022).

One such complex event can produce a number of effects in the heliosphere, one of which is the acceleration of solar wind particles. There is a distinction between particles accelerated by a SF in the lower Sun's atmosphere and those accelerated locally by the CME shock. The later are often referred to as energetic storm particles (ESPs) (Desai & Giacalone, 2016).

Additionally, the passage of a CME can affect the primary cosmic rays (CRs) potentially resulting in a sudden drop in the observed CR flux, followed by a

recovery phase that takes place over the several following days. This effect is known as a Forbush decrease (FD) and can be observed by Earth-based CR detectors.

A previous study of the relationship between transient modulations in the fluxes of energetic protons and cosmic rays (measured near and at Earth respectively) indicated an existence of two classes of FD events (Savić et al., 2023). The main objective of this work is to expand this analysis and investigate whether a specific set of space weather (SW) parameters can be successfully used as input parameters for classification. The proposed procedure would aim to separate FD events into classes as indicated by the aforementioned analysis, while increasing the statistical significance and potentially the reliability of the analysis. Additional positive outcome of a successful classification would be the selection of a subset of SW parameters that prove to be good input variables. These variables could then be further used for the prediction of FD magnitudes utilizing some regression algorithm.

2. Motivation

As simultaneous ESP and FD events are very likely a consequence of the passage of an ICME, a relationship between them was assumed. To establish this possible connection, correlation of characteristics of proton fluence spectra and FD parameters was investigated (as described in more detail in Savić et al. (2023)).

The proton fluence spectra were calculated from in situ measurements at L1 by SOHO/ERNE instrument (Torsti et al., 1995), and fitted by a double-power law, as shown for one selected event on Figure 1.

Exponents obtained from these fits were used to parameterize the spectra shape, and some degree of correlation between these exponents and FD magnitudes was established. However, this analysis also indicated a possible existence of two classes of FD events, as illustrated in Figure 2. The plot shows the dependence of the FD magnitude corrected for the magnetospheric effect on one of the proton fluence spectra exponents. The green oval indicates a supposed class of events that exhibit a stronger correlation between these two variables, while the red oval indicates a class of events where this correlation is apparently weaker. One possible way to define the boundary between these two classes could be by introducing a cut on the intensity of the event.

Due to relatively low statistics of events where proton fluence can be reliably determined, one idea for extending this analysis is to try and utilize other space weather parameters in order to increase statistics and more strongly establish the assumed existence of two classes of FD events.

October 2001-2 (second event)
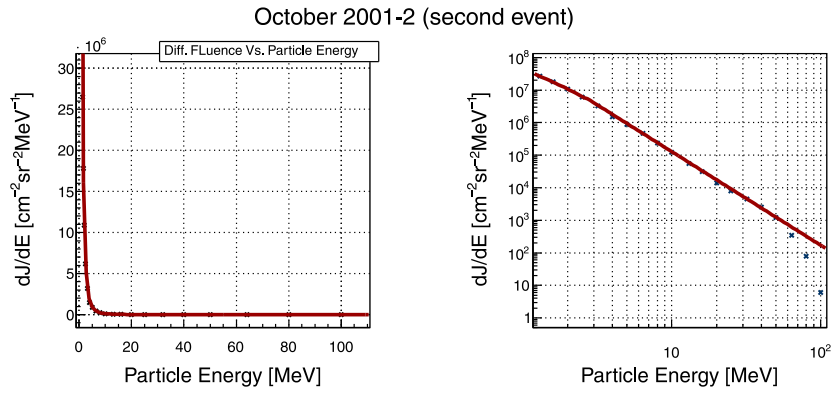
Figure 1. Proton fluence spectra at L1 for one event during October 2001, in linear (left) and logarithmic scale (right).
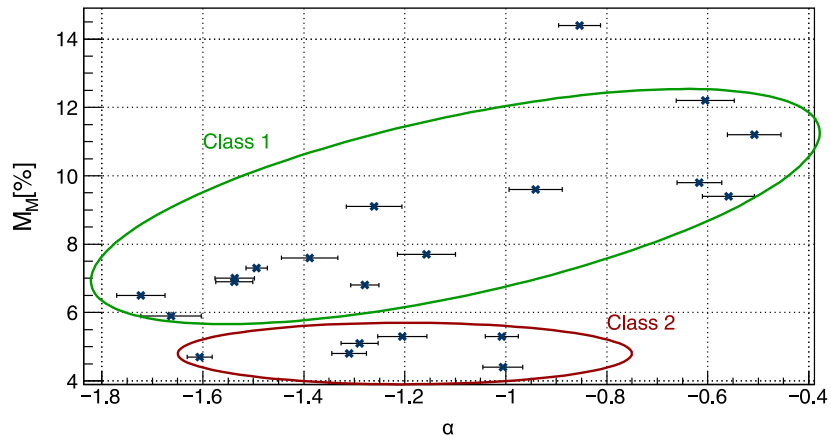

Figure 2. The dependence of the FD magnitude corrected for the magnetospheric effect (M_M) on one of the exponents used to parameterize the proton fluence spectra (α). Two assumed classes of FD events are indicated by the green and red ovals.

3. Methods and Results

IZMIRAN catalogue of Forbush effects (IZMIRAN, 2016) was used as the source of SW related data, as it contains an extensive list of FD events and associated SW parameters. The parameters selected from the IZMIRAN catalogue to be used in the analysis presented here fall into several cathegories: parameters describing the source (Otype, Stype) or the characteristics of the CME (Vmean, CMEwidth); solar wind parameters (Vmax, KTmax, KTmin); parameters describing interplanetary or geomagnetic field (Bzmin, Kpmax, Apmax, Dstmin); and parameters related to the associated solar flare (Xmagn, Sdur, SSN).

Several machine-learning-based classification methods implemented in the TMVA analysis network (Hoecker et al., 2007) were employed in order to establish the optimal FD magnitude for the separation of two classes (boundary criteria mentioned in Section 2), as well as to determine the optimal classification algorithm. Comparing the efficiency of various methods available in the TMVA (shown of Figure 3), it was found that the optimal separation between two classes is achieved with FD magnitude cut set to 6%, as separation efficiency seems to drop-off beyond that for most methods. Support vector machine (SVM) (Cortes & Vapnik, 1995) was identified as the overall best-performing algorithm.
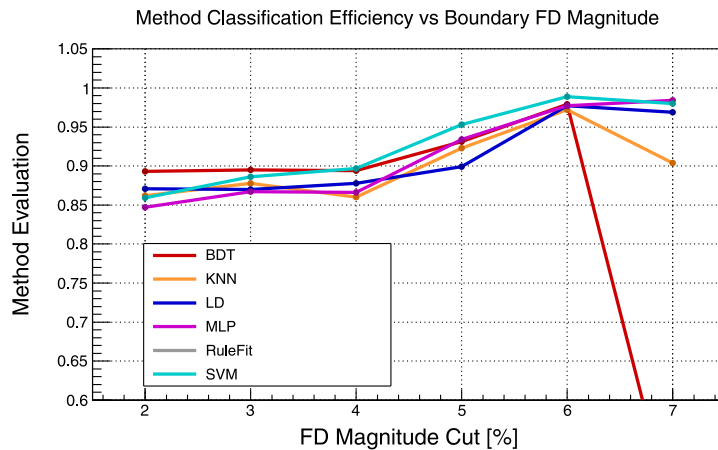
Figure 3. Comparison of the classification efficiency of various TMVA methods dependence on the FD magnitude cut used for class separation.

SVM implementation in the scikit-learn package (Pedregosa et al., 2011) was utilized to identify which of the SW parameters could reliably classify FD events. Third-degree polynomial kernel was found to have the most flexible and efficient performance.
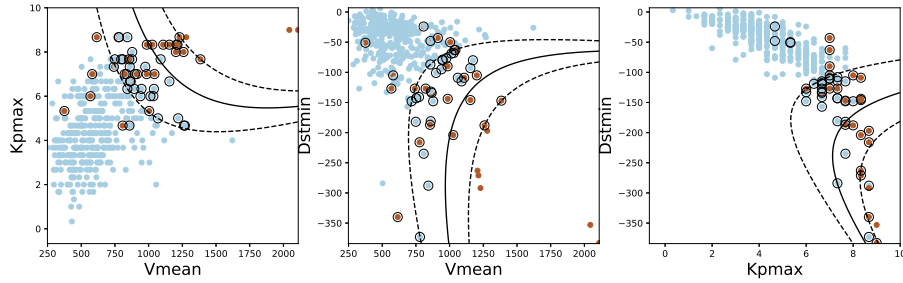
Figure 4. Example of SVM classification using some of SW parameters (mean CME velocity, maximum Kp index and minimal Dst index over the event's duration) that proved to be good input variables for FD classification.

Obtained results appear to confirm the assumption regarding the existence of two classes of FD events. Furthermore, a subset of SW parameters that provide a more reliable classification of FD events was determined. These include mean CME velocity (Vmean) and geomagnetic indices (Kpmax, Apmax, Dstmin), with a possible inclusion of the solar wind speed (Vmax) and minimal hourly component of the interplanetary magnetic field (Bzmin). Decision boundaries between some pairs of mentioned good input variables are showed on Figure 4. Other SW variables proved to be less well suited for classification (as illustrated in Figure 5, for KTmin and KTmax).
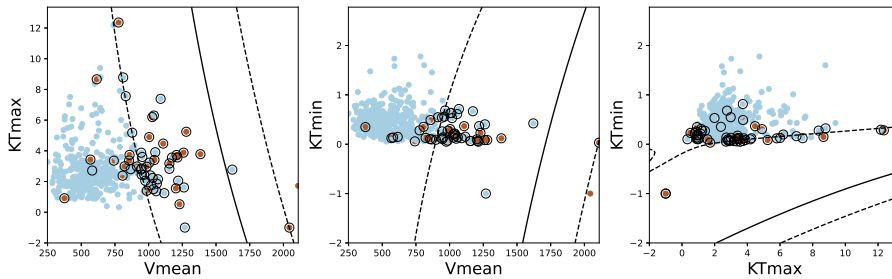
Figure 5. Example of SVM classification using some of SW parameters (KTmax, KTmin) that proved to be less well suited input variables for FD classification.

The identified good variables could prove useful in a potential future extension of the analysis. More specifically, they could serve as an input for a regression procedure that would potentially allow the prediction of FD magnitudes.

This prediction would provide either estimates of FD magnitude as measured by Earth-based detectors or, more importantly, estimates of FD magnitudes corrected for the magnetospheric effect.

4. Conclusions

The potential existence of two classes of FD events was investigated. To increase statistical robustness and reduce uncertainties, the analysis was expanded to include a wider set of various space weather parameters. Machine learning techniques were employed in an attempt to separate FD events into two assumed classes, using a number of selected SW parameters as input variables. We compared the efficiency of different machine learning algorithms, and established the optimal boundary value of FD intensity to be used for class separation. The SVM algorithm was selected for the analysis based on its overall performance, efficiency and flexibility, and used to select a subset of space weather variables to be used for reliable classification of FD events. This subset of good variables variables could prove useful for a future extension of the analysis, where they would provide an input for a regression procedure used to predict FD magnitudes.

References

Cortes, C. & Vapnik, V., Support Vector Networks. 1995, *Machine Learning*, **20**, 273

Desai, M. & Giacalone, J., Large gradual solar energetic particle events. 2016, *Living Reviews in Solar Physics*, **13**, 3, DOI: 10.1007/s41116-016-0002-5

Gopalswamy, N., The Sun and Space Weather. 2022, *Atmosphere*, **13**, DOI: 10.3390/atmos13111781

Hoecker, A., Speckmayer, P., Stelzer, J., et al., TMVA - Toolkit for Multivariate Data Analysis. 2007, *arXiv e-prints*, physics/0703039, DOI: 10.48550/arXiv.physics/0703039

IZMIRAN. 2016, Space weather prediction center (IZMIRAN), http://spaceweather.izmiran.ru/eng/index.html

Kahler, S. W., Solar flares and coronal mass ejections. 1992, *Annual Review of Astron and Astrophys*, **30**, 113, DOI: 10.1146/annurev.aa.30.090192.000553

Pedregosa, F., Varoquaux, G., Gramfort, A., et al., Scikit-learn: Machine Learning in Python. 2011, *Journal of Machine Learning Research*, **12**, 2825

Savić, M., Veselinović, N., Dragić, A., et al., New insights from cross-correlation studies between solar activity indices and cosmic-ray flux during Forbush decrease events. 2023, *Advances in Space Research*, **71**, 2006, DOI: 10.1016/j.asr.2022.09.057

Torsti, J., Valtonen, E., Lumme, M., et al., Energetic Particle Experiment ERNE. 1995, *Solar Physics*, **162**, 505, DOI: 10.1007/BF00733438

Yashiro, S. & Gopalswamy, N., Statistical relationship between solar flares and coronal mass ejections. 2008, *Proceedings of the International Astronomical Union*, **4**, DOI: 10.1017/S1743921309029342

Data quality assurance for atmospheric probing and modeling: characterization of Belgrade Raman lidar station

Z. Mijić[1] , **L. Ilić**[1,2] **and M. Kuzmanoski**[1]

[1] *Institute of Physics Belgrade, Pregrevica 118, 11080 Belgrade, Serbia,*
(E-mail: zoran.mijic@ipb.ac.rs, maja.kuzmanoski@ipb.ac.rs)

[2] *now at Barcelona Supercomputing Center, Plaça Eusebi Güell, 1-3,*
08034 Barcelona, Spain, (E-mail: luka.ilic@ipb.ac.rs)

Abstract. Using the lidar (Light Detection And Ranging) technique atmospheric probing and observations of atmospheric aerosol optical properties may be conducted remotely with high spatial and temporal resolution. As an EARLINET (the European Aerosol Research LIdar Network) joining lidar station, Belgrade Raman lidar system has provided aerosol profiling data for potential atmospheric and climatological studies as well as assessment of planetary boundary layer evolution and conducting dedicated measurements during airborne hazard. A comprehensive quality-assurance program and self-testing check-up tools have been developed to examine the performance and temporal stability of a lidar system. The capabilities of the Belgrade Raman lidar system, as well as its experimental characterization related to zero bin assessment, analog to photon-counting signal delay, Rayleigh-fit and telecover tests to evaluate system accuracy, are presented in this study.

Key words: Remote sensing – Atmosphere – Optical properties – Data – Quality assurance

1. Introduction

For more accurate weather predictions and a better understanding of climate change and solar influence, it is essential to quantify the impact that clouds and atmospheric aerosols play in the Earth's radiation budget (Stocker et al., 2013; Boucher et al., 2013). Depending on aerosol composition and size distribution the amount of scattered and absorbed radiation (both incoming solar and outgoing terrestrial) can differ significantly. Aerosol radiative forcing has been identified as one of the biggest climate change unknowns due to its short lifespan and high spatial and temporal variability (Stocker et al., 2013). To quantify the influence of aerosols on the climate system using an integrated approach of ground-level and airborne in-situ measurements, ground-based remote sensing, and space-based observations combined with numerical modeling are required.

Change in the incoming solar radiation flux induces disturbances in different atmospheric layers (Aplin & Harrison, 2003; Maurya et al., 2014). Several studies have investigated the effect of solar eclipse on various atmospheric properties (Ilić et al., 2018; Kolarž et al., 2005; Nymphas et al., 2009). Atmospheric lidar (Light Detection And Ranging) can be used to determine heights of planetary boundary layer (PBL) using aerosols as tracers, providing opportunity to investigate PBL evolution-based processes. Decrease in height and evolution change of PBL during a solar eclipse have been observed (Ilić et al., 2018; Amiridis et al., 2007; Kolev et al., 2005).

Lidar, an active remote sensing technique, has proved itself to be the optimal tool for profiling height-resolved atmospheric aerosol optical parameters. Various aerosol lidar techniques have been developed during the last several decades operating at one or multiple wavelengths. The lidar principle is based on laser emission of short-duration light pulses into the receiver field of view. The intensity of the light backscattered by atmospheric molecules and particles is measured versus time (through the telescope receiver, collimating optics, a bandpass filter for daylight suppression) by an appropriate detector. The signal profile is recorded by an analog-to-digital converter or by a photon-counting device and accumulated for a selected integration period spanning time intervals from seconds to minutes. In order to establish a comprehensive and quantitative statistical data base of the horizontal and vertical distribution of aerosols on the continental scale the lidar network called EARLINET (the European Aerosol Research LIdar Network) was founded in 2000 (Pappalardo et al., 2014). The development of the quality assurance strategy (Freudenthaler et al., 2018), the optimization of instruments and data processing (Wandinger et al., 2016), and the dissemination of data have contributed to significant improvement of the network towards a more sustainable observing system. With the addition of new stations EARLINET has significantly enhanced its observation capacity during the past few years. Additionally, the Single Calculus Chain (SCC) was developed eliminating inconsistencies in the optical products retrieval processes and in the signal error calculation, automating the data evaluation, and enabling near real time (NRT) data processing (D'Amico et al., 2015, 2016; Papagiannopoulos et al., 2020; Mattis et al., 2016). Such network development allowed its contribution to calibration and validation of optical products retrieval from satellite missions (Abril-Gago et al., 2022).

In this study the capabilities of the EARLINET joining Belgrade Raman lidar system combined with its experimental characterization using self-testing check-up tools developed across the network to evaluate system accuracy are presented. Aerosol optical properties retrieved from such lidar measurements can be used to evaluate aerosol satellite measurements, e.g., Earth Clouds, Aerosols and Radiation Explorer (EARTHCARE) mission (Illingworth et al., 2015), and to improve aerosol representation in climate models.
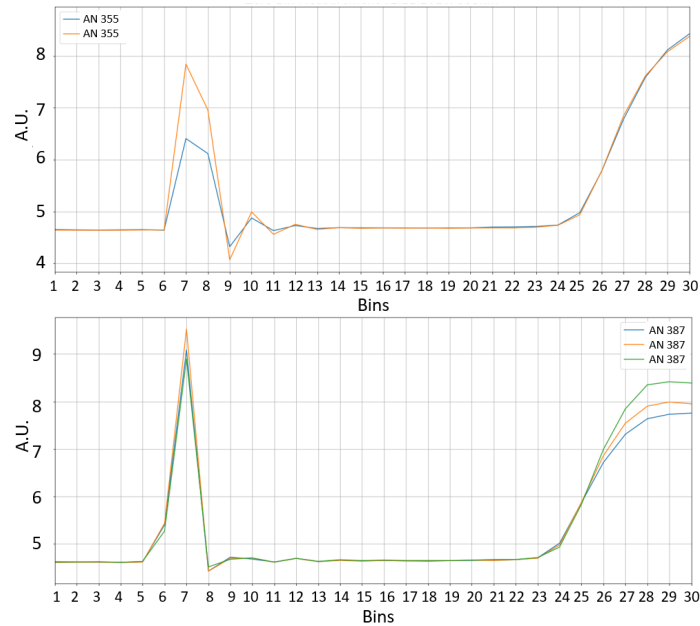
Figure 1. Zero bin assessment for elastic 355 nm (above) and Raman 387 nm (below) channels. Different color lines represent successive average signals from diffuse reflections of twenty laser shots.

2. Methodology

Raman lidar system at the Institute of Physics Belgrade (IPB), Serbia (44.860 N, 20.390 E) is bi-axial lidar system (telescope-laser axes distance is 200 mm) with combined elastic and Raman detection designed to perform continuous measurements of aerosols in the lower free troposphere (Ilić et al., 2018). Transmitter unit is based on the third harmonic frequency of a water cooled, pulsed Nd:YAG laser, emitting pulses of 65 mJ output energy at 355 nm with a 20 Hz repetition rate. In order to improve the maximum range and the precision of the system the beam expander is used to reduce the laser beam divergence (0.33 mrad) expanding the beam's diameter by 3 times. The optical receiving unit consists of two sub-units, a receiving telescope and wavelength separation unit. The optical receiver is a Cassegrain reflecting telescope with a primary mirror of 250 mm diameter and a focal length of 1250 mm. Photomultiplier tubes Hamamatsu R9880U-110 (PMT) are used to detect elastic backscatter lidar signal at 355 nm and Raman signal at 387 nm (Nitrogen vibrational scattering).
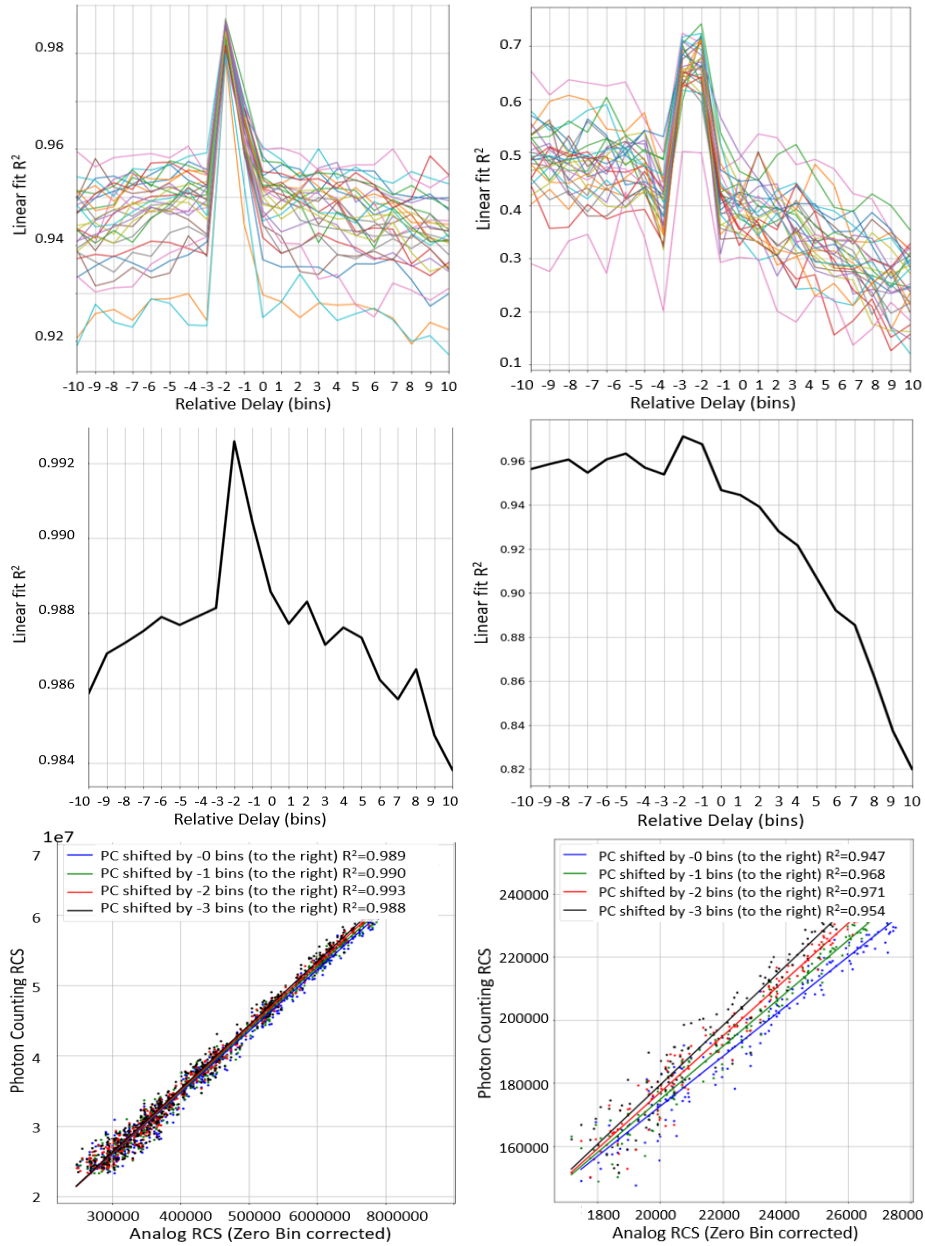
Figure 2. Analysis of the relative delay between zero-bin-corrected analog RCS and the PC RCS for 355 nm (left column) and 387 nm (right column) channels. Measurements of 30 1-minute profiles with 1200 shots each were used. A linear regression between AN and PC data was performed in the gluing region. Correlation coefficient as a function of relative delay between analog and photon counting signals (above). Correlation coefficient as a function of relative delay between analog and photon counting mean signals (center). Fit between the PC RCS and AN RCS channels (below).
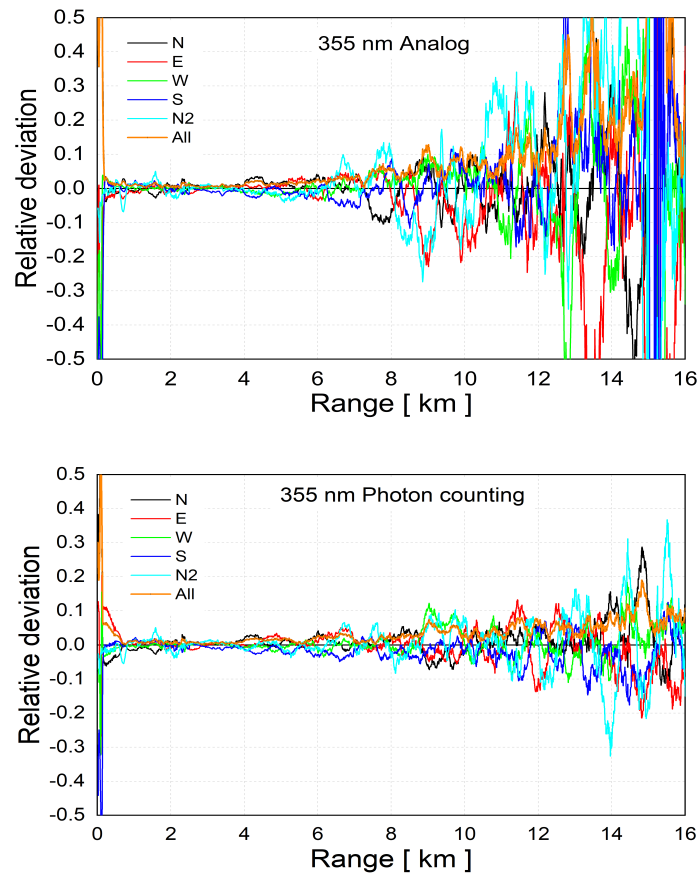
Figure 3. Relative deviations of signals collected in the four telescope sectors compared to the mean analog (above) and photon counting 355 nm signal (below), normalized in the 1500-2500 m range.

Interference filters with 0.96 nm and 0.45 nm FWHM before each PM tube are used to reduce the background noise. The detectors are operated both in the analog and photon-counting mode and the spatial raw resolution of the detected signals is 7.5 m. Averaging time of the lidar profiles is of the order of 1 min corresponding to 1200 laser shots. The Licel transient recorder is comprised of a fast transient digitizer with on board signal averaging, a discriminator for single photon detection and a multichannel scaler combined with preamplifiers for both systems. For analog detection, the signal is amplified according to the input range selected and digitized by a 12-Bit-20 MHz A/D converter. At the same time the signal part in the high frequency domain is amplified and a 250 MHz fast discriminator detects single photon events above the selected threshold voltage.
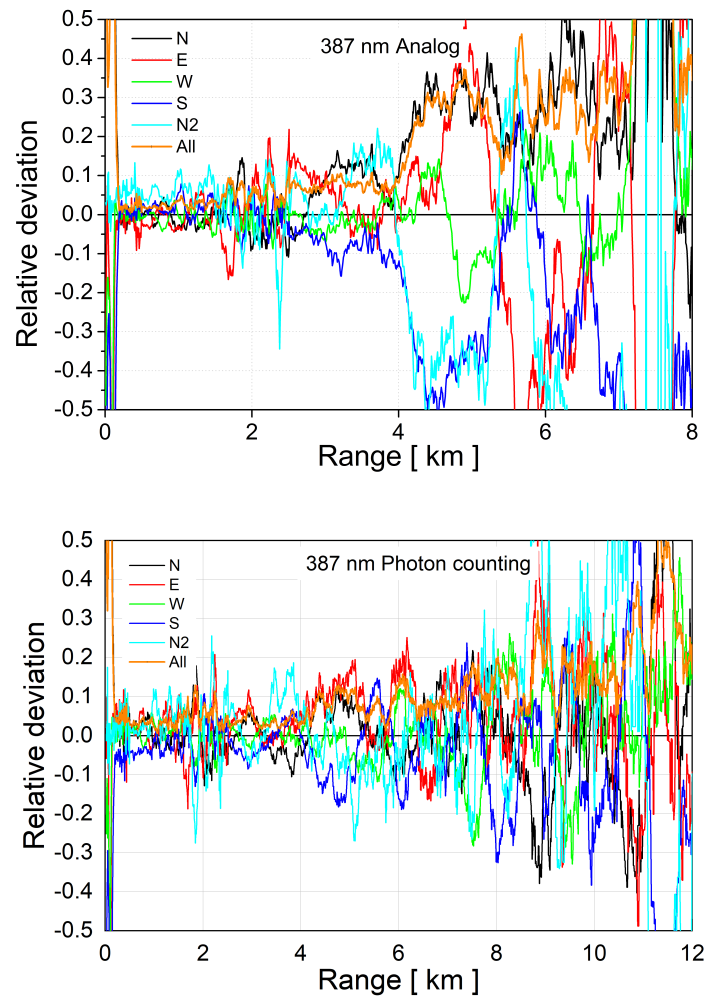
Figure 4. Relative deviations of signals collected in the four telescope sectors compared to the mean analog (above) and photon counting (below) 387 nm signal, normalized in the 1500-2500 m range.

In order to monitor and improve the quality of the lidar systems and their optical products, the quality assurance methods for both hardware and retrieval algorithms (Freudenthaler et al., 2018; D'Amico et al., 2015, 2016) have been established through the lidar network. System alignment is one of the fundamental setup tests because the partial overlap between the laser beam and the receiver field of view has a substantial impact on lidar measurements of particle optical characteristics (Freudenthaler et al., 2018). The fact that the ray bundles from various telescopic aperture regions go through the optical setup

in various ways and with various incidence angles on the optical components can be used to assess the lidar system alignment i.e., full overlap between laser beam and telescope field of view. It is necessary to do a series of measurements using a telescope that is only partially covered so that each measurement actually represents the collection of backscattered light by a specific sector of the telescope in order to evaluate the alignment. Following the procedure described in Freudenthaler et al. (2018), a version of so-called telecover test using the set up of the telescope with four sectors was conducted in this study. For the fine alignment of the system in the far field, the range-corrected lidar signal is compared to the attenuated Rayleigh backscatter coefficient at a range interval which is considered aerosol free. To determine the lidar signal distortions due to the electronic noise the so-called dark measurement was performed. Dark signal was measured with fully covered telescope so that no light from the atmosphere and laser backscattered pulses could be detected. The lidar signals were preprocessed taking into the account 3 min dark signal (for both analog and photon counting channels) corresponding to 3600 laser shots. Such temporal averaged dark measurement with sufficient signal-to-noise ratio was subtracted from the lidar signals to improve the accuracy. In addition, experimental verification of the zero range of the signal detection was conducted (Barbosa et al., 2014).

3. Results and Discussion

3.1. Zero bin test

A trigger-delay between the actual laser pulse emission and the backscatter signal recording's presumed zero range (zero bin) can introduce notable inaccuracies in the near range signal. Particularly, the inversion of Raman signals can be significantly distorted since the signal slope in the near range varies considerably when the zero bin for range correction is changed (Freudenthaler et al., 2018). The signal peaks obtained from light reflected from a diffuse scattering target placed right above the emission part of the lidar system in order to block the laser path are presented in Figure 1. In order to prevent signal saturation the telescope was covered so that only a portion of the diffused light can enter the telescope. The first bin of the signal peak is the assessed zero bin. Since the analog to photon counting (AN-PC) signal delay might be different among LICEL transient recorder modules, the AN-PC delay should be further calculated for each module separately. In this paper the cross-correlation of the two range corrected signals was used to calculate the analog-pc delay (Barbosa et al., 2014). Analysis of the relative delay between zero-bin-corrected analog RCS and the PC RCS signals is presented in Figure 2 with the same system alignment as in Figure 3. For measurement of this delay, 30 profiles of 1200 shots each were used. A linear regression between AN and PC data was performed as a function of time delay from -10 to 10 bins. A distinct peak at -2 relative delay bins is clearly exhibited for elastic channel (with respect to zero-bin-corrected

AN signal). The main peaks for relative delay in the case of Raman channel are distributed between two range-bins, but the best assessment for relative delay corresponds also to -2 bins.

3.2. Telecover test

To check the laser-telescope alignment the telecover test using quarters of the telescope was used. This quadrant test used four sectors named North (N)-oriented from the telescope optical axis towards the laser optical axis, East (E), West (W) and South (S). The North2 (N2) signals were acquired using the same telecover sector as the N signals, but at the end of the measurement time sequence, thus deviations in the N and N2 signals reveal the effect of the changing environment during the measurements. Figure 3 and Figure 4 show relative deviations of signals collected with quadrant telescope sectors under stable atmospheric conditions on April 27, 2020 for both 355 nm and 387 nm channels, respectively. Signals obtained with a partly covered telescope are examined in terms of each sector deviation relative to the average of all signals in order to verify lidar response in the near field. The threshold for the accepted relative deviation of each sector signal is adopted to be 0.05. From the obtained results it can be seen that the Raman lidar response in the near field is below threshold and well alligned starting from 300 m. Although the telecover test is useful for the assessment of the far range response of the lidar system usually the additional test called Rayleigh fit should be applied.

3.3. Rayleigh fit test

To test the lidar alignment in the far range the Rayleigh fit procedure was used. For that purpose, the fitting of normalized lidar signal to the calculated attenuated Rayleigh backscatter coefficient (β_m^{attn}) in a range where we assume clean conditions (aerosol-free atmosphere) was performed. In Figure 5 and Figure 6 Rayleigh fit and corresponding relative deviations from the calculated Rayleigh signal for the elastic 355 nm and Raman 387 nm channels are presented. The 30 min measurements were performed during the night on the same day and with the lidar setup as presented in Figure 3. Molecular signals were calculated from the obtained Global Data Assimilation System (GDAS) profiles for the same day at 23UT following Bucholtz (1995)(Bucholtz, 1995). From Figure 5 it can be seen that the lidar system is well aligned up to the 14 km for elastic channel with the relative error less than 1% of the attenuated Rayleigh backscatter signal while Raman channel signal to noise ratio is acceptable up to the 8 km. Once the system is properly aligned it can be used for systematic aerosol measurements.
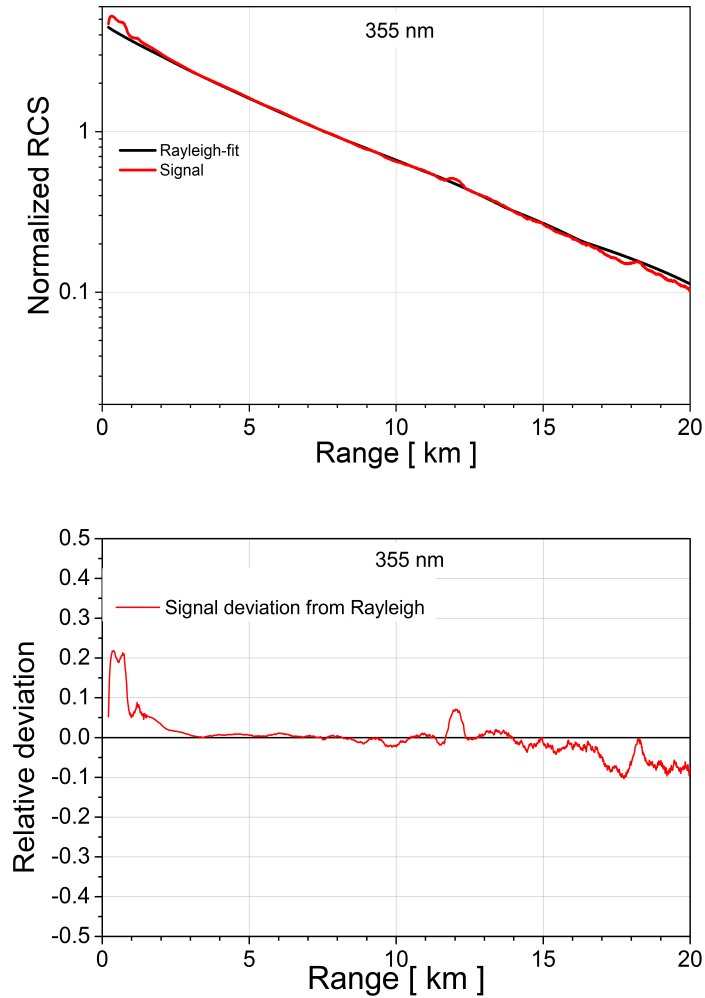
Figure 5. Photon counting 355 nm lidar signal (red) averaged over 30 minutes and calculated Rayleigh signal (black) from local radiosonde data of the same night, both normalised between 5 and 10 km range (above). Relative deviation from the calculated Rayleigh signal (below).
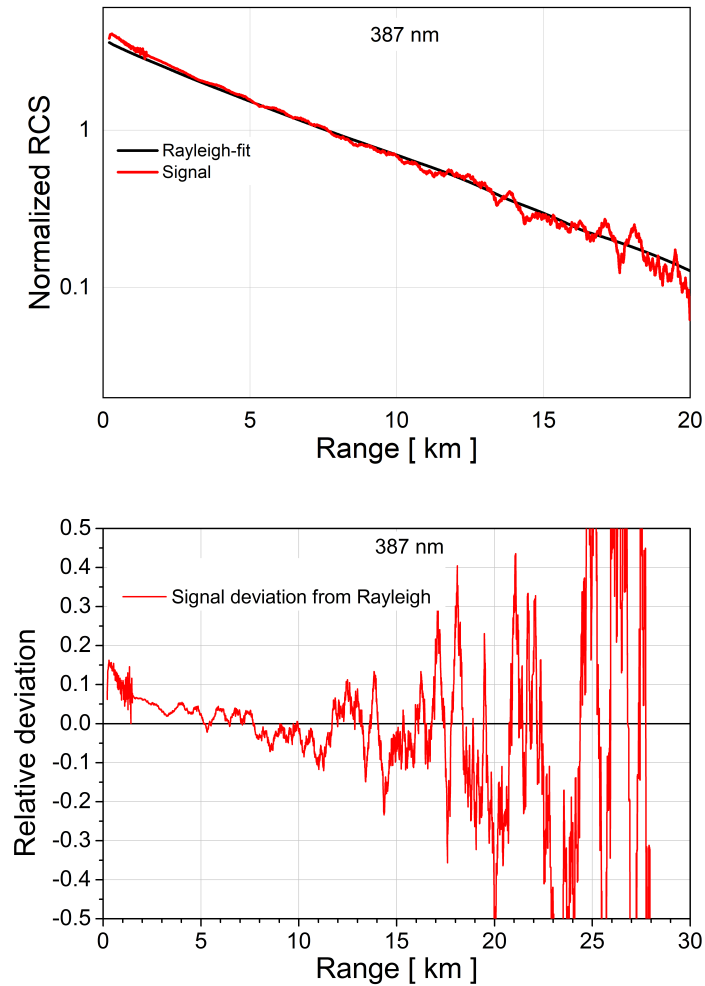
Figure 6. Photon counting 387 nm lidar signal (red) averaged over 30 minutes and calculated Rayleigh signal (black) from local radiosonde data of the same night, both normalised between 5 and 10 km range (above). Relative deviation from the calculated Rayleigh signal (below).

4. Summary

Lidar systems are optimal tools for providing range-resolved aerosol optical parameters and information on the atmospheric structure not only for climatological purposes but also in emergency situations when near real time delivery of the data and fast data processing is required. Although several lidar instrument

intercomparison campaigns have been conducted within the network, it is not possible to evaluate all systems in their specific setup due to the constant technological development and subsequently systems upgrade together with improving measurements experiences. To overcome limited capacity for providing direct intercomparisons a complementary quality-assurance procedures and tools have been developed for regular internal system check-ups across the lidar network. In this paper the capabilities of the Belgrade Raman lidar system is assessed and characterization related to zero bin assessment, analog to photon-counting signal delay, Rayleigh-fit and telecover tests to evaluate system accuracy, are presented. Under described system setup the full overlap of the telescope field of view and laser beam is measured and the system alignment is assessed in the near field starting from 300 m. In the far range the Rayleigh fit procedure for elastic 355 nm channel exhibited good signal to noise ratio and alignment up to 14 km, but Raman channel at 387 nm demonstrated significant signal noise above 8 km. In addition, the cross correlation of the two range corrected analog and photon count signals was used to assess the analog-pc delay characteristic for each transient record module.

As a unique system in the region capable to perform remote monitoring of atmospheric aerosols it is expected to perform systematic measurements on a regular schedule in the near future and contribute to the collection of aerosol vertical distribution database in Europe. Lidar measurements of aerosol optical properties can be used for model evaluation (Meier et al., 2012; Binietoglou et al., 2015). Furthermore, the assimilation of lidar observations of aerosol vertical distribution (Cheng et al., 2019) can improve model estimation of aerosol impact on climate. In addition, changes in atmospheric properties caused by specific events, like solar eclipse-induced planetary boundary layer height changes or airborne particles transport can be observed. Having in mind geographical distribution of currently active lidar stations in Europe, Belgrade Raman lidar station can provide valuable data for intercomparison and validation of optical products for future satellite missions, but automatization of the measurement process and the upgrade to the multiwavelength lidar system are essential to develop in the future.

References

Abril-Gago, J., Guerrero-Rascado, J. L., Costa, M. J., et al., Statistical validation of Aeolus L2A particle backscatter coefficient retrievals over ACTRIS/EARLINET stations on the Iberian Peninsula. 2022, *Atmospheric Chemistry and Physics*, **22**, 1425, DOI: 10.5194/acp-22-1425-2022

Amiridis, V., Melas, D., Balis, D. S., et al., Aerosol Lidar observations and model calculations of the Planetary Boundary Layer evolution over Greece, during the March 2006 Total Solar Eclipse. 2007, *Atmospheric Chemistry and Physics*, **7**, 6181, DOI: 10.5194/acp-7-6181-2007

Aplin, K. & Harrison, R., Meteorological effects of the eclipse of 11 August 1999 in cloudy and clear conditions. 2003, *Proceedings of the Royal Society of London. Series A: Mathematical, Physical and Engineering Sciences*, **459**, 353, DOI: 10.1098/rspa.2002.1042

Barbosa, H. M. J., Barja, B., Pauliquevis, T., et al., A permanent Raman lidar station in the Amazon: description, characterization, and first results. 2014, *Atmospheric Measurement Techniques*, **7**, 1745, DOI: 10.5194/amt-7-1745-2014

Binietoglou, I., Basart, S., Alados-Arboledas, L., et al., A methodology for investigating dust model performance using synergistic EARLINET/AERONET dust concentration retrievals. 2015, *Atmospheric Measurement Techniques*, **8**, 3577, DOI: 10.5194/amt-8-3577-2015

Boucher, O., Randall, D., Artaxo, P., et al. 2013, *Clouds and aerosols* (Cambridge, UK: Cambridge University Press), 571–657

Bucholtz, A., Rayleigh-scattering calculations for the terrestrial atmosphere. 1995, *Appl. Opt.*, **34**, 2765, DOI: 10.1364/AO.34.002765

Cheng, Y., Dai, T., Goto, D., et al., Investigating the assimilation of CALIPSO global aerosol vertical observations using a four-dimensional ensemble Kalman filter. 2019, *Atmospheric Chemistry and Physics*, **19**, 13445, DOI: 10.5194/acp-19-13445-2019

D'Amico, G., Amodeo, A., Baars, H., et al., EARLINET Single Calculus Chain – overview on methodology and strategy. 2015, *Atmospheric Measurement Techniques*, **8**, 4891, DOI: 10.5194/amt-8-4891-2015

D'Amico, G., Amodeo, A., Mattis, I., Freudenthaler, V., & Pappalardo, G., EARLINET Single Calculus Chain – technical – Part 1: Pre-processing of raw lidar data. 2016, *Atmospheric Measurement Techniques*, **9**, 491, DOI: 10.5194/amt-9-491-2016

Freudenthaler, V., Linné, H., Chaikovski, A., Rabus, D., & Groß, S., EARLINET lidar quality assurance tools. 2018, *Atmospheric Measurement Techniques Discussions*, **2018**, 1, DOI: 10.5194/amt-2017-395

Ilić, L., Kuzmanoski, M., Kolarž, P., et al., Changes of atmospheric properties over Belgrade, observed using remote sensing and in situ methods during the partial solar eclipse of 20 March 2015. 2018, *Journal of Atmospheric and Solar-Terrestrial Physics*, **171**, 250, DOI: https://doi.org/10.1016/j.jastp.2017.10.001, vertical Coupling in the Atmosphere-Ionosphere System: Recent Progress

Illingworth, A. J., Barker, H. W., Beljaars, A., et al., The EarthCARE Satellite: The Next Step Forward in Global Measurements of Clouds, Aerosols, Precipitation, and Radiation. 2015, *Bulletin of the American Meteorological Society*, **96**, 1311 , DOI: https://doi.org/10.1175/BAMS-D-12-00227.1

Kolarž, P., Šekarić, J., Marinković, B., & Filipović, D., Correlation between some of the meteorological parameters measured during the partial solar eclipse, 11 August 1999. 2005, *Journal of Atmospheric and Solar-Terrestrial Physics*, **67**, 1357, DOI: https://doi.org/10.1016/j.jastp.2005.07.016

Kolev, N., Tatarov, B., Grigorieva, V., et al., Aerosol Lidar and in situ ozone observations of the planetary boundary layer over Bulgaria during the solar eclipse of 11 August 1999. 2005, *International Journal of Remote Sensing*, **26**, 3567, DOI: 10.1080/01431160500076939

Mattis, I., D'Amico, G., Baars, H., et al., EARLINET Single Calculus Chain - technical - Part 2: Calculation of optical products. 2016, *Atmospheric Measurement Techniques*, **9**, 3009, DOI: 10.5194/amt-9-3009-2016

Maurya, A. K., Phanikumar, D. V., Singh, R., et al., Low-mid latitude D region ionospheric perturbations associated with 22 July 2009 total solar eclipse: Wave-like signatures inferred from VLF observations. 2014, *Journal of Geophysical Research: Space Physics*, **119**, 8512, DOI: https://doi.org/10.1002/2013JA019521

Meier, J., Tegen, I., Mattis, I., et al., A regional model of European aerosol transport: Evaluation with sun photometer, lidar and air quality data. 2012, *Atmospheric Environment*, **47**, 519, DOI: https://doi.org/10.1016/j.atmosenv.2011.09.029

Nymphas, E., Adeniyi, M., Ayoola, M., & Oladiran, E., Micrometeorological measurements in Nigeria during the total solar eclipse of 29 March, 2006. 2009, *Journal of Atmospheric and Solar-Terrestrial Physics*, **71**, 1245, DOI: https://doi.org/10.1016/j.jastp.2009.04.014

Papagiannopoulos, N., D'Amico, G., Gialitaki, A., et al., An EARLINET early warning system for atmospheric aerosol aviation hazards. 2020, *Atmospheric Chemistry and Physics*, **20**, 10775, DOI: 10.5194/acp-20-10775-2020

Pappalardo, G., Amodeo, A., Apituley, A., et al., EARLINET: towards an advanced sustainable European aerosol lidar network. 2014, *Atmospheric Measurement Techniques*, **7**, 2389, DOI: 10.5194/amt-7-2389-2014

Stocker, T. F., Qin, D., Plattner, G.-K., et al. 2013, *Technical summary* (Cambridge, UK: Cambridge University Press), 33–115

Wandinger, U., Freudenthaler, V., Baars, H., et al., EARLINET instrument intercomparison campaigns: overview on strategy and results. 2016, *Atmospheric Measurement Techniques*, **9**, 1001, DOI: 10.5194/amt-9-1001-2016

Low intensity solar flares' impact: numerical modeling

A. Kolarski[ID]**, V.A. Srećković**[ID] **and F. Arnaut**[ID]

Institute of Physics Belgrade, University of Belgrade, Pregrevica 118,
11080 Belgrade, Serbia (E-mail: aleksandra.kolarski@ipb.ac.rs)

Abstract. Solar flares, as strong explosions on the Sun's surface, are well known driving agents that severely affect the near-Earth environment, producing additional ionization within the sunlit Earth's atmospheric layers. X-ray solar flares can be classified regarding their effects on the lower ionosphere and its electron density profile. The focus of this research is on the study of disturbances induced by X-ray solar flares in order to predict the impact of possible weak solar events. In this paper we examined solar activity of lower intensity by conducting numerical modeling using several models and based on data obtained by very low frequency radio signals and from the Geostationary Operational Environmental Satellite (GOES) database on solar X-ray radiation.

Key words: Solar activity – Solar X-ray flares – Radio signal perturbations – GOES

1. Introduction

Solar flares (SFs) are powerful bursts of electromagnetic radiation originating from the Sun's surface Bothmer et al. (2007). Among the categories of SF from A to X-class, B-and C-class SFs represent a low to low-to-moderate level of intensity (Grubor et al., 2008; Hayes et al., 2021). Although B-and C-class flares are considered to have low level intensity, they still possess the potential to cause disruptions in communication and navigation systems, if they are directed towards the Earth and especially during periods of quiet solar activity such as periods of solar minimum(s). During periods of solar minimum, which refers to the phase of the 11-year solar cycle with minimal solar activity, B- and C-class SFs become significant, as they often constitute the majority of solar flares observed in these periods.

Low class SFs, especially during periods of solar minimum, can induce disturbances in the ionosphere, leading to noticeable effects on terrestrial communication. The primary effect of SFs, in general, on the ionosphere is the augmentation in electron density. The intense X-ray and ultraviolet radiation released during SFs can ionize the upper atmosphere, creating additional free

electrons (Šulić et al., 2016; Curto, 2020; Žigman et al., 2007). These free electrons can affect radio wave propagation by altering the refractive properties of the ionosphere. As a result, the density of the ionosphere increases temporarily, influencing the behavior of radio signals passing through it (Kelly, 2009).

Very Low Frequency (VLF) technology plays a crucial role in studying solar flares and their effects on the lower ionosphere. VLF technology utilizes a range of electromagnetic waves with frequencies from 3 to 30 kHz, with the ability to propagate over long distances without losses and penetrate through both soil and water, making them bounce within the Earth-ionosphere waveguide (Ratcliffe et al., 1972; Silber & Price, 2017). VLF technology finds particular relevance in the study of solar flares due to its ability to capture and analyze the effects of SFs and to indirectly provide data of relevance to ionopsheric plasma property variations during these events (Kolarski et al., 2011; Šulić & Srećković, 2014; Srećković et al., 2017; Arnaut et al., 2023). By observing such alterations, valuable insights into the Sun-Earth "connection" can be gained and an enhanced overall understanding of space weather phenomena. The study of SFs of low intensity during solar minimum and their impact on the ionosphere provides valuable insights into the complex interactions between Sun and Earth's upper atmosphere (Barta et al., 2022; Grodji et al., 2022).

2. Observations

Transit between solar cycle (SC) 23 and 24 implies the period of solar activity is characterized by quiet Sun, i.e., solar minimum. The solar minimum of the 23/24 solar cycle often refers to the period mainly related to years 2008 and 2009, i.e. a period with quiet Sun between the descending branch of the SC 23 and the ascending branch of the SC 24. During this period there were not many SFs reported. More precisely only 8 C class SF events occurred in January, April, November and December and 1 M class SF occurred in March during 2008. Likewise 28 C class SF events occurred in July, September, October and December of 2009. When mutually compared in terms of background solar radiation, year 2008 was a bit calmer with X-ray background flux up to A8.1 compared to 2009 with X-ray background flux up to B1.4, but both of low background solar radiation conditions enabled studying of low class SFs and their influence on Earth's ionosphere. Results of monitoring solar activity during the 23/24 solar minimum using VLF technology and the European mid-latitude lower ionospheric response to some of the low class SFs from this period based on records obtained by BEL VLF station in Belgrade (Serbia) and estimated electron densities using the Long Wave Propagation Capability (LWPC) methodology can be found in Kolarski et al. (2022a).

In this paper focus is on the utilization of two numerical methods, so called FlareED and easyFit that were developed by Srećković et al. (2021a,b) on the cases of low intensity SFs (lower C- and upper B-class SFs). Moreover the aim

of present paper is to test methods' efficiency and sensitivity when applied to cases of SFs from the lower part of the soft X-ray irradiance spectrum. We note that initially FlareED and easyFit methods were developed for SF events of mid to high intensity (upper C-, M- and lower X-class SFs, e.g. Srećković et al. (2021b); Kolarski et al. (2022b)).

Table 1. Estimated electron densities at nominal height of 74 km by employed different approaches: classical using LWPC, FlarED, easyFit and ML methods.

dd/mm/yyyy	27/10/2009	16/12/2009	23/12/2009
SF class	B8.3	C3.7	C6.4
max X-ray flux time (UT)	13:11	13:02	10:17
Ne LWPC (m^{-3})	$3.79 \cdot 10^8$	$1.37 \cdot 10^9$	$1.17 \cdot 10^9$
Ne easyFit (m^{-3})	$4.20 \cdot 10^8$	$1.01 \cdot 10^9$	$2.33 \cdot 10^9$
Ne FlarED (m^{-3})	$3.47 \cdot 10^8$	$9.64 \cdot 10^8$	$1.64 \cdot 10^9$
Ne ML (m^{-3})	$4.20 \cdot 10^8$	$1.02 \cdot 10^9$	$2.28 \cdot 10^9$

Along with these two methods that were already used for purposes of exploring the influences of stronger SFs on mid-latitude lower ionospheric plasma properties and are used in this study as well, here we also present results from a novel numerical method relying on machine learning (ML) techniques that is applied to low intensity SFs. Machine learning (ML) techniques have demonstrated extensive applicability in various domains, including research, engineering, and industry. Therefore, these techniques offer significant informational value that is not readily identifiable through other statistical methods, thereby offering a novel perspective on the data. One prominent category of widely used algorithms comprises tree, or forest-based techniques, such as Random Forest (RF) (Breiman, 2001) or XGBoost (XGB) (Chen & Guestrin, 2016). A typical ML workflow involves the initial preparation of the training and testing datasets, which include both the features and the target variables. Subsequently, the model is trained using the train dataset, following which the evaluation phase can be initiated using the test dataset, i.e., testing the trained model on a test dataset and constructing evaluation metric statistics. Once satisfactory model (hyper)parameters have been obtained, the model can be utilized for predicting the target variable on other datasets. The XGB algorithm was utilized in this study to derive the β and H' parameters (the so called Wait's parameters, Wait & Spies 1964) (target variables; multi-output ML task) from X-ray irradiance data and other features that were derived from the statistical properties of the X-ray irradiance data (feature data). The XGB model was fine-tuned in relation to the number of trees and the learning rate.

From period 2008 - 2009 several days with reported X-ray solar activity were singled out and inspected in detail: 03 November 2008, 05 July 2009, 27 October 2009, 10 December 2009, 16 December 2009, 21 December 2009 and

23 December 2009. Days were primarily chosen for analysis based on reported X-ray SFs that were "visible" on BEL VLF recordings, in order to provide it possible to compare results related to estimated electron densities obtained by the classical approach (such as Kolarski et al. 2022a) and by using FlareED and easyFit methods for interpretable cases, on the one hand and to avoid cases of stronger C-class events on the other (like M1.7 on 25 March 2008 with max. X-ray flux at 18:56UT or C7.6 & C7.2 on 18 & 22 December 2009, with max. X-ray flux at 18:55UT & 04:56UT respectively).
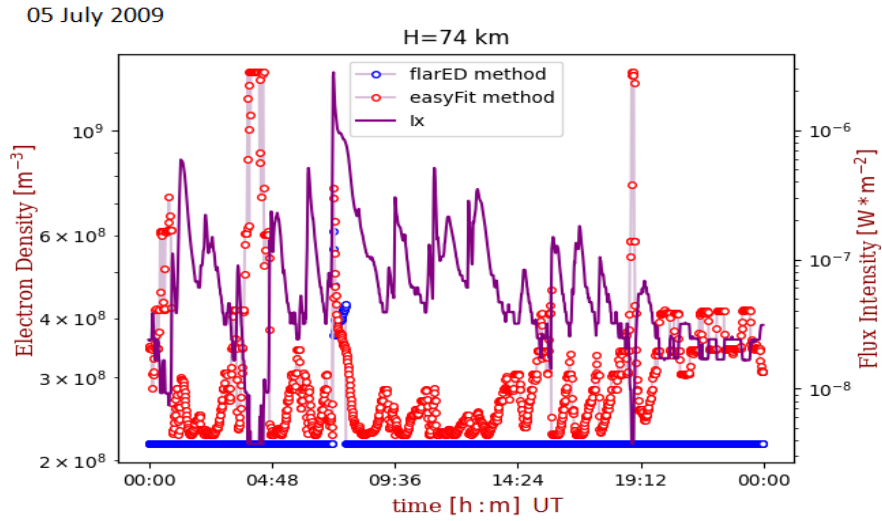
Figure 1. X-ray flux from GOES-15, and Ne ($h = 74$ km) as a function of UT during 05 July 2009. The dashed line with circles shows results acquired by FlarED and easyFit methods.

During 03 November 2008, there were only 3 SFs reported with 2 of them of B-class with intensities in the range B2.4-2.9 and 1 of C-class of intensity C1.6, background flux was of A0.0 and sunspot number was 18. During 05 July 2009, there were 14 SFs reported with 13 of them of B-class with intensities in the range B1-5.9 and 1 of C-class of intensity C2.7, background flux was of A2.2 and sunspot number was 26. During 27 October 2009, there were 23 SFs reported with 18 of them of B-class with intensities in the range B1-8.4 and 5 of C-class with intensities in the range C1.1-1.7, background flux was of A4.2 and sunspot number was 29. During 10 December 2009, there were only 3 SFs reported with 2 of them of B-class with intensities in the range B1.4-6 and 1 of C-class of intensity C3.4, background flux was of A0.0 and sunspot number was 13. During 16 December 2009, there were 9 SFs reported with 6 of them of B-class with intensities in the range B3-8.6 and 3 of C-class with intensities in

the range C1.4-5.3, background flux was of B1.2 and sunspot number was 30. During 21 December 2009, there were 12 SFs reported with 10 of them of B-class with intensities in the range B1.6-8.6 and 2 of C-class with intensities in the range C1-2.5, background flux was of A9.3 and sunspot number was 42. During 23 December 2009, there were 5 SFs reported with 4 of them of B-class with intensities in the range B1.6-8.6 and 1 of C-class of intensity C6.4, background flux was of A7.5 and sunspot number was 23.
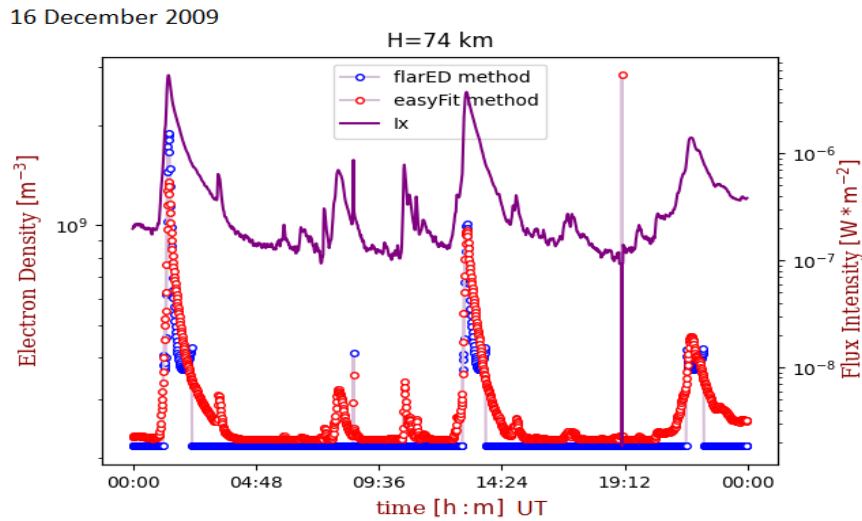
Figure 2. X-ray flux from GOES-15, and Ne ($h = 74$ km) as a function of UT during 16 December 2009. The dashed line with circles shows results acquired by FlarED and easyFit methods.

3. Results and discussion

As previously mentioned, the factor of flare induced perturbation "visibility" on BEL VLF recordings was of prime significance. However, numerical methods FlareED and easyFit were conducted for chosen days in 24h continuity manner, in order to explore these events that were not "visible" in Belgrade due to nocturnal conditions. Figures 1-5 give an overview of the obtained results by application of numerical methods FlareED (blue) and easyFit (red) to the cases chosen for analysis. Aside from all previously mentioned factors, difference between the X-ray flux (violet) characteristic in terms of standalone SF events separated by periods with no activity and numerous back-to-back SFs was subject of interest in the conducted analysis as well. Solar soft X-ray flux is taken from Geostationary Operational Environmental Satellite (GOES) archive database (https://satdat. ngdc.noaa.gov/sem/goes/data/avg/).
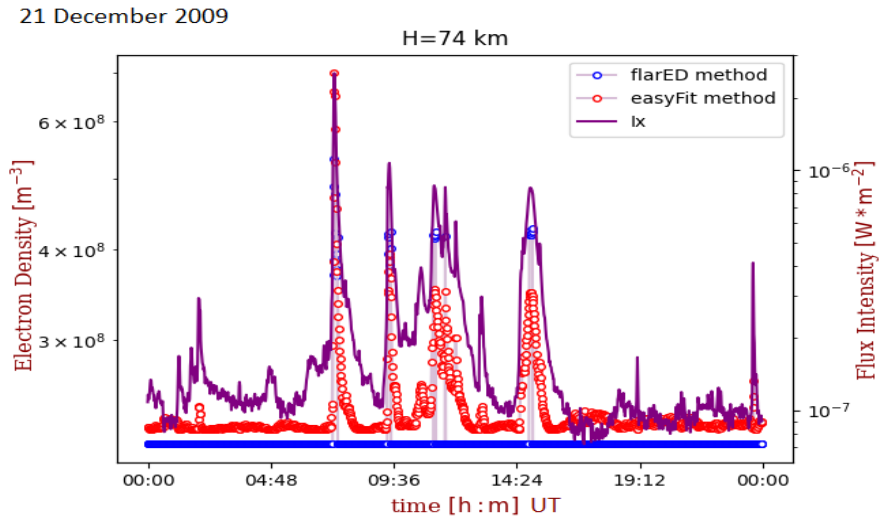
Figure 3. X-ray flux from GOES-15, and Ne ($h = 74$ km) as a function of UT during 21 December 2009. The dashed line with circles shows results acquired by FlarED and easyFit methods.
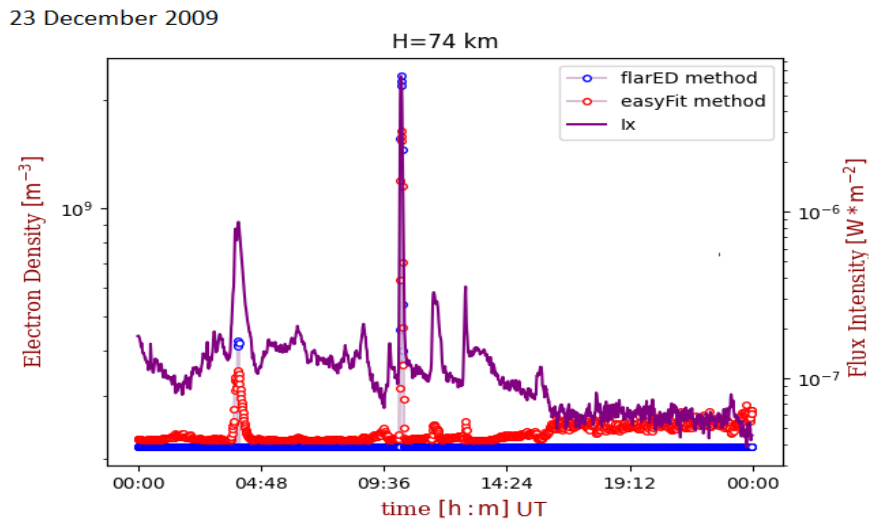
Figure 4. X-ray flux from GOES-15, and Ne ($h = 74$ km) as a function of UT during 23 December 2009. The dashed line with circles shows results acquired by FlarED and easyFit methods.
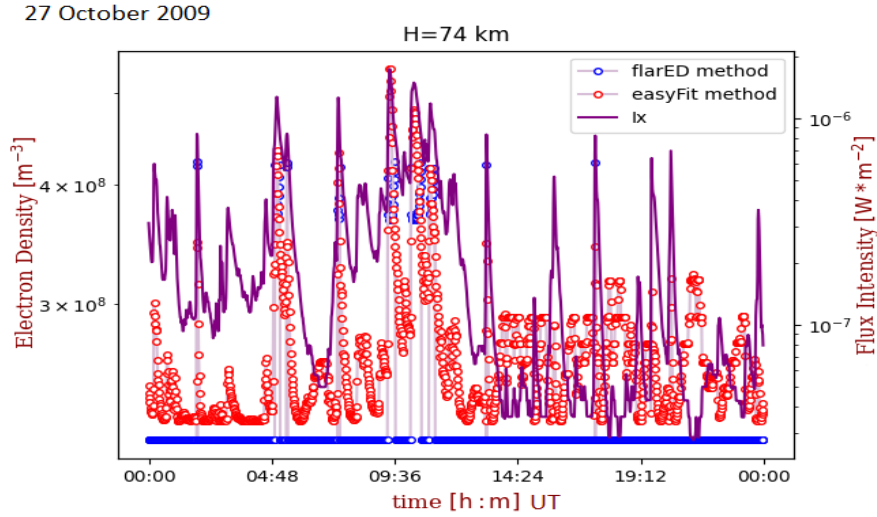
27 October 2009

Figure 5. X-ray flux from GOES-15, and *Ne* (*h* = 74 km) as a function of UT during 27 October 2009. The dashed line with circles shows results acquired by FlarED and easyFit methods.

In general, the easyFit method provided significantly more detailed insight in processed data in terms of sensitivity when applied on cases of low intensity X-ray SFs, in range of low B-class SFs to moderate C-class SFs of B1-C6.4, in terms of mimicking solar soft X-ray flux variation as compared to the FlareED method. FlareED method proven not to be sensitive to very low intensity SFs, giving practically unperturbed parameters as output in such cases. However, in cases of higher intensity SFs, FlareED method gave better results in terms of reaching maximal values in relation to peaks of solar soft X-ray flux variation. On the other hand, both methods gave either some false and/or positive-exaggerated output results. Both methods have proven to be more efficient in cases of more standalone SFs than these of high back-to-back occurrence, with the easyFit method superior in efficiency of recognizing X-ray flux outages, compared to FlareED method that showed no ability at all.

Results regarding electron densities at a nominal height of 74 km, as obtained by the application of classical approach based on NAA/24.0 kHz signal recordings from the Belgrade VLF database in the case of three X-ray SF events of low intensity: a) low intensity C-class solar flare event C3.7 from the 16 December 2009 at 13:02UT, b) moderate intensity C-class solar flare event C6.5 from the 23 December 2009 at 10:17UT and c) moderate intensity B-class solar flare event B8.35 from the 27 October 2009 at 13:11UT (Kolarski et al., 2022a) are compared with the results obtained by application of numerical methods the
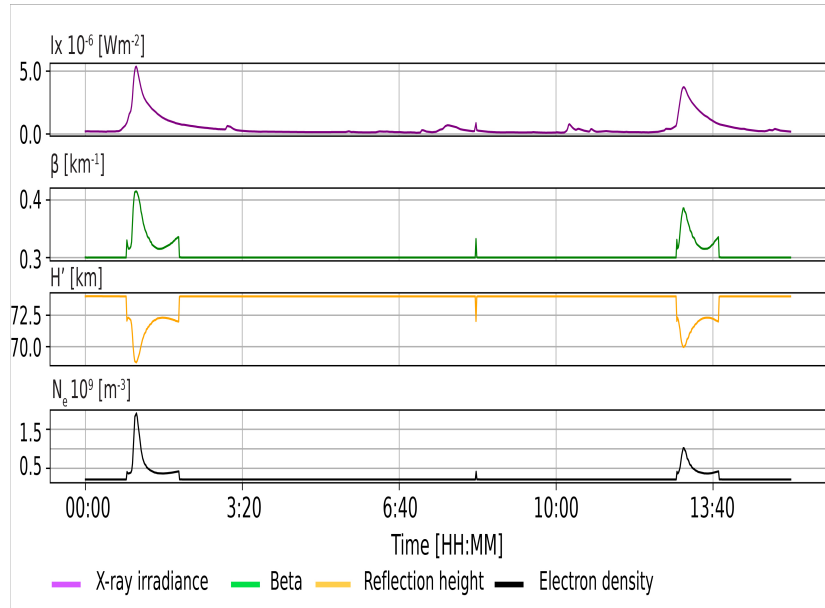
Figure 6. X-ray flux from GOES-15, β and H' parameters and Ne ($h = 74$ km) as a function of UT during 16 December 2009 as results acquired by method relying on ML.

FlareED and the easyFit in the case of these SF events and presented in Table 1. In the case of the B8.3 SF, the lowest in intensity of these three SFs, both methods gave electron density of the same order of magnitude, with the result from the easyFit method slightly overestimated and from the FlarEd method slightly underestimated compared to one from the classical approach, with the result from the FlarEd method closer in absolute value. In the case of C3.7 SF, medium in strength of these three SFs, both methods gave electron density underestimated compared to one from classical approach, with the result obtained from the easyFit method closer in absolute value. In the case of C6.4, the highest in strength of these three SFs, both methods gave electron density of the same order of magnitude, with the result from the easyFit method significantly overestimated and from the FlarEd method much overestimated compared to one from classical approach, with the result from the FlarEd method closer in absolute value. In all the cases, the FlareED method gave the results lower in absolute value compared to corresponding from the easyFit, for approximately 17.4%, 3.7% and 29.6% for these SFs, from lowest to highest in intensity, respectively. The results obtained based on the applied ML technique are in general very close to those obtained from the easyFit numerical method (Table 1), proving that this novel approach is as efficient as other two applied numerical
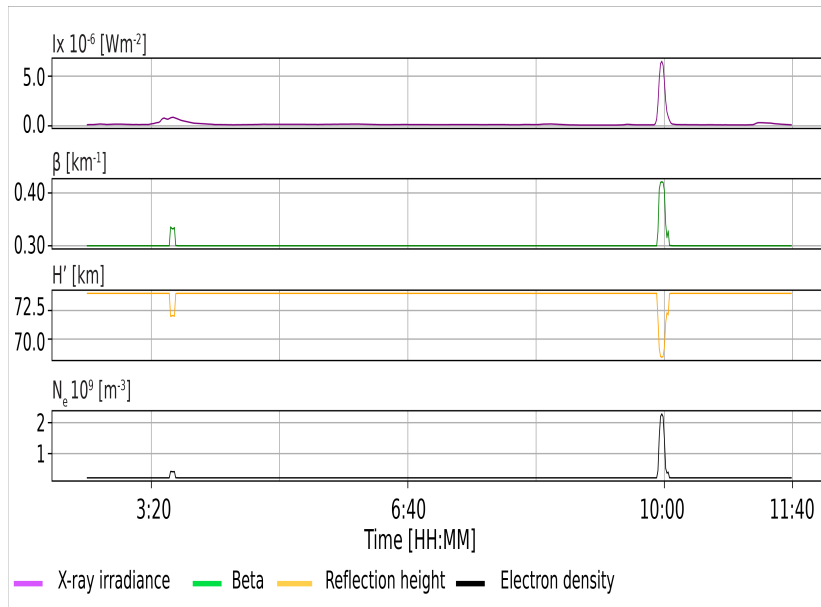
Figure 7. X-ray flux from GOES-15, β and H' parameters and Ne ($h = 74$ km) as a function of UT during 23 December 2009 as results acquired by method relying on ML.

methods in the cases of low intensity SFs. The ML based approach gave the same electron density value in the case of B8.3 SF, slightly higher (for 0.99%) value in the case of C3.7 SF and somewhat lower value (for 2.15%) in the case of C6.4 SF. Figures 6-8 present output results from the applied ML workflow for these three SFs, with X-ray flux in violet, sharpness in green, reflection height in orange and estimated electron density in black.

4. Summary

Overall, B - and C-class SFs occurring during solar minimum have a significant impact on the ionosphere. Impacts on the lower ionosphere of B - and C-class SFs during the 23/24 solar minimum has shed some light on the complex relationship between solar activity and Earth's upper atmosphere. Low class solar flares, although considered notably weaker in comparison to more powerful flares, still have the potential to significantly affect ionospheric dynamics especially during solar minimum periods. Understanding the ionospheric response to low intensity SFs during solar minimum is essential for understanding the potential adverse effects that such events can have on terrestrial communication systems and enhancing our overall space weather prediction capabilities.
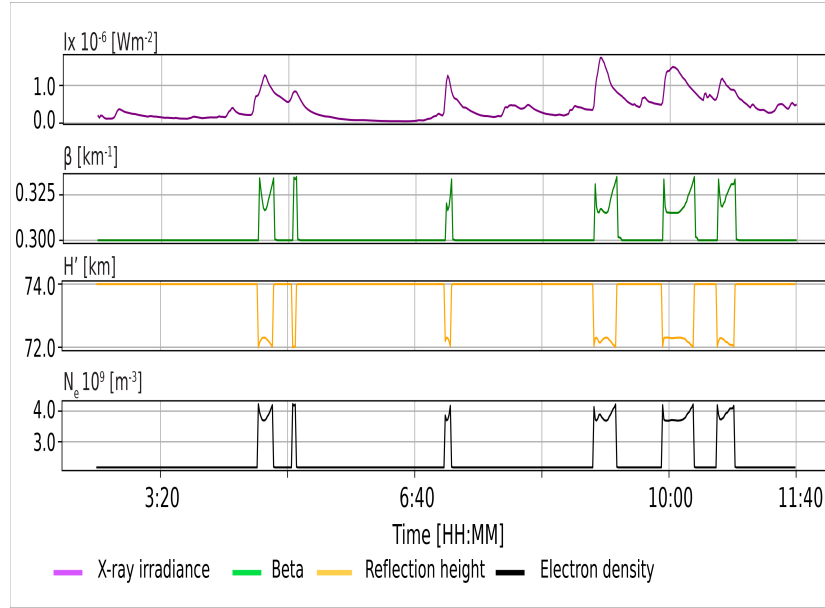
Figure 8. X-ray flux from GOES-15, β and H' parameters and Ne ($h = 74$ km) as a function of UT during 27 October 2009 as results acquired by method relying on ML.

Numerical methods FlareED and easyFit were applied to SFs of low intensity ranging from B1 to C6.4 during seven selected days from period covering solar minimum between SCs 23 and 24, with the aim to test these two methods' efficiency and sensitivity when going through calculations related to SFs of low intensity, mainly from upper B-class and lower C-class solar X-ray flux. Both methods gave satisfactory results in terms of efficiency in cases of events stronger in intensity, with the easyFit method absolutely superior in cases of X-ray flux variations of very low intensity. A novel ML based approach gave results very similar to these obtained by easyFit method, giving great potential for applications in future studies.

When compared with results obtained from the classical approach using the LWPC methodology, in case of three SFs that cover the entire analyzed soft X-ray flux range (B8.3, C3.7 and C6.4) and can be taken as typical examples from their range, results obtained from FlareED method are lower in value compared to ones from easyFit. Compared to classical approach, in case of a) B8.3 SF Ne(easyFit) and Ne(FlarED) are for approximately 11% higher and 9% lower compared to Ne(LWPC), respectively. In case of b) C3.7 Ne(easyFit) and Ne(FlarED) are for approximately 20% lower and 30% lower compared to Ne(LWPC), respectively. In case of c) C6.4 SF Ne(easyFit) and Ne(FlarED) are for approximately 99% higher (almost twice higher) and 40% higher compared to Ne(LWPC), respectively.

The findings from this research can potentially contribute to the development of improved forecasting models, enabling better prediction and preparedness for ionospheric disruptions caused by low class SFs. The study of low class SFs during solar minimum and their impact on the ionosphere highlights the need for continued research and monitoring of such events to enhance our understanding of space weather phenomena and protect technological infrastructure from potential disruptions.

References

Arnaut, F., Kolarski, A., & Srećković, V. A., Random Forest Classification and Ionospheric Response to Solar Flares: Analysis and Validation. 2023, *Universe*, **9**, DOI: 10.3390/universe9100436

Barta, V., Natras, R., Srećković, V., et al. 2022, Multi-instrumental investigation of the solar flares impact on the ionosphere occurring in December 2006, Tech. rep., Copernicus Meetings

Bothmer, V., Daglis, I. A., & Bogdan, T. J., Space Weather: Physics and Effects. 2007, *Physics Today*, **60**, 59, DOI: 10.1063/1.2825074

Breiman, L., Random forests. 2001, *Machine learning*, **45**, 5

Chen, T. & Guestrin, C., Xgboost: A scalable tree boosting system. 2016, in *Proceedings of the 22nd acm sigkdd international conference on knowledge discovery and data mining*, 785–794

Curto, J. J., Geomagnetic solar flare effects: a review. 2020, *Journal of Space Weather and Space Climate*, **10**, 27, DOI: 10.1051/swsc/2020027

Grodji, O. D. F., Doumbia, V., Amaechi, P. O., et al., A Study of Solar Flare Effects on the Geomagnetic Field Components during Solar Cycles 23 and 24. 2022, *Atmosphere*, **13**, 69, DOI: 10.3390/atmos13010069

Grubor, D., Šulić, D., & Žigman, V., Classification of X-ray solar flares regarding their effects on the lower ionosphere electron density profile. 2008, *Annales Geophysicae*, **26**, 1731, DOI: 10.5194/angeo-26-1731-2008

Hayes, L. A., O'Hara, O. S. D., Murray, S. A., & Gallagher, P. T., Solar Flare Effects on the Earth's Lower Ionosphere. 2021, *Solar Physics*, **296**, 157, DOI: 10.1007/s11207-021-01898-y

Kelly, M. C. 2009, *The Earth's Ionosphere: Plasma Physics and Electrodynamics, Second Edition*

Kolarski, A., Grubor, D., & Šulić, D., Diagnostics of the Solar X-Flare Impact on Lower Ionosphere through the VLF-NAA Signal Recordings. 2011, *Open Astronomy*, **20**, 591, DOI: 10.1515/astro-2017-0342

Kolarski, A., Srećković, V. A., & Mijić, Z. R., Monitoring solar activity during 23/24 solar cycle minimum through VLF radio signals. 2022a, *Contributions of the Astronomical Observatory Skalnate Pleso*, **52**, 105, DOI: 10.31577/caosp.2022.52.3.105

Kolarski, A., Srećković, V. A., & Mijić, Z. R., Response of the Earth's Lower Ionosphere to Solar Flares and Lightning-Induced Electron Precipitation Events by Analysis of VLF Signals: Similarities and Differences. 2022b, *Applied Sciences*, **12**, 582, DOI: 10.3390/app12020582

Ratcliffe, J. A. et al. 1972, *An introduction to ionosphere and magnetosphere* (CUP Archive, Cambridge, UK)

Silber, I. & Price, C., On the use of VLF narrowband measurements to study the lower ionosphere and the mesosphere–lower thermosphere. 2017, *Surveys in Geophysics*, **38**, 407, DOI: 10.1007/s10712-016-9396-9

Srećković, V. A., Šulić, D. M., Ignjatović, L., & Vujčić, V., Low Ionosphere under Influence of Strong Solar Radiation: Diagnostics and Modeling. 2021a, *Applied Sciences*, **11**, 7194, DOI: 10.3390/app11167194

Srećković, V. A., Šulić, D. M., Vujčić, V., Jevremović, D., & Vyklyuk, Y., The effects of solar activity: Electrons in the terrestrial lower ionosphere. 2017, *Journal of the Geographical Institute" Jovan Cvijic", SASA*, **67**, 221, DOI: 10.2298/IJGI1703221S

Srećković, V. A., Šulić, D. M., Vujčić, V., Mijić, Z. R., & Ignjatović, L. M., Novel Modelling Approach for Obtaining the Parameters of Low Ionosphere under Extreme Radiation in X-Spectral Range. 2021b, *Applied Sciences*, **11**, 11574, DOI: 10.3390/app112311574

Šulić, D. M. & Srećković, V. A., A Comparative Study of Measured Amplitude and Phase Perturbations of VLF and LF Radio Signals Induced by Solar Flares. 2014, *Serbian Astronomical Journal*, **188**, 45, DOI: 10.2298/SAJ1488045S

Šulić, D. M., Srećković, V. A., & Mihajlov, A. A., A study of VLF signals variations associated with the changes of ionization level in the D-region in consequence of solar conditions. 2016, *Advances in Space Research*, **57**, 1029, DOI: 10.1016/j.asr.2015.12.025

Wait, J. R. & Spies, K. P. 1964, *Characteristics of the Earth-ionosphere waveguide for VLF radio waves* (US Department of Commerce, National Bureau of Standards, Boulder, CO, USA)

Žigman, V., Grubor, D., & Šulić, D., D-region electron density evaluated from VLF amplitude time delay during X-ray solar flares. 2007, *Journal of Atmospheric and Solar-Terrestrial Physics*, **69**, 775, DOI: https://doi.org/10.1016/j.jastp.2007.01.012

Study of spectral index of giant radio galaxy from Leahy's Atlas: DA 240

V. Borka Jovanović[1] , **D. Borka**[1] and **P. Jovanović**[2]

[1] *Department of Theoretical Physics and Condensed Matter Physics (020),*
Vinča Institute of Nuclear Sciences - National Institute of the Republic of
Serbia, University of Belgrade, P.O. Box 522, 11001 Belgrade, Serbia,
(E-mail: vborka@vinca.rs), (E-mail: dusborka@vinca.rs)
[2] *Astronomical Observatory, Volgina 7, P.O. Box 74, 11060 Belgrade, Serbia,*
(E-mail: pjovanovic@aob.rs)

Abstract. Here we investigate the giant radio galaxy DA 240, which is a FR II source. Specifically, we investigate its flux density, as well as the spectral index distribution. For that purpose, we used publicly available data for the source: Leahy's atlas of double radio-sources and NASA/IPAC Extragalactic Database (NED). We used observations at 326 MHz (92 cm) and at 608 MHz (49 cm) and obtained spectral index distributions between 326 and 608 MHz. For the first time we give spectral index map for these frequencies. We found that the synchrotron radiation is the dominant radiation mechanism over most of the area of DA 240, and also investigated the mechanism of radiation at some characteristic points, namely its core and the hotspots. The results of this study will be helpful for understanding the evolutionary process of the DA 240 radio source.

Key words: galaxies: active – galaxies: jets – galaxies: nuclei – radio continuum: galaxies – galaxies: individual: DA 240

1. Introduction

Double Radio sources Associated with Galactic Nuclei (DRAGNs) are clouds of radio-emitting plasma which have been shot out of active galactic nuclei (AGN) via narrow jets. More precisely, a DRAGN would be a radio source containing at least one of the following types of extended, synchrotron-emitting structures: jet, lobe, and hotspot complex (Leahy, 1993).

AGNs are emitting the most radiation from galaxies, and in case of radio galaxies, a lot of their radiation is emitted at radio wavelengths. Giant radio galaxies (GRGs) belong to a unique class of objects with very large radio structures. Originally, they were defined to be the radio galaxies with projected linear sizes greater than 1 Mpc (Willis et al., 1974). This limit applied to a spatially flat ($\Omega_\kappa = 0$) Friedmann cosmological model with the Hubble constant $H_0 = 75$

km s^{-1} Mpc^{-1}, deceleration parameter $q_0 = 0.5$ and zero cosmological constant ($\Omega_\Lambda = 0$). Nowadays, the GRG size limit is equivalent to 700 kpc (Tang, 2021) in a ΛCDM cosmology with the parameters by Planck Collaboration from 2016, i.e. in the flat cosmological model with H$_0$ = 67.8 km s^{-1} Mpc^{-1} and $\Omega_m = 0.308$ (Planck Collaboration, 2016). Due to this comparatively large angular extent of the GRG population, astronomers can observe their fine structures with detailed imaging.

DRAGN DA 240 was among the first GRGs to be recognized as such (more precise, 3C 236 and DA 240 are the first two discovered GRGs, both identified as Fanaroff-Riley II types). A study of its environment can be found in Peng et al. (2004). It consists of two radio clouds about 40′ long, and a comparatively weak central core (Artyukh & Ogannisyan, 1988). This giant radio source, with linear size spanning over 1.3 Mpc, is placed at a distance of 215 Mpc. There are also other researchers who investigated radio source DA 240 (Mack et al., 1997; Chen et al., 2011a,b, 2018a,b; Peng et al., 2015; Milley, 2019).

2. Data and method

Regarding Earth-space (and also space-Earth) communication ranges, there is a wide spectral window in radio band in which Earth's ionosphere does not reflect extraterrestrial radio waves and where atmosphere is transparent for them. This range of radio frequencies, observable from Earth, spans from ∼10 MHz (30 m) to ∼1 THz (0.3 mm). Particularly, for DA 240 there are freely available ground-based observational data at the following frequencies: 326, 608, 2695, 4750 and 10550 MHz. Among these, for this paper we choose observations only at 326 and 608 MHz because of their completeness, and due to good visibility of this source over the whole its area, as well. This is not the case for other three frequencies, where only the regions around hotspots and jets are clearly visible, while the radio lobes are pretty faint at these frequencies.

For our calculations, we used Flexible Image Transport System (FITS) data files containing the flux densities in Jy (1 Jy = 10^{-26} W m^{-2} Hz^{-1}) of a chosen radio source. We described the structure of FITS format, as well as what is useful for our investigation, in our previous paper Borka Jovanović et al. (2023). Besides its flexibility and storage efficiency, here we want to point out the long term archiving i.e. all versions of the FITS format are backwards-compatible, so one can compare data from more observations (details at `https://heasarc.gsfc.nasa.gov/docs/heasarc/fits_overview.html`).

The observed data are available in `An Atlas of DRAGNs` i.e. the "3CRR" sample of Laing, Riley & Longair (1983). Besides FITS files, this sample gives the readers very useful information from the literature on the DRAGNs, with tables and references, too. There are the Introductory Pages, Description Pages (with full details) and the Listings of individual DRAGNs. Also, we used astronomical database compiled by NASA and IPAC, i.e. NED database - a comprehensive

database of multiwavelength data for extragalactic objects, with the information and bibliographic references regarding these objects.

Hence, the easily searchable and accessible data are provided at:

– J. P. Leahy, A. H. Bridle, R. G. Strom, An Atlas of DRAGNs (2013): http://www.jb.man.ac.uk/atlas/ (Leahy, Bridle & Strom, 2013),

– NASA/IPAC Extragalactic Database: http://ned.ipac.caltech.edu/ (Mazzarella & the NED Team, 2002).

The observations of DA 240 at 326 and 608 MHz were carried out using "The Westerbork Synthesis Radio Telescope" (WSRT) radio telescope. It is located in Netherlands, previously ran by Netherlands Foundation for Research in Astronomy, underwent more upgrades and a major (phased array upgrade of the WSRT) was completed in 2019, resulting in the WSRT-Apertif system. Nowadays, WSRT-Apertif telescope is operated as a survey instrument by ASTRON – the Netherlands Institute for Radio Astronomy.

It is useful here to notice that we used the calibrated data, i.e. the data and images after they are processed using analysis techniques and programs like CLEAN algorithm (see Strom, Baker & Willis (1981) and references therein). Particularly, regarding the resolutions of the processed data used here, their values are: $20''$ at 326 MHz and $9.2''$ at 608 MHz.

We used observations of DA 240 at two frequencies, 326 MHz (Willis & O'Dea, 1990) and 608 MHz (Willis et al., 1974). The calculation method, which we have developed, was first published in Borka (2007), with the most detailed explanation given in Borka Jovanović (2012), and further elaborated in Borka Jovanović et al. (2012), also. The area of the investigated radio source, as well as the flux densities, are determined in these three ways: I - flux density contours (isolines S_ν); II - flux density 2D profiles, for constant declination; III - 3D profiles (by doing the procedure in all three ways, it can easily be checked whether the results and analysis are good).

As a telescope is most sensitive to extended emission at long wavelengths (i.e. smaller frequencies), the WSRT could provide detailed and sensitive maps of DA 240 at long wavelengths. So, it had a resolvong power sufficient to separate this large object from unrelated confusing sources. As noted in original discovery paper by Willis et al. (1974), a remarkable feature is the huge range of surface brightness over the intensity map, as well as the prominence of the eastern component. Also, it has strong linear polarization: an integrated percentage polarization at 49 cm of 8.3%.

3. The flux density distribution of giant radio galaxy DA 240

The radio source DA 240 (cross-identifications: DA 240; CGCG 262-029; CGCG 0744.6+5556; MCG +09-13-057; 4C +56.16; 2MASX J07483682+5548591) is an

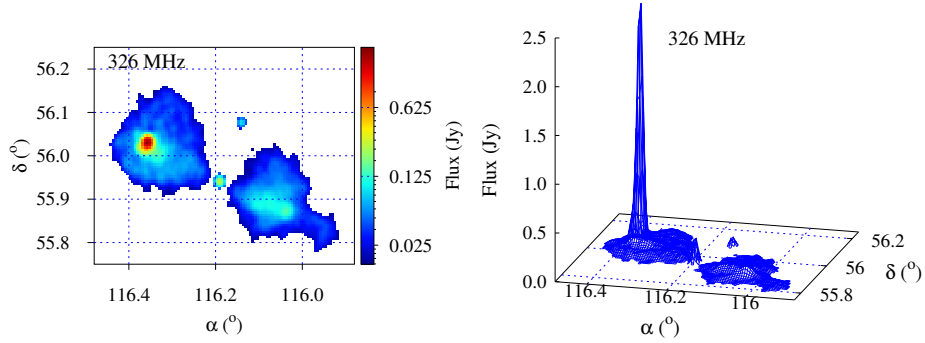example of Classical Double radio sources. Its projected linear size is about 1350 kpc.

Figure 1. 2D plot (left) and 3D plot (right) of DA 240 flux density distribution (in Jy), presented in Equatorial coordinate system (α, δ), at 326 MHz.
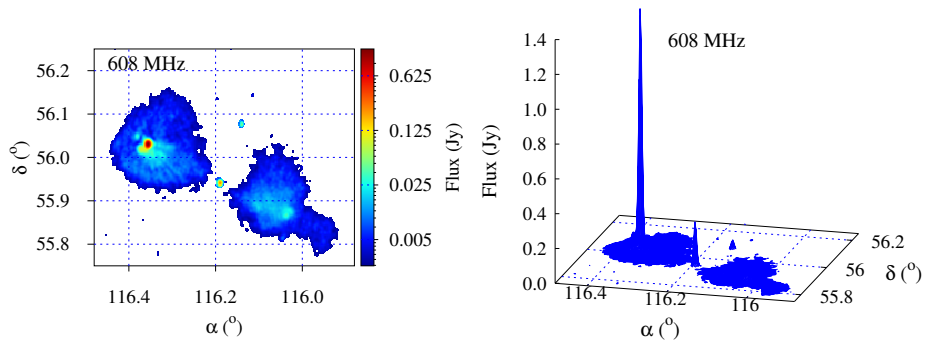

Figure 2. The same as in Fig. 1, but for 608 MHz.

From the observations of DA 240 at two frequencies, 326 MHz (92 cm) and 608 MHz (49 cm), we determined the contours which represent the lower boundaries of the source. We found that the minimal fluxes are the following: $S_{\nu,min} = 0.016$ Jy at 326 MHz, and $S_{\nu,min} = 0.0023$ Jy at 608 MHz. The areas of DA 240, with the flux density distributions (in Jy) over these areas, we presented by two-dimensional and three-dimensional plots in Figs. 1 and 2. From these radio maps, the spherical radio lobes can be clearly seen, as well as their hotspots at the end of each beam.

We also give an examples of flux profiles for some constant declinations, at the both frequencies. In Fig. 3 we give the profile for $\delta = 56°.03$ containing

north-eastern hotspot (left) and for $\delta = 55°.87$ containing south-western hotspot (right), at 326 MHz; while in Fig. 4 we give profiles for the same δ but at 608 MHz.

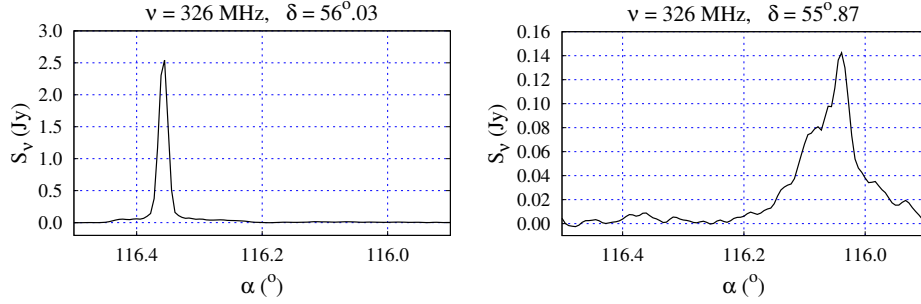**Figure 3.** The 326 MHz flux profiles for constant declinations $\delta = 56°.03$ (left) and $\delta = 55°.87$ (right), containing northern and southern hotspots.
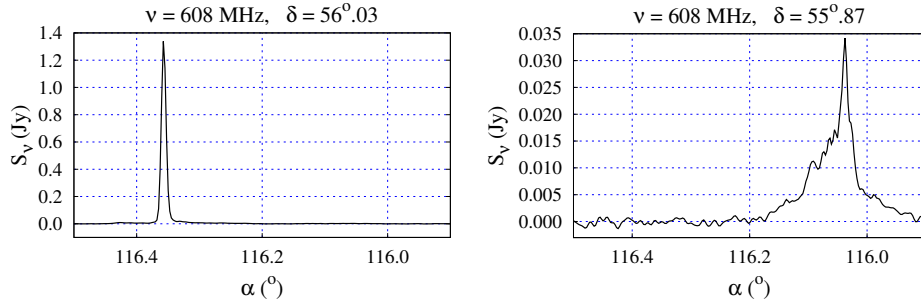

Figure 4. The same as in Fig. 3, but for 608 MHz.

4. Spectral index distribution between 326 and 608 MHz

The amount of flux density S_ν as a function of frequency ν is given by the expression:

$$S_\nu \sim \nu^{-\alpha}, \tag{1}$$

where α is a constant, called the "radio spectral index".

The radio spectral index α can be obtained using the flux density at different frequencies and taking the negative slope of the relation (1). Therefore, we calculate it by the following equation:

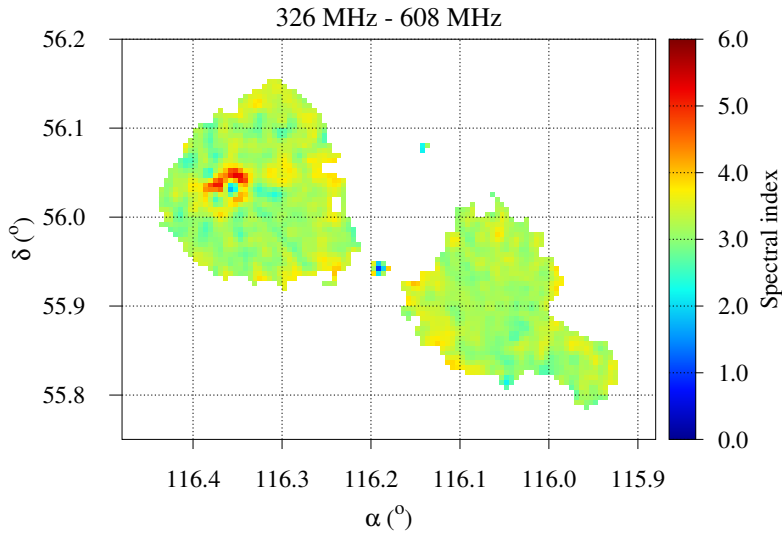$$\alpha = -\frac{\log\left(\dfrac{S_{\nu_1}}{S_{\nu_2}}\right)}{\log\left(\dfrac{\nu_1}{\nu_2}\right)}.\tag{2}$$

Figure 5. Spectral indices between 326 and 608 MHz over the area of DA 240.

To obtain the radio spectral index α between two frequencies, in each point over the area of the source, we need values of fluxes at the same coordinates (α, δ). As we have used data with different resolutions, first we had to reduce them to the same resolution, and then to apply Eq. (2). For that purpose we used bilinear interpolation for resampling observations with higher resolution (608 MHz) to the nearest existing coordinates at lower resolution (326 MHz). In that way, the data were comparable, and we were able to calculate spectral index.

The spectral index is used for classification of radio sources and studying the origin of radio emission:

– If $\alpha > 0.1$ the emission is non-thermal (synchrotron) and it means that it does not depend on the temperature of the source,

– for $\alpha < 0$ it is thermal and depends only on the temperature of the source.

We calculated spectral indices between 326 and 608 MHz, over the whole area of DA 240, and we show how they change over this area in Fig. 5.

From the colorbar in Fig. 5 we can read the values of radio spectral index α, and we can notice that over the area of DA 240 it ranges from ≈ 0 to positive values, meaning this: $\alpha > 0$ corresponds to non-thermal mechanism of radiation while $\alpha < 0$ corresponds to thermal mechanism of radiation. When the spectral index is zero, the flux density is independent of frequency, and the spectrum is said to be flat.

As is it can be seen from the presented radio-index map, the spectral index is almost always higher than zero, except in only few small parts where it is around zero. As expected, the largest values of spectral index are in the regions around hotspots (especially eastern one), while the lowest values are in vicinity of AGN, which is dominated by thermal radiation mechanism. This indicates that the non-thermal (synchrotron) emission is by far the most dominant radiation mechanism over the whole source (except at AGN).

5. Discussion and conclusions

We used the available flux densities of DA 240 at 326 and 608 MHz to provide the spectral index distribution derived between these two frequencies. At both frequencies, the flux structure is characterized with obvious hotspots and the core. We can notice a large variations of flux density over the intensity map, with its highest value at the eastern component, which is dominant high brightness region. In the spectral index map this tendency is even more pronounced.

For the first time we give spectral index map of DA 240 between 326 and 608 MHz. We show that synchrotron radiation is the dominant emission mechanism over the majority of the area of the source, except in the central core.

Our investigation of the giant radio galaxy DA 240, i.e. of the flux density and spectral index distribution, is leading to the following conclusions:

– by using publicly available data (Leahy's atlas of double radio-sources, as well as the NED database), we were able to investigate flux densities at 326 MHz (92 cm) and 608 MHz (49 cm),

– although we have developed method of calculation for main Galactic radio loops I-VI, it is applicable (and also rather efficient) to all SNRs, end to extragalactic radio sources, as well,

– from our results, a remarkable feature can be noticed: the huge range of flux density over the intensity map, as well as the prominence of the eastern component,

– there are two lobes, with a prominent hotspot in the north-east component, and a weaker one to the south-west,

- the distribution of spectral index α enables to follow how α varies over the area, to read its values, and also to determine the origin of the radiation,

- synchrotron radiation is the dominant emission mechanism over the whole area of the source.

References

Artyukh, V. S., Ogannisyan, M. A.: 1988, *Sov. Astron. Lett.* **14**, 301

Borka, V.: 2007, *Mon. Not. R. Astron. Soc.* **376**, 634

Borka Jovanović, V.: 2012, *Publ. Astron. Obs. Belgrade*, **91**, 121

Borka Jovanović, V., Borka, D., Skeoch, R., Jovanović, P.: 2012, *Publ. Astron. Obs. Belgrade*, **91**, 255

Borka Jovanović, V., Borka, D., Arsenić, A., Jovanović, P.: 2023, *Adv. Space. Res.*, **71**, 1227

Chen, R., Peng, B., Strom, R. G., Wei, J., Zhao, Y.: 2011a, *Astron. Astrophys.*, **529**, A5

Chen, R., Peng, B., Strom, R. G., Wei, J., Zhao, Y.: 2011b, *Mon. Not. R. Astron. Soc.*, **412**, 2433

Chen, R.-R., Strom, R., Peng, B.: 2018a, *Astrophys. J.*, **858**, 83

Chen, R.-R., Peng, B., Strom, R.: 2018b, *PASP*, **130**, 054102

Leahy, J. P.: 1993, "DRAGNs", in Proceedings: Jets in Extragalactic Radio Sources, Eds. H.-J. Roser and K. Meisenheimer, *Lecture Notes in Physics* **421**, 1

Laing, R. A., Riley, J. M., Longair, M. S.: 1983, *Mon. Not. R. Astron. Soc.* **204**, 151

Leahy, J. P., Bridle, A. H., Strom, R. G.: 2013, An Atlas of DRAGNs - online: http://www.jb.man.ac.uk/atlas/

Mack. K.-H., Klein, U., O'Dea, C. P., Willis, A. G.: 1997, *Astron. Astrophys. Suppl. Ser.*, **123**, 423

Mazzarella, J. M. and the NED Team, "Using the NASA/IPAC Extragalactic Database (NED) and Federated Virtual Observatory Archives for Multiwavelength Studies of AGN", in Proceedings: AGN Surveys, Eds. Green, R. F., Khachikian, E. Ye. and Sanders, D. B.: 2002, Astron. Soc. Pacific Conference Series **284**, 379

Miley, G.: 2019, *PoS Westerbork* **005**, 72

Peng, B., Strom, R. G., Wei, J., Zhao, Y. H.: 2004, *Astron. Astrophys.* **415**, 487

Peng, B., Chen, R.-R., Strom, R.: 2015, *PoS AASKA14* **109**, 487

Planck Collaboration Int. XIII.: 2016, *Astron. Astrophys.* **594**, A13

Strom, R. G., Baker, J. R., Willis, A. G.: 1981, *Astron. Astrophys.* **100**, 220

Tang, H.: *Doctoral Thesis: Giant Radio Galaxies as Probes of the Low Density Intergalactic Medium*, University of Manchester, UK (2021)

Willis, A. G., Strom, R. G. & Wilson, A. S.: 1974, *Nature*, **250**, 625

Willis, A. G., O'Dea, C. P.: 1990, *Proceedings of the IAU Symposium 140*, eds. R. Beck, P. P. Kronberg and R. Wielebinski, 455